Characterization of clouds and their radiative effects using ground-based instrumentation at a low-mountain site

Inaugural-Dissertation
zur
Erlangung des Doktorgrades
der Mathematisch-Naturwissenschaftlichen Fakultät
der Universität zu Köln

vorgelegt von
Kerstin Ebell
aus Beckum

Köln

2010

Berichterstatter:	Prof. Dr. S. Crewell Prof. Dr. M. Kerschgens
Tag der mündlichen Prüfung:	26.11.2010

Abstract

The interaction of clouds with radiation and aerosols is the greatest source of uncertainty in future climate projections. Part of the reason is the limited amount of observations of clouds and hence the limited knowledge of cloud macro- and microphysical statistics in connection to their effects on the radiative budget and on the vertical redistribution of energy within the atmosphere.

In 2007, the Atmospheric Radiation Measurement program's (ARM) Mobile Facility (AMF) was operated for a nine-month period in the Murg Valley, Black Forest, Germany, in support of the Convective and Orographically-induced Precipitation Study (COPS). Based on the measurements of the AMF and COPS partner instrumentation, the present study aims at improving the data basis of cloud macro- and microphysical statistics and to assess the potential of the derived cloud properties to estimate the radiative effects of clouds. The synergy of various instruments is exploited to derive a data set of high quality thermodynamic and cloud property profiles with a temporal resolution of 30 s. While quality filters in the cloud microphysical retrieval techniques mostly affect the representativity of ice and mixed clouds in the data sample, water clouds are very well represented in the derived 364,850 atmospheric profiles. In total, clouds are present 72% of the time with multi-layer mixed phase (28.4%) and single-layer water clouds (11.3%) occurring most frequently.

In order to evaluate the derived thermodynamic and cloud property profiles, radiative closure studies are performed with independent radiation measurements. In clear sky, average differences between calculated and observed surface fluxes are less than 2.1% and 3.6% for the shortwave and longwave, respectively. In cloudy situations, differences, in particular in the shortwave, are much larger, but most of these can be related to broken cloud situations. The cloud radiative effect (CRE), i.e. the difference of cloudy and clear-sky net fluxes, has been analyzed for the whole nine-month period. The largest surface (SFC) net CRE has been found for multi-layer water ($-110\,\mathrm{W\,m^{-2}}$) and mixed clouds ($-116\,\mathrm{W\,m^{-2}}$). The estimated uncertainties in the modeled SFC and top of atmopshere (TOA) net CRE are up to 39% and 26%, respectively. For overcast, single-layer water clouds, sensitivity studies reveal that the SW CRE uncertainty at the SFC and TOA is likewise determined by uncertainties in liquid water path (LWP) and effective radius, if the LWP is larger than $100\,\mathrm{g\,m^{-2}}$. For low LWP values, uncertainties in SFC and TOA shortwave CRE are dominated by the uncertainty in LWP. Uncertainties in CRE due to uncertainties in the shape of the liquid water content (LWC) profile are typically smaller by a factor of two compared to LWP uncertainties. For the difference between the cloudy and clear-sky net heating rates, i.e. the cloud radiative forcing (CRF), of water clouds, the LWP and its vertical distribution within the cloud boundaries are the most important factors.

In order to increase the accuracy of LWC profiles and consequentially of the estimates of CRE and CRF, advanced LWC retrieval techniques, such as the Integrated Profiling Tech-

nique (IPT), are needed. The accuracy of a LWC profile retrieval using typical microwave radiometer brightness temperatures and/or cloud radar reflectivities is investigated for two realistic cloud profiles. The interplay of the errors of the a priori profile, measurements and forward model on the retrieved LWC error and on the information content of the measurements is analyzed in detail. It is shown that the inclusion of the microwave radiometer observations in the LWC retrieval increases the number of degrees of freedom, i.e. the independent pieces of information in the measurements, by about 1 compared to a retrieval using measuremets from the cloud radar alone. Assuming realistic measurement and forward model errors, it is further demonstrated, that the error in the retrieved LWC is 60% or larger, if no a priori information is available, and that a priori information is essential for a better accuracy. The results of the present work strongly suggest to improve the LWC a priori profile and the corresponding error estimates in the IPT. However, there are few observational datasets available to construct accurate a priori profiles of LWC, and thus more observational data are needed to improve the knowledge of the a priori profile and the corresponding error covariance matrix.

Zusammenfassung

Die Wechselwirkung von Wolken mit Strahlung und Aerosolen stellt die größte Unsicherheitsquelle in Projektionen des zukünftigen Klimas dar. Ein Grund dafür ist die begrenzte Anzahl an Wolkenbeobachtungen und die daraus resultierende unzulängliche Kenntnis wolkenmakro- und wolkenmikrophysikalischer Eigenschaften, sowie des Effektes der Wolken auf die Strahlungsbilanz und auf die vertikale Verteilung der Energie in der Atmosphäre.

Im Jahr 2007 wurde die Mobile Facility (AMF) des Atmospheric-Radiation-Measurement-Programmes (ARM) im Murgtal, Schwarzwald, für neun Monate betrieben. Dabei war sie ein Teil der Convective and Orographically-induced Precipitation Study (COPS). Das Ziel dieser Arbeit ist die Datengrundlage wolkenmakro- und wolkenmikrophysikalischer Eigenschaften zu verbessern, indem AMF-Messungen sowie Messungen anderer COPS-Instrumente ausgewertet werden. Zudem wird das Potenzial der abgeleiteten Wolkeneigenschaften im Hinblick auf die Abschätzung des Strahlungseffektes von Wolken untersucht. Die Synergie verschiedener Instrumente wird ausgenutzt, um einen Datensatz hochwertiger thermodynamischer und wolkenmikrophysikalischer Profile mit einer zeitlichen Auflösung von 30 s abzuleiten. Während Qualitätsfilter im Retrievalverfahren der Wolkeneigenschaften vor allem die Repräsentativität von Eis- und Mischwolken im Datensample beeinträchtigen, werden Wasserwolken sehr gut durch die abgeleiteten 364.850 atmosphärischen Profile erfasst. Insgesamt treten Wolken 72 % der Zeit auf, wobei mehrschichtige Mischwolken (28,4 %) und einschichtige Wasserwolken (11,3 %) am häufigsten vorkommen.

Um die abgeleiteten atmosphärischen Profile zu evaluieren, werden Strahlungsschließungsstudien mit unabhängigen Strahlungsmessungen durchgeführt. Im wolkenfreien Fall sind die mittleren Unterschiede zwischen berechneten und beobachteten kurzwelligen bzw. langwelligen Strahlungsflüssen kleiner als 2,1 % bzw. 3,6 %. In bewölkten Situationen sind die Unterschiede wesentlich größer, wobei diese häufig in Zusammenhang mit durchbrochener Bewölkung stehen. Der ,,Cloud Radiative Effect“ (CRE), welcher die Differenz der Nettostrahlungsflüsse im bewölkten und unbewölkten Fall darstellt, wurde für die betrachteten neun Monate untersucht. Mehrschichtige Wasser- und Mischwolken verursachen den größten Netto-CRE am Boden mit $-110\,\mathrm{W\,m^{-2}}$ bzw. $-116\,\mathrm{W\,m^{-2}}$. Die Unsicherheiten im berechneten Netto-CRE am Boden betragen bis zu 39 % und am Oberrand der Atmosphäre bis zu 26 %. Für einschichtige Wasserwolken, die den Himmel komplett bedecken, ist in Sensitivitätsstudien gezeigt worden, dass die Unsicherheit im kurzwelligen CRE am Boden und am Oberrand der Atmosphäre gleichermaßen durch die Unsicherheiten im Flüssigwasserpfad (LWP) und im Effektivradius bestimmt werden, wenn der LWP größer als $100\,\mathrm{g\,m^{-2}}$ ist. Für kleine LWP-Werte dominiert die Unsicherheit im LWP die Unsicherheiten im kurzwelligen CRE am Boden und am Oberrand der Atmosphäre. Unsicherheiten im CRE, die durch Unsicherheiten in der Profilform des Flüssigwassergehaltes (LWC) hervorgerufen werden, sind typischerweise um einen Faktor 2 kleiner im Vergleich zu Unsicherheiten bezüglich des LWPs.

Für die Differenz der bewölkten und wolkenfreien Netto-Heizraten, genannt ,,Cloud Radiative Forcing“, von Wasserwolken sind der LWP und seine vertikale Verteilung innerhalb der Wolkengrenzen die wichtigsten Faktoren.

Um die Genauigkeit von LWC-Profilen und damit auch die Genauigkeit des berechneten CREs und CRFs zu verbessern, werden weiterentwickelte LWC-Retrievalverfahren wie die ,,Integrated Profiling Technique“ (IPT) benötigt. Die Genauigkeit eines LWC-Retrievalverfahrens, welches Helligkeitstemperaturen eines Mikrowellenradiometers und/oder Radarreflektivitäten eines Wolkenradars verwendet, wird für zwei realistische Wolkenprofile untersucht. Das Zusammenspiel der A-priori-Profil-, Mess- und Vorwärtsmodellfehler wird im Hinblick auf den abgeleiteten LWC-Fehler und auf den Informationsgehalt der Messungen genau untersucht. Es wird gezeigt, dass im Vergleich zu einem Retrieval, welches nur Wolkenradarmessungen nutzt, die Hinzunahme von Mikrowellenradiometerbeobachtungen die Anzahl der Freiheitsgrade, also die Anzahl der unabhängigen Informationen in den Messungen, um ungefähr 1 erhöht. Unter der Annahme realistischer Mess- und Vorwärtsmodellfehler wird weiterhin gezeigt, dass wenn keine A-priori-Information verfügbar ist, der Fehler des abgeleiteten LWCs 60 % oder größer ist. Die A-priori-Information ist daher essentiell, um die Genauigkeit zu verbessern. Die Ergebnisse dieser Arbeit zeigen deutlich, dass das A-priori-LWC-Profil und die Beschreibung des A-priori-Fehlers in der IPT verbessert werden müssen. Es existieren jedoch nur wenige Beobachtungsdatensätze, aus denen akkurate A-priori-LWC-Profile abgeleitet werden können. Daher werden mehr Beobachtungsdaten benötigt, um die Kenntnis des A-priori-Profils und der entsprechenden Fehlerkovarianzmatrix zu verbessern.

Contents

Chapter 1

Introduction

Clouds play an important role in the Earth's climate system. They participate in moisture transport by forming precipitation that returns the evaporated water to the surface and are therefore an important part of the hydrological cycle. Moreover, they affect the Earth's climate by modulating the vertical and horizontal distribution of solar radiative heating, latent heating, and cooling by thermal radiation that drive the atmospheric circulation. Thus, they form the most direct link between atmospheric radiation and dynamics. Despite the relevance of clouds for the climate system, the present knowledge of clouds and the complex atmospheric processes associated with them is fragmentary and far from complete. Consequently, the ability of state-of-the-art atmospheric models to reproduce observed cloud parameters is often inadequate. Moreover, many cloud processes occur on small spatial scales that are not resolved by present-day weather and climate prediction models, implying that most cloud processes must be parameterized. In a broader perspective, the representation of clouds and their interaction with radiation and aerosols is probably the greatest source of uncertainty in the projection of future climate (*IPCC*, 2007; *IPCC*, 2001). This state of affairs can at least partly be ascribed to the huge variability that clouds exhibit in space and time making them hard to monitor and model.

1.1 Motivation

In a recent survey of 14 leading climate scientists on the time-dependent response of the climate system, all experts ranked the uncertainty in cloud radiative feedbacks as contributing most to the uncertainty about future global mean temperature change (*Zickfeld* et al., 2010). The outcome of this survey reflects the statement of the latest Intergonvernmental Panel on Climate Change (IPCC) assessment report (AR4) that "cloud feedbacks [of climate change] remain the largest source of uncertainty" (*IPCC*, 2007). In particular, clouds and their interaction with radiation and aerosols are not well understood imposing large uncertainties in the corresponding climate radiative forcing (*IPCC*, 2007; *IPCC*, 2001). The radiative forcing, as defined by the IPCC, is the net change in irradiance at the tropopause after stratospheric equilibrium is reached, but with a fixed tropospheric state. The largest uncertainties in radiative forcing are related to aerosols, whereby aerosol forcings are categorized into direct and indirect effects. The direct effect is associated with scattering and absorption of shortwave and longwave radiation by aerosols. Indirect aerosol effects are related to mechanisms by which aerosols modify the microphysical properties of clouds. These modifications in turn

affect the radiative properties of clouds, their lifetime and the cloud amount. An increase in aerosol concentration, for example, can lead to an increase of the albedo of clouds under the assumption of a constant cloud liquid water content. This effect is known as the first indirect effect, cloud albedo effect or Twomey effect. In the third IPCC assessment report (*IPCC*, 2001), the cloud albedo effect was found to be a key uncertainty in the climate radiative forcing. Although a best estimate of the radiative forcing associated with the cloud albedo effect is now given in the IPCC AR4 with a value of $-0.7\,\mathrm{W\,m^{-2}}$ and a 90% confidence range from $-1.8\,\mathrm{W\,m^{-2}}$ to $-0.3\,\mathrm{W\,m^{-2}}$, the uncertainties remain large and the level of scientific understanding low. This radiative forcing still carries the greatest uncertainty of all climate forcing mechanisms reported by the IPCC AR4.

Part of the reason for the discussed uncertainties is the limited amount of observations of clouds and hence the limited knowledge of cloud macro- and microphysical statistics in connection to their effects on the radiative budget and on the vertical redistribution of energy within the atmosphere. Compared to other meteorological parameters like temperature, pressure, and humidity, cloud observations are sparse, even though these observations are essential in order to better understand the complex processes associated with clouds including their interaction with radiation. This understanding is important for the improvement of the representation of clouds and cloud processes in numerical weather prediction (NWP) and climates models.

In order to make progress in these important topics, the Atmospheric Radiation Measurement (ARM) program was founded in 1989 with funding from the U.S. Department of Energy. In particular, the goal of the ARM program is "to increase our understanding of the interaction between clouds and atmospheric fluxes, and then to capture that knowledge in improved climate models" (*Ackerman and Stokes*, 2003). To this end, three permanent climate research sites have been established by the ARM program in different climate regimes, namely in the Southern Great Plains, in the Tropical Western Pacific on the islands Manus and Nauru, and at Barrow located at the North Slope of Alaska. These measurement sites are equipped with various active and passive remote sensing instruments together with standard meteorological instrumentation including, for example, a cloud radar, various radiometers, lidar-ceilometers, radiosondes and instruments for aerosol observations. These measurements are particularly suited for observing clouds, aerosol and radiation and are therefore very valuable for cloud-radiation interaction studies.

In addition to these permanent sites, the ARM Mobile Facility exists with instrumentation and data systems similar to the fixed sites. The portability and flexibility of the ARM Mobile Facility (AMF) allows for the exploration of clouds and other meteorological questions around the world. Outside the USA, long-term measurement campaigns with the AMF of 6 month or longer have been performed in Niger, China, on the Azores, and in Germany. In Germany, the AMF was deployed from 1 April to 31 December 2007 in the Murg Valley, Black Forest (48° 32' 24.18" N, 8° 23' 48.72" E, Altitude: 511.43 m above MSL, marker M in Fig. 1.1). This AMF deployment was part of the Convective and Orographically-induced Precipitation Study (COPS; *Wulfmeyer* et al., 2008) field campaign from 1 June to 31 August 2007. Due to the poor quality of quantitative precipitation forecasts over low-mountain regions, the COPS experiment aimed at an improved understanding of the physical and chemical processes in precipitation formation and at a better representation of these processes in NWP models. For COPS, five supersites were set up with synergetic remote sensing instruments from the Vosges mountains to Stuttgart (cf. Fig. 1.1). The instrumentation at the supersites were complemented by aircraft measurements, two mobile X-band radars, and radiosonde stations among others. In addition to its standard instrumentation, the AMF was equipped with

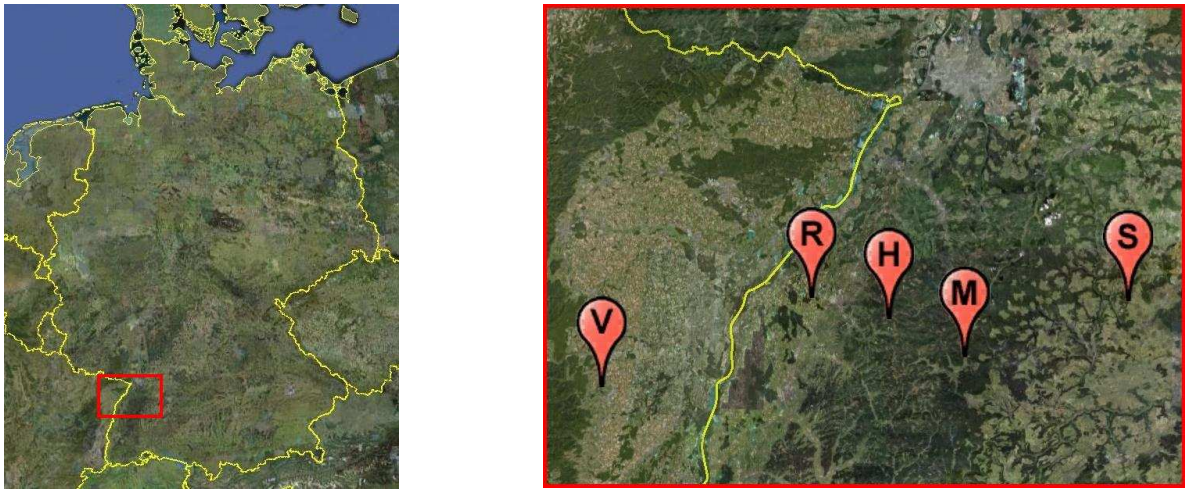

Figure 1.1: Location of COPS area (red rectangle, left) in Germany and the five supersites in the COPS domain (right), namely in the Vosges mountains (V), the Rhine valley (R), on the mountain Horninsgrinde (H), in the Murg valley (M) and near to Stuttgart (S). (*Google Earth*, 2010).

further instrumentation: two microwave radiometers of the University of Cologne, aerosol and Doppler wind lidars of the Leibniz Institute for Tropospheric Research in Leipzig, a microrain precipitation radar of the University Hohenheim, a global positioning system (GPS) receiver of the German Research Center for Geosciences in Potsdam, and soil moisture sensors of the Research Center Karlsruhe.

Based on the nine-month measurements in the Murg Valley, the present study aims at improving the data basis of cloud macro- and microphysical statistics and to assess the potential of the derived cloud properties to estimate the radiative effects of clouds. To this end, state-of-the-art ground-based cloud property retrieval algorithms are used to derive cloud property profiles with a high temporal and vertical resolution. By means of a state-of-the-art broadband radiative transfer model, the radiative effects of clouds are analyzed and uncertainties due to uncertainties in the derived cloud property profiles are assessed.

1.2 Studies on clouds and their interaction with radiation

The radiative effects of clouds have been studied for a long time, but most of these earlier studies have focused on the effect of clouds on the radiation balance at the top of atmosphere (TOA) employing satellite data. Major satellite experiments in this respect are the Earth Radiation Budget Experiment (ERBE) with scanning radiometer measurements on the satellite Nimbus 7 (*Barkstrom*, 1984) and the Scanner for Radiation Budget (ScaRaB) missions (*Kandel*, 1998) from 1994 to 1995 and from 1998 to 1999. Present-day experiments are the Clouds' and the Earth's Radiant Energy System (CERES; *Wielicki* et al., 1996) on the Tropical Rainfall Measurement Mission (TRMM) satellite and on the satellites Terra and Aqua of the NASA[1] Earth Observing System and the Geostationary Earth Radiation Budget (GERB) experiment on board the Meteosat Second Generation (MSG) satellite (*Harries* et al., 2005). All these instruments provide quantitative measures of the instantaneous effects of clouds

[1]National Aeronautics and Space Administration

on the TOA radiation balance. In addition, the International Satellite Cloud Climatology Program (ISCCP; *Schiffer and Rossow*, 1983; *Rossow and Schiffer*, 1999) provides global distributions of total cloud cover and optical properties.

These data sets have been widely used to estimate the difference between the cloudy and clear-sky net TOA fluxes called the cloud radiative effect (CRE) at the TOA. Due to the reflection of solar radiation back into space, the shortwave CRE at TOA is negative implying a cooling of the Earth-atmosphere system. In the thermal part of the electromagnetic spectrum, the CRE at the TOA is positive, since clouds absorb and re-emit radiation originating from the ground and thus contribute to the Earth's greenhouse effect. Which effect of a single cloud, i.e. the heating or the cooling effect, dominates depends on the vertical position of the cloud and its optical properties. Globally averaged, the net effect of high, thin clouds is estimated to be 1.3 to $2.4\,\mathrm{W\,m^{-2}}$, while for low clouds a pronounced cooling effect of about -15 to $-18\,\mathrm{W\,m^{-2}}$ has been found (*Chen* et al., 2000; *Hartmann* et al., 1992). The net cloud effect at the TOA, i.e. the sum over the CRE of all cloud types, is estimated to be -20 to $-34\,\mathrm{W\,m^{-2}}$ (*Hartmann* et al., 1992; *Wielicki* et al., 1995; *Rossow and Zhang*, 1995, *Chen* et al., 2000) implying that clouds have on average a cooling effect on the climate system. In particular, low clouds provide 55 to 60% to the annually averaged net cloud effet at the TOA.

Although the satellite measurements give an insight into the net effect of clouds on the Earth-atmosphere system, they contain less information on the effect of clouds on the atmospheric and the surface radiation balance. The assessment of the effect of clouds on the atmospheric and surface radiation budget usually envolves model simulations. In particular, the cloud climatology of the ISCCP is often applied to a radiative transfer model in order to calculate the radiative fluxes at the surface and in the atmosphere (e.g., *Rossow and Zhang*, 1995; *Chen* et al., 2000; *Zhang* et al., 2004). Due to absorption and scattering of solar radiation by clouds, the shortwave CRE at the surface is negative. Since the downwelling longwave flux at the surface is increased in cloudy situations, the longwave CRE at the surface is positive. Globally, the SW CRE dominates the net CRE at the surface whose global average is about -20 to $-28\,\mathrm{W\,m^{-2}}$ (*Rossow and Zhang*, 1995; *Chen* et al., 2000; *Zhang* et al., 2004). Thus, the negative CRE at the TOA is primarily related to the negative CRE at the surface.

The residual negative CRE at the TOA is associated with an atmospheric cooling effect of the clouds whose global mean effect is estimated to be about -2 to $-5\,\mathrm{W\,m^{-2}}$ (*Rossow and Zhang*, 1995; *Chen* et al., 2000; *Zhang* et al., 2004). Note that this net atmospheric cooling is an average over the effects of all cloud types and that the net atmospheric CRE can be even positive for specific cloud types (*Chen* et al., 2000). A positive net atmospheric CRE arises as follows. The net atmospheric CRE is generally dominated by the LW atmospheric CRE. The longwave atmospheric CRE is determined by a balance of two opposing effects. On the one hand, the occurrence of clouds leads to an atmospheric heating effect due to the decrease in the effective emission temperature of the atmosphere. On the other hand, adding clouds increases the emissivity of the atmosphere in the water vapor window (8-14 μm wavelength) and hence lead to a cooling effect. The latter effect becomes more important in the higher latitudes, where the water vapor opacity is smaller than in the tropics (*Rossow and Zhang*, 199). For high-level clouds, the first effect overcompensates the second one, especially in the tropics. For low-level clouds, the second effect dominates since low-level clouds are relatively inefficient in decreasing the effective emission temperature due to their vicinity to the surface.

The previously mentioned studies allow for an assessment of the net cooling or heating effects of clouds at the TOA, the surface and in the atmospheric column. In addition, it is important, though much more difficult, to describe the vertical distribution of the radiative energy within

the atmosphere. The vertical distribution of radiative heating influences the local cloud structure, large-scale dynamics, and the hydrological cycle (*Stephens*, 2005). In some studies, efforts have been made to observe radiative heating directly with airborne measurements (*Masuda* et al., 2000; *Buchholtz* et al., 2010). In general, vertical heating rate profiles are calculated with a radiative transfer model given some specification on the vertical profiles of temperature, humidity, clouds, and aerosol. In several studies, the ISCCP data are used to obtain the cloud properties necessary to calculate radiative heating rates (*Bergman and Hendon*, 1998; *Ramsey and Vincent*, 1995; *Zhang* et al., 2004). However, the ISCCP cloud climatology relies on passive satellite measurements in the visible and infrared electromagnetic spectrum which provide limited information about the cloud vertical structure (*Zhang* et al., 2004). A better information on the vertical distribution of cloud properties is gained from the CloudSat satellite (*Stephens* et al., 2002), which was launched in April 2006 and carries the first millimeter wavelength cloud radar in space. The CloudSat cloud property profiles are operationally applied to a broadband radiative transfer model in order to derive fluxes and heating rates with a vertical resolution of 240 m, which have been used to analyze cloud induced effects in these variables (*L'Ecuyer* et al., 2008). Although the vertical cloud structure is better captured by CloudSat compared to passive remote sensing techniques, the information on the cloud properties relies on the cloud radar measurements alone.

More sophisticated surface-based remote sensing techniques enable increasingly detailed measurements of cloud properties, which can be used to compute more accurate fluxes and heating rates. In particular, the most accurate estimates of vertically resolved cloud properties and corresponding surface irradiances can be gained from the synergy of ground-based instruments including at least a cloud radar, lidar, microwave radiometer and radiation sensors. Unfortunately, the deployment of these instruments in such a combination is mostly restricted to short time periods, for example during measurement campaigns. Such instrumentation performs long-term operations only at a few anchor sites world wide. These sites include the three permanent and two mobile facilities of the ARM program and sites organized in the Cloudnet program (*Illingworth* et al., 2007), namely Cabauw, Chilbolton, SIRTA[2] at Palaiseau and Lindenberg. These sites are particularly valuable in observing low altitude clouds, which are difficult to capture by satellite instrumentation, but reveal a strong impact on the energy budget of the Earth-atmosphere system as described before.

In particular, some efforts have been made to study clouds and their interaction with radiation using the various ARM measurements. *Dong* et al. (2005), for example, derived a climatology of midlatitude continental clouds from observations of cloud radar, lidar, microwave radiometer and radiosondes at the ARM Southern Great Plains (SGP) Central Facility site. In a sequel study, *Dong* et al. (2006) combined the derived cloud climatology with surface radiation measurements in order to asses surface CRE for different cloud types and to identify the dominant drivers for the surface CRE. They found that the SW CRE is driven by solar zenith angle and cloud hydrometeors while water vapor changes are most important for the LW CRE. *Mace* et al. (2006a) and *Mace* et al. (2006b) were able to derive vertically resolved cloud properties from one year of observations at the SGP site. The derived cloud properties were applied to a broadband radiative transfer model, in order to derive fluxes and heating rates with a vertical resolution of 90 m. Given this data set, *Mace* et al. (2006b) analyzed the CRE of SW and LW irradiances as a function of cloud type. They found that the predominant atmospheric CREs at the SGP site are associated with thin cirrus cloud layers and thick low-level clouds, in part because they appear more frequently than other types of clouds. In addition, they analyzed the cloud radiative forcing (CRF) of different

[2]Site Instrumental de Recherche par Télédétection Atmosphérique.

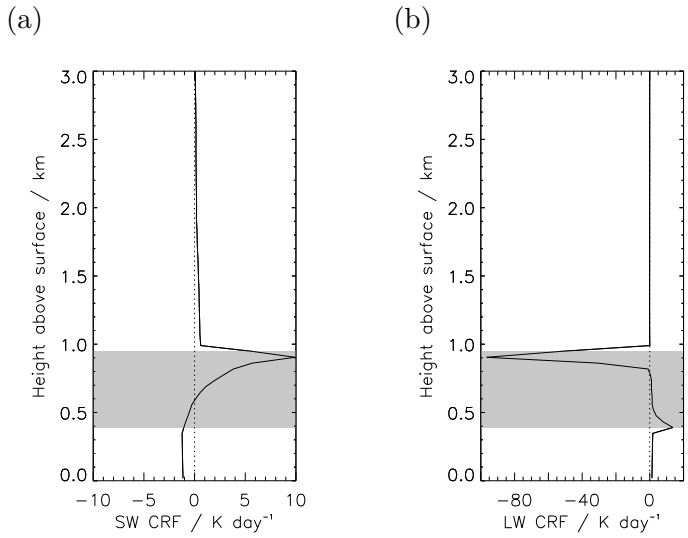

Figure 1.2: SW (a) and LW (b) CRF of a single-layer water cloud (indicated by the shaded area) at the AMF site in the Murg Valley on 25 October 2007 at 12:40 UTC. The LWP of the cloud is about $130\,\mathrm{g\,m^{-2}}$.

cloud types, where the CRF is defined in this context as the difference between the cloudy and clear-sky atmospheric heating rates. In the present work, the term CRF will be used in this meaning. *Mace* et al. (2006b) came to the conclusion that studying solely the CRE at the surface, TOA, and atmosphere considerably masks the cloud radiative forcing variability in the atmospheric profile which is important for capturing the essential feedbacks by clouds to the general circulation.

SW CRF is always positive at cloud top due to the enhanced absorption of solar radiation primarily by atmospheric gases (see example for one cloud case in Fig. 1.2a). Since cloud droplets strongly scatter radiation, they increase the photon path length and therefore the gaseous absorption. Because of the reflection of solar radiation at cloud top, heating by atmospheric gases in upper height levels slightly increases, too. Below the cloud, the SW CRF is negative due to the attenuation of solar radiation by the clouds resulting in less gaseous absorption compared to the clear-sky case. In the LW (Fig. 1.2b), cooling occurs at cloud top, due to the flux exchange between the air above the cloud and the optically thick cloud. The lower the cloud top height, the higher the cloud top temperature and the stronger is the cloud top cooling. In the lower parts of the cloud, heating occurs due to the absorption of the longwave flux from the surface and the re-emission of longwave radiation corresponding to the cloud's temperature. For low-level clouds, the LW cloud top cooling is several times larger than the LW cloud base warming since the cloud base is close to the surface. If cloud base and cloud top are shifted to larger heights, the relative importance of LW warming compared to LW cooling increases.

In order to assess the CRF of tropical clouds, *Mather* et al. (2007) compiled a data set of thermodynamic and cloud property profiles using ARM observations at the tropical western pacific islands Manus and Nauru. On the basis of these profiles, they calculated radiative fluxes and heating rates and found a net warming due to high and midlevel clouds. At Nauru, boundary layer clouds prevailed with a cooling effect in and above the cloud layer and a net warming below. In a sequel study, *Mather and McFarlane* (2009) analyzed radiative heating rate profiles with respect to different cloud classes occuring at both tropical sites. While

the frequency of specific cloud types differed between the two sites, the atmospheric heating rate characteristics of individual cloud classes were remarkably similar. Therefore, *Mather and McFarlane* (2009) concluded that if the frequency distribution of cloud classes in a given tropical area could be estimated, the radiative heating over this area could be assessed using the ARM observations at the fixed point sites.

When assessing the CRE and the CRF, it is important to quantify uncertainties in these variables. In particular, uncertainties in the derived microphysical cloud properties have to be evaluated and their effects on the derived radiative fluxes and heating rates has to be analyzed. The microphysical cloud properties encompass, for example, the cloud water content, which can be either liquid or solid, and the particle size. *Mather* et al. (2007) estimated the uncertainty in the heating rates due to uncertainties in the ice cloud properties to be 10 to 20% above a height of 8 km. For water clouds, uncertainties in the heating rates were found to be in the same order of magnitude and mostly related to the liquid water content of the cloud. The relative importance of accurate cloud water content and cloud droplet size with respect to the radative effect of clouds was also discussed by *Sengupta* et al. (2003). They analyzed the SW CRE at the surface for overcast boundary layer stratocumulus clouds and found a higher sensitivity of the solar flux to the total liquid water content compared to the cloud droplet size.

Uncertainties in the derived CRE and CRF were also assessed by *Mace* et al. (2006b) based on a validation statistic derived from radiative flux measurements at the surface and the top of atmosphere. While the overall SFC and TOA CRE was derived with an uncertainty of up to 12%, the uncertainty in CRE related of different cloud types is considerably larger. For the CRF, *Mace* et al. (2006b) estimated uncertainties which are several times larger than the derived CRF itself, meaning even the sign of the forcing, i.e. cooling or warming, is ambiguous. For most of the described studies, the authors therefore agree on the need to improve the cloud property retrieval techniques in order to better estimate the CRE and CRF.

These studies also underline the huge variability of clouds and their radiative effects depending on the atmospheric and climatic conditions. Workshops by the ARM program have demonstrated that the need for observations in different climatic locations is great. In order to sample the wide range of climatic conditions, there is a scientific consensus that more fixed sites should be established in future, for example in Greenland, southeastern Asia and in the Amazon rain forest (*U.S. Department of Energy, Office of Science*, 2010).

1.3 State-of-the-art ground-based retrieval techniques for cloud properties

Clouds are characterized by their macrophysical and microphysical properties. The macrophysical properties encompass the cloud boundaries and the phase of the cloud. The microphysical properties are related to the cloud particle size distribution, which results from a number of complex processes, for example, aggregation, nucleation, diffusion, collision and coalescence (*Rogers and Yau*, 1989).

Liquid water and ice clouds are typically characterized by the liquid water content (LWC) and ice water content (IWC), respectively, and by the corresponding effective radii $r_{\mathrm{eff,liq}}$ and $r_{\mathrm{eff,ice}}$. These parameters can be directly calculated from the moments of the cloud particle

size distribution $N(D)$, where N is the concentration of the cloud particles of diameter D. The kth moment $\mathcal{M}_k$ of the distribution is given by

$$\mathcal{M}_k = \int_0^\infty D^k \, N(D) \; dD. \tag{1.1}$$

The LWC, typically given in $\mathrm{g\,m^{-3}}$, is related to the third moment of the drop size distribution and can be calculated as

$$\mathrm{LWC} = \int_0^\infty \rho_l \frac{\pi D^3}{6} N(D) \; dD, \tag{1.2}$$

where ρ_l the density of liquid water. For the IWC, ρ_l in Eq. (1.2) has to be replaced by the density of ice particles, which may be different for different particle types. The effective radius, which is the area-weighted mean radius of the particles, is defined as the ratio of the third and the second moment of the size distribution:

$$r_{\mathrm{eff}} = \frac{\mathcal{M}_3}{\mathcal{M}_2}. \tag{1.3}$$

In radiative transfer models, clouds are typically characterized by LWC, IWC and the effective radii. Therefore, only the relevant moments of the particle size distribution have to be known in general.

Since in-situ measurements of cloud properties, for example from aircraft measurements, are sparse, the information of active and passive ground-based remote sensing instruments is typically used in order to derive cloud boundaries and cloud phase, as well as the microphysical properties including LWC, IWC, and the correspondig effective radii. Active sensors such as lidars and cloud radars provide vertically resolved cloud information, while passive sensors such as microwave radiometers generally measure path-integrated cloud properties. The cloud base height can be accurately derived from lidar/ceilometer measurements. Lidars send out light pulses in the optical region of the electromagnetic spectrum and measure their backscattering from the atmosphere. The backscattered signal is proportional to D^2. Since the lidar signal is often extinguished in the lower parts of the cloud due to the strong scattering of the light puls by the cloud particles, upper cloud levels can be only detected by a cloud radar. A cloud radar works similar to a lidar, but measures at lower frequencies, for example at 35, 94 or 95 GHz. In contrast to a lidar, which is very sensitive to small particles like cloud droplets and aerosol, a radar is sensitive to larger particles such as rain and drizzle drops. As a measure for the cloud radar backscattered signal, the radar reflectivity factor Z is commonly used, which is the sixth moment of the drop size dristibution:

$$Z = \int_0^\infty D^6 N(D) \, dD. \tag{1.4}$$

Z is usually given in the logarithmic form $\mathrm{dB}Z = 10 \log_{10} \left(\frac{Z}{1\,\mathrm{mm^6 m^{-3}}} \right)$ with Z given in the units of $\mathrm{mm^6 m^{-3}}$. In the following, the term radar reflectivity is synonymously used for radar reflectivity factor.

By combining radar and lidar measurements, the vertical dimensions of a cloud can be well described (*Wang and Sassen*, 2001; *Hogan and O'Connor*, 2004). It is much more difficult to determine the phase of the cloud particles, whose knowledge is an important precondition for the application of appropriate cloud microphysical retrieval algorithms. In some studies, temperature thresholds are used in order to distinguish liquid and ice parts of the cloud (*Mather* et al., 2007; *Mace* et al., 2006a, 2006b). *Wang and Sassen* (2001) developed a

categorization algorithm based on combined lidar, radar, microwave radiometer (MWR), and infrared radiometer measurements in order to categorize clouds into 8 different classes. *Turner* et al. (2003) showed that the cloud phase can be derived from spectral infrared measurements. However, *Wang and Sassen* (2001) and *Turner* et al. (2003) only determined, whether liquid and/or ice water occured, but not in which height. *Hogan and O'Connor* (2004) combined the measurements of a similar instrumentation as in *Wang and Sassen* (2001) in oder to derive a more detailed categorization product using also information on the Doppler spectrum. This product includes information on the vertical occurrence of different type of targets including cloud droplets, ice, rain, and drizzle, among others.

Corresponding to the detected phase of the particles, retrieval algorithms for LWC and $r_{\mathrm{eff,liq}}$, or IWC and $r_{\mathrm{eff,ice}}$ can be applied. The vertical profile of cloud radar reflectivity is commonly used to retrieve vertical information on LWC (e.g., *Mace* et al., 2006a; *Mather* et al., 2007; *McFarlane* et al., 2008). Since the radar reflectivity and the liquid water content are both functions of the cloud droplet spectrum (cf. Eqs. (1.2) and (1.4)), attempts have been made to relate the radar reflectivity Z with the liquid water content (*Atlas*, 1954; *Sauvegeot and Omar*, 1987; *Fox and Illingworth*, 1997). Such relationships are typically of the form $Z = a\mathrm{LWC}^b$. Since the cloud droplet spectrum is highly variable even within a cloud (*Khain* et al., 2008), no unique Z-LWC relation exists. If a few drizzle drops are present in a cloud, they dominate the reflectivity, but contribute negligibly to the LWC. This effect leads to large errors in the derived LWC values (see, for example, Fig. 2 in *Löhnert* et al., 2008) and the empirical relationships fail.

To better constrain LWC profiles, passive atmospheric emission measurements in the microwave region can be used, which are very well suited to derive the vertically integrated liquid water content, the liquid water path (LWP; e.g., *Westwater*, 1978). In the microwave regime, the cloud emission is proportional to the frequency squared and the cloud contribution to the signal strongly increases with frequency. Two-channel microwave radiometers usually measure brightness temperatures at a frequency in the window region where liquid water dominates the emission, namely between 30 and 36 GHz, and at another one on the wing of a water vapor absorption line (e.g., 24 GHz). The latter channel is used to correct for the influence of water vapor in the LWP retrieval. The accuracy of such dual-channel retrievals is typically 25-30 $\mathrm{g\,m^{-2}}$ (*Turner* et al., 2007). The uncertainty can be improved by including additional frequencies into the retrieval, for example the 90 or 150 GHz channel, which are both very sensitive towards liquid water (*Crewell and Löhnert*, 2003). In order to further decrease the uncertainty of LWP in cases where the LWP is low ($<$100 $\mathrm{g\,m^{-2}}$), *Turner* (2007) followed a sensor synergy approach combining MWR and spectral infrared data. He showed that the random error for LWP using this synergetic approach is less than 4% in cases with LWP lower than 50 $\mathrm{g\,m^{-2}}$.

The need for sensor synergy, that is the combination of information from different active and passive remote sensing instruments, to derive LWC profiles has been identified in the past (e.g., *Frisch* et al., 1998; *Löhnert* et al., 2004). For example, *Frisch* et al. (1998) derived profiles of LWC by applying the normalized square root of the radar reflectivity as a vertical weighting function to the LWP of the MWR. *Löhnert* et al. (2004) and *Löhnert* et al. (2008) integrated ground-based microwave radiometer, cloud radar and a priori information, e.g. from radiosondes, in the framework of the optimal estimation equations, (see *Rodgers*, 2000). This so-called Integrated Profiling Technique (IPT) has been successfully used to derive profiles of temperature, humidity and liquid water content and corresponding error estimates. *Löhnert* et al. (2007) showed that for simulated cloud cases the IPT could reproduce the modeled LWC with mean accuracies of 30%.

Radar reflectivity and MWR measurements can be combined in order to retrieve profiles of $r_{\text{eff,liq}}$ (*Frisch* et al., 2002). Radar reflectivity measurements can also be used alone, if an estimate of the droplet concentration is made (*Frisch* et al., 2002). Infrared measurements also include information on $r_{\text{eff,liq}}$ if the cloud is semitransparent in the infrared, which is the case if the LWP is less than $60\,\text{g}\,\text{m}^{-2}$. For these cases, *Turner* (2007) derived a cloud-layer mean $r_{\text{eff,liq}}$ combining MWR and spectral infrared information via an inversion procedure. In comparison to in situ aircraft measurements, the observed $r_{\text{eff,liq}}$ could be well reproduced by the retrieval technique with a median difference of $0.11\,\mu$m.

In order to derive the IWC, radar reflectivity measurements are commonly related to IWC employing a power law relationship as in Z-LWC retrievals (e.g., *Sassen* et al., 2002; *Liu and Illingworth*, 2000; *Atlas* et al., 1995). As for LWC, many empirical Z-IWC relationships exist due to the variety in ice particle size distributions occuring at different temperatures and also due to the variety in the density of the ice particles (*Liu and Illingworth*, 2000). *Liu and Illingworth* (2000) demonstrated that incorporating the temperature T would make the retrieved IWC significantly more accurate. *Hogan* et al. (2006) thus derived an empirical formula relating IWC to the radar reflectivity Z and the temperature T and estimated the uncertainty of the derived IWC to $-46\%/+85\%$. In other studies, a synergetic approach was followed. *Donovan and van Lammeren* (2001), *van Zadelhoff* et al. (2004) and *van Zadelhoff* et al. (2007) combined radar and lidar measurements in the framework of inversion procedures to provide profiles of IWC and $r_{\text{eff,ice}}$. *van Zadelhoff* et al. (2007) compared the lidar-radar retrieved IWC to in situ data obtained during aircraft flights on two days. They found for the linear fit of the retrieved and observed IWCs (in $\text{g}\,\text{m}^{-3}$) a slope parameter of 0.93 and an intercept parameter of 0.012. A shortcoming of these techniques is that they can only be applied to regions of a cloud detected by both radar and lidar. *Donovan* (2003) extended the radar-lidar retrieval by *Donovan and van Lammeren* (2001) and included the mean Doppler velocity of the cloud radar measurements into the algorithm. *Matrosov* (1999) derived the vertically integrated IWC, the ice water path (IWP), from cloud layer-mean radar reflectivity and from estimates of cloud optical thickness derived from infrared radiometer measurements. This IWP was used to scale the IWC profiles of various Z-IWC relationships. The benefit of infrared measurements was also recognized by *Mace* et al. (1998) and *Turner* (2005), who employed spectral infrared information in order to derive IWP and cloud-layer mean $r_{\text{eff,ice}}$. Recently, *Delanoë and Hogan* (2008) developed a variational scheme for profiles of IWC and $r_{\text{eff,ice}}$ employing radar, lidar, and spectral infrared radiometer measurements. Using simulated radar and lidar data, *Delanoë and Hogan* (2008) demonstrated the capability of the algorithm to accurately retrieve IWC and $r_{\text{eff,ice}}$. However, in order to provide a better estimate of the accuracy of this retrieval, in situ observations are needed. Due to a more flexible combination of the measurements, the retrieval by *Delanoë and Hogan* (2008) could overcome the shortcoming of the previous radar-lidar algorithms, i.e. their limited application.

1.4 Focus of the study

Although ground-based observations have a large potential in order to improve the understanding of the radiative effects of clouds, only a few studies exist that address these points in the framework of long-term cloud studies. In this respect, the nine-month measurements of the ARM Mobile Facility in the Black Forest provide a unique opportunity to characterize clouds in a mid-latidude low-mountain region and to analyze their effects on the atmospheric

fluxes and heating rates. The present work complements previous studies performed for different climatic regions and locations, for example the Tropical Western Pacific (*Mather* et al., 2007; *Mather and McFarlane*, 2009), the Southern Great Plains (*Dong* et al., 2006; *Mace* et al., 2006b), and Alaska (*Shupe and Intrieri*, 2004).

The data of a sophisticated target classification scheme (*Hogan and O'Connor* (2004), 2004) is exploited in the present work in order to provide a description of the macrophysical properties of the clouds. State-of-the-art microphysical retrieval schemes and products are applied to derive cloud liquid and ice water content profiles and corresponding effective radii. Such a data set is not only valuable for cloud-radiation interaction studies, but also for the evaluation of the representation of clouds in numerical weather prediction models.

The data set of microphysical cloud properties is complemented by retrieved thermodynamic profiles allowing for the performance of radiative transfer calculations. To this end, the broadband radiative transfer model RRTMG (*Clough* et al., 2005) is applied. On the one hand, the radiative transfer results are used to assess the quality of the derived atmospheric profiles by means of radiative closure studies. On the other hand, they allow for an evaluation of the radiative effect and forcing of clouds at the AMF site. In particular, focus is put on the effect of low-level water clouds. Although they are the simplest cloud type to be observed, the accurate description of their microphysical properties is still challenging and large deviations are seen between different retrieval algorithms (*Turner* et al., 2007). Globally, low-level clouds occur quite frequently with a mean cloud amount of 27% (*Chen* et al., 2000). Due to their frequent occurrence and their strong impact on the Earth-atmosphere radiation balance, understanding these clouds is of peculiar interest.

In addition to a baseline radiative transfer simulation, sensitivity studies are performed to estimate uncertainties in the CRE and CRF of water clouds due to uncertainties in the derived microphysical properties. In this respect, the individual importance of accurate LWC and $r_{\mathrm{eff,liq}}$ profiles is assessed.

As stated, sensor synergy is essential for the retrieval of cloud microphysical properties. Combining different measurements can increase the information content and accuracy of a retrieval, which can in turn improve estimates of cloud radiative effects. This topic is discussed in the present study with respect to the retrieval of LWC profiles employing the Integrated Profiling Technique (*Löhnert* et al., 2004). This technique combines a priori, cloud radar and MWR information via an optimal estimation approach. In particular, the interplay of a priori and measurement information in the LWC retrieval is assessed and the associated effect on the retrieved LWC error and on the information content of the measurements is analyzed.

The present study is structured as follows. In Chapter 2, the basic principles of radiative transfer in the atmosphere are presented, followed by a description of the broadband radiative transfer model RRTMG. Information on all measurements and data products related to the present work is given in Chapter 3. Chapter 4 provides an overview on the retrieval and analysis strategy of this study. The retrieval of the microphysical and thermodynamic profiles, as well as of additional information needed for the radiative transfer calcluations, is described in detail. Furthermore, an overview of the different radiative transfer sensitivity studies is given. In Chapter 5, the cloud statistics based on the derived macro- and microphysical cloud properties are presented including a discussion on the limitations of the retrieval technique. The derived thermodynamic and cloud property profiles are evaluated in Chapter 6 by means of radiative closure studies. The assessment of the accuracy of the atmospheric profiles is a necessary precondition for a meaningful assessment of the CRE and CRF of these clouds. The CRE and CRF are analyzed with a focus on water clouds. Uncertainties in the CRE and

CRF due to uncertainties in the microphysical cloud properties are estimated. In Chapter 7, the Intergrated Profiling Technique (IPT) is presented. On the basis of this technique, the individual roles of a priori information and measurements in the LWC retrieval is investigated and their effect on the information content of the measurements and on the the LWC error is analyzed. Afterwards, the performance of the IPT with respect to its application to the measurements during the AMF deployment is discussed. Finally, a summary is presented in Chapter 8 along with an outlook for future research.

The analysis of LWC errors and of the information content of cloud radar and MWR measurements in the LWC retrieval as presented in Chapter 7 has recently been published:

- Ebell, K., U. Löhnert, S. Crewell und D.D. Turner, On characterizing the error in a remotely sensed liquid water content profile, *Atmospheric Research*, 98, 57–68, 2010.

The publication by *Ebell* et al. (2010) is a follow-up of the publication by *Crewell* et al. (2009):

- Crewell, C., K. Ebell, U. Löhnert, and D.D. Turner, Can liquid water profiles be retrieved from passive microwave zenith observations?, *Geophysical Research Letters*, 36, doi:10.1029/2008GL036934, 2009.

Chapter 2

Radiative transfer in the atmosphere

The theory of radiative transfer describes the complex interaction of electromagnetic radiation with matter. The electromagnetic spectrum comprises gamma rays, X rays, ultraviolet (UV), visible (VIS), infrared (IR), microwaves, television signals, and radio waves (Fig. 2.1). According to Plancks law, solar radiation can be described as radiation emitted from a blackbody at a temperature of about 6000 K. Solar radiation thus ranges from Gamma rays to the infrared spectrum, whereby only 0.4% of the energy of solar radiation is emitted at wavelengths above 5 μm. Terrestrial radiation is essentially all energy which is radiated by the Earth-atmosphere system at thermal infrared wavelengths with 99% of the emitted energy between wavelengths from 4 to 100 μm and with only 0.4% emitted at wavelengths below 5 μm. This separation allows solar and terrestrial radiation, in the following also called shortwave and longwave radiation, to be treated independently. In order to describe the interaction of shortwave and longwave radiation with the Earth-atmosphere system, radiative transfer models are needed. In particular, the complex processes of absorption, emission, and scattering by the atmospheric particulates including molecules, aerosols, and cloud particles have to be described by these models.

In this chapter, the basic principles of radatiative transfer in the atmosphere are roughly summarized. Detailed information can be found in many textbooks, for example in *Chan-*

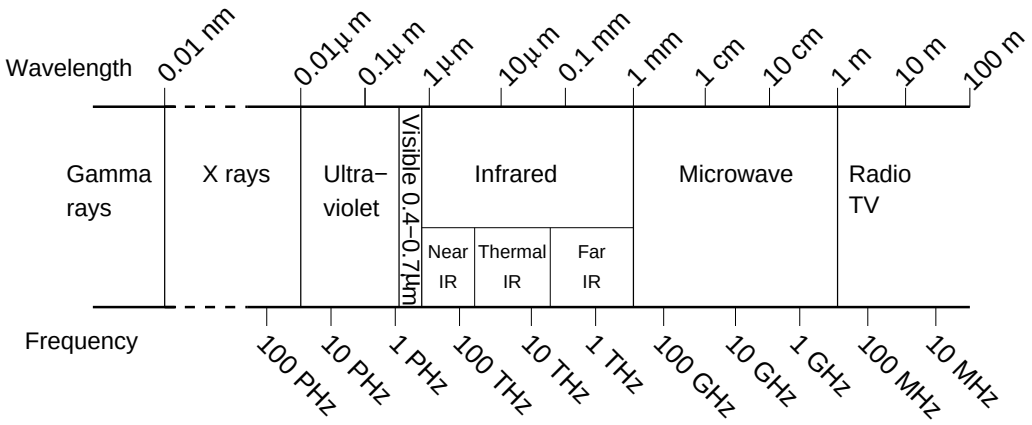

Figure 2.1: The electromagnetic spectrum (after *Petty* (2006)).

drasekhar (1960), *Van de Hulst* (1981), and *Liou* (2002), or in a more condensed manner in *Petty* (2006). A short summary of this topic is also given by *Drusch and Crewell* (2005). In the first section (Secion 2.1), the basic radiative quantities are presented followed by an overview of the concepts of absorption, emission, and scattering of radiation in a medium and in the atmosphere in particular (Section 2.2). Absorption, emission, and scattering can be characterized by certain radiative properties. The radiative properties of clouds and the connection to their microphysical properties are described in Section 2.3. Section 2.4 deals with the radiative transfer equation, which accounts for all interaction processes of radiation with the atmosphere and forms the basis of every radiative transfer model. In the present study, the radiative transfer model RRTMG is applied, which is described in the last section of this chapter.

2.1 Basic radiative quantities and definitions

The monochromatic intensity (or radiance) is given as the differential amount of energy dE_λ per time interval dt, wavelength interval $d\lambda$, effective area $\cos\theta\, dA$, and solid angle $d\Omega$:

$$I_\lambda = \frac{dE_\lambda}{d\Omega\, d\lambda\, dt\, \cos\theta\, dA}. \tag{2.1}$$

The solid angle is defined as

$$d\Omega = \sin\theta\, d\theta\, d\phi, \tag{2.2}$$

where θ and ϕ denote the zenith and azmimuth angles, respectively (Fig. 2.2). The monochromatic flux density or monochromatic irradiance F_λ is the monochromatic intensity projected to the normal and integrated over the full hemisphere:

$$F_\lambda = \int_\Omega I_\lambda\, \cos\theta\, d\Omega. \tag{2.3}$$

Integration of the monochromatic flux density over the entire electromagnetic spectrum, that is over all wavelengths, leads to the the total flux density of radiant energy F:

$$F = \int_0^\infty F_\lambda\, d\lambda, \tag{2.4}$$

which is given in the units of $\mathrm{W\,m^{-2}}$. In the following, the flux density is denoted as flux for short (although in the strict sense, flux has units of W). Depending on the context, the flux may be derived for a certain part of the electromagnetic spectrum, e.g. for the solar or terrestrial spectral intervals. From Eqs. (2.3) and (2.4) upwelling $F^\uparrow$ and downwelling $F^\downarrow$ fluxes can be derived using appropriate limits for Ω. Downward and upward flux components can be combined to the net flux F^{net},

$$F^{net} = F^\downarrow - F^\uparrow, \tag{2.5}$$

which is the net downward flow of radiative energy through a unit horizontal area. In the atmosphere, upward, downward, and net fluxes can be derived for any given height z. Assuming a thin layer of the atmosphere with its base at height z_1 and its top at z_2, the net flux $F^{net}(z_1)$ gives the rate at which energy leaves the bottom of the layer and $F^{net}(z_1)$ likewise the rate at which energy enters the top of the layer. If the net flux divergence in this layer does not equal zero, the internal energy of the layer must change due to the principle of

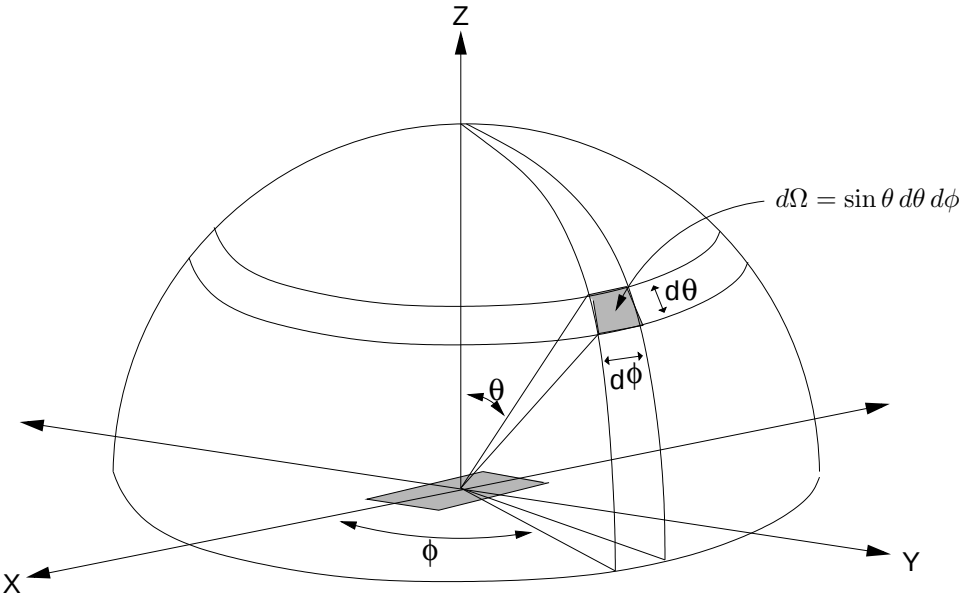

Figure 2.2: The relationship between solid angle and polar coordinates (after *Petty* (2006)).

energy conservation. The change of the internal energy can be expressed in terms of the rate of temperature change. A radiative heating rate $\mathrm{HR} = \frac{\partial T}{\partial t}$ at any level z is thus given by

$$\mathrm{HR} = \frac{1}{\rho\,(z)\; C_p} \frac{\partial F^{net}\,(z)}{\partial z}, \tag{2.6}$$

where $\rho\,(z)$ is the air density at level z and C_p=1005 $\mathrm{Jkg^{-1}K^{-1}}$ is the specific heat capacity of air at constant pressure. For a differential layer $z_2 - z_1$, Eq. (2.6) may be written as

$$\mathrm{HR} = \frac{1}{\rho\, C_p} \frac{F^{net}\,(z_2) - F^{net}\,(z_1)}{z_2 - z_1}, \tag{2.7}$$

whereby the heating rate is typically given in the units of $\mathrm{K\,day^{-1}}$.

2.2 Radiation interaction processes with the atmosphere

Radiation interacts with matter by the three mechanisms absorption, scattering, and emission. For solar radiation in the atmosphere, interactions are limited to absorption and scattering, since its source, the Sun, is external to the Earth-atmosphere system. For the thermal part of the spectrum, all three processes occur.

2.2.1 Absorption

Absorption and emission of radiation take place when the atoms or molecules undergo transitions from one energy state to another, namely changes in their translational and electronic energy and, for molecules also in rotation and vibration. The resulting absorption lines create distinct patterns in the wavelength spectrum of the radiation which reaches the ground.

When radiation is absorbed in a medium, the intensity of the radiation is weakened. Assuming, for example, radiation traversing a medium along a path $d\mathbf{s}$, the radiation's intensity $I_\lambda(\mathbf{s}, \mathbf{\Omega})$ may be reduced by $dI_\lambda(\mathbf{s}, \mathbf{\Omega})$ with

$$dI_\lambda(\mathbf{s}, \mathbf{\Omega}) = -\beta_{a,\lambda}(\mathbf{s})\ I_\lambda(\mathbf{s}, \mathbf{\Omega})\ ds. \tag{2.8}$$

Here, $\mathbf{\Omega} = (\mu, \phi)$ and $\beta_{a,\lambda}$ is the volume absorption coefficient at a given wavelength λ. The units of the volume absorption coefficient are given in the terms of inverse length (m^{-1}). The volume absorption coefficient $\beta_{a,\lambda}$ may also be expressed as the product of the density of a material ρ and its mass absorption coefficient $k_{a,\lambda}$ (given in units of area per mass):

$$\beta_{a,\lambda} = k_{a,\lambda}\,\rho. \tag{2.9}$$

or by the number density N of the particles and the absorption cross section $\sigma_{a,\lambda}$

$$\beta_{a,\lambda} = N\,\sigma_{a,\lambda}, \tag{2.10}$$

where $\sigma_{a,\lambda}$ has dimensions of area. In the atmosphere, clouds, aerosols and a mixture of a variety of gases exist, which all absorb radiation. In order to account for all contributors to absorption, β_a has to be extended to the sum over all individual coefficients

$$\beta_a = \sum_i \beta_{a,i} = \sum_i \rho_i\,k_{a,i} = \sum_i N_i\,\sigma_{a,i}, \tag{2.11}$$

where the index λ has been omitted for brevity.

If the radiation budget in a wavelength interval has to be determined, broadband calculations have to be carried out in order to correctly describe wavelength dependent characteristics and interactions of all gases which absorb in this interval. Due to the non-linearity, a simple averaging over the spectral absorption coefficients would lead to erroneous results. A widespread method to cope with the complex line spectra is the k-distribution method, see for example *Liou* (2002). The integration of the absorption coefficient k_a over a complex line spectrum within a spectral interval is replaced by an integral over a much smoother cumulative probability function $g(k_a)$ allowing for much larger discretization steps. The k-distribution method is only valid for homogeneous paths, where the absorption coefficient is constant, implying that temperature and pressure do not change. In order to account for the vertical non-homogeneity of the atmosphere, a simple correlation of different temperatures and pressures is assumed resulting in the so-called correlated k-distribution method.

In addition to the discrete absorption lines, continuum absorption takes place which does not exhibit a line-like structure but varies smoothly with frequency. At the very short wavelengths in the solar spectrum, the continuum absorption can be explained by photoionization and photodissociation which are well understood. In addition, significant continuum absorption by water vapor takes place in the infrared and microwave bands which is not well understood. The strength of the continuum tends to increase steadily with fequency through the microwave and far IR bands but is weak again in the thermal and NIR bands.

2.2.2 Thermal emission

In order to understand thermal emission processes, the laws of blackbody radiation are substantial. For a blackbody, it is assumed that the absorption is complete. Then, the monochromatic intensity of radiation emitted by the blackbody is given by the Planck function $B_\lambda(T)$,

which only depends on the blackbody's temperature T and wavelength λ such that

$$B_\lambda(T) = \frac{2h_P c^2}{\lambda^5 \left(e^{h_P c/k_B \lambda T} - 1\right)}. \tag{2.12}$$

Here, c is the velocity of light and h_P and k_B are the Planck and Boltzmann constants which are experimentally found to be $6.626 \cdot 10^{-34}\,\mathrm{J\,s}$ and $1.381 \cdot 10^{-23}\,\mathrm{J\,K^{-1}}$, respectively. From Eq. (2.12), it is evident that the blackbody radiant intensity increases with temperature and that the wavelength of the maximum intensity λ_{max} is shifted to smaller wavelengths with increasing temperature, a relation described by Wien's displacement law:

$$\lambda_{max} = \frac{k_W}{T}, \tag{2.13}$$

with Wien's constant $k_W = 2897\,\mu\mathrm{mK}$.

Planck's function only gives the monochromatic intensity emitted by a blackbody. In order to derive the total radiant intensity, the Planck function has to be integrated over all wavelengths

$$B(T) = \int_0^\infty B_\lambda(T)\,d\lambda = \frac{2\pi^4 k_B^4}{15c^2h_P^3}T^4. \tag{2.14}$$

The flux density emitted by a blackbody F_{BB} can be calculated by integrating over the 2π steradians of the solid angle of one hemisphere. Since blackbody radiation is isotropic, i.e. uniform for all angles, Eq. (2.14) is simply multiplied by π leading to

$$F_{BB} = \frac{2\pi^5 k_B^4}{15c^2h^3}T^4 = \sigma T^4. \tag{2.15}$$

Eq. (2.15) is the so-called Stefan-Boltzmann law where σ is the Stefan-Boltzmann constant with $\sigma = 5.67 \cdot 10^{-8}\,\mathrm{Wm^{-2}K^{-4}}$.

Since real surfaces might deviate from the ideal of a blackbody, they may emit radiation of less intensity than predicted by the Planck function. The ratio of the emitted intensity I_λ to intensity of the Planck function B_λ is the emissivity ε_λ

$$\varepsilon_\lambda = \frac{I_\lambda}{B_\lambda(T)}. \tag{2.16}$$

Under the condition of thermodynamic equilibrium characterized by uniform temperature and isotropic radiation, the same amount of radiation that is absorbed by the medium must be emitted. Thus the absorption coefficient $\beta_{a,\lambda}$ must be equal to the emissivity ε_λ which is stated in Kirchhoff's law:

$$\varepsilon_\lambda = \beta_{a,\lambda}. \tag{2.17}$$

For a blackbody, $\varepsilon_\lambda = \beta_{a,\lambda} = 1$, while for the so-called gray body, absorption and emission are incomplete and result in $\varepsilon_\lambda = \beta_{a,\lambda} < 1$. Kirchhoff's law only holds for systems in thermodynamic equilibrium when molecules much more rapidly exchange energy with each other than with the radiation field. This assumption is valid for atmospheric volumes below 60–70 km height in form of a local thermodynamic equilibrium but breaks down at extremely high altitudes, where the density of air molecules is small.

Assuming again radiation that traverses a medium along a path $d\mathbf{s}$, the enhancement of intensity caused by emission can now be described by

$$dI_{\lambda,emit}(\mathbf{s}, \mathbf{\Omega}) = \beta_{a,\lambda}(\mathbf{s})\; B(T(\mathbf{s}))\; ds, \tag{2.18}$$

which makes use of Planck's and Kirchhoff's law. The latter one enables the use of the volume absorption coefficient in the emission term, since emissivity and absorptivity are identical.

2.2.3 Scattering

Scattering is a physical process by which a particle in the path of an electromagnetic wave continuously abstracts energy from the incident wave and re-radiates that energy in all directions. In the atmosphere, scattering occurs on many particle size scales, from gas molecules ($\sim 10^{-4}\,\mu$m) to water droplets ($\sim 10\,\mu$m), ice crystals ($\sim 100\,\mu$m), and large raindrops and hailstones (~ 1 cm). The scattering characteristics of a particle depend on the ratio of the particle diameter to the wavelength of the incident radiation and is described in detail below.

Scattering reduces the intensity of radiation traversing a medium along a path $d\mathbf{s}$. Analogue to absorption, a volume scattering coefficient $\beta_{s,\lambda}$, a mass scattering coefficient $k_{s,\lambda}$, and a scattering cross section $\sigma_{s,\lambda}$ are defined. The corresponding total scattering coefficients in the atmosphere are the sum of the individual components. The reduction in $I_\lambda(\mathbf{s}, \mathbf{\Omega})$ due to scattering can therefore be expressed as

$$dI_{\lambda,s}(\mathbf{s}, \mathbf{\Omega}) = -\beta_{s,\lambda}(\mathbf{s})\; I_\lambda(\mathbf{s}, \mathbf{\Omega})\; ds. \tag{2.19}$$

On the other hand, multiple scattering from other directions into the path of propagation may increase the intensity. Here, the scattering phase function p is introduced which describes the angular distribution of scattered energy from any direction $\mathbf{\Omega}'$ to the direction of interest $\mathbf{\Omega}$. The phase function p is normalized to unity such that for perfect scattering in the absence of any absorption becomes one:

$$\frac{1}{4\pi}\int_{4\pi} p\left(\mathbf{\Omega}, \mathbf{\Omega}'\right)\; d\Omega' = 1. \tag{2.20}$$

The enhancement of intensity caused by multiple scattering can then be written as

$$dI_{\lambda,s}(\mathbf{s}, \mathbf{\Omega}) = \frac{\beta_{s,\lambda}(\mathbf{s})}{4\pi}\int_{4\pi} p\left(\mathbf{s}, \mathbf{\Omega}, \mathbf{\Omega}'\right) I_\lambda\left(\mathbf{s}, \mathbf{\Omega}'\right)\; d\Omega'\, ds. \tag{2.21}$$

Since radiative transfer models often deal with fluxes rather than intensities, it is sufficient to know the relative strength of forward scattering with respect to backward scattering. An important parameter in this respect is the asymmetry factor g which is defined as

$$g = \frac{1}{2}\int_{-1}^{1} p(\cos\Theta)\,\cos\Theta\, d\cos\Theta, \tag{2.22}$$

where Θ is the scattering angle, i.e. the angle between the incident and scattered waves. Values for g range from -1 to 1. If $g > 0$ ($g < 0$), scattering occurs preferentially in the forward (backward) direction. If scattering into the forward and backward directions is identical, as it is for isotropic and Rayleigh scattering, g is zero.

In general, the scattering characteristics of a particle depends on the particle size, the wavelength, the complex refraction index, and the particle shape. In particular, the dimensionless size parameter $x = \frac{2\pi r}{\lambda}$, where r is the particle radius, indicates which scattering theory, Rayleigh, Lorenz-Mie or geometric optics, may be applied. If the particle size is much larger than the wavelength, i.e. $x \gg 1$, the geometric optics or ray tracing approach can be used which will not be presented here in detail. In this formalism, electromagnetic waves are considered as a bundle of seperate parallel rays that are diffracted, reflected, and refracted by the particle. In the following sections, the Rayleigh and Lorenz-Mie formalisms are presented in brief.

Rayleigh scattering

If a particle is considerably smaller than the wavelength of the radiation, i.e. $x \ll 1$, it can be considered as an electric dipole which oscillates when excited by radiation. For a homogeneous, isotropic, spherical particle whose radius is much smaller than the wavelength, e.g. unpolarized sunlight inciding on a molecule, *Rayleigh* (1871) found for the scattered intensity I:

$$I = \frac{I_0}{R^2}\alpha^2 \left(\frac{2\pi}{\lambda}\right)^4 \frac{1+\cos^2\Theta}{2}, \tag{2.23}$$

where I_0 is the incident intensity, R the distance between the molecule and the point of observation, and α the polarizability of the particle. The inverse dependence of the scattered intensity on the wavelength to the fourth power causes light at shorter wavelengths to be scattered more effectively. From Eq. (2.23), it is evident that Rayleigh scattering has maxima in the forward and backward directions, and minima in the side directions. The phase function of Rayleigh scattering for incident unpolarized sunlight is given by

$$p\left(\cos\Theta\right) = \frac{3}{4}\left(1+\cos^2\Theta\right). \tag{2.24}$$

Since for Rayleigh scattering the scattering into the forward and backward directions is identical, the asymmetry factor g is zero.

Lorenz-Mie scattering

If the size parameter x is similar to or larger than 1, that is if the particle size is larger or equals the wavelength, scattering events are called Lorenz-Mie scattering. While exact solutions for scattering by non-spherical particles in this regime do not exist, the Lorenz-Mie formalism analytically solves the problem for the special case of a spherical particle. *Lorenz* (1890) and *Mie* (1908) independently derived the solution for the interaction of a plane wave with an isotropic homogeneous sphere. They used the wave equation for electromagnetic radiation formulated in spherical polar coordinates, which is a separable partial differential equation and can be solved. The corresponding solution can be written as an infinite series of products of orthogonal basis functions including spherical harmonics for the angular dependence and spherical Bessel functions for the radial dependence. A comprehensive treatment of the Lorenz-Mie solution is beyond the scope of this section and can be found for example in *Liou* (2002) and *Van de Hulst* (1981). The solution for the scattering cross sections and the scattering phase matrix can be described by a an infinite series of the so-called Mie scattering coefficients. Defining the scattering efficiency of a sphere with a radius r as

$$Q_s = \frac{\sigma_s}{\pi\, r^2}, \tag{2.25}$$

the scattering efficiency for Lorenz-Mie scattering, for example, is given by

$$Q_s = \frac{2}{x^2}\sum_{n=1}^{\infty}\left(2n+1\right)\left(|a_n|^2+|b_n|^2\right). \tag{2.26}$$

The coefficients a_n and b_n are the Mie coefficients and are functions of the size parameter x and the complex index of refraction m. In practical calculations of Q_s, the sum is truncated after a certain number of terms which in general must be larger than x.

The phase functions of Mie scattering are quite complex and are characterized by a strong forward peak and a minimum at a scattering angle of 105° for large size parameters. For size parameters about or larger than 10^4, geometric optics can describe the scattering phase function of the particle except for the narrow forward at 0° and the intensified scattering at 180°. In fact, for $x \gtrsim 2000$, the Mie theory is less practicable and geometric optics is the preferred method to describe scattering by particles.

For irregularly shaped particles, such as ice particles, the Lorenz-Mie formalism is not appropriate and more sophisticated techniques have to be applied like the T-matrix method (*Mishchenko* et al., 1996) or the discrete dipole approximation (*Draine and Flatau*, 1994).

2.2.4 Extinction in the atmosphere

Extinction describes the losses in radiant energy due to both absorption and scattering. Thus, an extinction coefficient $\beta_{e,\lambda}$ (and similarly $k_{e,\lambda}$ and $\sigma_{e,\lambda}$) can be defined as

$$\beta_{e,\lambda} = \beta_{a,\lambda} + \beta_{s,\lambda}. \tag{2.27}$$

Eqs. (2.8) and (2.19) can therefore be combined to describe the reduction of $I_\lambda(\mathbf{s}, \mathbf{\Omega})$ by extinction:

$$dI_{\lambda,s}(\mathbf{s}, \mathbf{\Omega}) = -\beta_{e,\lambda}(\mathbf{s})\ I_\lambda(\mathbf{s}, \mathbf{\Omega})\ ds. \tag{2.28}$$

In the atmosphere, extinction occurs due to atmospheric gases, clouds, and aerosols. In a cloud-free atmosphere, the intensity of radiation is primarily reduced by absorption and Rayleigh scattering due to various gases like water vapor (H_2O), carbon dioxide (CO_2), ozone (O_3), nitrous oxide (N_2O), methane (CH_4), and molecular oxygen (O_2). At wavelengths shorter than 0.4 μm, the atmosphere is almost completely opaque, due to absorption by O_2 and O_3. In the visible, apart from a few weak and narrow absorption bands due to O_2 and O_3, scattering by air molecules (Rayleigh scattering) is the dominant factor in the extinction of solar radiation. In the NIR band (0.7 μm$< \lambda <$4 μm), the prime absorber is water vapor with contributions from CO_2, CH_4, and N_2O. In the thermal IR band (4 μm$< \lambda <$50 μm), water vapor is again the dominant absorber with almost total absorption at 5-8 μm and above 18 μm. Significant absorption also occurs due to CO_2 near 4 μm and between 13-18 μm, and due to O_3 between 9-10 μm. Other absorbers with distinct absortions bands are N_2O and CH_4. Note that in the thermal IR, extinction due to scattering processes is negligible. As mentioned in Section 2.2.1, continuum absorption by water vapor also contributes to the atmospheric absorption in the IR and microwave bands.

The contribution of aerosols to the extinction of radiation in the atmosphere is difficult to characterize in a general way since their concentration and composition is highly variable. In general, the scattering and absorption properties of aerosols depend on their size and composition. Black carbon, for example, strongly absorbs solar radiation while sulphate aerosol is essentially an entirely scattering aerosol across the solar spectrum with a small degree of absorption in the near infrared (NIR) spectrum. Although the contribution of aerosols to the total extinction of the atmosphere is rather small, they may not be generally neglected in radiative transfer modelling, in particular with regard to climate applications.

Clouds both scatter and absorb radiation. Interestingly, clouds almost purely scatter radiation in the visible band. Due to the strong photon path enhancement by scattering, clouds also increase the amount of absorption of radiation by atmospheric gases. In the NIR band and beyond, the extinction of clouds rapidly changes to strong absorbtion by the cloud

droplets themselves. In order to describe the relative importance of scattering to absorption processes, the single-scatter albedo $\tilde{\omega}_\lambda$ is introduced as

$$\tilde{\omega}_\lambda = \frac{\beta_{s,\lambda}}{\beta_{e,\lambda}}. \tag{2.29}$$

Thus, the single-scatter albedo of clouds is almost 1 for visible radiation and rapidly decreases below 1 when moving into the NIR band. For most of the IR bands, $\tilde{\omega}_\lambda$ is between 0.5 and 0.8, while for microwaves, the single-scatter albedo is virtually 0. The radiative properties of a cloud can be characterized by its optical depth τ, the single-scatter albedo $\tilde{\omega}_\lambda$, and the scattering phase function p, which is described by the asymmetry parameter g for many purposes. The optical thickness of a cloud layer τ_c is defined as

$$\tau_c = \int_{z_{bot}}^{z_{top}} \beta_e\,(z)\,dz, \tag{2.30}$$

where z_{bot} and z_{top} are the cloud base and cloud top height, respectively. The parameters τ_c, $\tilde{\omega}_\lambda$, and g depend on the complex index of refraction of the cloud particulates and the size parameter x. The index of refraction depends in turn on the wavelength and on the composition and phase of the particles. Thus, the details of the behaviour of $\tilde{\omega}_\lambda$ with wavelength can significantly differ for liquid and ice clouds and for different particle sizes. At specific wavelengths, a water droplet can be significantly less/stronger absorbing than an ice particle having the same size. In the solar regime, as a rule of thumb, water clouds with larger droplets are more absorbing and have a lower $\tilde{\omega}_\lambda$ than water clouds with smaller droplets.

2.3 Connection of cloud radiative parameters with cloud microphysical properties

Given the cloud droplet size distribution and assuming spherical particles, the radiative parameters τ_c, $\tilde{\omega}_\lambda$, and g can be calculated from Mie theory. In particular, the extinction and scattering efficiencies are computed for a number of radii spanning the droplet sizes of interest and then integrated over the corresponding size distribution. However, such calculations are very time consuming and not practical for NWP and climate models. Therefore, it is desirable to parameterize the radiative parameters by a few moments of the drop size distribution. For water clouds in the visible and NIR spectrum, i.e., if the size parameter is large, the extinction coefficient β_e has a very weak dependence on the wavelength and is directly related to the LWP of a cloud and to the effective droplet radius r_{eff}:

$$\beta_e = \frac{3\,\text{LWC}}{2\,\rho_l\,r_{\text{eff}}}, \tag{2.31}$$

where ρ_l is the density of water. Integration of Eq. (2.31) over the geometrical thickness of the cloud yields the cloud optical thickness τ_c

$$\tau_c = \frac{3\,\text{LWP}}{2\,\rho_l\,r_{\text{eff}}}, \tag{2.32}$$

which only depends on the liquid water path and the effective radius. However, this relation is not valid for longwave radiation. In general, it is desirable to parameterize $\tilde{\omega}_\lambda$ and g in terms of r_{eff}, too, and to extend the parameterizations to the longwave spectrum. Such parameterizations have been suggested, for example, by *Slingo* (1989) and *Hu and Stamnes* (1993). For ice clouds, parameterizations for τ_c, $\tilde{\omega}_\lambda$, and g in terms of IWC and effective radius exist analogue to those for water cloud radiative properties, e.g., *Ebert and Curry* (1992), *Fu* (1996), and *Fu* et al. (1998).

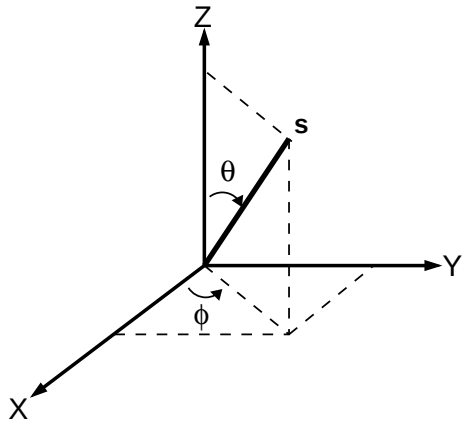

Figure 2.3: Geometry for plane-parallel atmospheres.

2.4 The radiative transfer equation

In order to account for the gains and losses in the radiant energy traversing a thin medium due to absorption, emission, and scattering, Eqs. (2.28), (2.21), and (2.18) have to be added:

$$\begin{aligned}\frac{dI_\lambda(\mathbf{s},\mathbf{\Omega})}{ds} = &-\beta_{e,\lambda}(\mathbf{s})\; I_\lambda(\mathbf{s},\mathbf{\Omega}) \\ &+\beta_{a,\lambda}(\mathbf{s})\; B(T(\mathbf{s})) \\ &+\frac{\beta_{s,\lambda}(\mathbf{s})}{4\pi}\int_{4\pi} p\left(\mathbf{s},\mathbf{\Omega},\mathbf{\Omega}'\right) I_\lambda\left(\mathbf{s},\mathbf{\Omega}'\right)\, d\Omega'.\end{aligned} \tag{2.33}$$

In Eq. (2.33), local thermodynamic equilibrium has been assumed such that emission is equal to absorption based on Kirchhoff's and Planck's laws. This general form of the radiative transfer equation (RTE) is only valid for monospectral radiation, as indicated by the index λ. Furthermore, the radiation is assumed to be unpolarized. If polarization effects are considered in the RTE, the scalar RTE (Eq. (2.33)) is extended to the vector radiative transfer equation (VRTE). I is replaced by the so-called Stokes vector $\mathbf{I} = (I, Q, U, V)$ and absorption and extinction coefficients as well as the phase function become matrices. The components Q, U, and V describe the degree of linear polarization, the plane of polarization, and the ellipticity, respectively. Since the VRTE is not relevant for the present study, hereafter, the RTE refers to the scalar radiative transfer equation.

2.4.1 The RTE for a plane-parallel atmosphere

In many radiative transfer applications, the RTE for a plane-parallel atmosphere is used. A plane-parallel atmosphere implies that atmospheric parameters are horizontally homogeneous and vary only in the vertical direction. In this case, the dependency on $\mathbf{s}$ is reduced to a dependency on the vertical coordinate z (Fig. 2.3) with

$$ds = \frac{dz}{\cos\theta} = \frac{dz}{d\mu}. \tag{2.34}$$

Substitution of Eq. (2.34) in Eq. (2.33) and using μ and ϕ to express $\mathbf{\Omega}$ gives

$$\begin{aligned}\mu\frac{dI_\lambda(z,\mu,\phi)}{dz} =& -\beta_{e,\lambda}(z)\ I_\lambda(z,\mu,\phi)\\ &+\beta_{a,\lambda}(z)\ B(T(z))\\ &+\frac{\beta_{s,\lambda}(z)}{4\pi}\int_{4\pi} p\left(z,\mu,\phi,\mu',\phi'\right) I_\lambda\left(z,\mu',\phi'\right)\ d\mu'\,d\phi'.\end{aligned} \tag{2.35}$$

The optical thickness or depth of all atmospheric contributors is defined as

$$\tau(z) = \int_z^\infty \beta_{e,\lambda}\left(z'\right)\ dz' \tag{2.36}$$

and is measured downward from the upper boundary. Instead of using z as the vertical coordinate, it is convenient to introduce τ, so that Eq. (2.35) becomes

$$\begin{aligned}\mu\frac{dI_\lambda(\tau,\mu,\phi)}{d\tau} =& I_\lambda(\tau,\mu,\phi)\\ &-(1-\tilde{\omega}_\lambda(\tau))\ B(T(\tau))\\ &-\frac{\tilde{\omega}_\lambda(\tau)}{4\pi}\int_{4\pi} p\left(\tau,\mu,\phi,\mu',\phi'\right) I_\lambda\left(\tau,\mu',\phi'\right)\ d\mu'\,d\phi'.\end{aligned} \tag{2.37}$$

Summarizing the last two terms on the right hand side of Eq. (2.37) in the source function J_λ leads to the basic RTE in a plane-parallel atmosphere

$$\mu\frac{dI_\lambda(\tau,\mu,\phi)}{d\tau} = I_\lambda(\tau,\mu,\phi) - J_\lambda(\tau,\mu,\phi), \tag{2.38}$$

which includes absorption, emission, and multiple scattering processes.

2.4.2 Two-stream approximation of the RTE

Equation (2.37) is an integrodifferential equation which cannot be solved analytically except under extremely restrictive assumptions. Therefore, a number of numerical and approximate solution methods exists, which will not be discussed in detail here but can be found in *Lenoble* (1985) and in *Liou* (2002), for example. In NWP and climate models, accurate atmospheric heating rates and therewith radiant fluxes are needed. Therefore, the so-called two-stream method is commonly used, where radiant fluxes are quite accurately derived rather than intensities. In particular, the computational costs are relatively small compared to other techniques, since the angular dependency in Eq. (2.37) is reduced to an upward and a downward component (two streams). The RTE is therefore split into two parts, one ascociated with the upward component and the other one associated with the downward component. Both equations are integrated over the corresponding hemisphere assuming azimuthal independence, which may be fulfilled for a homogeneous medium. By doing so, a pair of coupled, first-order differential equations, the two-stream equations, for the upward ($F^\uparrow$) and downward ($F^\downarrow$) fluxes, depending on the optical thickness τ, can be derived. Multiple-scattering is then representend by the upward and downward fluxes multiplied by the corresponding integrated phase function in forward and backward direction. The discretization of these first-order differential equations, which is equivalent to subdividing the atmosphere into layers of constant optical properties, leads to a set of linear equations. These equations can be formulated for the solar and terrestrial fluxes, respectively, and solved by an elimination-backsubstitution algorithm if appropriate boundary conditions are specified.

2.4.3 Boundary conditions

For solar radiation, the derived set of linear equations from the two-stream approximation includes equations for the direct solar flux and for the diffuse upward and downward solar fluxes, which represent solar radiation that has already been scattered in the atmosphere. At the TOA, the downward diffuse solar and longwave components are zero and the downward direct solar component is simply the solar constant I_0 multiplied by μ, where I_0 is about $1366 \pm 3\,\mathrm{W\,m^{-2}}$ depending on the Earth-Sun distance and the Sun's activity. At the lower boundary, the surface, the upward solar diffuse flux may be expressed as

$$F^{\uparrow}_{SW\,dif} = \alpha_{dir} F^{\downarrow}_{SW\,dir} + \alpha_{dif} F^{\downarrow}_{SW\,dif}, \tag{2.39}$$

where α_{dir} and α_{dif} are the shortwave albedos for the direct and diffuse radiation, respectively. The albedo or reflectivity is given as the ratio of the reflected to the incident flux. In general, the reflectivity depends on the type of the surface and may be different for different wavelengths and different directions of the incident radiation. For vegetation surfaces, for example, the reflectivity sharply increases at a wavelength of about $0.7\,\mu$m. The presence of chlorophyll in vegetation leads to strong absorption at wavelengths lower than $0.7\,\mu$m. Therefore, in radative transfer models, a solar surface albedo is often defined for the UV/visible and for the NIR wavelengths, respectively. For many remote sensing applications, the anisotropic reflection of a surface must be accurately described by means of a bidirectional reflection function, which depends on the directions of the incident and observed radiation. However, in NWP and climate models, Lambertian surfaces are commonly assumed, which state that the reflected radiation is isotropic and does not depend on the incident direction.

Since the surface emits corresponding to Planck's and Kirchhoff's laws, the longwave boundary condition at the surface is given by

$$F^{\uparrow}_{LW} = \alpha_{LW} F^{\downarrow}_{LW} + \varepsilon \pi B\left(T_s\right), \tag{2.40}$$

with the longwave albedo α_{LW}, the emissivity of the surface ε given as $\varepsilon = 1 - \alpha_{LW}$ and the surface temperature T_s. Since α_{LW} is very small ($\sim$0.004), the upward flux $F^{\uparrow}_{LW}$ at the suface is dominated by the emission term.

2.5 The broadband radiative transfer model RRTMG

In order to evaluate the interaction of clouds with solar and terrestrial radiation at the AMF site, the rapid radiative transfer model RRTMG (*Clough* et al., 2005; *Mlawer* et al., 1997; *Barker* et al., 2003) is applied in the present study. The RRTMG is a broadband radiative tranfer model developed by the Atmospheric and Environmental Research (AER), Incorporated. AER has developed many publicly available radiative transfer models including the line-by-line radiative transfer model LBLRTM, the Monochromatic Radiative Transfer Model MonoRTM, and the continuum model MT-CKD. The RRTMG is based on the rapid radiative transfer model RRTM, but has been adopted for the application in global circulation models (GCMs). The RRTMG accurately derives atmosperic fluxes and heating rates. In particular, comparisons between the RRTMG and line-by-line calculations using the validated LBLRTM revealed differences in fluxes and heating rates of less than $1\,\mathrm{W\,m^{-2}}$ and 0.1 (0.3) $\mathrm{K\,day^{-1}}$ in the troposphere (stratosphere), respectively. At present, the RRTMG is implemented in many NWP and climate models including among others the ECMWF[1] Integrated Forecasting

[1]ECMWF: European Centre for Medium-Range Weather Forecasts

System (*Morcrette* et al., 2008), the NCEP[2] Global Forecast System, and the climate model ECHAM5[3].

The RRTMG consists of 14 contiguous bands in the shortwave and 16 in the longwave spectrum (Table 2.1). In the model, sources for absorption in the longwave and for extinction in the shortwave part of the spectrum are water vapor, carbon dioxide, ozone, methane, oxygen, nitrogen, aerosols, and Rayleigh scattering.

The RRTMG utilizes the correlated-k approach (Section 2.2.1) whereby the gaseous absorption data are directly obtained from the LBLRTM. In contrast to the RRTM, the RRTMG uses less $g(k_a)$-intervals (112 in the shortwave, 140 in the longwave) for the integration over the absorption in each spectral band. In order to account for multiple scattering, a two-stream algorithm after *Oreopoulus and Barker* (1999) is applied. The optical properties of water clouds, i.e. cloud optical thickness τ_c, single-scattering albedo $\tilde{\omega}_\lambda$ and asymmetry parameter g, are calculated for each spectral band according to the parameterization of *Hu and Stamnes* (1993). Corresponding properties of ice clouds are determined from the parameterization of *Ebert and Curry* (1992). Optionally, the parameterization by *Fu* (1996) may be used.

Table 2.1: Shortwave and longwave spectral intervals in the RRTMG.

Shortwave / μm	Longwave / μm
NIR	28.571 - 1000
3.846 - 12.195	20.000 - 28.571
3.077 - 3.846	15.873 - 20.000
2.500 - 3.077	14.286 - 15.873
2.151 - 2.500	12.195 - 14.286
1.942 - 2.151	10.204 - 12.195
1.626 - 1.942	9.259 - 10.204
1.299 - 1.626	8.475 - 9.259
1.242 - 1.299	7.194 - 8.475
0.778 - 1.242	6.757 - 7.194
0.625 - 0.778	5.556 - 6.757
UV / Visible	4.808 - 5.556
0.442 - 0.625	4.444 - 4.808
0.345 - 0.442	4.202 - 4.444
0.263 - 0.345	3.846 - 4.202
0.200 - 0.263	3.077 - 3.846

The RRTMG is a one-dimensional plane-parallel homogeneous (PPH) radiative transfer scheme. In order to represent partial cloudiness in such PPH schemes, i.e. if the cloud fraction in a model grid box is smaller than 1, each layer is typically characterized by two sets of optical properties and fluxes, one for the cloudy and one for the cloud-free part. This formulation also requires assumptions for the overlapping of clouds in adjacent layers. Commonly, a maximum-random overlap is applied which states that clouds are maximally overlapped in adjacent layers and randomly overlapped if they are separated by one or more cloud-free layers.

In the RRTMG, sub-grid cloud variability is optionally accounted for by using the Monte-Carlo Independent Column Approximation (MCICA; *Pincus* et al., 2003) with options for random, maximum-random and maximum cloud overlap assumptions. The MCICA is a modification of the Independent Column Approximation (ICA). In the ICA method, the broadband flux at some level is the sum of the clear-sky and cloudy flux weighted with the clear-sky and cloudy fraction. The cloudy flux is determined by a double-integral, which is over all g-intervals and over the distribution of a number of possible states of the cloudy atmosphere. Instead of computing the contribution of every cloud state to every wavelength interval, in the MCICA, a cloud state is randomly chosen for each g-interval. By doing so, the computational costs are significantly reduced making the MCICA applicable to NWP and climate models. In order to derive a set of possible cloud states, a stochastic cloud generator is called in the RRTMG, which produces a set of homogeneous sub-columns. This set as a

[2]NCEP: National Centers for Environmental Prediction
[3]ECHAM5: Global climate model based on the ECMWF GCM

Table 2.2: Input parameters for the radiative transfer model RRTMG. The dimension of a certain parameter may be defined by the number of horizontal columns (ncol), the number of vertical model layers (nlay), the number of vertical model levels, i.e. layer boundaries, (nlev), and the number of shortwave and longwave spectal intervals (nbndsw, nbndlw).

Parameter	Dimension	Unit
Pressure at model layer center	(ncol, nlay)	Pa
Pressure at layer boundary	(ncol, nlev)	Pa
Temperature at model layer center	(ncol, nlay)	K
Temperature at layer boundary	(ncol, nlev)	K
Surface temperature	(ncol)	K
H_2O volume mixing ratio	(ncol, nlay)	1
O_3 volume mixing ratio	(ncol, nlay)	1
CO_2 volume mixing ratio	(ncol, nlay)	1
CH_4 volume mixing ratio	(ncol, nlay)	1
N_2O volume mixing ratio	(ncol, nlay)	1
O_2 volume mixing ratio	(ncol, nlay)	1
UV/VIS surface albedo for direct radiation	(ncol)	1
Near IR surface albedo for direct radiation	(ncol)	1
UV/VIS surface albedo for diffuse radiation	(ncol)	1
Near IR surface albedo for diffuse radiation	(ncol)	1
Flux adjustment factor for Earth-Sun distance	(ncol)	1
Cosine of solar zenith angle	(ncol)	1
Solar constant	1	$\mathrm{W\,m^{-2}}$
In-cloud liquid water path	(ncol, nlay)	$\mathrm{g\,m^{-2}}$
In-cloud ice water path	(ncol, nlay)	$\mathrm{g\,m^{-2}}$
Cloud water drop effective radius	(ncol, nlay)	μm
Cloud ice effective radius	(ncol, nlay)	μm
Cloud fraction	(ncol, nlay)	1
Aerosol optical depth	(ncol,nlay,nbndsw/nbndlw)	1
Aerosol single scattering albedo	(ncol,nlay,nbndsw)	1
Aerosol asymmetry parameter	(ncol,nlay,nbndsw)	1

whole reproduces a certain probability function of cloud liquid and ice within each layer and obeys the chosen overlap assumption in the vertical.

In Table 2.2, the various input parameters for the RRTMG model are summarized. The retrieval of the corresponding parameter values used in the present study is described in detail in Chapter 4. The required information relies on measurements of various instruments and on different data prodcts which are presented in the following chapter.

Chapter 3

Data and instrumentation

In the present study, various information from different instruments and different data products is combined to describe the characteristics of clouds in a low-mountain region during a nine-month period. In this chapter, the employed instruments and data sets are presented. They are essential for the retrieval and the evaluation of the thermodynamic and cloud property profiles and for the interpretation of the results of the radiative transfer calculations. A complete overview of all instrumentation and corresponding observed/derived parameters is given in Table 3.1, while each instrument and data set is presented seperately in detail in the following sections.

3.1 AMF measurements

The ARM Mobile Facility (AMF; Fig. 3.1) consists of multiple active and passive instruments including standard meteorological surface instrumentation, radiometers for different wavelength regimes, and instrumentation for atmospheric profiling. In the following, only those measurements are presented in detail which are directly used in this study or are linked to employed meteorological data products (Section 3.4). The main instruments in this respect are the AMF cloud radar, microwave radiometers, micropulse lidar, ceilometer, radiosondes, and the AMF radiation sensors for downwelling and upwelling shortwave and longwave surface fluxes.

3.1.1 Cloud radar

The AMF cloud radar (*Lhermitte*, 1987; *Clothiaux* et al., 1995) is a zenith pointing W-band Doppler radar at 95 GHz that operates in co-polarization or cross-polarization mode. The radar reports estimates for the first three spectral moments of the Doppler spectrum, i.e. reflectivity, radial velocity, and spectral width, for each range gate. Each profile is an average over 2.14 seconds. The radar has a relatively narrow beamwitdth (<1°), resulting in a small sampling volume. The spatial resolution of the radar bin is 43 m for a range from 132 m above the instrument up to 14,700 m, corresponding to 341 levels. The raw data are available from the standard ARM cloud radar product, which is further processed in the Cloudnet target categorization retrieval (Section 3.4.1). In this retrieval, radar reflectivity profiles are averaged in 30-s intervals and corrected for gaseous and liquid attenuation (Section 3.4.1).

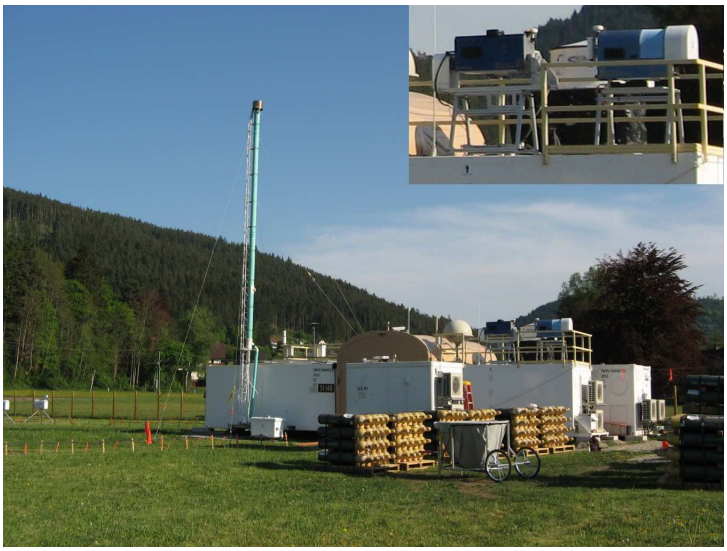

Figure 3.1: ARM Mobile Facility in the Murg Valley, Black Forest. View from northwest. The image detail (top right) shows the University of Cologne's MWRs DPR (left) and HATPRO (right) located at the top of the AMF container.

In addition, the linear depolarization ratio (LDR), that is the ratio of the cross-polar to the co-polar reflectivity, is derived. Furthermore, time- and height-dependent estimates of the random error in Z are reported. The corrected radar reflectivity values are used in the Cloudnet IWC retrieval (Section 3.4.2) and for the LWC retrieval in the present study (Chapter 4).

3.1.2 Lidar-ceilometer

The AMF is further equipped with two lidar devices, a micropulse lidar and a Vaisala ceilometer (*Spinhirne*, 1993; *Campbell* et al., 2002). The ceilometer sends out light pulses with a wavelength of 905 nm and measures atmospheric backscatter with a temporal resolution of 15 s and a vertical resolution of 30 m in 252 range gates up to a height of 7.5 km. The micropulse lidar (MPL) measures at a wavelength of 532 nm and has a temporal averaging time of 30 s. The range resolution is 30 m up to a height of 60 km, whereas the maximum range for the determination of cloud base height is 18 km. The ceilometer and the MPL have a narrow field of view with a beamwidth of about 0.6 mrad and 100 mrad, respectively. For the Cloudnet categorization product, the backscatter profile is needed, which implies further data processing of the raw lidar data including calibration and data quality checks. In particular, the spot size of the outgoing MPL pulse creates an image larger than the detector field of view at near ranges of 3-5 km or less. This results in an under-representation of the near-range signal. In order to correct the measured backscatter profile in this respect, multiplicative factors have to be applied to the lidar signal. These factors depend on the range and are characteristic for the optical overlap between the outgoing spot size and the detector field of view. Due to the overlap function of the MPL, its sensitivity is very low below 2 km height. Thus, the backscatter profile used as input for the categorization retrieval is a combination of the backscatter profiles from both MPL and ceilometer. The latter is used to obtain a sufficient sensitivity in the lowest 2 km.

3.1.3 Radiometer

The AMF includes three MWR systems: a standard two-channel MWR with frequencies at 23.8 and 31.4 GHz, a 90/150 GHz MWR, and a microwave radiometer profiler with twelve frequencies in the range of 22-30 GHz and 51-59 GHz. Only the first mentioned instrument is relavent to this study. The LWP and integrated water vapor (IWV) of the two-channel MWR, which are based on a statistical algorithm, are used in the retrieval of the atmospheric profiles as described in Chapter 4. Both variables are derived using the MWR retrieval algorithm MWRRET (*Turner* et al., 2007). In this algorithm, brightness temperature offsets are applied before the statistical retrieval is performed, leading to a reduced LWP bias in clear-sky cases. Thus, the MWRRET product provides more accurate LWP and IWV estimates than the standard ARM LWP product without the offset correction. The temporal resolution of this data set is 20 s.

LWP values are also needed in the Cloudnet target categorization retrieval to correct for liquid attenuation of the radar reflectivity (see Section 3.4.1). This LWP has been derived from the method by *Gaussiat* et al. (2007) using the two-channel MWR brightness temperatures.

Another AMF radiometric system is the multi-filter rotating shadowband radiometer (MFRSR), which was operated nearly continuously during the AMF deployment. The MFRSR (*Harrison* et al., 1994) makes precise simultaneous measurements of the solar irradiances at six wavelengths (415, 500, 615, 673, 870, and 940 nm) in 20-s intervals throughout the day. Time series of direct solar beam extinctions and horizontal diffuse fluxes are derived from these measurements. Apart from water vapor at 940 nm, the other gaseous absorbers within the MFRSR channels are NO_2 (at 415, 500, and 615 nm) and $O3_3$ (at 500, 615, and 670 nm). Aerosols and Rayleigh scattering contribute to the atmospheric extinction in all MFRSR channels. From the MFRSR observations, the optical depth of the atmosphere can be derived at five wavelengths. Furthermore, the aerosol optical depths (AODs) at these five wavelengths, and subsequently the Angstrom exponent n_a, can be inferred in clear-sky situations. The Angstrom exponent is used in the Angstrom relationship (*Angstrom*, 1929) which describes the spectral dependence of the aerosol optical thickness τ_a:

$$\frac{\tau_{a,\lambda}}{\tau_{a,\lambda_0}} = \left(\frac{\lambda}{\lambda_0}\right)^{n_a}, \tag{3.1}$$

where $\tau_{a,\lambda}$ is the aerosol optical thickness at wavelength λ and τ_{a,λ_0} the optical thickness at a reference wavelength λ_0. Given the AODs and Angstrom exponent of the MFRSR, the AODs can be derived for the RRTMG spectral intervals.

The AMF is further equipped with a collection of radiometers which provide continuous measurements of broadband shortwave and longwave irradiances for downwelling and upwelling components. The so-called SKYRAD system consists of a set of radiometers measuring downwelling sky irradiances. Downwelling shortwave (0.3-3.0 μm) global hemispheric irradiance is measured by an unshaded pyranometer with a hemispheric field of view. Diffuse hemispheric and direct normal irradiances are measured by a shaded pyranometer with a hemispheric field of view and by a solar tracking pyrheliometer with a 5.7° field of view, respectively. Downwelling longwave (4-50 μm) irradiance is determined by a shaded, hemispheric pyrgeometer. Furthermore, a UV-biometer measures hemispheric ultraviolet irradiance (UV-B). The ground radiation (GNDRAD) platform for the upwelling broadband shortwave and longwave fluxes consists of an inverted pyranometer and pyrgeometer, which are equivalent to the SKYRAD instruments. The observed fluxes are available with a 1-minute time resolution

in the ARM skyrad60s and gndrad60s data streams. Uncertainties are reported to be 6% (at least 10-20 $\mathrm{W\,m^{-2}}$) for the pyranometer measurements, 2.5% (at least 4 $\mathrm{W\,m^{-2}}$) for the pyrgeometer observations, and 3% (at least 4 $\mathrm{W\,m^{-2}}$) for the pyrheliometer measurements. In addition, the AMF is equipped with two infrared radiometers, a downwelling and an upwelling version, providing measurements of the equivalent blackbody brightness temperature of the scene in their field of views with an accuracy of 0.5 K. In contrast to the downwelling version, the upwelling version has a wide field of view (∼31°) in order to measure the radiating temperature of the ground surface.

In addition to the standard ARM skyrad60s and gndrad60s products, the ARM Radiative Flux Analysis product is employed in this study. The Radiative Flux Analysis is a technique that uses surface broadband radiation measurements in order to detect periods of clear skies. The detected clear-sky data are used to fit functions which are then employed to derive continuous clear-sky estimates (*Long and Ackerman*, 2000; *Long and Turner*, 2008). The accuracy of the clear-sky estimate is in general within the measurement uncertainty of the instrument itself. The LW clear-sky estimates become less accurate if the interpolated humidity and temperature profiles across the day strongly deviate from the observed ones. Problematic situations in this respect are sharp temporal changes in humidity and temperature, which can not be accounted for in the retrieval. However, *Long and Turner* (2008) showed that for different ARM sites, the differences between measured and estimated LW clear-sky fluxes are within 4 $\mathrm{W\,m^{-2}}$ in at least 70% of the time.

3.1.4 Additional instruments and measurements

Surface wind speed, wind direction, air temperature, relative humidity, barometric pressure, and rain-rate are available every minute from the measurements of the ARM Mobile Facility Surface Meteorology station. Time series of hemispheric sky images are provided by the total sky imager (TSI) during daylight hours. Fractional sky cover is retrieved from the TSI measurements for periods where the solar elevation is greater than 10°. During the nine-month deployment of the AMF, radiosondes have been regularly launched every 6 hours at 00, 06, 12, and 18 UTC measuring vertical profiles of pressure, temperature, humidity, and wind speed and direction. These data are summarized in the ARM SONDE product. In this study, the data of the SONDE product are only used if they pass certain quality checks described in detail in *Nörenberg* (2008). These quality checks include threshold checks of the measured temperature, the geopotential height, the dewpoint, the precipitable water, and the temperature gradient using look-up tables from the Météo France global telecommunication system quality control manual (*Météo France*, 1997).

3.2 Microwave radiometers HATPRO and DPR

In addition to the AMF instrumentation, two microwave radiometers of the University of Cologne were deployed at the AMF measurement site. The humidity and temperature profiler (HATPRO; *Rose* et al., 2005) simultaneously measures brightness temperatures at 14 channels in the K- (22-32 GHz) and in the V-band (51-58 GHz). The dual polarization radiometer DPR measures brightness temperatures at 90 and 150 GHz. At 150 GHz, two channels are available to measure vertically and horizontally polarized radiation. The half power beam width of both instruments is between 2 ° and 4 ° depending on the channel. The HATPRO instrument has been installed on 21 April 2007 and operated nearly continuously

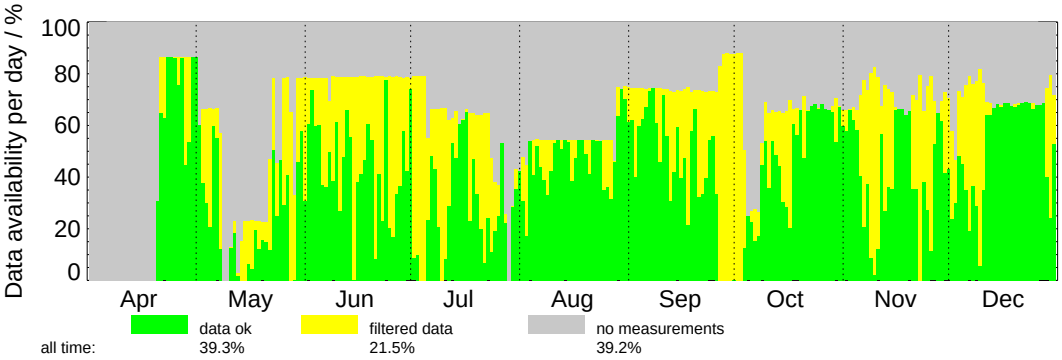

Figure 3.2: HATPRO LWP and IWV data availability in 2007 (30-s time grid).

until 31 December 2007 (Fig. 3.2). During its deployment, several operation modes have been applied including zenith pointing observations, elevation, and azimuth scans. From the end of August to the end of December 2007, the latter two operation modes were combined. In this manner, full 3D scans were performed additionally to the zenith observations and elevation scans. LWP and IWV are derived from the HATPRO brightness temperatures using a statistical retrieval algorithm (*Löhnert and Crewell*, 2003). Due to the different measurement strategies, the temporal resolution of the data varies from one second to several minutes. The HATPRO LWP and IWV values are used to derive the thermodynamic and cloud property profiles as described in Section 4.1. The brightness temperatures of the zenith and elevation observations are input data for the Integrated Profiling Technique (see Chapter 7).

The DPR was installed on 2 May 2007 and measured continuously in zenith direction with 1-s resolution until 5 October 2007. For this time period, the measured brightness temperatures at 90 and 150 GHz are also included in the IPT. For both instruments HATPRO and DPR, the data have been carefully inspected, also by eye, and filtered out, if the measurements are not reliable, in particular if the radome is wet. In this case, the measured signal is contaminated by the emission signal of the water film on the instrument. Thus, MWR measurements are not available during and directly after rain events (i.e., when the radome slowly dries) and when dew has formed on the instrument. This data filtering reduces the data availability of the HATPRO measurements from 61% to about 39% (Fig. 3.2).

3.3 Global positioning system

At the AMF site, the German Research Centre for Geosciences Potsdam employed a global positioning system (GPS) receiver which was part of a GPS receiver network covering the COPS domain. As the GPS signals propagate from different GPS satellites to the receiver on the ground they are delayed by the atmosphere. The delay is caused by the dry air gases and by the atmospheric water vapor yielding a dry or hydrostatic slant delay and a slant wet delay, respectively. Since the GPS satellites are rarely at zenith with respect to the receiver, the observations need to be transformed to zenith. The zenith hydrostatic delay can be well determined from the local surface pressure. The zenith wet delay, which is related to the IWV, can be calculated directly by subtracting the zenith dry delay from the zenith total delay. The IWV is the average over all observations during a certain period of time. The accuracy of the derived GPS IWV is typically about 1-2 $\mathrm{kg\,m^{-2}}$ (*Dick* et al., 2001).

GPS measurements are available every 15 minutes and in 93% of the time during the AMF deployment.

3.4 Cloudnet data products

The Cloudnet program started on 1 April 2001 and aims to develop and validate cloud remote sensing synergy algorithms and to provide data for the improvement of the representation of clouds in climate and weather forecast models. Within the Cloudnet program, several cloud remote sensing stations are operated, which employ a suite of remote sensing instruments, including at least a Doppler cloud radar, a lidar ceilometer, a dual- or multi-wavelength microwave radiometer, and a rain gauge. The initial Cloudnet cloud remote sensing stations are in Chilbolton (United Kingdom), Palaiseau (France), and Cabauw (The Netherlands). However, the Cloudnet retrieval algorithms are also applied to other observational sites which provide the required measurements, including the fixed and mobile measurement sites of the ARM program, the Lindenberg site of the Deutscher Wetterdienst and the Italian site Potenza.

In order to apply the synergistic retrieval algorithms for cloud properties, the observations by the different instruments need to be preprocessed including calibration and regridding of the data. Many of the preprocessing tasks are performed in the Cloudnet target categorization retrieval, which categorizes the backscatter targets in each radar/lidar pixel into a number of different classes. The various Cloudnet algorithms are subsequently applied to the target categorization dataset to derive LWC, IWC, and other products, for example ice effective radius, turbulence, and drizzle parameters.

In this study, two Cloudnet products are employed, the target categorization product and the IWC product by *Hogan* et al. (2006). The target categorization product forms the basis of this study, since it allows for a statistical analysis of the occurrence of clouds at the AMF site, including the analysis of their macrophysical properties and the analysis of the cloud phase. The determination of liquid and ice parts of the cloud is essential for the retrieval of the cloud microphysical properties in Chapter 4. In the following section, the target categorization product will be presented in detail followed by a concise description of the Cloudnet IWC retrieval.

3.4.1 Target categorization

A detailed description of the categorization procedure is given in *Hogan and O'Connor* (2004). The basic principle of the target classification is that the radar is sensitive to large particles such as rain and drizzle drops, ice particles, and insects, while the lidar is sensitive to higher concentrations of smaller particles, such as cloud droplets and aerosol. Key instruments for the target categorization retrieval are a cloud radar, a cloud lidar, a MWR and a rain gauge. The observations of these instruments are supplemented by temperature, pressure, humidity, and wind speed data obtained from a NWP model or radiosondes.

For the AMF site, the following measurements are used in the retrieval: radar reflectivity, 30-s standard deviation of the raw velocities and the LDR of the ARM 95 GHz cloud radar, the combined MPL-ceilometer attenuated backscatter coefficient (Section 3.1.2), the LWP of the

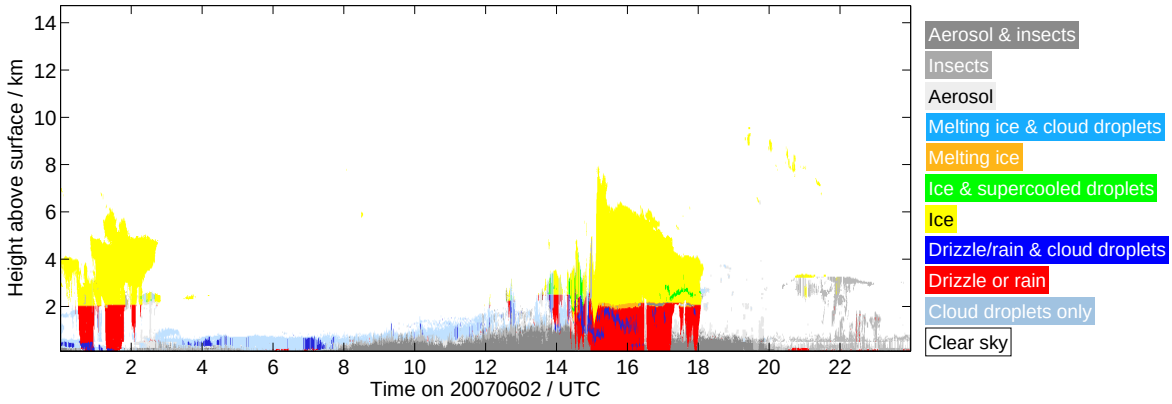

Figure 3.3: Cloudnet target classification on 2 June 2007.

ARM two-channel MWR using the algorithm by *Gaussiat* et al. (2007)[1] and the measurements of the ARM optical rain gauge. In the retrieval, the radar reflectivity profile is corrected for ground clutter in the lowest 10 range gates. Note that the 30-s standard deviation of the raw velocities and the LDR of the radar are not in the standard ARM WACR radar product and have to be calculated. Temperature, pressure, humidity, and wind speed data are taken from the 6-hourly radiosonde ascents.

As a first step, all observations are averaged to a common grid with a temporal resolution of 30 s and a height grid equivalent to the cloud radar grid, which has a vertical resolution of approximately 43 m with a maximum height of 14,700 m. Likewise, the rain rate and liquid water path are interpolated to the 30-s time grid. Since different types of targets may be present in one radar pixel, a 6-bit field is derived for each radar pixel. Five bits present different target types: cloud droplets, falling hydrometeors, melting ice particles, aerosol particles, and insects. An additional 'cold' bit indicates if the wet-bulb temperature is less than 0 °C implying that falling particles are most likely ice particles and not rain or drizzle. Given this bit field, each radar pixel can be classified in terms of the occurrence of cloud droplets, drizzle, rain, ice, supercooled droplets, melting ice, aerosol, and insects. As an example, the target classification of 2 June 2007 is depicted in Fig. 3.3.

Melting ice is detected using the radar Doppler velocity which shows a sharp increase in fall speed at the point of melting. The cold bit is derived from the temperature profile of the closest radiosonde. If a melting layer is detected, the cold bit is adjusted such that it is set in all radar pixels above the top most melting pixel. For the cloud droplet bit, the attenuated lidar backscatter coefficient and the radar reflectivity are analyzed. Here, the fact is used that the base of liquid clouds appears as a strong lidar echo which is confined over a few hundred meters due to the strong extinction of the lidar signal by the cloud layers. The high lidar backscatter of liquid droplets even enables the identification of supercooled liquid layers embedded within ice clouds. Although the lidar signal may be extinguished a few hundred meter above cloud base height, the radar may still receive a signal which allows for the determination of cloud top. For the falling bit, radar reflectivity values with and without clutter are analyzed. Basically, all radar echos not identified as clutter are assigned to be 'falling' with the exception of drizzle-free liquid cloud pixels. In profiles without cloud droplets and surface precipitation, radar echos in the warm region, where the cold bit is

[1] In this LWP retrieval, lidar information is used to detect clear-sky periods. For these periods, the retrieval coefficients are optimally adjusted so that the retrieved LWP is zero.

not set, are assumed to be caused by insects. In order to diagnose insects below the first cloud base, radar reflectivity thresholds are used. The cloud radar LDR also assists in the discrimination between insects and cloud/drizzle. Insects have a much higher LDR than spherical liquid water droplets, and discrimination between the two is usually straightforward using, for example, a threshold of −10 dB. Finally, a pixel is assumed to be dominated by aerosol if a finite lidar signal is present at or below 6000 m and the cold bit, the droplet bit, and the falling bit are not set.

In order to facilitate the application of other retrieval algorithms, the radar reflectivity profile is also stored in the categorization product and corrected for the effects of both liquid and gaseous attenuation. The two-way gaseous attenuation is predominantly due to water vapor and oxygen and is estimated using the themodynamic profiles of the radiosonde. In water cloud regions detected by the classification, the gaseous attenuation is taken into account for a relative humidity of 100%. For the determination of liquid water attenuation in the cloud droplet pixels, an adiabatic LWC profile is assumed which is scaled such that its integrated value matches the MWR LWP.

This objective method of target categorization has been shown to be robust (e.g., *Protat* et al., 2010), but some situations remain where clouds are not detected or missclassified. Since the first liquid layer of a cloud usually strongly attenuates the lidar signal, in multi-layered cloud cases, subsequent layers are frequently not detected by the lidar. The detection of these subsequent cloud layers primarily relies on cloud radar measurements. However, liquid layers in the absence of precipitation are often close to the detection limit of cloud radars. Furthermore, the radar reflectivity of supercooled liquid layers will often be dominated by the scattering from co-existing ice and it is difficult to determine their presence unambiguously from radar data alone. Additionally, liquid layers close to the surface can also pose problems for detection. This includes fog which frequently occurred in the Murg valley in the early morning hours. Vertically pointing pulsed cloud-radar systems have a 'blind zone' close to the surface and the full overlap of transmitter and receiver of lidar systems is often more than 200 m above the surface. The identification of a fog layer is usually possible, but to capture information about its vertical extent is difficult.

3.4.2 IWC

On the basis of the target categorization, meteorological products are derived using the various Cloudnet retrieval algorithms. In the present study, the Cloudnet IWC product by *Hogan* et al. (2006) is utilized. *Hogan* et al. (2006) derived an empirical formula relating IWC to the radar reflectivity Z and the temperature T from a large mid-latitude aircraft dataset:

$$\log_{10}(\mathrm{IWC}) = 0.00058\,Z\,T + 0.0923\,Z - 0.00706\,T - 0.992, \tag{3.2}$$

where Z is is given in logarithmic units of dBZ, T in °C, and IWC in g m^{-3}. The IWC algorithm is applied to all radar bins where ice is diagnosed by the categorization procedure and a radar echo is detected. The retrieval performs well in about 65% of the nine month measurement period (Fig. 3.4). IWC can not be derived in cases where an ice cloud is present but is only detected by the lidar (12% of the time), or where rain below the ice attenuates the radar signal in a way that can not be quantified (10.2% of the time). When a liquid cloud occurrs below the ice, the IWC is retrieved using radar reflectivity values which are corrected for the liquid attenuation. However, if the microwave radiometer data are not available and a liquid cloud occurrs below ice, the retrieval is still performed but its reliability is questionable

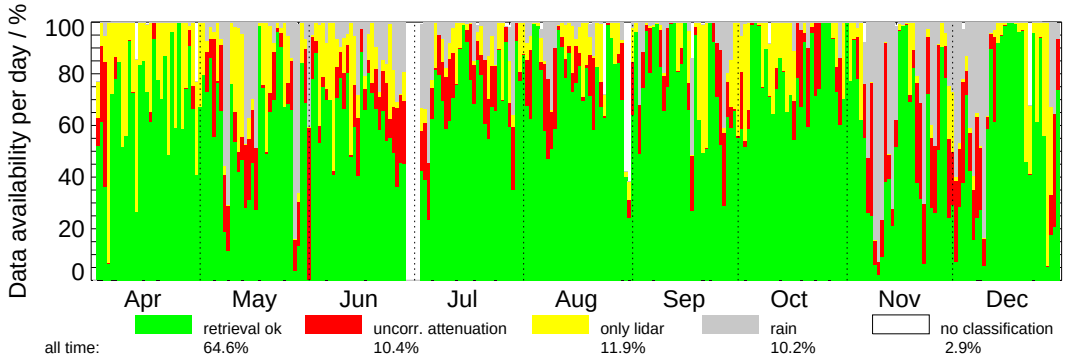

Figure 3.4: Cloudnet IWC data availability in 2007 (30-s time grid). The retrieval can not be performed if the radar signal is not corrected for liquid attenuation (red), the ice cloud has only been detected by the lidar (yellow), if rain is present (grey), or if the target classification is not available (white). Note that the times where the retrieval is flagged as 'ok' also include clear-sky cases.

due to the uncorrected liquid water attenuation. The retrieval of IWC without attenuation correction occurs in 10.4% of all cases during the nine month period.

3.5 COSMO-DE model

COSMO-DE is a non-hydrostatic limited-area atmospheric prediction model designed for the simulation of atmospheric processes on the meso-β (20-200 km) and meso-γ-scale (2-20 km). In the present work, COSMO-DE profiles of temperature, humdity, and pressure are used if radiosonde information is not available. Since April 2007, COSMO-DE is operationally used at the Deutscher Wetterdienst (DWD) in a horizontal resolution Δx of 2.8 km. The model is a part of the DWD's operational NWP system together with the global model GME ($\Delta x = 30$ km), the model COSMO-EU ($\Delta x = 7$ km) and the corresponding data assimilation schemes. Due to its high spatial resolution, COSMO-DE explicitly simulates large-scale convection and the interaction with fine-scale topography. It is based on the primitive hydrothermodynamical equations describing fully compressible non-hydrostatic flow in a moist atmosphere without any scale approximations. The atmosphere is considered a multicomponent continuum consisting of dry air, water vapor, liquid water, and water in solid state. The model equations are formulated with respect to a rotated latitude/longitude-grid. In the vertical, a generalized terrain-following coordinate is used with a vertical resolution of about 19 m near the surface to 1 km in the upper model layers. The model variables are staggered on an Arakawa-C grid in the horizontal and a Lorenz grid in the vertical with scalar variables, namely temperature, pressure, humidity, and bulk water variables, defined at the center of a grid box and the normal velocity components and the turbulent kinetic energy defined on the box faces. The model domain comprises 461 $\times$ 421 grid cells and 50 vertical layers covering Germany, Switzerland, Austria, and parts of adjacent countries.

Physical processes which can not be explicitly simulated by the model have to be parameterized in terms of scale-resolving variables. The parameterization schemes of COSMO-DE are based on those of COSMO-EU with some modifications due to the reduced grid mesh size. Since large-scale convection is explicitly simulated, only small-scale shallow convection is parameterized after *Tiedtke* (1989). Grid-scale clouds and precipitation are represented

by a three-category ice or graupel scheme including the mixing ratios of cloud water, cloud ice, snow, graupel, and rain as prognostic variables. Sub-grid scale clouds, which play a crucial role for cloud-radiation processes, are diagnosed employing an empirical function, which depends on relative humidity, height and convective activity. A detailed description of the model's physics and dynamics is given in *Doms* et al. (2005) and *Baldauf* et al. (2007). Since the main application of COSMO-DE is the forecast of convective events, a model run is started every 3 hours for a forecast period of 21 hours.

Simulated profiles of temperature, humdity, and pressure are used which are extracted from operational COSMO-DE forecasts for the model grid cell corresponding to the location of the AMF. The column output is always taken from the latest forecast and is available hourly.

3.6 GERB instrument

The Geostationary Earth Radiation Budget (GERB) instrument provides accurate measurements of the sunlight reflected from the Earth and of the thermal IR radiation that is emitted by the Earth-atmosphere system(*Harries* et al., 2005). This gives the net TOA response of the Earth-atmosphere system to the incoming solar energy that is essential for atmospheric physics and climate studies. In the present study, GERB data are used to evaluate calculated shortwave and longwave fluxes at the TOA. The GERB instrument operates on the European Meteosat Second Generation satellite (MSG). Its 256-element detector array is aligned north-south and rotates from east to west scanning the Earth in 256x282 pixels within 3 minutes. Alternating scans are performed for the two wavelength channels of the GERB instrument. The detector either observes the total spectrum of radiation from the Earth (0.32-100.00 μm) or shortwave radiation (0.32-4.00 μm). The longwave radiation is obtained by subtracting the shortwave from the total flux measurements.

The raw GERB measurements are calibrated, geolocated, and rectified. Geolocated means that a latitude and longitude is determined for the point where the line of sight of each pixel intersects the surface of the Earth. Since the orbit of the satellite platform slightly deviates from an ideal geostationary orbit, data have to be rectified, i.e., interpolated onto an equiangular geocentric grid (as viewed from the satellite position and orientation), in order to allow for averaging of different scans. The satellite position and orientation is determined from the data of another instrument on the satellite, the Spinning Enhanced Visible and Infrared Imager (SEVIRI; *Schmetz* et al., 2002). SEVIRI information is also used in the radiance and flux processing to account for variations of the instrument sensitivity with wavelength and to convert radiance to flux measurements, for example. Finally, the GERB data are transformed from the coarse GERB resolution, i.e. 50 km at nadir, to the 3×3 SEVIRI pixel resolution, nominally 9 km at nadir. This level 2 product with a temporal resolution of 15 minutes is used in the present study. Note that the solar flux is set to an error value if the solar zenith angle is greater than 80°. In order to spatially match the GERB data to the AMF location, the GERB data have been extracted from the pixel corresponding to the position of the AMF measurement site. Data are available from 1 May to 18 August 2007 and from 29 October to 28 December 2007. In between, Meteosat-9 was switched to a safe configuration and no data were taken.

Table 3.1: Overview of different instruments and data utilized in this study.

Instrument/Product	Temporal resolution (s)	Vertical resolution/ range (m)	Observed/derived parameter related to this study
AMF			
95-GHz cloud radar	2.14	43 / 14,700	Profiles of radar reflectivity, Doppler velocity, and linear depolarization ratio
Micropulse lidar	30	30 / 60,000	Profiles of attenuated backscatter coefficient
Ceilometer	15	15 / 7,500	Profiles of attenuated backscatter coefficient
Two-channel MWR	20	N/A	Liquid water path, integrated water vapor
MFRSR	20	N/A	Aerosol optical depth, Angstrom exponent
Pyranometer	60	N/A	Downward/upward broadband SW flux
Pyrgeometer	60	N/A	Downward/upward broadband LW flux
Radiative Flux Analysis	60	N/A	Clear-sky estimates of downward/upward broadband SW/LW flux, cloud flag
Infrared radiometer	60	N/A	Ground-surface temperature
Surface meteorological instrumentation	60	N/A	Temperature, pressure, relative humidity, rain rate
Radiosonde	6 hours	∼8 / variable; only used if >10,000	Profiles of temperature, pressure, and relative humidity
Total sky imager	30	N/A	Cloud cover
MWRs of University of Cologne			
HATPRO	1 s	N/A	Brightness temperatures, liquid water path, integrated water vapor
DPR	2	N/A	Brightness temperatures
GPS	15 min	N/A	Integrated water vapor
Cloudnet products			
Target categorization	30	43 / 14,700	Profiles of classified targets and attenuation corrected radar reflectivity
IWC from radar/temperature method	30	43 / 14,700	Profiles of ice water content
COSMO-DE model	1 hour	19 m - 1 km / 22,000	Profiles of temperature, pressure, and specific humidity
GERB	15 min	N/A	Upward SW/LW flux at TOA

Chapter 4

Experimental design of the study

For the analysis of cloud statistics and the study of cloud-radiation interactions, information on the cloud macro- and microphysical properties is essential and has to be derived first. If cloud property profiles are succesfully derived and the atmospheric thermodynamic state is known, too, radiative transfer calculations can be performed using the derived atmospheric profiles as model input. On the one hand, these calculations allow for an evaluation of the derived profiles by means of radiation closure studies using independent measurements of shortwave and longwave irradiances that are presented in Chapter 6. On the other hand, if the radiative transfer calculations are performed twice, with and without clouds, the effects of clouds on the fluxes and heating rates can be directly assessed. Results of such studies are analyzed in the Chapters 6 and 7.

In this chapter, the experimental design of the present study is presented including the retrieval technique for the atmospheric profiles (Section 4.1), the setup of the radiative transfer model RRTMG and the different sensitivity studies (Section 4.2). Figure 4.1 provides an overview of the retrieval of the atmospheric profiles as well as of the strategy of the study and is explained in detail in the next sections.

4.1 Retrieval of atmospheric profiles

In order to study cloud-radiation interactions, a realistic description of the atmospheric state, that is the thermodynamics as well as the cloud macrophysical, microphysical, and radiative properties, is needed for the AMF site. For the compilation of such a data set, information from different active and passive remote sensing instruments has to be merged into a single data stream, which characterizes the atmospheric column as good as possible. The key instruments used in this study encompass cloud radar, microwave radiometer, lidar, GPS and radiosonde data, as well as meteorological data from surface instrumentation. The devices employed have been introduced in the previous chapter.

The compilation of high quality thermodynamic and cloud properties from multiple sensors and data sets is a demanding task. The data sets have to be spatially and temporally interpolated and care has to be taken that the thermodynamic and cloud profiles are consistent with each other. If one single measurement is missing or does not pass the quality checks, the whole profile might be excluded from the analysis. Although this procedure significantly reduces the amount of available data, it is necessary to assure that the derived atmospheric profiles provide a clean data basis for radiative transfer calculations.

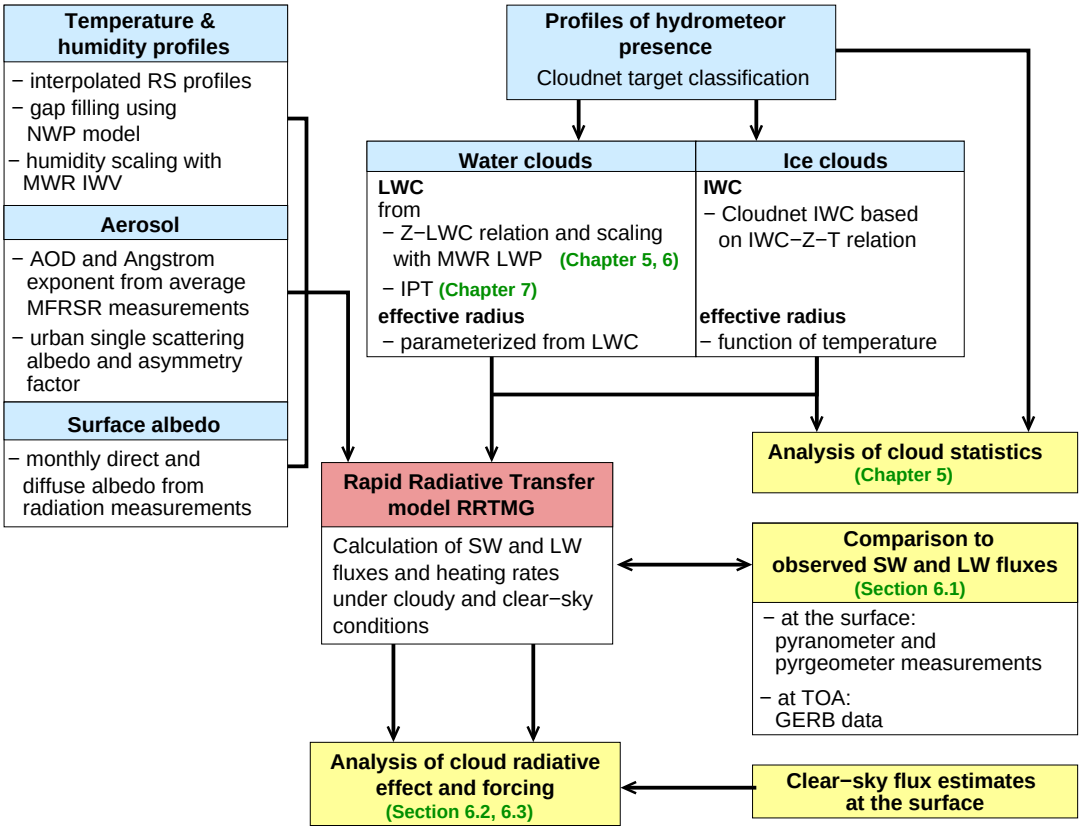

Figure 4.1: Overview of the study: retrieval of atmospheric profiles and of additional input parameters needed for the radiative transfer calculations (blue), the application of the broadband radiative transfer model RRTMG (red) and the analysis strategy (yellow).

In the following, the technique used to derive the thermodynamic and cloud properties is explained in detail. The different data sets used in this respect have already been introduced in Chapter 3. Starting point in the data processing is the Cloudnet target categorization product (Section 3.4.1), which identifies the presence of different hydrometeor types for a temporal ($\Delta t = 30\,\mathrm{s}$) and vertical ($\Delta z = 43\,\mathrm{m}$) grid. The same vertical and temporal resolution is used for the atmospheric profiles of the final data set which are defined up to a height of about 30 km. The target categorization is the precondition for the subsequent application of adequate algorithms to derive cloud microphysical properties for the different hydrometeor types.

4.1.1 Thermodynamic profiles

Vertical information on temperature, humidity and pressure primarily stems from temporally interpolated radiosonde ascents, which were performed every 6 hours during the nine-month measurement period. However, due to subsequent quality checks, the data of about 9% of the radiosonde ascents have been rejected (cf. Section 3.1.4). Radiosonde ascents that did not exceed heights of 10 km above surface are also excluded from the analysis. The remaining radiosonde data are vertically interpolated to the final height grid. If necessary, climatological data are used to extend the thermodynamical profiles up to a height of 30 km. These profiles are then temporally interpolated to the 30-s grid. If more than 12 hours lie between two valid radiosonde ascents, the hourly output of COSMO-DE is linearly interpolated to describe the

thermodynamic profile at a given point of time. Finally, the temperature of the lowest height level is set to the 2-m air temperature of the ARM meteorological instrumentation, which is available with a 1-minute resolution.

To account for temporal variations in atmospheric water vapor at the AMF and to correct the well-known upper-tropospheric dry bias in RS92 radiosonde data (*Vömel* et al., 2007; *Cady-Pareira* et al., 2008), MWR measurements of the integrated water vapor (IWV) are used to scale the temporally interpolated humidity profile from the radiosonde or the COSMO-DE model. The MWR IWV is either from the University of Cologne's HATPRO instrument or, if the HATPRO measurements are not available, from the AMF two-channel MWR. The primary restriction to the MWR data is that they can not be used when the instrument's radome is wet due to dew or rain. In this case, the atmospheric profile is discarded.

Since some MWR IWV measurements are not filtered correctly before and after rain events, they are compared to GPS IWV measurements, which are not affected by rain, to ensure that the MWR and GPS IWVs do not differ by more than $3\,\mathrm{kg\,m^{-2}}$. If the IWV difference is above this threshold, the whole profile is rejected. If the MWR IWV is consistent with the GPS IWV, it is used to scale the humidity profile as follows. If the IWV of the temporally interpolated radiosonde or COSMO-DE humidity profile ($\mathrm{IWV_{SONDE}}$) is larger than the IWV of the MWR ($\mathrm{IWV_{MWR}}$), the humidity in each height is simply scaled with the factor $\mathrm{IWV_{MWR}/IWV_{SONDE}}$. However, in case of a dry radiosonde relative to the MWR, a simple scaling of the humidity profile might lead to unrealistically high values of supersaturation with respect to water. Thus, an iterative approach by *Mather* et al. (2007) is applied. In their approach, the relative humidity (RH) is gradually increased by a uniform fraction of $100 - RH(z)$, where $RH(z)$ is the relative humidity as a function of height. If RH is 100% in a layer, the humidity in this layer is not increased any further. The humidity profile is varied in this way until the difference between $\mathrm{IWV_{MWR}}$ and $\mathrm{IWV_{SONDE}}$ is less than $0.01\,\mathrm{kg\,m^{-2}}$.

4.1.2 Cloud properties and their uncertainties

If a level in the atmospheric column is classified as cloudy, the cloud liquid and/or cloud ice water content as well as the particle size have to be determined. Profiles of cloud liquid water content are derived using the radar reflectivity profiles together with the LWP measured by the MWR. The radar reflectivity profiles are taken from the Cloudnet categorization product and are already corrected for gaseous attenuation and also for liquid attenuation in the absence of rain or melting layers. The LWP of the MWR is again either from the University of Cologne's HATPRO instrument or, if the HATPRO measurements are not available, from the AMF two-channel MWR. If an atmospheric column contains only pure water bins, i.e. no bins containing a water-ice mixture, the LWC of the corresponding radar bins is calculated using the Z-LWC relationship by *Fox and Illingworth* (1997), $Z = a\mathrm{LWC}^b$, where the parameters a and b were empirically determined to be 0.012 and 1.16, respectively. Subsequently, the MWR LWP is used to scale the LWC profile derived from the radar.

If water and ice are co-existing in a bin, as it is the case in the presence of melting ice or ice and supercooled droplets, the Z-LWC relationship can not be applied. In this case, it is difficult to separate the radar signal into the contributions from liquid water and from ice. This separation can be done for some cases using a detailed analysis of the Doppler spectrum (*Shupe* et al., 2004) not employed here. For profiles containing such bins, the MWR LWP is distributed evenly throughout all radar bins containing liquid water in this study. Note that

particles in mixed or melting layers are assumed to be either liquid or solid meaning that mixed phase particles are not accounted for.

In addition to this basic retrieval algorithm for LWC, the Integrated Profiling Technique (IPT) has been applied. The IPT combines MWR, cloud radar, and a priori information in a one-dimensional variational retrieval in order to retrieve profiles of LWC, temperature, and humidity, and corresponding error estimates. Note that the results presented in the following two chapters are related to the basic LWC retrieval algorithm. A detailed description of the IPT and the analysis of its performance are presented in Chapter 7.

In order to derive the effective cloud liquid radius, the approach of *Frisch* et al. (1995) is applied. The authors assumed a lognormal cloud droplet distribution. The modal radius r_m of this distribution is calculated as

$$r_\mathrm{m} = \left(\frac{3\mathrm{LWC}}{4\pi\rho_l N \exp\left(\frac{9}{2}\sigma_x^2\right)} \right)^{\frac{1}{3}}, \tag{4.1}$$

where ρ_l is the density of water, σ_x the logarithmic spread of the distribution and N the droplet concentration, which is assumed to be constant with height. Summarizing the results of various in situ measurements, *Miles* et al. (2000) found typical values of $N = 288\,\mathrm{c\,m^{-3}}$ and $\sigma_x = 0.38$ for continental stratus and stratocumulus clouds with standard deviations of $159\,\mathrm{c\,m^{-3}}$ and 0.14, respectively.

The k-th moment of the lognormal cloud droplet distribution is

$$\mathcal{M}_k = r_\mathrm{m}^k \exp\left(\frac{k^2}{2}\sigma_x\right). \tag{4.2}$$

Since the effective radius is defined as the third moment divided by the second moment, it is related to the modal radius by

$$r_\mathrm{eff,liq} = r_\mathrm{m} \exp\left(\frac{5}{2}\sigma_x^2\right) \tag{4.3}$$

for a lognormal drop size distribution.

For ice clouds, the Cloudnet IWC product according to *Hogan* et al. (2006) is used (Section 3.4.2). The effective cloud ice radius is calculated following *Ivanova* et al. (2001) who relate it to the temperature T (in ℃) by

$$r_\mathrm{eff,ice} = 37.65 + 0.2948\,T. \tag{4.4}$$

Uncertainties in the derived cloud properties can lead to large uncertainties in the calculated radiative fluxes and heating rates, and thus need to be quantified. In addition to a baseline radiative transfer simulation, several sensitivity studies are peformed. For these studies, one parameter, namely LWC, IWC, $r_\mathrm{eff,liq}$, or $r_\mathrm{eff,ice}$, is systematically increased and decreased in a manner that is described as follows. For clouds including liquid water, the uncertainty of the measured LWP is considered, taking into account that the uncertainty increases with increasing LWP in a non-linear fashion. Based on retrieval simulations, the LWP uncertainty is determined to be $22\,\mathrm{g\,m^{-2}}$ at small LWP values and increases to $45\,\mathrm{g\,m^{-2}}$ at $500\,\mathrm{g\,m^{-2}}$. For profiles containing low LWPs (less than $70\,\mathrm{g\,m^{-2}}$), the LWC profile is simply scaled with the fraction $(\mathrm{LWP_{PROF}} \pm \Delta\mathrm{LWP})/\,\mathrm{LWP_{PROF}}$. If the LWP is less than $22\,\mathrm{g\,m^{-2}}$, such a reduction

of LWP would lead to negative LWP values given the uncertainties above. In this case, the new LWP is set to $0.01\,\mathrm{g\,m^{-2}}$. For larger LWP values, a scaling as described above would lead to too small individual LWC errors of about 10% only. Since the LWC derived from radar and radiometer measurements shows uncertainties of 30% or larger (*Löhnert* et al., 2001; *Ebell* et al., 2010), the LWC is varied by 30% in cases with LWP $> 70\,\mathrm{g\,m^{-2}}$. The effective radius of liquid clouds is varied by the larger of 25% or $1\,\mu$m, which represents a realistic uncertainty of this variable (cf. Fig. 2 in *Sengupta* et al., 2003).

For ice clouds, the uncertainties given in the Cloudnet IWC data are used, which exhibit a bias error of 0.923 dB and a typical random error of 1.76 dB. Combining these errors, uncertainties in IWC are between -46% and $+85\%$, which are in same order of magnitude as reported in *Hogan* et al. (2006). The effective radius for ice clouds is varied by -50% and $+100\%$.

4.2 Radiative transfer calculations

The broadband radiative transfer simulations were performed with the Rapid Radiative Transfer Model for GCM applications (RRTMG) that is presented in detail in Section 2.5. In addition to the derivation of atmospheric profiles as laid out in the previous section, several other input parameters of this model have to be determined (cf. Table 2.2). For the concentrations of ozone, methane, oxygen and nitrogen, for example, profiles of the US standard atmosphere are applied in this study. Carbon dioxide is assumed to have a constant concentration of 380 ppm.

In order to account for the effect of aerosols, vertical profiles of aerosol optical thickness, single-scattering albedo and asymmetry parameter have to be included into the RRTMG. For a few short periods in June, July, and August 2007, vertical aerosol information from Raman-lidar observations and from aircraft measurements are available. However, these measurements are very sparse and therefore not representative for the nine-month measurement period. Therefore, the aerosol optical depths of the AMF multi-filter rotating shadowband radiometer (MFRSR) have been used. A comparison of the AOD derived by the MFRSR to aircraft measurements on 15 July 2007 showed a reasonable agreement between both data sets. Together with the Angstrom exponent derived from the MFRSR, the corresponding AODs of the RRTMG mid-interval wavelengths have been calculated via the Angstrom relationship. For the Black Forest site, information on AOD is available on 76 days with daily median values of AOD at 550 nm ranging from 0.05 to 0.26. Since the daily data availability strongly varies between a few minutes and several hours, it is difficult to include adequate temporal variations of AOD in the radiative transfer calculations. Thus, a constant AOD is assumed with a typical value of 0.16 at 550 nm for the entire time period, which is vertically scaled using an exponential weighting function with a scaling height of about 1.3 km. For the single-scattering albedo and the asymmetry parameter, values for urban aerosol are applied which were computed from the OPAC data base (*Hess* et al., 1998).

Since the RRTMG requires a direct-beam and a diffuse SW surface albedo for the ultraviolet/visible and near infrared bands, these values are calculated from the measured upward and downward shortwave fluxes at the surface following the approach of *Yang* et al. (2008). Note that the radiative fluxes at the AMF site are not only influenced by the grassland on which the AMF is located but also by the forested hills surrounding the Murg valley. Firstly, a monthly diffuse albedo α_{dif}^{month} is computed from those measurements for which the downward SW flux is dominated by the diffuse flux, that is when the fraction of the downward

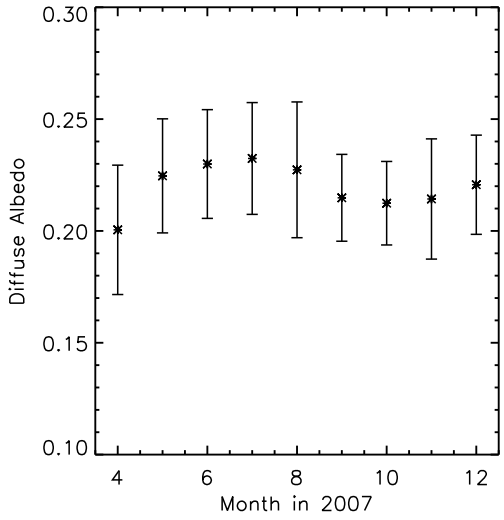

Figure 4.2: Monthly mean diffuse SW surface albedo and its standard deviation at the AMF site.

diffuse SW flux to the total downward SW flux is larger than 0.98 (Fig. 4.2). On average, the variability of the derived monthly mean diffuse albedo amounts to about 15%. In addition to variations in the surface characteristics, e.g. in vegetation or soil moisture, the variation of the diffuse albedo may be also a result of the applied sampling method. For certain samples, the downward diffuse fluxes still contain up to 2% of the direct-beam fluxes inducing uncertainties in the derived diffuse albedo.

In a second step, values for the direct albedo α_{dir} are calculated from the measured SW flux components and the corresponding monthly diffuse albedo via

$$\alpha_{dir} = \frac{F^{\uparrow}_{SWdir}}{F^{\downarrow}_{SWdir}}, \quad \text{with} \tag{4.5}$$

$$F^{\uparrow}_{SWdir} = F^{\uparrow}_{SWtotal} - \alpha^{month}_{dif}\left(F^{\downarrow}_{SWtotal} - F^{\downarrow}_{SWdir}\right) \text{ and} \tag{4.6}$$

$$F^{\downarrow}_{SWdir} = F^{\downarrow}_{SWtotal} - F^{\downarrow}_{SWdif}. \tag{4.7}$$

In order to describe the dependence of the direct albedo on the diffuse albedo and on the cosine of the solar zenith angle (SZA), a polynomial function of the form

$$\frac{\alpha_{dir}}{\alpha^{month}_{dif}} = \frac{1 + c1}{1 + c2 \cdot \cos(\theta)} \tag{4.8}$$

is fitted to the calculated direct albedo values for each month in order to reduce the noise in the individual values (see example for one month in Fig. 4.3) which is related to the variability of the diffuse albedo as discussed before. Given the corresponding monthly diffuse albedo and the cosine of the SZA, both albedo components can be well defined. In Table 4.1, the derived monthly mean diffuse albedos and the constants $c1$ and $c2$ are summarized. However, this technique, which uses the broadband measurements at the AMF site, is unable to derive a spectrally resolved albedo. For the radiative transfer calculations, the UV/visible band and near IR band albedos are therefore assumed to be identical.

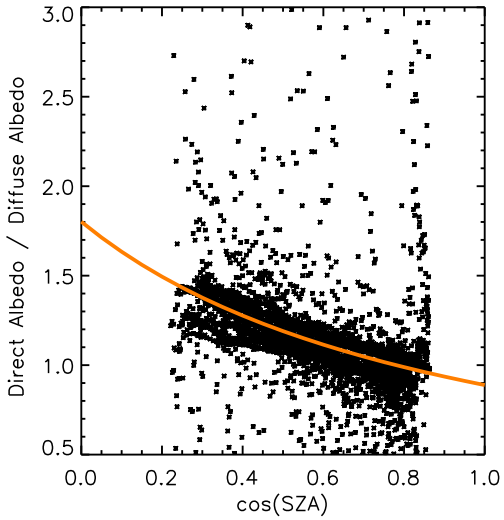

Figure 4.3: Distribution of direct-beam albedo normalized by the monthly mean diffuse albedo as a function of the cosine of solar zenith angle in August 2007; observations (black) and polynomial fit of observations (orange).

Table 4.1: Derived monthly mean diffuse albedos in 2007 at the AMF site and parameters c1 and c2 for the polynomial fit of the direct-beam albedo.

Month	04	05	06	07	08	09	10	11	12
α_{dif}^{month}	0.20	0.22	0.23	0.23	0.23	0.21	0.21	0.21	0.22
$c1$	1.05	1.33	1.25	1.10	0.80	1.11	1.14	1.28	1.01
$c2$	1.07	1.78	1.68	1.35	1.03	1.37	1.46	2.08	1.69

Having determined the various input parameters for the RRTMG, radiative transfer calculations have been peformed providing shortwave and longwave flux and heating rate profiles. Note that cloud fraction is set to 1 in all model layers where the cloud water content is larger than zero. Since the model repeats the calculations under the assumption of cloud-free conditions, the effects of clouds on the radiative fluxes and heating rates can easily be assessed. To this end, two quantities are derived, the cloud radiative effect (CRE) and the cloud radiative forcing (CRF) according to the formulation of *Mace* et al. (2006b). As introduced in Section 1.2, the CRE is defined as the difference between the cloudy and clear-sky net fluxes

$$\text{CRE} = F_{cloudy}^{net} - F_{clear}^{net}, \tag{4.9}$$

and is derived for the surface (SFC) and the top of atmosphere (TOA). The atmospheric (ATM) CRE is then calculated by

$$\text{ATM CRE} = \text{TOA CRE} - \text{SFC CRE}. \tag{4.10}$$

The CRE may be derived for the shortwave and longwave parts separately or combined to a net CRE, which is the sum of the shortwave and longwave components. The values of CRE are positive for warming and negative for cooling of surface, TOA, or atmosphere. The effect of clouds on the SW, LW, and net radiative heating rate profiles is described by the CRF, that is the difference between the corresponding cloudy and clear-sky heating rate profiles

$$\text{CRF} = \text{HR}_{cloudy} - \text{HR}_{clear}. \tag{4.11}$$

Table 4.2: Sensitivity studies with the RRTMG.

Exp. no.	Description	Magnitude of parameter variation
1	baseline simulation	
Modification of thermodynamic and aerosol profiles		
2	temperature variation	$\pm$ 1 K
3	humidity variation	$\pm$5%
4	variation in AOD	$\pm$0.1 at 550 nm
Modification of cloud microphysical properties		
5	LWC variation	at least $\pm$30% (cf. Section 4.1.2)
6	$r_{\text{eff,liq}}$ variation	MAX[25%,1 μm]
7	IWC variation	$-46/+85$%
8	$r_{\text{eff,ice}}$ variation	$-50/+100$%
9	scaled constant LWC profile	
10	scaled modified adiabatic LWC profile	

In order to assess the uncertainty in the derived fluxes and accordingly in the CREs and CRFs due to uncertainties in the input variables, sensitivity studies are conducted where the thermodynamic and cloud property profiles are modified. The different RRTMG experiments are summarized in Table 4.2. For each of the experiments 2-10, two simulations are performed in which the corresponding parameter has been increased and decreased, respectively. The humidity is modified by $\pm$5% and the temperature profile by $\pm$ 1 K. The aerosol optical depth of 0.16 at 550 nm is set to a value of 0.06 (0.26), which represents the observed lower (upper) boundary value at the AMF site. The cloud microphysical properties are modified corresponding to the uncertainties described in Section 4.1.2. In addition, the sensitivity of the results to the LWC profile shape is analyzed. To this end, two simulations are performed in which the LWP in a profile is conserved but redistributed within the cloud. In experiment 9, a constant LWC profile is assumed. Since the LWC profiles of stratiform clouds are often close to quasi-adiabatic (*Korolev* et al., 2007), a modified adiabatic profile (*Karstens* et al., 1994) is generated for experiment 10. The adiabatic LWC (LWC_{ad}) is calculated first and then corrected for effects of dry entrainment, freezing drops, and precipitation using an empirical relationship by *Warner* (1955):

$$\text{LWC}\,(h) = \text{LWC}_{ad}\,(h)\;[1.239 - 0.145\ln\,(h)]\,, \tag{4.12}$$

where h is the height above cloud base.

Following the strategy outlined in this chapter, the analysis of the clouds at AMF site and their radiative effects can be performed starting with a discussion on the data availability of the derived data set and the analysis of the cloud property profiles in the following chapter.

Chapter 5

Cloud statistics at the AMF site

On the basis of the Cloudnet target classification and of the various retrieval algorithms for the cloud microphysical properties as presented in Section 4.1.2, macrophysical and microphysical cloud statistics have been derived for the clouds at the AMF site. The results are presented in this chapter. First, an overview of the atmopheric conditions during the nine-month deployment of the AMF is given. The characterization of the cloud microphysical properties is only possible for the subset of the Cloudnet profiles where all essential measurements are available. The data availability of the retrieved microphysical properties is discussed in Section 5.2. In Section 5.3, the temporal and vertical cloud occurrence is analyzed, while the statistics of the derived microphysical properties are discussed in Section 5.4.

5.1 Atmospheric conditions

The Black Forest region has a typical mid-latitude moderate climate and is mainly under the influence of westerly flow and anticyclonic situations. In the summer time, cloud and precipitation formation are often driven by convective processes. In general, the development of clouds in low-mountain regions is simultaneously influenced by mesoscale and synoptic-scale systems, land-surface processes and the orography. The north-south orientation of the Murg Valley and the prevailing westerly flow and anticyclonal situations in southern Germany might therefore influence the cloud fields in the Murg Valley.

From April to December 2007, mean values of daily 2-m temperature ranged from -7 to 23 °C at the AMF site with mean temperatures below 0 °C mainly occurring in the second half of December (Fig. 5.1a). The daily maximum 2-m temperature in summer rarely exceeded 27 °C, while the daily minimum temperature did not fall below -11 °C in winter (Fig. 5.1b). In April, Germany was under the influence of high pressure most of the time. April was a very dry month with only two days with precipitation amounts larger than 0.1 mm (Fig. 5.1c). According to long-term weather records, it was the driest April in Germany since more than 100 years. In contrast, May was a very wet month with an accumulated precipitation amount of 271 mm. From 7 to 14 May, a strong westerly upper flow developed between a low over the Norwegian Sea and a high pressure system over the Azores and the western Mediterranean Sea. As a result, several surface frontal waves with embedded thunderstoms moved eastward over Germany leading to daily precipitation amounts of about 60 and 80 mm at the AMF site on 7 and 8 May. Due to the intrusion of easterly and south-westerly warm and humid air masses, June and July were also very wet months with precipitation amounts

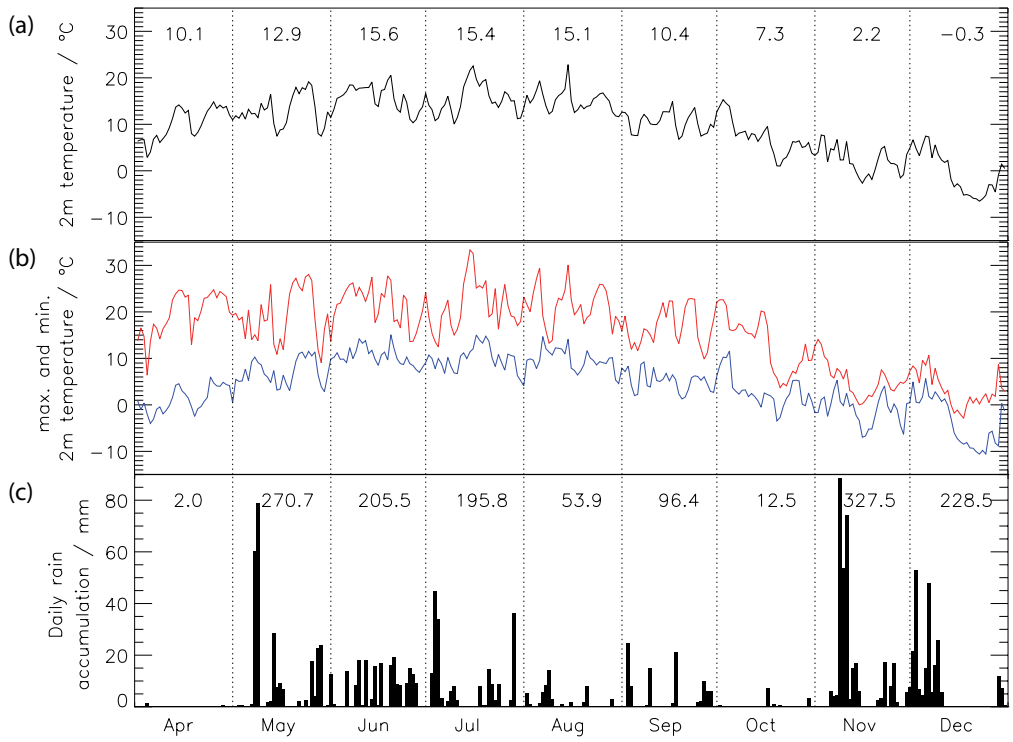

Figure 5.1: 2-m temperature and daily precipitation amounts at AMF site. (a) Daily mean 2-m temperatures with monthly mean values at the top of the plot. (b) Daily minimum (blue) and maximum (red) 2-m temperatures. (c) Daily accumulated precipiation amounts with monthly accumulated values at the top of the plot.

larger than 10 mm on 10 and 5 days, respectively. The large precipiation amounts on 4, 5 and 29 July are related to convective areas embedded in stratiform clouds and rain bands moving across the AMF site. As was the case in June and July, the weather conditions in August were very changeable, while in September cylonic, north-westerly flows prevailed with several cold fronts passing Germany from northwest to southeast. The October weather was mainly characterized by high pressure over Central Europe and the intrusion of dry polar air masses which led to overall sunny conditions. The November showed the largest precipitation amounts per day as well as in monthly total. The inflow of moist maritime air masses from the northwest caused large precipitation amounts on 9 (89 mm), 10 (54 mm), and 11 November (74 mm). In the first half of December, a mild westerly flow was prevailing leading to more than 90% of the total precipiation in this month. Afterwards, a high pressure system over Central Europe brought cold and dry weather.

5.2 Data availability

The accurate determination of significant cloud statistics for the time of the AMF deployment depends on high data availability and quality. With in total 768,838 30-s Cloudnet profiles, an excellent coverage of 97% of the nine-month deployment period is given. This allows for a robust description of the occurrence of clouds as well as their categorization into different cloud types. Except for the unusually dry April with a rain frequency of about 0.2%, the cloud frequency is larger than 60% in each month with peaks in May (77%) and November

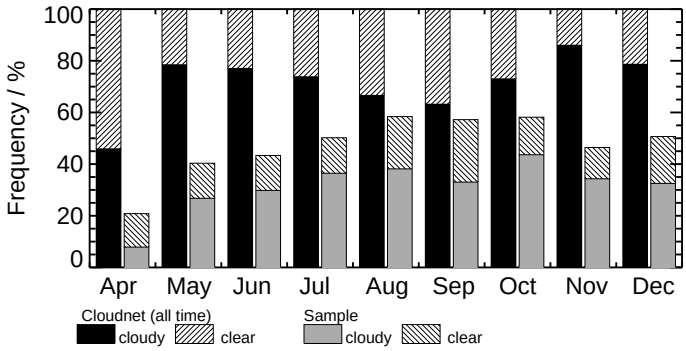

Figure 5.2: Data availability of Cloudnet data and data sample. The total number of Cloudnet profiles is 768,838. The data sample includes 364,850 profiles. The frequency is given relative to the total number of Cloudnet profiles.

(86%) as shown in Fig. 5.2. In order to obtain a high quality data set for the analysis of the interaction of clouds and radiation, it is necessary to apply the quality filters discussed in Section 4.1. Situations with rain are discarded since in these cases, the wet radome of the MWR contaminates the measurements. During the nine-month measurement period, rain has been detected by the AMF optical rain gauge in 10.5% of the time, with November, December, and May revealing the highest rain occurrence of 26, 18 and 16%, respectively. Other reasons to eliminate a profile are missing MWR data and missing Cloudnet IWC Information. MWR information is not available in 21.8% of the cases. In further 10.7% of the time, the MWR IWV is not consistent with the GPS measurements. Due to rain or uncorrected attenuation in the radar reflectivity, IWC information is not available in 23.7% of all cases, while ice has been detected by the lidar alone during 11.9% of the time. These quality filters yield a clean data set, in the following called the data sample, of 364,850 profiles. This corresponds to 47% of the Cloudnet profiles. The data availability of the data sample, which comprises a complete set of thermodynamic and cloud properties is highest for the late summer months with values of up to 58% and lowest in April due to the delayed setup of some of the instruments (Fig. 5.2).

5.3 Cloud occurrence of different cloud types

Since the phase of a cloud strongly affects the radiative fluxes, the analysis is refined by considering different cloud types. These types are water clouds (WC), ice clouds (IC) and mixed-phase clouds (MC), which can occur as single- (SL) or multi-layer (ML) clouds. Clouds are categorized as multi-layer, if cloud layers are separated by one or more height bins. In this scheme, pure water clouds with ice clouds above are assigned as multi-layer mixed clouds. Fig. 5.3 gives an overview of the occurrence of the different cloud types between April and December 2007 at the AMF site. The cloud frequency from the original Cloudnet categorization is shown together with the values for the data sample. The Cloudnet data shows that clouds were present during 72% of the time. These clouds were mostly multi-layer mixed clouds (28.4%), followed by single-layer water (11.3%), single-(10.5%) and multi-layer ice (10.2%) and single-layer mixed clouds (9.4%). Multi-layer water clouds were only detected in 2.3% of the time, although this value may be underestimated due to the attenuation of the lidar in the lowest liquid layer.

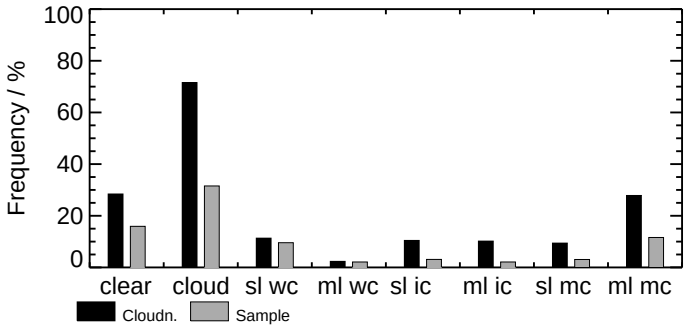

Figure 5.3: Cloud type frequency distributions of the Cloudnet categorization data and the final atmospheric data set (data sample). The frequency is given in % relative to the total number of Cloudnet profiles. Single-layer (SL) and multi-layer (ML) water (WC), ice (IC) and mixed clouds (MC).

Except for in April, multi-layer mixed clouds dominate the cloud occurrence in each month (Fig. 5.4). In April, ice clouds prevail with a frequency of occurrence of about 34%, while in the other months, the frequency of single- and multi-layer ice clouds ranges from 6 to 11%, respectively. In September and October, single-layer water clouds make up a large part (about 30%) of the total cloud occurrence with a monthly frequency of occurrence of 18% and 20%, respectively. In October, these clouds are related to a persistent stratocumulus cloud layer which has been observed between 23-28 October. Multi-layer water clouds are the least common cloud type with a maximum value of 6% in June.

The cloudy periods are evenly distributed through the diurnal cycle. The same is true when considering mixed clouds only. The frequency of occurrence of water clouds slightly increases (about 4%) during daytime hours, while that of ice clouds is maximal during the evening and nighttime hours, i.e. between 18 and 03 UTC (not shown).

While the all-time and monthly occurrence of SL and ML water clouds is well represented in the data sample (Figs. 5.3 and 5.4), the data availability of the other cloud types is significantly reduced. The reason for this are the limited observing capabilities for higher clouds where a quantitative analysis is often prevented by the attenuation of the radar and lidar signals, especially during rain events. The attenuation problem is mainly related to mixed cloud cases where water layers and/or rain are below the ice cloud.

The observed vertical distribution of the different cloud types in the atmospheric column is shown in Fig. 5.5. Most clouds occur in the lowest 2 km of the atmosphere. Such clouds are present in about 22% of all profiles. Single- and multi-layer water clouds prevail in the lowest 2.5 km above the surface, while pure ice clouds dominate the cloud occurrence above 8 km height. With respect to single-layer clouds, ice clouds have the largest median geometrical thickness (1,457 m), followed by mixed clouds (986 m) and water clouds (343 m). Regarding the median cloud base heights, mixed clouds reveal the lowest values with 454 m (SL) and 626 m (ML), and ice clouds the largest ones with 5,426 m (SL) and 4,654 m (ML). SL and ML water clouds have typical cloud bases of 883 m and 669 m, while the median cloud base height of all clouds is found to be 883 m. Due to the prevalence of ice clouds in April, median cloud base height of the lowest cloud is about 7.5 km in this month. From May to December, cloud base height decreases with values ranging from 1,600 m (May) to 300 m and 400 m in November and December (not shown), where MC with low cloud bases dominate the cloud

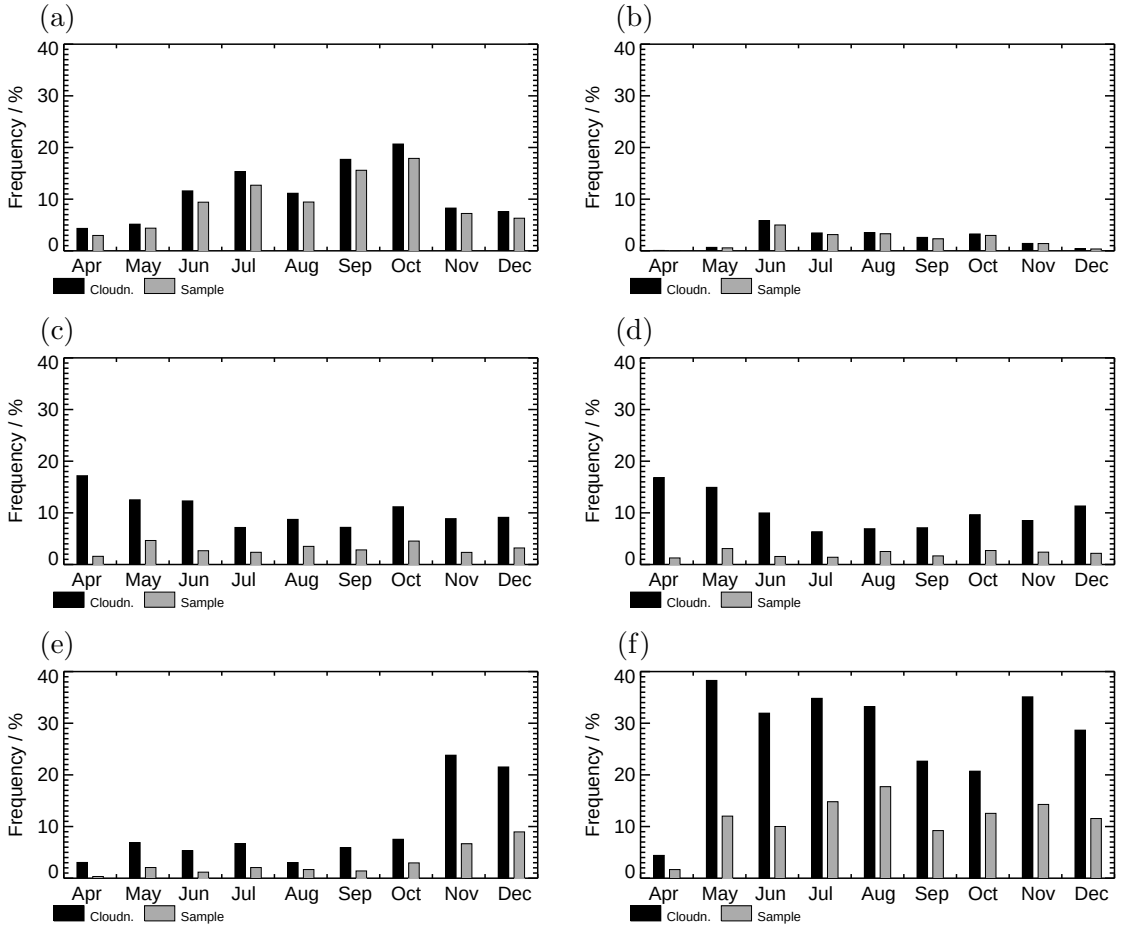

Figure 5.4: Monthly cloud type frequency distributions of the Cloudnet categorization data and the final atmospheric data set (data sample). The frequency is given relative to the total number of Cloudnet profiles. (a) Single-layer and (b) multi-layer water clouds; (c) single-layer and (d) multi-layer ice clouds; (e) single-layer and (f) multi-layer mixed clouds.

occurrence.

5.4 Cloud microphysical properties

While the cloud macrophysical properties have been analyzed for all Cloudnet profiles in the nine-month measurements period, the analysis of the cloud microphysical properties is restricted to the times when valid MWR and Cloudnet IWC information is available. The microphysical properties derived using the technique described in Section 4.1.2 are shown as frequency distributions of LWC, IWC, $r_{\mathrm{eff,liq}}$ and $r_{\mathrm{eff,ice}}$ in Fig. 5.6. Liquid water is primarily found in the lowest 3 km. The median LWC sharply increases with height in the lowest 700 m resulting in a maximum median value with respect to all profiles of $0.035\,\mathrm{g\,m^{-3}}$. Above this height, the median LWC gradually decreases. The median LWC profile of SL WC only has a similar shape with a maximum value of about $0.0053\,\mathrm{g\,m^{-3}}$. The median LWP of all profiles, including clear sky situations, is $10.7\,\mathrm{g\,m^{-2}}$. If only cloud periods are considered, the median LWP increases to $35.4\,\mathrm{g\,m^{-2}}$ for SL WC and $62.6\,\mathrm{g\,m^{-2}}$ for ML MC (Table 5.1), which is significantly lower than the values given by *Turner* et al. (2007b) for the ARM

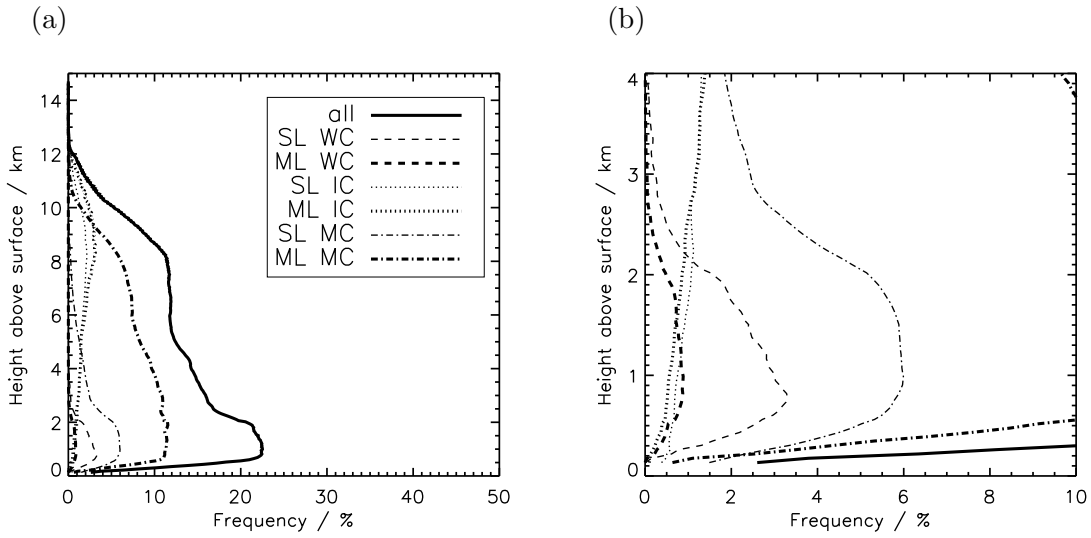

Figure 5.5: Frequency distributions of different cloud types in the atmospheric column. Frequency is normalized by level. Cloud types are single-layer (SL) and multi-layer (ML) water (WC), ice (IC) and mixed clouds (MC). (b) shows an image detail of (a).

sites at the North Slope of Alaska at Barrow ($58.3\,\mathrm{g\,m^{-2}}$), at the Southern Great Plains in Oklahoma ($126.1\,\mathrm{g\,m^{-2}}$), in the Tropical Western Pacific at Nauru ($81.5\,\mathrm{g\,m^{-2}}$) and at Darwin ($78.5\,\mathrm{g\,m^{-2}}$). Note that *Turner* et al. (2007b) derived these values from 30 s measurements for cloudy periods in 2004 with cloud base heights below 3 km. Because statistical properties of LWP are rather sensitive to the averaging time and definition of cloudy scences (*van Meijgaard and Crewell*, 2005), the different analysis procedures can lead to discrepancies. If the same analysis techniques as in the present study are applied to measurements of other mid-latitude but flat-terrain sites, namely the Cloudnet sites Lindenberg and Chilbolton, the LWP of SL WC in 2007 derived for the AMF site is also lower by about $5\,\mathrm{g\,m^{-2}}$ (12%) and $14\,\mathrm{g\,m^{-2}}$ (29%), respectively.

Maximum IWC values are located in a height of about 5 km resulting in a median value of $0.003\,\mathrm{g\,m^{-3}}$ (Fig.5.6b). In the lower levels, the diagnosed IWC values span a wide range from less than 10^{-4} to $1\,\mathrm{g\,m^{-3}}$. Here, the IWC is primarily related to ice clouds detected in November and December. At higher altitudes, the cloud radar sensitivity is diminished, raising the threshold for the detection of small IWC values. This effect can be well observed at the left flank of the IWC distribution. On the other hand, IWC values greater than $0.1\,\mathrm{g\,m^{-3}}$ are rare at high altitudes due to the reduction of available water. Therefore, IWC values range from 0.001 to $0.01\,\mathrm{g\,m^{-3}}$ between 6 and 11 km height. These heights also correspond to the maximum occurrence of SL and ML ice clouds. The form of the IWC frequency distribution resembles the distribution for the tropical ARM site at Manus and Nauru (*Mather* et al., 2007) surprisingly well although the height of the maximum IWC occurrence is shifted from 12.5 km at Manus and Nauru in the Tropics to 8.5 km in the Black Forest. With about $0.004\,\mathrm{g\,m^{-3}}$, the maximum IWC is about the same at both locations. The shape and magnitude of the median and mean IWC profile is rather similar to those of the three Cloudnet sites Cabauw, Chilbolton and Palaiseau with maximum values around 5 km altitude (*Illingworth* et al., 2007).

It should be noted that the mixed clouds included in this study are dominated by the water phase. The median IWP of single- and multi-layer mixed clouds, namely $0.5\,\mathrm{g\,m^{-2}}$ and

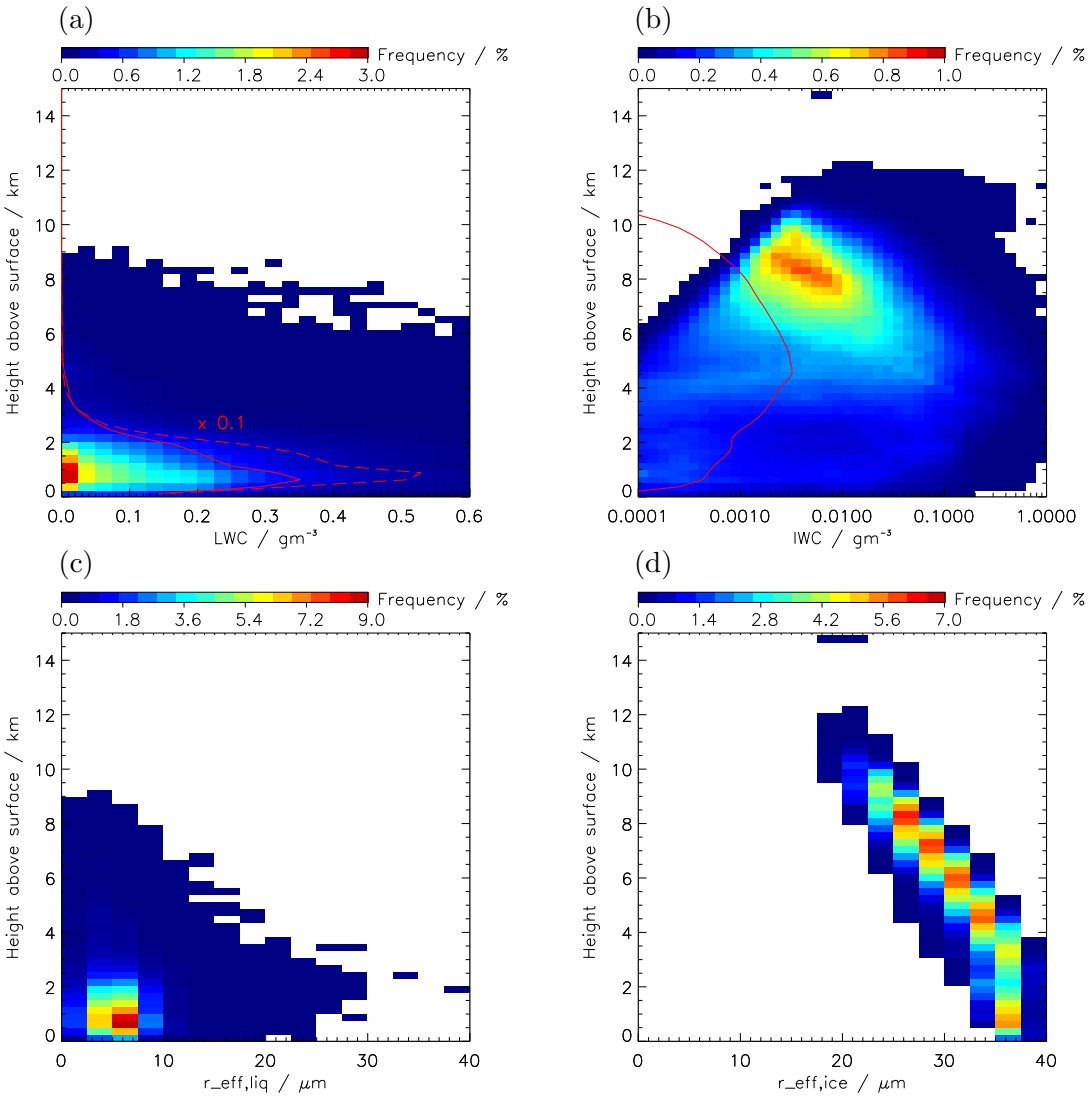

Figure 5.6: Frequency distribution of the derived microphysical cloud properties in the atmospheric column. Frequency is normalized by the total number of profiles. (a) Liquid water content (LWC); (b) ice water content (IWC); (c) cloud liquid effective radius ($r_{\mathrm{eff,liq}}$); (d) cloud ice effective radius ($r_{\mathrm{eff,ice}}$). The red solid lines indicate the median LWC and IWC profiles of all clouds, the dashed line the median LWC profile of all single-layer water clouds. Note that the median LWC profiles are scaled by a factor of 10.

$2.4\,\mathrm{g\,m^{-2}}$, is smaller by one order of magnitude than that of SL and ML ice clouds. Single-layer and multi-layer mixed clouds with large IWC are likely to precipitate and are therefore likely to be eliminated during the sampling of the atmospheric data set.

Since the effective radius of liquid clouds is parameterized in terms of the LWC, the frequency distribution of $r_{\mathrm{eff,liq}}$ is correlated with that of the LWC (Fig. 5.6c). The largest values of the effective radius can be found in the lowest 3 km above the surface with the most frequent values lying between 2.5 and 10 μm. The range of the derived ice effective radii is from 17 μm at high altitudes to 40 μm at lower heights (Fig. 5.6d). Since the ice effective radius is directly related to the temperature by virtue of Eq. 4.4, the decrease of the temperature with height is reflected in the vertical distribution of $r_{\mathrm{eff,ice}}$.

Table 5.1: Statistics of the different cloud types using the derived cloud property data set. LWP, IWP, $r_{\text{eff,liq}}$, $r_{\text{eff,ice}}$ and cloud thickness are median values. Results are shown for the 30-s profiles and for 5- and 15-min averages analyzed in the radiative transfer studies (Chap. 6). Cloud types are single-layer (SL) and multi-layer (ML) water (WC), ice (IC) and mixed clouds (MC).

	all clouds	SL WC	ML WC	SL IC	ML IC	SL MC	ML MC
30-s resolution							
Number of profiles	242,555	73,619	16,151	23,861	16,157	23,672	89,090
LWP / $\mathrm{g\,m^{-2}}$	37.5	35.4	50.0	-	-	62.8	62.6
IWP / $\mathrm{g\,m^{-2}}$	0.1	-	-	7.1	10.9	0.5	2.4
$r_{\text{eff,liq}}$ / μm	5.3	5.4	4.9	-	-	5.5	5.3
$r_{\text{eff,ice}}$ / μm	31.1	-	-	29.1	29.0	35.3	31.2
Cloud thickness / m	-	343	-	1,457	-	986	-
Cloud base height / m	883	883	669	5,426	4,654	454	626
5-min average, $\cos(\mathrm{SZA}) > 0.3$							
Number of profiles	5,871	1,194	198	128	53	156	1,757
LWP / $\mathrm{g\,m^{-2}}$	44.1	56.6	58.1	-	-	52.8	72.2
IWP / $\mathrm{g\,m^{-2}}$	4.6	-	-	11.4	14.8	1.5	6.2
$r_{\text{eff,liq}}$ / μm	5.4	5.8	5.0	-	-	5.0	5.6
$r_{\text{eff,ice}}$ / μm	30.4	-	-	27.8	29.4	34.9	30.4
Cloud thickness / m	-	429	-	1,672	-	986	-
Cloud base height / m	969	797	669	6,411	4,397	1,483	754
15-min average, $\lvert\cos(\mathrm{SZA})\rvert > 0.3$							
Number of profiles	2,807	512	48	61	52	96	629
LWP / $\mathrm{g\,m^{-2}}$	53.8	66.6	84.5	-	-	76.0	74.7
IWP / $\mathrm{g\,m^{-2}}$	0.1	-	-	0.2	10.4	0.7	5.2
$r_{\text{eff,liq}}$ / μm	5.7	6.0	5.3	-	-	6.2	5.8
$r_{\text{eff,ice}}$ / μm	31.1	-	-	30.1	28.9	35.5	30.1
Cloud thickness / m	-	429	-	429	-	986	-
Cloud base height / m	669	583	369	1,697	3,754	74	583

Table 5.1 includes the statistics of the microphysical properties analyzed on the 30-s grid. In addition, the same quantities are derived on the basis of 5- and 15-minute intervals. A 5- or 15-minute interval is included into the analysis if 90% of the profiles in the interval were detected as cloudy. These longer periods are used in the analysis of broadband fluxes and heating rates (Chapter 6), since they comprise more persistent cloud situations. The atmospheric profiles are evaluated in terms of a radiative closure study for daytime periods (5-minute intervals, $\cos(\mathrm{SZA}) > 0.3$; Section 6.1), while the assessment of the CRE and CRF for 15-minute persistent cloud situations also includes the nighttime effects (Section 6.2, 6.3). However, due to shadowing effects of the surrounding hills which are not accounted for in the RRTMG simulations, dusk and dawn periods ($0 < \cos(\mathrm{SZA}) < 0.3$) have to be excluded. In order to equally weight night- and daytime cloud effects of the 15-minute persistent cloud situations, also periods with $-0.3 < \cos(\mathrm{SZA}) < 0$ are not accounted for in these studies. Thus, depending on the particular aim of a study, different cloud subsamples are used with

deviating cloud statistics. In most cases, LWP, IWP, and cloud thickness increase when going from 30-s to 5-minute statistics. The median LWP further increases when restricting to 15-minute persistent cloud situations. Interestingly, IWP of SL IC is rather small for this averaging interval. This is because about 70% of the 15-minute persistent SL IC situations are related to geometrically thin, low ice clouds which occurred in the last three months of the year. The median effective radii show only small variations among the different samples. Largest differences are found for the median cloud base height, which is smallest for the 15-minute samples. Especially for SL IC and MC, differences are up to 4,700 and 1,400 m among the different samples.

5.5 Summary and conclusions

Using the Cloudnet target classification and the retrieval techniques described in Chapter 4, the macro- and microphysical properties of clouds that are observed in the vertical column directly above the AMF site are characterized. The 768,838 30-s Cloudnet profiles provide a solid statistic on the occurrence of clouds and of the cloud types in the atmospheric column over the AMF site between April and December 2007. Except for April, cloud frequency is larger than 60% resulting in an overall cloud occurrence of 72%. The most common clouds are multi-layer mixed and single-layer water clouds occurring 28.4% and 11.3% of the time, respectively. Single-layer water clouds occur primarily in the lowest 2.5 km above the surface with a median thickness of 343 m.

Quality filters in the retrieval technique assure that the resulting microphysical profiles are reasonable and give the best estimate for the atmospheric state at this time. These filters mostly affect the representativity of ice and mixed clouds in the resulting data sample of 364,850 clean profiles. In particular, for more than a half of the Cloudnet ice and mixed cloud profiles, it is not possible to derive microphysical properties due to the limited observation capabilities of the MWR and the cloud radar. On the one hand, MWR radiometer measurements and therefore LWP measurements are not available, if the radome is wet, i.e. during rain events or if dew has formed on the radome. On the other hand, IWC can not be derived from the cloud radar measurements, if the radar signal can not be corrected for liquid attenuation or if the scattered signal is below the cloud radar's sensitivity. Since satellites can observe most of the high clouds with or without lower clouds underneath, and ground-based instruments see most of the low clouds, the need to combine both observation systems is a logical consequence. In this way, ice and mixed clouds, where the latter occur most frequently, might be better captured.

In contrast to other cloud types, water clouds are well represented by the derived data sample. It has been shown that SL WC have a median effective radius and LWP of about 5.4 μm and 35.4 g m^{-2}, respectively. The LWP value found for the AMF site is lower than those found for the flat-terrain Cloudnet sites Chilbolton (49.6 g m^{-2}) and Lindenberg (40.0 g m^{-2}) for the same time period. A topic that deserves further research in this respect is the representativity of column measurements for a site in orographic terrain. Up to now, only clouds which occur directly above the AMF site have been analyzed without describing their horizontal variability, for example the cloud fraction or the horizontal distribution of the LWP. The surrounding orography may significantly influence the spatial cloud patterns by the forced uplift of air masses at the windward sites of the mountains. Scanning observations during a two-month period in summer, for example, revealed higher (10-20 g m^{-2}) LWP in the direction to the hill crests on both sides of the Murg valley (*Kneifel*, personal communication) which

are related to the prevailing westerly and anticyclonic flows in these months. In order to analyze the spatial variability of the LWP at the AMF site and associated orographic effects, the elevation and azimuth scans of the HATPRO instrument could be analyzed in more detail in future studies.

The derived data set of cloud property profiles provides a valuable tool for numerous applications like the evaluation of NWP and climate models, the investigation of case studies and the study of cloud radiation interactions. The latter topic is addressed in the following chapter.

Chapter 6

Cloud radiative effect and forcing at the AMF site

After having derived a comprehensive thermodynamic and cloud property data set, broadband radiative transfer calculations have been performed over the full period of the AMF deployment. In the first part of this chapter, the results of radiative closure studies for clear sky and cloudy situations are presented. These studies allow for an evaluation of the derived thermodynamic, aerosol, and cloud property profiles. The assessment of the accuracy of the atmospheric profiles is necessary for a meaningful assessment of the CRE and CRF of the clouds, which is presented in Sections 6.2 and 6.3, respectively. The CRE and CRF are analyzed with a focus on water clouds which are well represented in the derived data sample (cf. Section 5.2). In the analysis, uncertainties in LWP, $r_{\mathrm{eff,liq}}$, and in the LWC profile shape are also taken into account and the relative importance of these parameters is discussed.

6.1 Radiative closure studies with the RRTMG

In this section, calculated shortwave and longwave fluxes of the baseline simulation are compared to observed surface and TOA fluxes. At the surface, measurements of the AMF pyranometer and pyrgeometer are available every minute, while observed TOA fluxes are derived from the GERB instrument with a temporal resolution of 15 minutes. In order to better compare the hemispheric surface flux measurements to the calculated fluxes based on the column derived atmospheric profiles, the surface flux comparison is conducted for 5 minute averages. The TOA comparison is performed for 15-minute averages centered on the GERB observation time. Since the AMF site is located in a valley, the surrounding hills significantly affected the measured shortwave fluxes during dusk and dawn. These shadowing effects can not be reproduced by the RRTMG which does not account for topographic effects and horizontal photon transport. Thus, only those times are considered for which the cosine of the SZA is greater than 0.3 (SZA $< 72.5°$). In the next section, the results of the clear-sky surface flux comparisons are presented (Section 6.1.1), while the radiative fluxes in cloudy situations are analyzed in Section 6.1.2.

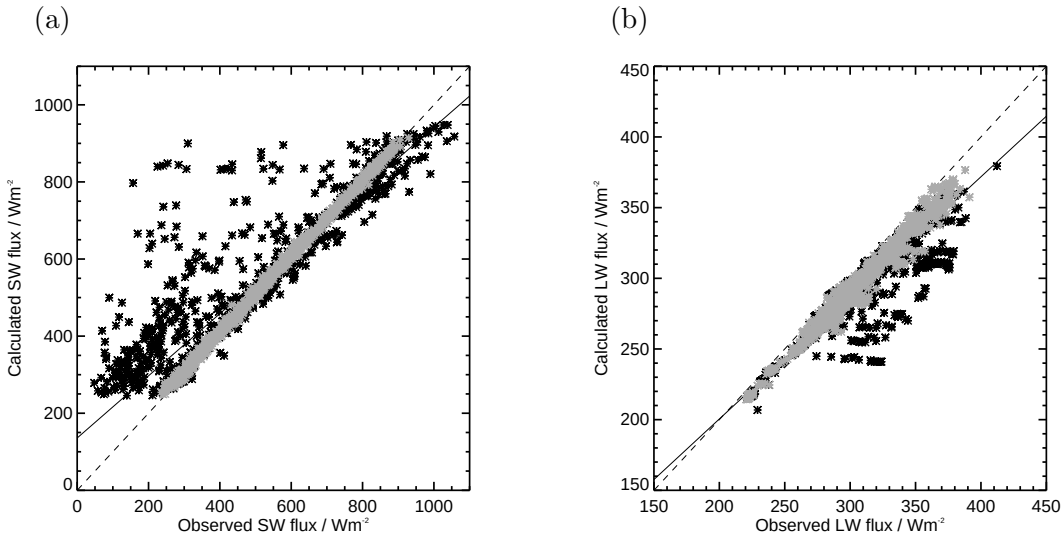

Figure 6.1: Clear-sky surface downwelling flux comparisons between calculated fluxes using the derived thermodynamic profiles and observed fluxes. Fluxes are 5-minute averages for times when the cosine of the solar zenith angle is larger than 0.3 (1734 values). Calculated fluxes are plotted against observed fluxes (a) in the shortwave and (b) in the longwave. The black asteriks indicate the times when clouds have been detected by the radiation measurements but not by the Cloudnet categorization retrieval. The one-to-one line (dashed line) and the linear fit (solid line) are plotted for reference.

6.1.1 Cloud-free atmosphere

In the following surface flux comparisons, all differences are presented in terms of calculated minus observed fluxes. The modelled 5-minute averages are classified as clear-sky if all profiles within the 5 minutes are classified as cloud-free by the Cloudnet target categorization. The direct comparison of simulated to observed fluxes reveals a considerable scatter, but also a bulk of data points aligned along the one-to-one line (Fig. 6.1). Bias and standard deviation are 33.6 $\mathrm{W\,m^{-2}}$ and 84.9 $\mathrm{W\,m^{-2}}$ in the shortwave and -15.6 $\mathrm{W\,m^{-2}}$ and 13.3 $\mathrm{W\,m^{-2}}$ in the longwave comparison (Table 6.1). The overestimation in the downwelling SW and the underestimation in the downwelling LW flux are related to situations in which the hemisphere was actually not cloud-free. To show this, a cloud flag derived from the radiation measurements (*Long and Ackerman*, 2000) is included into the analysis. All times for which a cloud was detected during the 5-minute averaging interval are marked as black asteriks in Fig. 6.1. Clouds have been detected by the radiation measurements in 52% of the cases detected as cloud-free. Due to multiple scattering effects at the cloud boundaries, the SW downwelling radiation may even be underestimated in some cases. There are two reasons for these differences. Firstly, the classification may simply miss a cloud and the profile is mistaken as cloud-free. Secondly, clouds are present but not located directly above the AMF site and thus not in the narrow field of view of the cloud radar, lidar, or microwave radiometers. If the clear-sky flux statistics are calculated only for the data subset where cloud flag indicates a cloud-free hermisphere, the results improve significantly showing only small bias values and root-mean-squared (RMS) differences (Table 6.1). The average differences are less than 2.1% and 3.6% for shortwave and longwave fluxes, respectively. These values are in the same order of magnitude as in clear-sky comparisons in other studies (*Mather* et al., 2007; *Dupont and Haeffelin*, 2008).

Table 6.1: Comparison statistics of calculated and observed downwelling surface clear-sky fluxes. Statistics are calculated on the basis of 5-minute flux averages for times when the cosine of the solar zenith angle is larger than 0.3 (1,734 values). The values in parentheses are the results for those times only when the Long cloud flag indicates clear-sky conditions (841 values). Differences are calculated minus observed fluxes.

	SW		LW	
BIAS / $\mathrm{W\,m^{-2}}$	33.6	(7.4)	−15.6	(−10.8)
RMS difference / $\mathrm{W\,m^{-2}}$	91.3	(11.8)	20.5	(11.9)
STDDEV / $\mathrm{W\,m^{-2}}$	84.9	(9.3)	13.2	(5.0)
Average difference / %	17.9	(2.1)	4.9	(3.6)
Explained variance	0.85	(1.00)	0.86	(0.98)
Slope of linear fit	0.80	(0.99)	0.85	(0.97)
Intercept of linear fit	135.7	(13.5)	29.1	(−0.3)

Table 6.2: Effects of modified humidity, temperature and aerosol profiles on downwelling surface clear-sky fluxes. Values are calculated on the basis of 5-minute flux averages for times when the cosine of the solar zenith angle is larger than 0.3 and the Long cloud flag indicates clear-sky conditions (841 values). The results for the sensitivity experiments are given as differences, i.e. new results minus results of the baseline simulation. The numbers in parentheses are the percental changes with respect to the control run. The mean SW and LW flux of the baseline simulation are $548.9\,\mathrm{W\,m^{-2}}$ and $292.2\,\mathrm{W\,m^{-2}}$, respectively.

	humidity		temperature		AOD	
	+5%	−5%	+1 K	−1 K	+0.1	−0.1
SW	−1.4 (−0.3)	1.4 (0.3)	−0.1 (0.0)	0.0 (0.0)	−21.7 (−3.9)	22.8 (4.2)
LW	2.0 (0.7)	−2.0 (−0.7)	4.8 (1.6)	−4.6 (−1.6)	0.1 (0.0)	0.0 (0.0)

In order to assess the uncertainty in the downwelling fluxes which is due to uncertainties in the temperature, humidity and aerosol profiles, sensitivity studies have been performed where one parameter has been changed (see Table 4.2). The sensitivity tests reveal that, in the SW part, the uncertainty in the downwelling fluxes is dominated by the uncertainty in the aerosol profile. A change of ±0.1 in AOD leads to a change in the mean SW surface downwelling flux by more than $20\,\mathrm{W\,m^{-2}}$ explaining the bias of $7.4\,\mathrm{W\,m^{-2}}$ (Table 6.2). In addition, an underestimation of the humidity by 5% would lead to a positive SW bias of $1.4\,\mathrm{W\,m^{-2}}$. For the longwave fluxes, the accuracy of the temperature profile is most important. An increase by 1 K causes a reduction of the LW bias by $4.8\,\mathrm{W\,m^{-2}}$. Keeping in mind that the temperature profile has been derived from temporal interpolation of 6-hourly radiosonde ascents and hourly model output, differences in derived and actual temperature profiles may be several Kelvin. The spatial drift of the radiosonde may further lead to discrepancies in the measured and and the actual thermodynamic profiles at the AMF site. An underestimation of humidity by 5% would explain $2\,\mathrm{W\,m^{-2}}$ of the LW bias. In general, the longwave flux at the surface is determined by both, temperature and atmospheric emissivity, which in turn depends on humidity. Therefore, a temperature and humidity underestimation in the retrieval/interpolation largely explains the bias in the longwave fluxes.

All in all, the agreement between the calculated and observed clear-sky surface fluxes is conclusive, especially when taking account of the uncertainties in the input variables. Thus,

the clear-sky comparison confirms that the thermodynamic profile data set is well suited for radiation studies. This comparison also underlines the difficulty to compare radiative fluxes of hemispheric measurements to those of column calculations, which can not capture the full spatial variability of the atmospheric state.

The calculated SW and LW upwelling clear-sky fluxes at the surface are directly related to solar surface albedo and surface temperature, respectively. A comparison to observed SW and LW fluxes reveals average differences of 5.4% and 1.5% which are within the measurement uncertainties of 6% and 2.5%, respectively. In the SW, a bias of $4.5\,\mathrm{W\,m^{-2}}$ and a standard deviation of $6.1\,\mathrm{W\,m^{-2}}$ are present. Since the downwelling SW flux at the surface is overestimated, an overestimation of the upwelling flux is expected assuming that the modelled surface albedo is correct. However, if a mean broadband solar surface albedo of 0.25 is assumed as derived from the calculated fluxes, the upwelling bias should be only about $2\,\mathrm{W\,m^{-2}}$. The remaining difference in the bias might be related to the representation of the albedo in the model. The differences in the SW upwelling flux are largest at large SZA and might be a result of the data processing for the diffuse albedo retrieval. The total downward fluxes, which have been accounted for in the diffuse albedo retrieval, contain up to 2% of direct-beam fluxes, which do depend on SZA. Furthermore, no spectral information on the albedo has been included in the radiative transfer calculations, which might lead to discrepancies between calculated and observed values.

In the longwave, bias and standard deviation are 4.7 and $9.0\,\mathrm{W\,m^{-2}}$. These differences may be caused by the different optical field of views of the infrared thermometer and the pyrgeometer. The narrowband radiating temperature reported by the upwelling IRT is very close to the physical temperature of the ground/vegetation in its field of view, which is only about 31° and does not cover the full hemisphere as the pyrgeometer. Although there might be still potential to refine the representation of the albedo and surface temperature, the results are reasonable as they lie within the measurement uncertainties.

6.1.2 Cloudy atmosphere

The comparison of the calculated and observed SW and LW fluxes is now extended to cloudy situations. First, the analysis is performed for all cloud conditions and is then refined with respect to different cloud types. Due to the coarse spatial resolution of the GERB data (about 9×9 $\mathrm{km^2}$), a discrimination between different cloud types and cloudy and clear sky scenes is difficult. The TOA comparison is therefore performed for all-sky conditions only, where cloudy and cloud-free scenes are not differentiated.

All cloud conditions

For the surface flux comparison, only those 5-minute averages are considered in the analysis for which 90% of the time were detected as cloudy. This constraint yields 5,871 values corresponding to about 500 hours of observations. For the moment, clouds are not distinguished into different cloud types. Derived median values for LWP, IWP, $r_{\mathrm{eff,liq}}$, and $r_{\mathrm{eff,ice}}$ for this data sample are $44.1\,\mathrm{g\,m^{-2}}$, $4.6\,\mathrm{g\,m^{-2}}$, $5.4\,\mu$m and $30.4\,\mu$m (Table 5.1). Note that due to more overcast situations, the LWP and IWV values are larger compared to the statistics based on the 30-s time interval.

For the SW downwelling fluxes, there is a significant scatter in the data (Fig. 6.2a) with a negative bias of $-38.2\,\mathrm{W\,m^{-2}}$ and a standard deviation of about $137\,\mathrm{W\,m^{-2}}$ (Table 6.3).

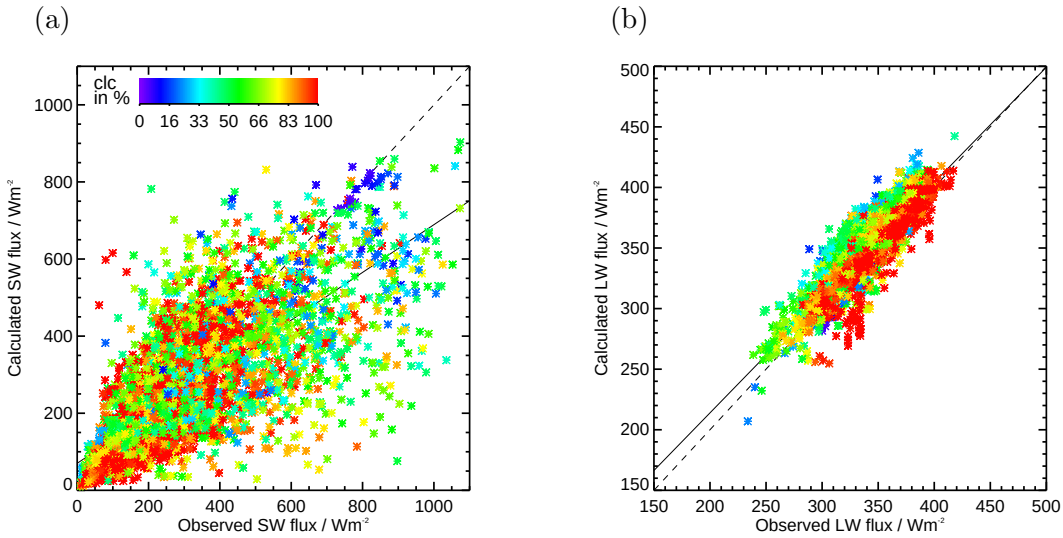

Figure 6.2: Cloudy surface downwelling flux comparisons between calculated fluxes using the derived thermodynamic and cloud microphysical profiles and observed fluxes. Fluxes are 5-minute averages for times when the cosine of the solar zenith angle is larger than 0.3. (a) Shortwave flux; (b) Longwave flux. The one-to-one line (dashed line) and the linear fit (solid line) are plotted for reference. The different colours indicate the cloud cover.

Observed values larger than 700 $\mathrm{W\,m^{-2}}$ are mostly related to broken cloud situations with a hemispheric cloud cover of 70% or less as derived from the AMF total sky imager. Observed and modelled fluxes differ especially in broken cloud situations due to the different sampling from the narrow field of view of the cloud radar, lidar and MWRs and the hemispheric irradiance measurements and due to the assumption of a plane-parallel atmosphere in the radiative transfer calculations. In order to assess the effect of horizontal cloud inhomogeneities and the corresponding 3-dimensional (3D) scattering effects in the analysis, comparisons between observed and calculated fluxes are performed for different cloud cover thresholds (Fig. 6.3a,c). Restricting the analysis to situations with larger cloud cover values can significantly reduce the differences between calculated and observed values, but also reduces the size of the sample. Assuming a cloud cover of 90% or more, for example, reduces the number of values to 2,651 or about 221 hours but also results in a lower standard deviation of about 73 $\mathrm{W\,m^{-2}}$ and in a lower bias of $-13\,\mathrm{W\,m^{-2}}$ (Fig. 6.3a,c; Table 6.3). However, even for overcast situations, 3D scattering effects and inhomogeneities in the cloud field will still cause discrepancies between observed and modelled fluxes in a way that can never be completely separated from effects due to uncertainties in the cloud properties.

For the longwave part (Fig. 6.2b), the results are much better than for SW with a small, positive bias of 6.5 $\mathrm{W\,m^{-2}}$ and a RMS difference of 13.5 $\mathrm{W\,m^{-2}}$ (Table 6.3). The average difference is less than 3% and the explained variance 0.83. Broken clouds also have a strong effect on the LW fluxes at the surface (Fig. 6.3b,d). Increasing the cloud cover threshold to 90%, for example, reduces the bias by 62% to 2.5 $\mathrm{W\,m^{-2}}$ and the standard deviation by 32% to 8.1 $\mathrm{W\,m^{-2}}$.

Calculated upward fluxes at the TOA are compared to GERB measurements (Fig. 6.4, Table 6.4). In order to reduce the discrepancy in the sampling from the point calculations and the satellite measurements, the fluxes derived by the RRTMG are averaged over 15 minutes with the averaging interval centered on the GERB observation times. Note that these fluxes

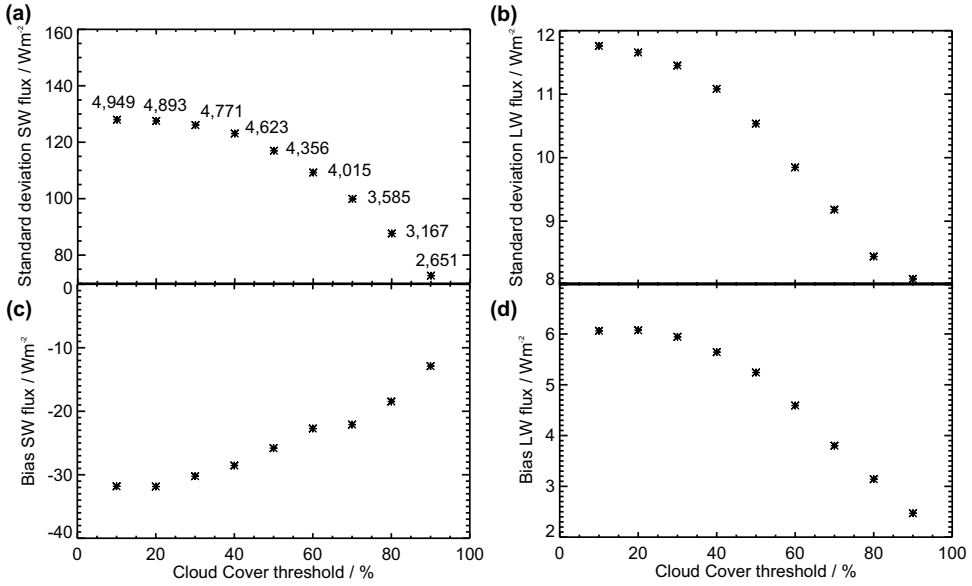

Figure 6.3: Sensitivity of standard deviation (top) and bias (bottom) of surface flux comparison to cloud cover. SW (a,c) and LW (b,d) flux comparison. The numbers related to the data points in (a) are the same for the points in (b-d) and indicate the sample size for the corresponding cloud cover threshold.

are averaged over all-sky conditions, i.e. over clear and cloudy periods, since a discrimination into pure cloudy and pure cloud-free scenes is difficult due to the different sampling volumes. At the TOA, the calculated LW fluxes fit the GERB measurements quite well with a small positive bias and an average difference of less than 6%. The calculated SW fluxes are on average larger than the satellite ones with a positive bias of $36.1\,\mathrm{W\,m^{-2}}$ and a standard deviation of $80\,\mathrm{W\,m^{-2}}$. This positive shortwave bias is primarily related to the surface albedo. For the radiative transfer calculations, albedo values for grassland have been applied, while the satellite sees mostly the forest areas surrounding the AMF location. Further examination of satellite derived albedo values from the MODIS[1] instruments show a typical albedo of 0.1 for a $5\times5\,\mathrm{km}$ area at the AMF site. This value is much lower than the average value of 0.25 that was derived from the radiative transfer calculations. Thus, in clear-sky conditions, the model will always overestimate the TOA upwelling SW flux compared to the satellite measurements.

Furthermore, it is well known that plane-parallel homogeneous (PPH) radiative transfer models have a positive shortwave cloud albedo bias (e.g., *Cahalan* et al., 1994, *Barker*, 1996; *Oreopoulos* et al., 2007), commonly referred to as the PPH albedo bias. An inhomogeneous cloud field has a lower mesoscale-average albedo than a plane-parallel cloud having the same microphysical structure and the same total liquid water. *Cahalan* et al. (1994) found for the PPH albedo bias of marine stratocumulus clouds at visible wavelengths a value of about +0.09 corresponding to a relative bias equal to 15% of the plane-parallel cloud albedo of 0.60. If this bias is related to the fractional global coverage of these clouds, *Cahalan* et al. (1994) estimated the resulting bias in the global albedo to be 8%, i.e. 0.025 assuming a global albedo of 0.3. Other studies employing satellite measurements provided additional estimates of average PPH cloud albedo bias that range from +0.02 to +0.3 depending on spectral range, cloud type, spatial resolution of the satellite data, and reference area size. Positive biases in

[1]Moderate Resolution Imaging Spectrometer on the satellites TERRA and AQUA

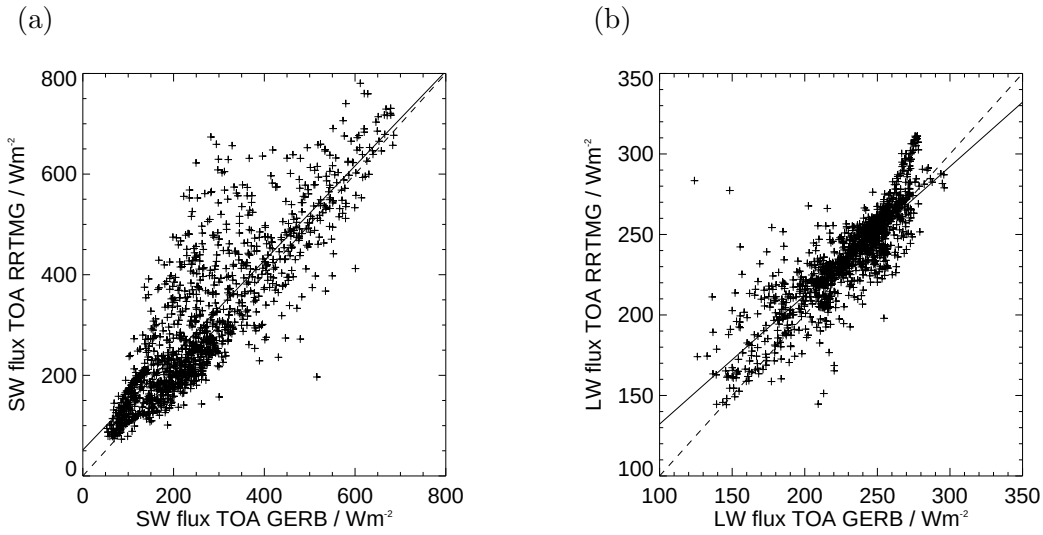

Figure 6.4: All sky upwelling flux comparisons at TOA between calculated fluxes using the derived thermodynamic and cloud microphysical profiles and observed GERB fluxes (1 May - 18 August and 29 October - 28 December 2007). Calculated fluxes are 15-min averages centered on the GERB observation time and only for times when the cosine of the solar zenith angle is larger than 0.3 (1,260 values). (a) Shortwave flux; (b) Longwave flux. The one-to-one line (dashed line) and the linear fit (solid line) are plotted for reference.

cloud albedo translate to positive biases in outgoing solar radiation at the TOA. *Oreopoulos* et al. (2007), for example, investigated the global PPH shortwave albedo bias of liquid clouds for two months using MODIS data. They found that largest biases occur at small SZA values leading to an increase in the upward TOA solar flux by 8.5-9 $\mathrm{W\,m^{-2}}$ with mean daytimes biases of 6.0-6.5 $\mathrm{W\,m^{-2}}$.

Mather et al. (2007) performed radiative closure studies similar to the present study for the tropicals islands Manus and Nauru. They calculated fluxes on the basis of derived cloud property profiles and compared the derived TOA fluxes with flux measurements derived by the GMS-5 satellite. For the SW, they found biases in the same order of magnitude as in the present study. The relative RMSD, i.e. the RMSD divided by the mean observed flux, was found to be 71% (97%) for Manus (Nauru), which is even larger than at the Black Forest site (33%).

In addition to the previously mentioned points, differences between observed and calculated fluxes are also due to uncertainties in the derived cloud macrophysical and microphysical properties. Uncertainties in the cloud boundaries and in the phase determination exist, but are difficult to quantify and are thus not investigated further in the present study. The potential uncertainty in the surface fluxes due to uncertainties in cloud microphysical properties is assessed in the following, where the surface flux evaluation is performed with respect to different cloud types.

Cloud types

In the following, the effect of the different cloud types on the surface fluxes is investigated on the basis of 5-minute flux averages. For the different cloud types, the median values for LWP,

Table 6.3: Comparison statistics of calculated and observed downward surface cloudy fluxes. Statistics are calculated on the basis of 5-minute flux averages and only for times when the cosine of the solar zenith angle is larger than 0.3. Flux differences are expressed as model minus observed flux.

	all clouds		clc>90%	
	SW	LW	SW	LW
Number of profiles	5,871		2,651	
BIAS / Wm^{-2}	−38.2	6.5	-12.9	2.5
RMS difference / Wm^{-2}	141.8	13.5	73.9	8.5
STDDEV / Wm^{-2}	136.5	11.9	72.7	8.1
Average difference / %	32.7	2.7	28.1	1.5
Explained variance	0.61	0.83	0.68	0.91
Slope of linear fit	0.61	0.95	0.77	0.99
Intercept of linear fit	70.1	23.7	29.1	5.0
Mean observed flux / Wm^{-2}	284.5	351.4	181.1	356.1

Table 6.4: Comparison statistics of calculated and observed upward TOA all-sky fluxes. Statistics are calculated on the basis of 15-minute flux averages and only for times when the cosine of the solar zenith angle is larger than 0.3 (1,260 values). Flux differences are expressed as model minus observed flux.

	SW	LW
BIAS / Wm^{-2}	36.1	6.2
RMS difference / Wm^{-2}	87.7	17.6
STDDEV / Wm^{-2}	80.0	16.5
Average difference / %	28.2	5.8
Explained variance	0.74	0.72
Slope of linear fit	0.94	0.80
Intercept of linear fit	51.7	52.2
Mean observed flux / Wm^{-2}	284.5	351.4

IWP and for the effective radii are listed in Table 5.1. The results of the flux comparisons (Figs. 6.5 and 6.6) are given for the shortwave and the longwave case in Table 6.5 and 6.6, respectively. In general, the performance in the SW region is worse than in the LW. The calculated SW fluxes reveal a negative bias of more than $30\,W\,m^{-2}$ for all clouds containing liquid water while pure ice clouds are nearly bias free. In the longwave, the observed fluxes of all cloud types are well reproduced with an average difference of less than 3%. Ice clouds show a negative bias of about $8\,W\,m^{-2}$ while clouds containing liquid water show a small positive bias of $7\,W\,m^{-2}$.

Single-layer water clouds and multi-layer mixed clouds are the two most common cloud types in the data set. Interestingly, the performance in terms of average difference and explained variance for SW and LW is in general slightly better for ML MC than for SL water clouds. This is most likely due to the fact that ML MC situations are often of stratiform nature and show a high optical thickness (higher LWP, Table 5.1; low surface SW irradiance, Table 6.5).

Uncertainties in LWC, IWC and the effective radii propagate to uncertainties in the SW and LW fluxes. In order to assess these effects, sensitivity studies have been performed with

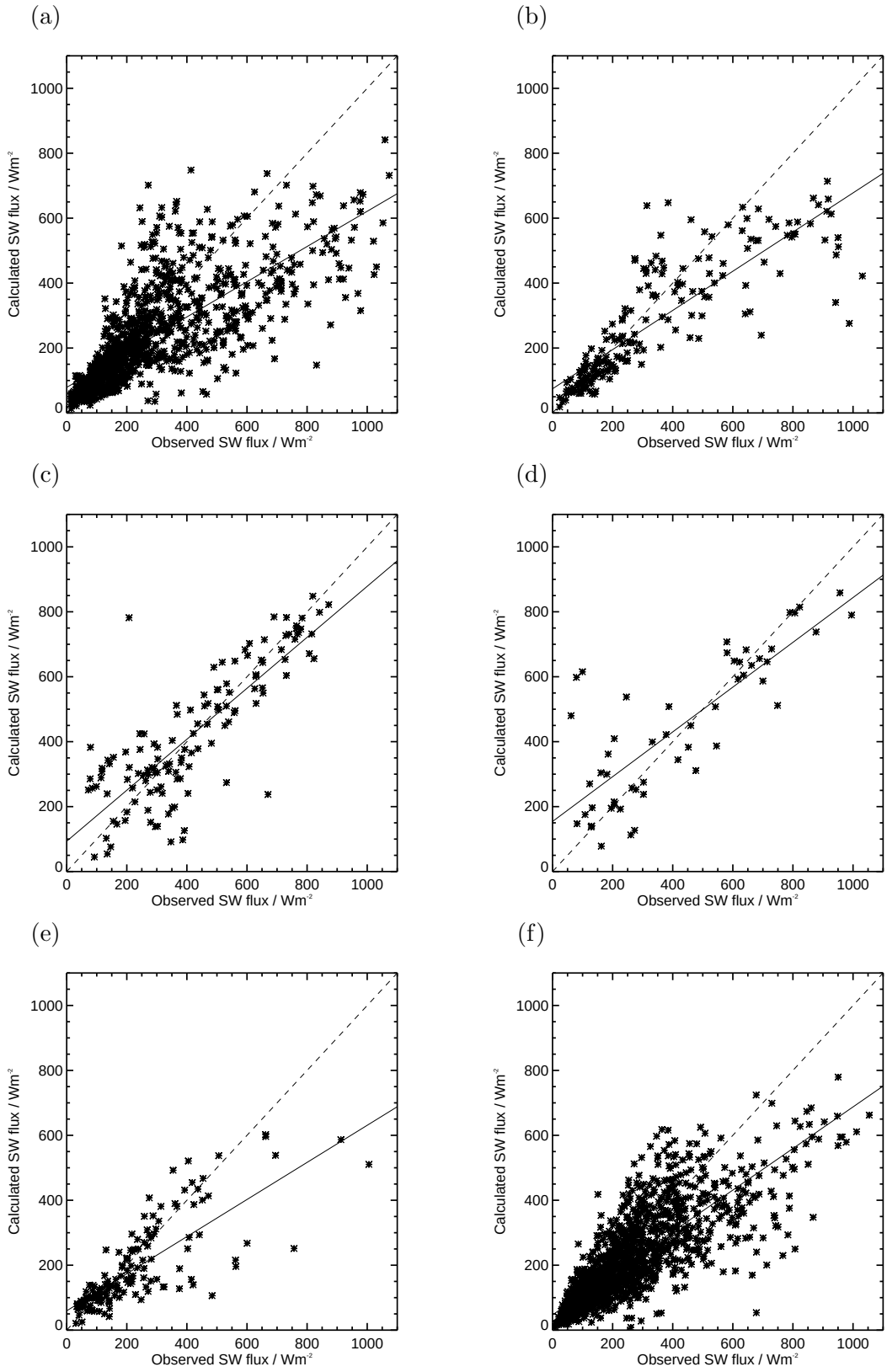

Figure 6.5: Comparisons between calculated and observed shortwave surface downwelling fluxes for different cloud types. Fluxes are 5-minute averages for times when the cosine of the solar zenith angle is larger than 0.3. (a) SL WC; (b) ML WC; (c) SL IC; (d) ML IC; (e) SL MC; (f) ML MC. The one-to-one line (dashed line) and the linear fit (solid line) are plotted for reference.

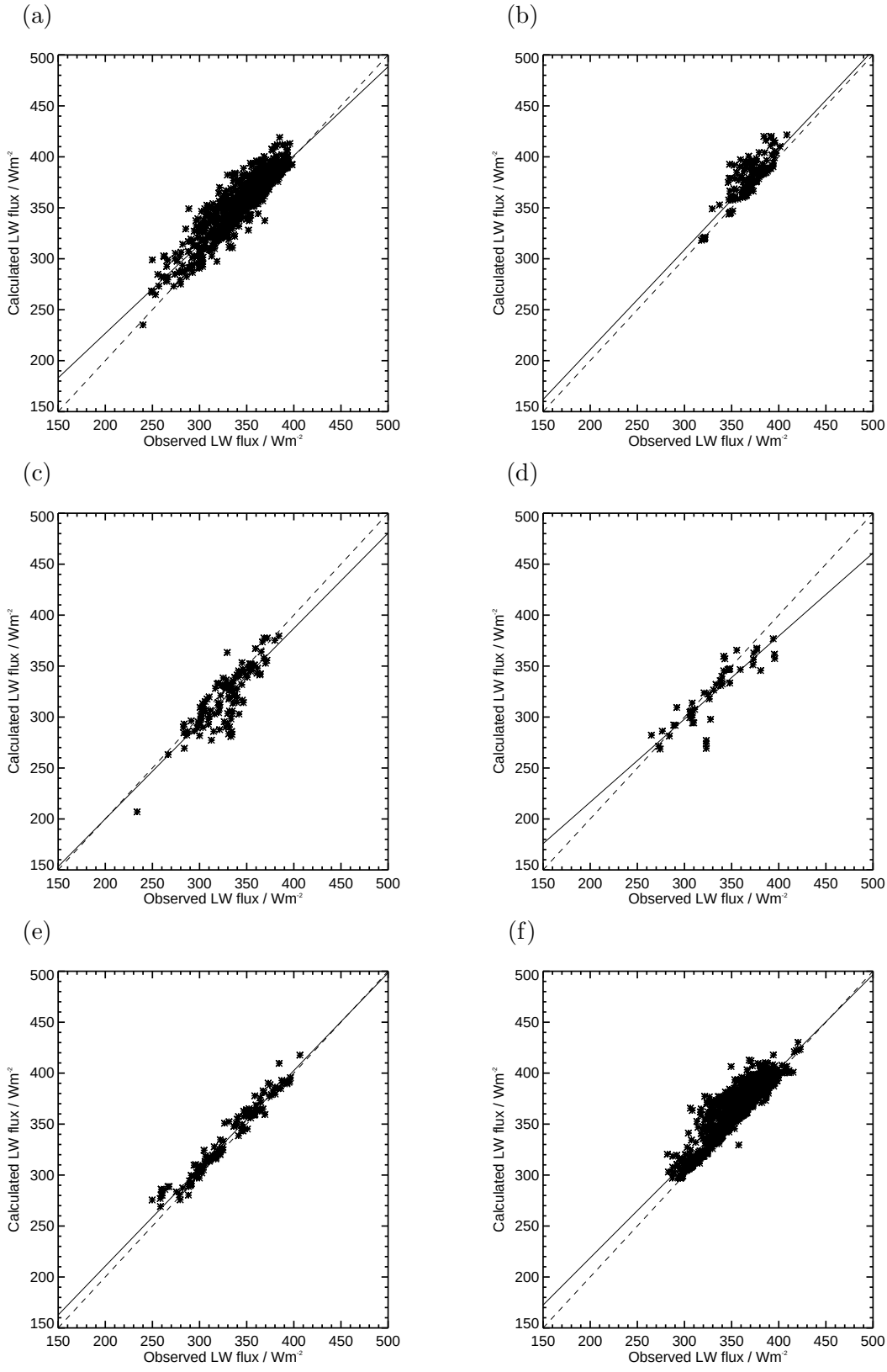

Figure 6.6: Same as Fig. 6.5 but for longwave surface fluxes.

Table 6.5: Comparison statistics of calculated and observed surface shortwave cloudy fluxes for different cloud types. Statistics are calculated on the basis of 5-minute flux averages for times when the cosine of the solar zenith angle is larger than 0.3. Differences are calculated minus observed fluxes. Cloud types are single-layer (SL) and multi-layer (ML) water (WC), ice (IC) and mixed clouds (MC).

	SL WC	ML WC	SL IC	ML IC	SL MC	ML MC
Number of profiles	1,194	198	128	53	156	1,757
BIAS / $\mathrm{W\,m^{-2}}$	−39.1	−56.4	2.7	23.2	−37.1	−30.3
RMS difference / $\mathrm{W\,m^{-2}}$	143.1	153.3	124.2	155.5	119.7	101.4
STDDEV / $\mathrm{W\,m^{-2}}$	137.6	142.5	124.2	153.7	113.8	96.8
Average difference / %	35.7	26.7	37.6	60.7	33.2	28.7
Explained variance	0.59	0.72	0.68	0.66	0.64	0.68
Slope of linear fit	0.54	0.60	0.79	0.69	0.57	0.64
Intercept of linear fit	78.8	74.5	93.4	154.2	59.5	47.1
Mean obs. flux / $\mathrm{W\,m^{-2}}$	257.6	330.2	421.9	422.0	225.5	215.1

Table 6.6: Same as Table 6.5 but for longwave fluxes.

	SL WC	ML WC	SL IC	ML IC	SL MC	ML MC
Number of profiles	1,194	198	128	53	156	1,757
BIAS / $\mathrm{W\,m^{-2}}$	7.7	7.2	−8.4	−7.7	5.5	7.4
RMS difference / $\mathrm{W\,m^{-2}}$	14.1	13.0	17.4	17.7	9.2	12.5
STDDEV / $\mathrm{W\,m^{-2}}$	11.8	10.8	15.2	15.9	7.3	10.0
Average difference / %	2.8	2.2	3.8	3.5	2.0	2.4
Explained variance	0.83	0.74	0.70	0.77	0.96	0.85
Slope of linear fit	0.87	0.98	0.93	0.81	0.96	0.93
Intercept of linear fit	52.3	15.1	13.1	53.6	18.9	33.5
Mean obs. flux / $\mathrm{W\,m^{-2}}$	348.8	369.8	328.4	330.6	325.7	354.5

the RRTMG by varying the cloud microphysical properties as described in Section 4.1.2 (experiments 5-8 in Table 4.2). The mean downward surface fluxes of the baseline and the sensitivity simulations as well as the corresponding observed values are depicted in Figure 6.7. In general, SW fluxes are more sensitive to changes in the microphysical properties than the LW fluxes, where the accurate detection of cloud boundaries is more important. Changes in LWC cause changes in the mean SW and LW fluxes of up to 42% and 5%, respectively. The effect on the surface fluxes due to changes in $r_{\mathrm{eff,liq}}$ is much smaller with maximum relative changes of 15% and 0.1% for the SW and LW. In contrast to uncertainties in $r_{\mathrm{eff,liq}}$, uncertainties in LWC alone can explain the difference between calculated and observed mean SW and LW fluxes for clouds containing liquid water. In particular, the negative bias in the SW and the positive bias in the LW may be explained by an overestimation of cloud optical thickness. Since the cloud optical thickness is proportional to $\mathrm{LWP}/r_{\mathrm{eff,liq}}$ (Eq. 2.32), an overestimation of cloud optical thickness may in turn be a result of an overestimation of LWP and/or of an underestimation of particle size.

Variations in IWC and $r_{\mathrm{eff,ice}}$ induce uncertainties in the same order of magnitude, which are largest for pure ice clouds with relative changes of 6% (SW) and 2% (LW). For these clouds, the observations lie within the derived uncertainties in the SW, while in the LW, the negative bias can not be explained by uncertainties in IWC and $r_{\mathrm{eff,ice}}$ alone. The LW bias for ice clouds is consistent with the clear sky bias and might additionally be caused by a humidity

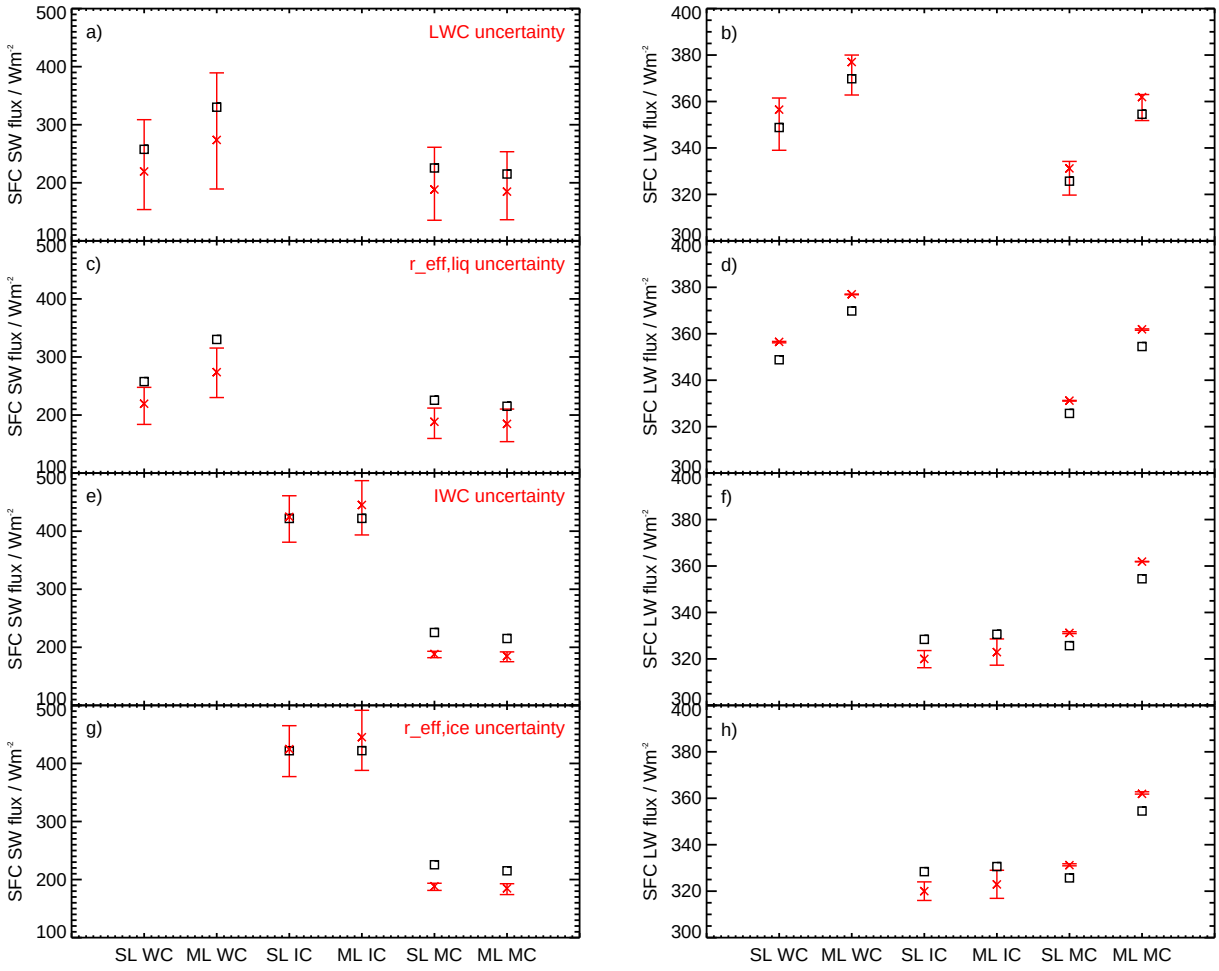

Figure 6.7: Comparison between calculated (red) and observed (black) mean surface downward fluxes in the SW (left) and LW (right) for different cloud types. Uncertainties shown for calculated fluxes are due to uncertainties in LWC, $r_{\mathrm{eff,liq}}$, IWC, and $r_{\mathrm{eff,ice}}$ (from top to bottom).

and/or temperature underestimation.

Since mixed clouds primarily consists of liquid water in this study (Table 5.1) and extinction of SW and emission of LW radiation is thus mainly determined by the liquid parts of the clouds, variations in IWC and $r_{\mathrm{eff,ice}}$ cause very small variations of 10.5 W m^{-2} (SW) and 0.6 W m^{-2} (LW) in the surface fluxes compared to the changes induced by varying LWC and $r_{\mathrm{eff,liq}}$. Note that systematic changes in the microphysical properties have hardly an effect on the large variability of the calcuated fluxes with standard deviations of 100-150 W m^{-2} in the SW and of 7-16 W m^{-2} in the LW part. As for the cloudy comparison, differences between observed and LW fluxes are also related to cloud field inhomogeneities and associated 3D radiative effects. Due to the plane-parallel assumption in the RRTMG, SW (LW) downwelling surface fluxes will be generally to small (large) compared to observations (cf. WC and MC in Fig. 6.5 and 6.6). Thus, to some extent, bias and standard deviation are reduced, if the analysis is restricted to more homogeneous cloud scenes. If, for example, only water clouds with cloud cover greater than 90% are considered, the SW (LW) bias is reduced to about -10 (1) W m^{-2} and the standard deviation to about 50 (4) W m^{-2}. For mixed clouds with a cloud

cover greater than 90%, SW (LW) bias and standard deviation are reduced to about -20 (4) $\mathrm{W\,m^{-2}}$ and 60 (6) $\mathrm{W\,m^{-2}}$, respectively. For these water and mixed clouds, 70 and 60% of the calculated fluxes, respectively, fit the observations within the LWC related uncertainties. The evaluation of fluxes for pure ice clouds in this respect is not possible, since the data sample is already very small for these particular cloud types and would reduce below 10 in both cases, if only full overcast ice-clouds are considered.

Summarizing, the results of the cloudy flux comparison indicate that the derived cloud property profiles are consistent with the surface radiation budget, especially in the longwave part, and that the largest differences in the SW are related to broken cloud situations. In order to better describe these situations, the cloud fraction in principle needs to be taken into account. This could be realized in future studies by employing the TSI measurements and the MCICA in the RRTMG. At the TOA, the calculated fluxes are in an agreement with the TOA radiation budget that is reasonable given the large differences in temporal and spatial sampling. It has been shown that, under overcast conditions, the bias and standard deviation for SW and LW surface fluxes for water clouds are small. This agreement motivates the use of the derived atmospheric profiles in the CRE and CRF calculations for overcast water clouds as described in the following sections.

6.2 Cloud radiative effect

In this section, the CRE defined as the difference between the cloudy and clear-sky net fluxes is analyzed. At the surface, the CRE can directly be derived from the observed SW and LW fluxes and the corresponding estimated clear-sky fluxes (Section 6.2.1). However, as in the RRTMG simulations, the shading effects of the mountains during dusk and dawn are not accounted for in the extimated clear-sky fluxes preventing an analysis for periods with $0 > \cos(\mathrm{SZA}) > 0.3$. In order to equally weight night- and daytime cloud effects, periods with $0 < |\cos(\mathrm{SZA})| < 0.3$ are therefore excluded in the following analyses.

The comparison between calculated and observed fluxes has shown that cloud situations, which are at least five minutes persistent above the AMF site are often not representative for the full hemisphere. Since the RRTMG in its chosen configuration does not account for broken cloud cover, reasonable estimates of the CRE and CRF can only be derived for overcast cloud conditions. Information on the cloud cover is available from the total sky imager, but for daytime periods only. In order to avoid different sampling criteria during night- and daytime, the analyses of the CRE and the CRF are performed for cloud situations which are at least 15 minute persistent. This tripling of the averaging time is motivated by the results of an analysis of total sky imager measurements. For daytime periods, this analysis showed that for 15-minute persistent cloudy scenes, the mean (median) cloud cover is about 90% (97%) as opposed to a mean cloud cover of 80% for 5-minute averages. These high cloud cover values justify the choice of a 15-minute samplig. Larger averaging intervals considerably decrease the sample size due to the stringent requirement that 90% of the profiles within the interval are attributed to a single cloud type.

6.2.1 Observed surface cloud radiative effect

The effect of clouds on the up- and downward SW and LW flux components during the deployment of the AMF can be seen in Fig. 6.8. There, monthly mean values of observed and

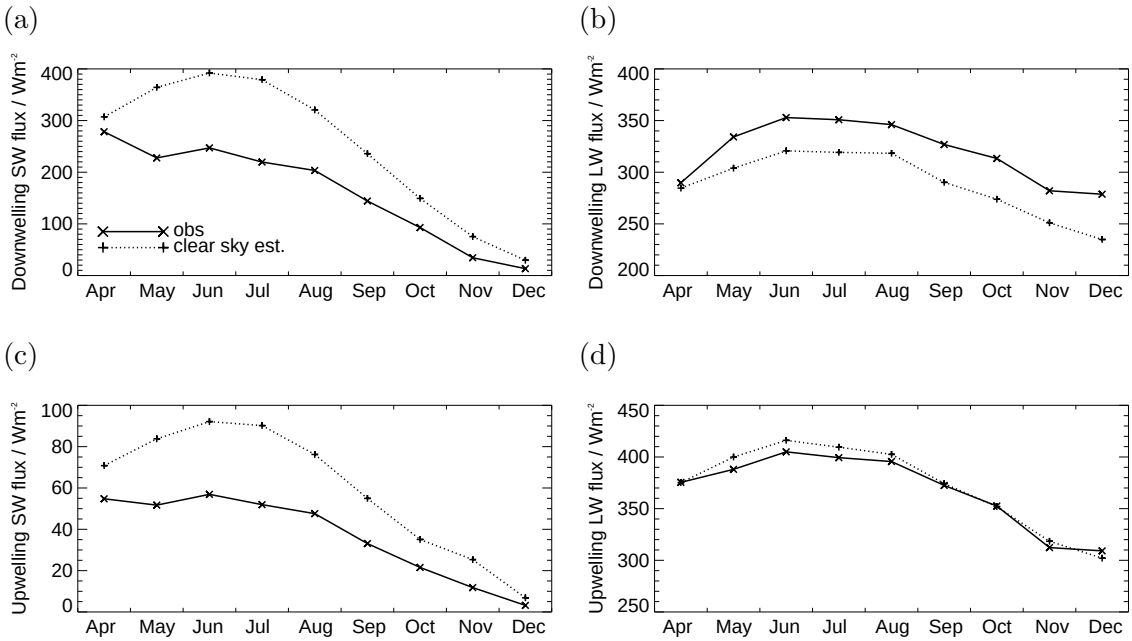

Figure 6.8: Monthly mean observed (solid line) and estimated clear-sky surface fluxes (dotted line). (a) Downwelling SW; (b) Downwelling LW; (c) Upwelling SW; (d) Upwelling LW. Monthly values are based on daily flux averages. Periods with $0 < |\cos(\mathrm{SZA})| < 0.3$ are excluded.

estimated clear-sky surface fluxes are depicted. The variation of the solar insolation during the year is reflected in the monthly mean values of the clear-sky estimated SW fluxes with a maximum value of about $400\,\mathrm{W\,m^{-2}}$ in June. It is reasonable that under cloudy conditions, the surface SW (LW) downward flux is reduced (enhanced) compared to clear-sky situations. Due to the prevailing cloud-free and thin cirrus conditions in April, the mean observed SW and LW downward fluxes are close to the clear-sky ones in this month. The upwelling LW surface flux is largely insensitive to clouds. In the summer months, the clear-sky upwelling flux is slighly larger compared to the observed value. This effect may be explained by the stronger surface warming and increase in surface temperature in cloud-free conditions.

Given the observed and estimated clear-sky surface flux components, monthly mean values of the CRE have been derived (Fig. 6.9). Clouds generally lead to a negative SW and a positive LW CRE at the surface. The variation in the solar insolation during the year is also reflected in the monthly mean values of the SW surface (SFC) CRE with maximum values in the summer months of up to $-170\,\mathrm{W\,m^{-2}}$ and decreasing values towards the end of the year with about $-15\,\mathrm{W\,m^{-2}}$ in December. In April, the SFC CRE is small for both LW and SW due to the previously mentioned prevailing cloud-free and thin cirrus conditions. The variability of the daily mean SW values is largest in June and August with about $30\,\mathrm{W\,m^{-2}}$. If daytime periods ($\cos(\mathrm{SZA}) > 0.3$) are considered only, variations in daily mean SFC SW CRE are up to $50\,\mathrm{W\,m^{-2}}$. In contrast to the SW CRE, the LW SFC CRE reveals a much smaller monthly variability with an almost constant mean value of about $40\,\mathrm{W\,m^{-2}}$ from May to December. In the LW, variations of daily mean CRE values are up to $10\,\mathrm{W\,m^{-2}}$. From April to September, the negative SW cloud radiative effect dominates the net cloud radiative effect given by the sum of the SW and LW components. In October, the negative SW and the positive LW CRE nearly compensate, while in November and December the LW

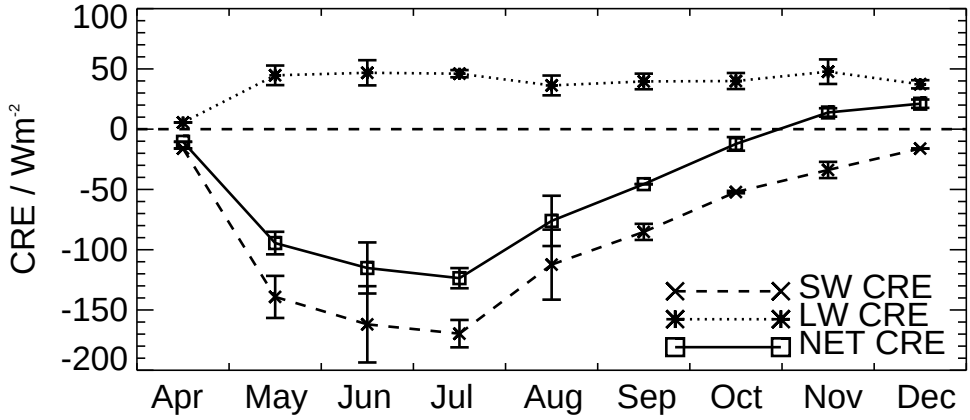

Figure 6.9: Monthly mean SW (dashed line), LW (dotted line), and net CRE (solid line) calculated from the observed and estimated clear-sky surface fluxes. The monthly mean values have been calculated from daily mean values, whose standard deviation is indicated by the vertical bars. Periods with $0 < |\cos(\mathrm{SZA})| < 0.3$ are excluded.

Table 6.7: Surface cloud radiative effect at the AMF site during the nine-month deployment for different cloud types. Values are based on 15-min averages. Periods with $0 < |\cos(\mathrm{SZA})| < 0.3$ are excluded. The numbers in parentheses indicate the proportion of the analyzed cloud profiles to the corresponding total number of 15-min persistent cloud situations including times when $0 < |\cos(\mathrm{SZA})| < 0.3$.

	N profiles	SW	LW	NET
SL WC	659 (79%)	−92	56	−36
ML WC	58 (92%)	−182	72	−110
SL IC	202 (69%)	−27	23	−4
ML IC	378 (71%)	−15	14	−1
SL MC	398 (85%)	−75	59	−16
ML MC	2,514 (78%)	−189	73	−116

CRE is the dominant factor in the net CRE. The positive net CREs of 14 and 21 $\mathrm{W\,m^{-2}}$ in November and December show that clouds at the AMF site have a warming effect on the surface relative to a cloudless atmosphere.

By including the Cloudnet target classification in the analysis, the surface CRE of the different cloud types can be derived (Table 6.7). The largest negative SW CREs can be found for clouds containing liquid water, especially for ML WC ($-182\,\mathrm{W\,m^{-2}}$) and ML MC ($-189\,\mathrm{W\,m^{-2}}$). The same cloud types reveal the largest positive LW CREs with values ranging from $56\,\mathrm{W\,m^{-2}}$ (SL WC) to $73\,\mathrm{W\,m^{-2}}$ (ML MC). Compared to the other cloud types, ice clouds reduce (increase) the SW (LW) downward flux at the surface less. SL and ML IC reveal a small negative SW surface cooling of −27 and $-15\,\mathrm{W\,m^{-2}}$ and a small positive LW CRE which nearly compensates the SW cooling. All clouds have a net cooling effect at the surface with largest values for ML WC ($-110\,\mathrm{W\,m^{-2}}$) and ML MC ($-116\,\mathrm{W\,m^{-2}}$). In general, the magnitude of the SW cooling and the LW warming by a cloud is not only a function of

its macro- and microphysical properties but also of the time of the day. During night, for example, all clouds exhibit a positive net CRE since the SW CRE is zero. More than half of the persistent ML WC and ML MC, which are taken into accounted in the previous analysis, occur during the night, i.e. in 67% and 60% of the corresponding cloud cases, while the other cloud types predominantly occur during daytime hours. Note that the derived values for the surface CRE might therefore change if also dusk and dawn periods are included in the analysis. If these periods would be included, the frequency of cloud occurrence during periods with $\cos(\mathrm{SZA}) < 0$ would increase for every cloud type in this study. Thus, the nighttime LW warming effect would have a stronger weight in the net effect leading to a presumably reduced negative net CRE at the surface compared to the values given in Table 6.7. However, since the cloud situations included in the analysis account for 70% or more of all 15-minute persistent cloud situations during the whole nine-month measurement period, it is assumed that the derived CRE provides a good estimate.

6.2.2 Modelled cloud radiative effect of water clouds

In addition to the SFC CRE, the radiative transfer simulations allow for the determination of the CRE at the top of atmosphere (Eq. (4.9)) and to derive the atmospheric cloud radiative effect (Eq. 4.10). In this section, focus is put on the CRE of persistent (15-minute) SL and ML water clouds. SL WC represent about 16% of the clouds, or the second most common cloud type by frequency, at the AMF site. In contrast to other cloud types, water clouds are well represented by the derived data sample accounting for about 80% of all 15-minute persistent water cloud situations considered in Table 6.7.

Single-layer water clouds are presumably less complex in their macrophysical and microphysical properties than other cloud types. However, uncertainties in LWC and effective radius also exist for these simpler clouds and will propagate to uncertainties of the radiative fluxes. Given the cloud microphysical profiles derived from the sampling method and their estimated uncertainties as described in Section 4.1.2, the associated uncertainty of the CRE and the individual roles of LWP and effective radius are quantified in the following. In addition, the importance of the LWC profile shape is investigated.

The mean SW, LW and net CREs of SL and ML water clouds are summarized in Tables 6.8 and 6.9 for the baseline run and the LWP and $r_{\mathrm{eff,liq}}$ sensitivity experiments. In comparison to the calculated SFC SW CREs using the AMF observed and estimated clear-sky fluxes (Table 6.7), the CRE for SL and ML WC is well reproduced by the radiative transfer calculations. In particular, differences in net SFC CRE are less or equal $5\,\mathrm{W\,m^{-2}}$.

SL and ML water clouds have a net cooling effect on the climate system. The warming of the atmosphere due to absorption in the shortwave is overcompensated by atmospheric longwave cooling. The positive LW CRE at the surface and the TOA can only partly compensate the cooling effect in the corresponding SW components. ML WC have typically larger LWPs than SL WC (see Table 5.1, 15-minute averages) leading to an enhanced SW CRE at the surface. The LW SFC CRE is similar for both cloud types, namely 70 and $68\,\mathrm{W\,m^{-2}}$, although ML WC typically have a higher LWP and lower cloud bases (Table 5.1). However, the LW SFC CRE also depends on the distribution of the LWC within the cloud boundaries which will be discussed at the end of this section.

Table 6.8: Mean cloud radiative effect (CRE, $\mathrm{W\,m^{-2}}$) of 15-minute persistent single-layer water clouds. The mean CRE is calculated for times with $|\cos(\mathrm{SZA})| > 0.3$ (512 values). The results for the sensitivity experiments are given as differences, i.e. new results minus results of the baseline simulation. The numbers in parentheses are the absolute values of the percental change with respect to the control run.

	baseline run	+ LWP err.	- LWP err.	+ $r_{\mathrm{eff,liq}}$ err.	- $r_{\mathrm{eff,liq}}$ err.
SW					
TOA	−93	−16 (17)	23 (25)	9 (10)	−11 (12)
ATM	13	2 (14)	−3 (21)	0 (0)	0 (1)
SFC	−106	−18 (17)	26 (24)	10 (9)	−11 (11)
LW					
TOA	10	1 (6)	−3 (25)	0 (0)	0 (0)
ATM	−60	−3 (5)	14 (23)	0 (1)	0 (0)
SFC	70	4 (5)	−16 (23)	0 (1)	0 (0)
NET					
TOA	−83	−15 (18)	20 (25)	9 (11)	−11 (14)
ATM	−46	−1 (3)	11 (23)	0 (1)	0 (1)
SFC	−35	−14 (39)	10 (26)	9 (25)	−11 (31)

Uncertainties in CRE due to LWP and $r_{\mathrm{eff,liq}}$

The basic radiative characteristics of SL and ML WC are not affected when varying the LWP and effective radius. However, the amount of cooling or heating can significantly change in the single components (Tables 6.8 and 6.9). In general, increasing the LWP and increasing the $r_{\mathrm{eff,liq}}$ yield opposite effects in the SW CRE. A larger LWP results in larger absorption of radiation and therefore in a more pronounced SW SFC and TOA CRE. Larger effective radii reduce the cloud albedo and thus increase the SW CRE at the SFC and the TOA. For the longwave part, changes in $r_{\mathrm{eff,liq}}$ have only minor effects on the CRE, since the LW CRE is mainly influenced by the LWP and the macrophysical properties of the cloud, namely the vertical extension and the position, which impacts the clouds temperature. For the net CRE, changes in LWP result in variations of the TOA and SFC cloud radiative effect between 18 and 39%, which are generally about twice as large as the changes due to modifications in $r_{\mathrm{eff,liq}}$. However, for SL WC, LWP and $r_{\mathrm{eff,liq}}$ nearly equally contribute to the uncertainty in the mean net SFC CRE. As the LW and SW atmospheric CRE, the net atmospheric CRE is nearly insensitive to changes in $r_{\mathrm{eff,liq}}$ and is more sensitive to changes in LWP, in particular to a reduction of this quantity.

For a better assessment of the influence of measurement uncertainties, the sensitivity of the shortwave CRE for the TOA, ATM and SFC with respect to the LWP of SL WC is analyzed (Fig. 6.10). To this end, the CRE has been normalized, i.e. divided by the clear-sky downwelling SW flux at the surface. In general, the shortwave CRE at the surface is negative, since the downwelling radiation is significantly reduced compared to clear sky. Due to backscattering of solar radiation at cloud top, the upwelling shortwave flux at the TOA is larger compared to clear sky situations, leading to a negative shortwave CRE at the TOA. In most cases, the atmospheric cloud radiative effect is positive, since the absorption of solar radiation results in a heating of the atmosphere.

When the LWP is low ($< 70\,\mathrm{g\,m^{-2}}$), small changes in this variable can lead to large variations

Table 6.9: Same as Table 6.8 but for multi-layer water clouds (48 values).

	baseline run	+ LWP err.	- LWP err.	+ $r_{\text{eff,liq}}$ err.	- $r_{\text{eff,liq}}$ err.
SW					
TOA	−160	−29 (18)	41 (26)	18 (11)	−20 (13)
ATM	23	3 (15)	−6 (25)	0 (2)	0 (0)
SFC	−183	−33 (18)	47 (26)	19 (10)	−20 (11)
LW					
TOA	12	1 (6)	−2 (19)	0 (1)	0 (0)
ATM	−55	−1 (2)	6 (10)	0 (0)	0 (0)
SFC	68	2 (3)	−8 (12)	0 (0)	0 (0)
NET					
TOA	−148	−28 (19)	39 (26)	18 (12)	−20 (14)
ATM	−32	2 (7)	0 (1)	0 (1)	0 (0)
SFC	−115	−30 (27)	39 (34)	19 (16)	−20 (17)

of the surface shortwave downwelling flux. Consequently, LWP uncertainties in this range induce large uncertainties in the CRE at the surface of 100% or more. Similar uncertainties in the same order of magnitude can also be found at the TOA. When the LWP increases and the cloud becomes more opaque, uncertainties in LWP play a minor role for the derived SFC and TOA cloud radiative effect. This holds especially for the longwave fluxes as seen in Tables 6.8 and 6.9. With regard to variations in the effective radius, the sensitivity of the CREs towards the LWP is different. For liquid water paths less than $50\,\mathrm{g\,m^{-2}}$, the uncertainty in $r_{\text{eff,liq}}$ has a small effect on the accuracy of the derived CRE at the surface and the TOA compared to the uncertainties related to LWP. For larger values of LWP, variations in CRE due to the uncertainty in the effective radius are roughly in the same order of magnitude as variations due to the LWP uncertainty. For a cloud with a LWP of $100\,\mathrm{g\,m^{-2}}$, the variations in SFC and TOA shortwave CRE are approximately 10%. As seen in Tables 6.8 and 6.9, when considering the atmospheric cloud radiative effect, the uncertainties in SFC and TOA CRE due to uncertainties in $r_{\text{eff,liq}}$ almost cancel each other.

Mace et al. (2006b) assessed the CRE at the ARM SGP site for the year 2000 and estimated corresponding uncertainties from comparisons to SFC and TOA observed fluxes and from error propagation techniques. They identified large uncertainties in the SW and net atmospheric CRE of low-level clouds, namely 32 and 24%, respectively, while in the present study uncertainties due to uncertainties in the microphysical properties are more pronounced at the SFC and TOA and partly compensated in the ATM CRE.

Sengupta et al. (2003) analyzed the normalized CRE at the surface of continental stratus clouds. They found the normalized CRE to be six times more sensitive to changes in LWP compared to changes in the effective radius given typical values of these variables over the ARM Southern Great Plains site. From these results, they concluded that the liquid water path is the dominant parameter for the solar transmission in continental stratus clouds. The results presented in this section have shown that the LWP is the dominant parameter for the SW surface CRE, and likewise for the normalized CRE, if the LWP is low. On the other hand, for LWP values larger than $100\,\mathrm{g\,m^{-2}}$, the uncertainty in CRE due to variations in $r_{\text{eff,liq}}$ is in the same order of magnitude as the uncertainty due to LWP variations. Therefore, the uncertainty in $r_{\text{eff,liq}}$ is in general not negligible when determining the SW surface CRE. It has to be mentioned that due to the limited sensitivity of most instruments, accurate retrievals

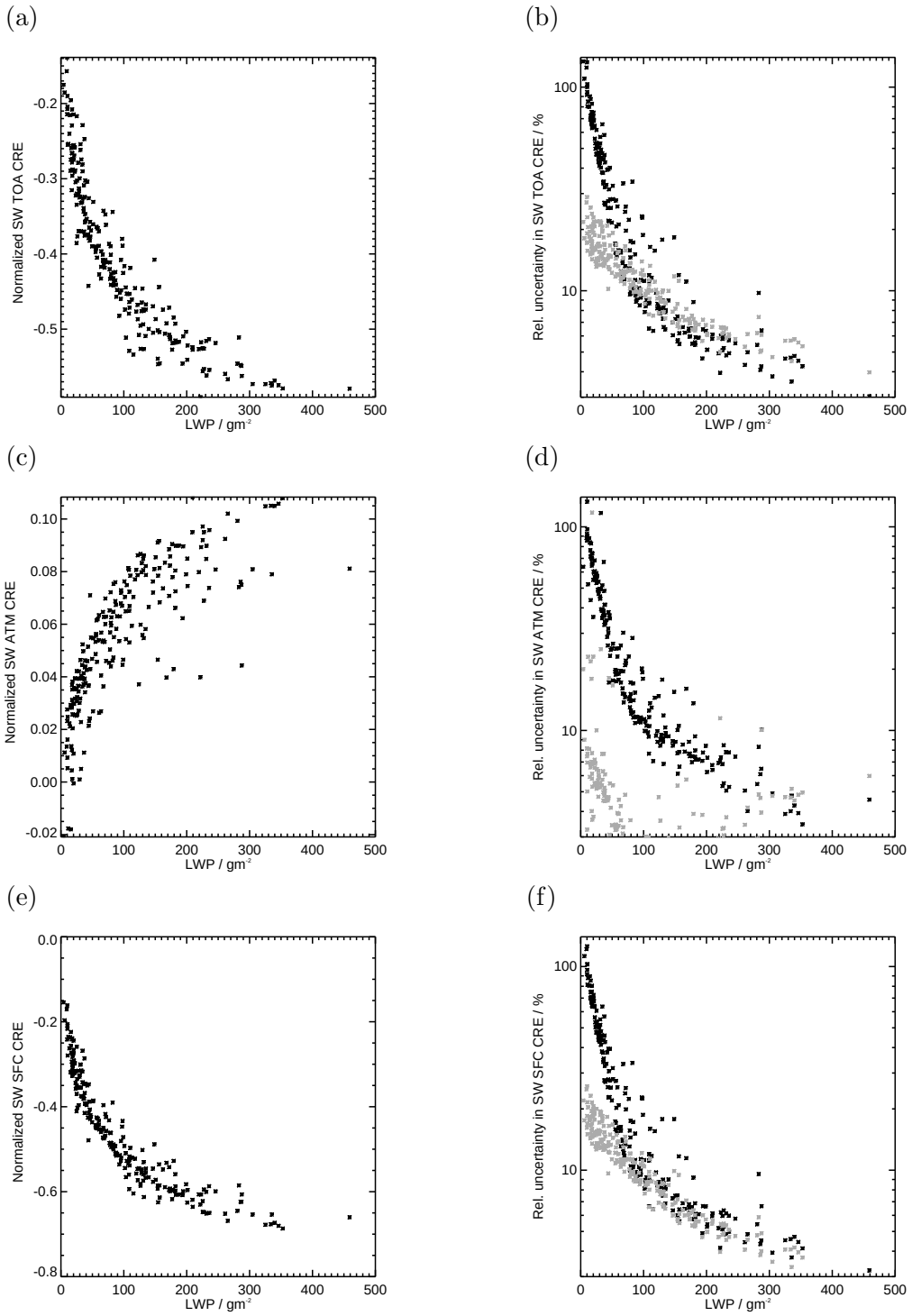

Figure 6.10: Shortwave cloud radiative (CRE) effect and its uncertainty of 15-minute persistent single-layer water clouds. The CRE is calculated for times with $\cos(\mathrm{SZA}) > 0.3$ (229 values). The CRE is normalized with the clear-sky downwelling flux at the surface and is plotted against the LWP of the cloud (left panels). (Right panels) Relative uncertainties in the CRE due to uncertainties in LWP (black asteriks) and in effective radius (grey asteriks). (a) and (b) CRE at the top of atmosphere (TOA); (c) and (d) atmospheric (ATM) CRE; (e) and (f) surface (SFC) CRE.

of LWP and $r_{\mathrm{eff,liq}}$ are difficult particularly for cloud cases where the LWP is small (e.g., *Turner* et al., 2007; *Turner*, 2007b), i.e. where the CRE reveals its highest sensitivity to uncertainties in the cloud microphysical properties.

Uncertainties in CRE due to LWC profile shape

Even if the LWP would be accurately derived, its vertical distribution within the cloud boundaries would still remain uncertain (as discussed in detail in Chapter 7). In addition to the LWC retrieval based on a Z-LWC relationship as described in Section 4.1.2, a constant and a modified adiabatic LWC profile have been used in two RRTMG experiments (experiments 9 and 10 in Table 4.2). Since the constant and the modified adiabatic profiles have been scaled such that their LWPs match the LWP of the baseline simulation, the effect of the profile shape on the CRE can be quantified. In Figure 6.11, the mean LWC of the different profiles are depicted for 15-minute persistent SL WC. The LWC is shown as a function of normalized height above cloud base ranging from 0 (cloud base) to 1 (cloud top). In the sampled SL WC, the mean LWC from the Z-LWC relationship increases with height up to a normalized height of 0.8 and then decreases rapidly due to entrainment of dry air from above. The profile shape of the modified adiabatic profile shows a similar LWC increase with height reaching slightly lower values. At cloud top, the entrainment of dry air is less pronounced in the modified adiabatic profile compared to the mean profile of the baseline simulation. The similarity of both profiles shapes indicates that the LWC profile shape of SL WC is often close to the adiabatic profile shape. Profile differences are largest for the constant LWC, which is tendentially larger (smaller) in the lower (upper) parts of the cloud compared to the LWC from the Z-LWC relationship. As a consequence, differences in the cloud radiative effect due to the profile shape are more pronounced for the constant profile than for the modified adiabatic one (Table 6.10). While the atmospheric CRE is nearly insensitive to variations of the profile shape, the differences in the TOA and SFC CRE are up to 8 W m^{-2} for SL WC corresponding to about 8% in the SW and up to 20% in the net CRE of the baseline run. For ML WC, the relative changes are in the same order of magnitude (not shown). The effect of the profile shape on the LW CRE is very small. The shifting of LWC to lower parts of the clouds in case of the constant LWC profile increases the emissivity in these heights. Therefore, this redistribution of LWC results in a small positive LW CRE at the surface of 1 W m^{-2}. In general, uncertainties in LWP are more than twice as large as uncertainties due to the profile shape. Nevertheless, the sensitivity studies showed that an accurate characterization of both LWP and profile shape are important for the evaluation of the CRE.

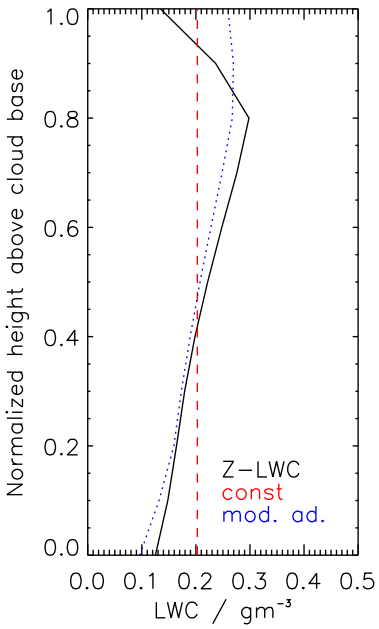

Figure 6.11: Mean LWC of 15-minute persistent SL WC as a function of height above cloud base. The height is normalized with the geometrical cloud thickness (0: cloud base, 1: cloud top). LWC from Z-LWC-relation (black), constant LWC profile (red), modified adiabatic profile (blue). The mean LWP is 97.3 g m^{-2} and the mean cloud thickness 550 m.

Table 6.10: Mean cloud radiative effect (CRE, $\mathrm{W\,m^{-2}}$) of 15-minute persistent single-layer water clouds. The mean CRE is calculated for times with $|\cos(\mathrm{SZA})| > 0.3$ (512 values). The results for the sensitivity experiments are given as differences, i.e. new results minus results of the baseline simulation. The numbers in parentheses are the absolute values of the percental change with respect to the control run.

	baseline run	const	mod. ad.
SW			
TOA	−93	−7 (8)	−5 (6)
ATM	13	1 (4)	0 (0)
SFC	−106	−8 (7)	−5 (5)
LW			
TOA	10	0 (0)	0 (1)
ATM	−60	−1 (1)	0 (0)
SFC	70	1 (1)	0 (0)
NET			
TOA	−83	−7 (9)	−5 (6)
ATM	−46	0 (0)	0 (0)
SFC	−35	−7 (20)	−5 (14)

6.3 Modelled cloud radiative forcing of water clouds

As for the CRE, the CRF, i.e. the difference between cloudy and clear-sky heating rates, of SL and ML WC is analyzed assuming 15-minute persistent cloud situations. The mean LWC profiles for these periods together with the mean SW, LW and net CRF are depicted in Fig. 6.12. The mean profiles of CRF arise from the typical heating and cooling features of each individual cloud type as described in Section 1.2. The distribution of the LWC of SL WC shows a distinct maximum at a height of 1.8 km. Above this height, SL WC heat the atmosphere in the SW by about $0.5\,\mathrm{K\,day^{-1}}$. Below this height, SL WC primarily have a SW cooling effect in the same order of magnitude. Due to LW cloud top cooling, LW cooling rates of up to $-6\,\mathrm{K\,day^{-1}}$ occur. Since the cloud bases are close to the surface, LW warming is only $1.5\,\mathrm{K\,day^{-1}}$ in the lowest 1.5 km. SW warming and cooling by the cloud counteracts the LW CRF, but can only partly compensate the LW warming in the lower levels and the strong cooling above.

For ML WC, the mean LWC profiles peaks at two heights, namely in 0.8 and 2 km yielding two maxima (minima) in the SW (LW) CRF slightly above these heights. SW cloud heating rates are up to $2\,\mathrm{K\,day^{-1}}$ and $0.5\,\mathrm{K\,day^{-1}}$ for the upper and lower parts of the ML WC, while LW cooling goes down to $-9\,\mathrm{K\,day^{-1}}$ and $-4.5\,\mathrm{K\,day^{-1}}$, respectively.

For SL WC, uncertainties in CRF due to uncertainties in LWP are up to $0.1\,\mathrm{K\,day^{-1}}$ in SW and $1\,\mathrm{K\,day^{-1}}$ in LW and net CRF corresponding to relative changes about 25% (shaded bands in Fig. 6.12b-d). The effect of changes in the effective radius on the CRF is at least an order of magnitude smaller than the variation due to the LWP. In SW CRF, an increase or decrease of the effective radius leads to variations of about $\pm 0.05\,\mathrm{K\,day^{-1}}$. The variations in the LW are typically an order of magnitude smaller.

For ML WC, where SW heating and LW cooling is more pronounced, differences in CRF due to variations in LWP (shaded bands in Fig. 6.12e-h) and $r_{\mathrm{eff,liq}}$ increase. Changes in LWP

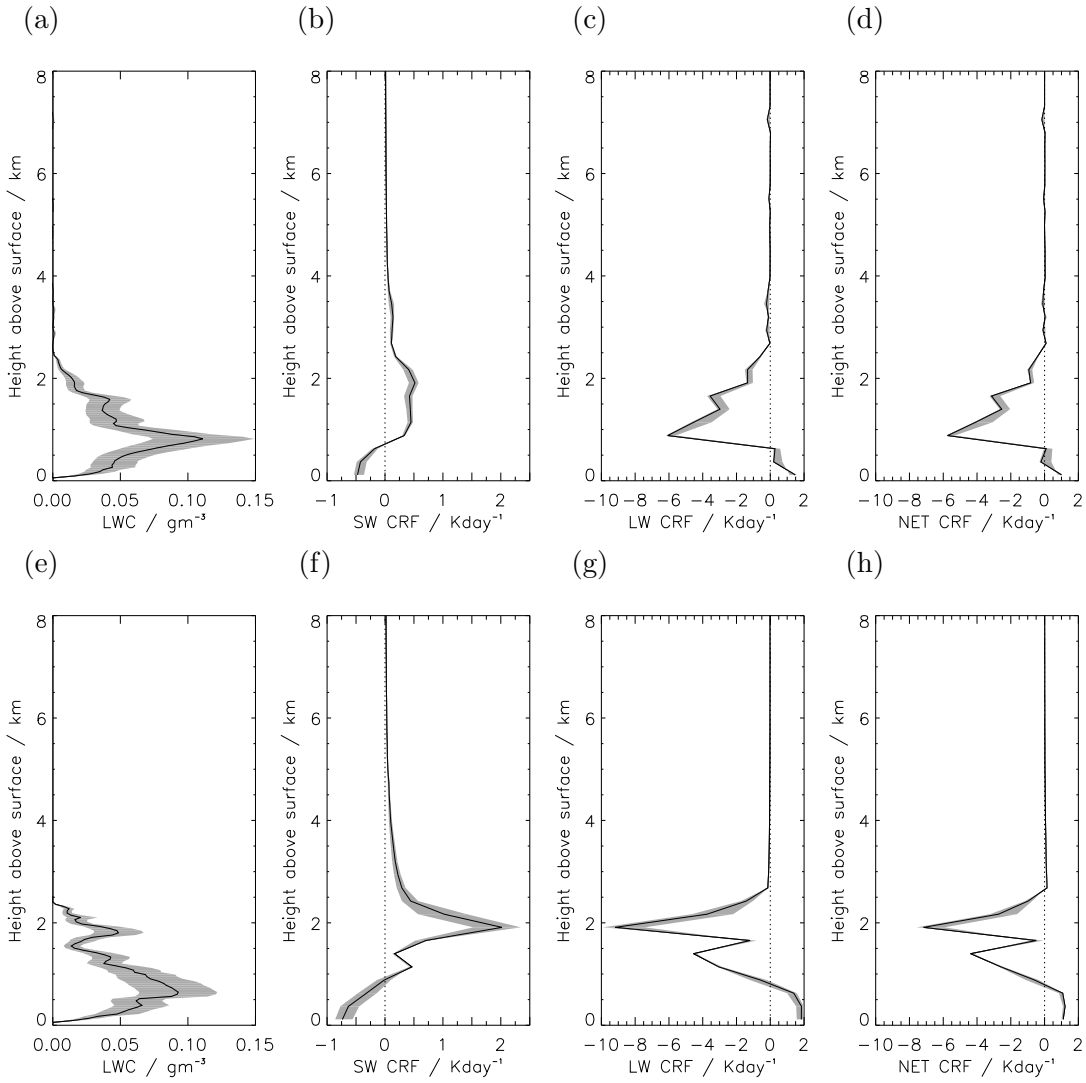

Figure 6.12: Mean LWC and mean cloud radiative forcing (CRF) of 15-minute persistent SL (top) and ML (bottom) WC (in 258 m height bins, i.e. average over 6 model layers). Times with $0 < |\cos(\mathrm{SZA})| < 0.3$ are excluded. SW (b,e), LW (c,f) and net CRF (d,g). The shaded area shows the uncertainty in CRF due to uncertainty in LWP.

lead to changes in SW and LW CRF of up to $0.5\,\mathrm{K\,day^{-1}}$ and $1.7\,\mathrm{K\,day^{-1}}$, corresponding to about 40%. As for SL WC, the effect of variations in $r_{\mathrm{eff,liq}}$ is considerably smaller with values of 0.1 and $0.06\,\mathrm{K\,day^{-1}}$ for SW and LW, respectively.

When varying the LWC profile shape of SL WC, differences in the SW CRF are in the same order of magnitude as those for LWP variations, namely up to $0.1\,\mathrm{K\,day^{-1}}$ (Fig. 6.13). Differences in LW and net CRF due to the modification of the LWC profile shape are smaller than $0.2\,\mathrm{K\,day^{-1}}$ and therefore smaller than the derived uncertainties due to the LWP. For both constant and modified adiabatic LWC profile shapes, LW cooling above 1 km height and LW heating in the lower levels are intensified compared to the baseline run. This change in the mean CRF is a result of the CRF differences of each individual cloud, which are typically largest at the cloud boundaries (not shown). An increase in LWC at cloud bottom and cloud top, for example, results in a stronger LW cloud top cooling and a stronger LW cloud base

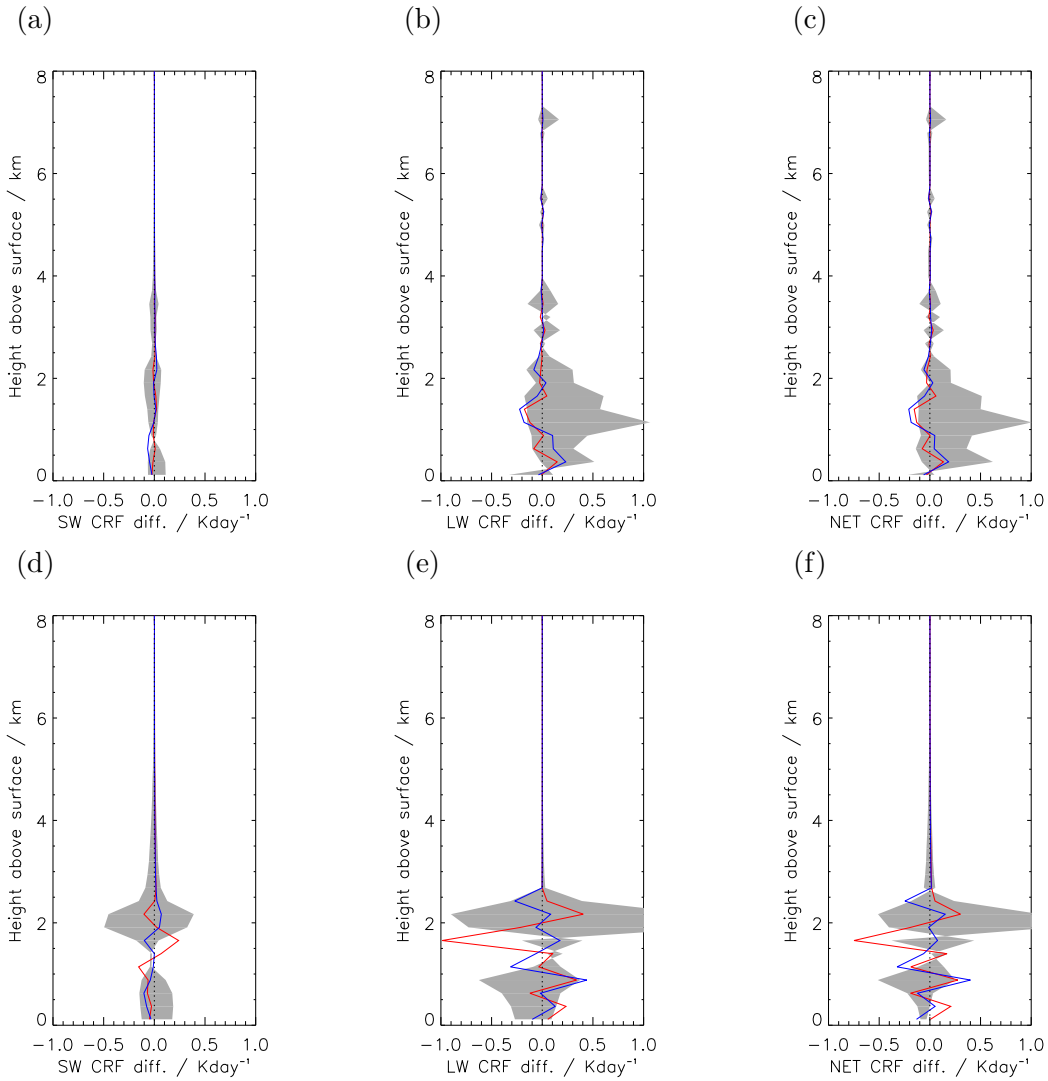

Figure 6.13: Differences in mean cloud radiative forcing (CRF) of 15-minute persistent SL (top) and ML (bottom) WC (in 258 m height bins, i.e. average over 6 model layers). Differences due to constant LWC profile (red) and modified adiabatic profile (blue). Times with $0 < |\cos(\mathrm{SZA})| < 0.3$ are excluded. SW (a,d), LW (b,e) and net CRF (c,f). The shaded area shows the uncertainty in CRF due to uncertainty in LWP.

warming compared to the baseline simulation.

For ML WC, differences in CRF show very complex patterns due to the various vertical positions of the cloud layers and in-cloud liquid water distributions. Variations in CRF are larger for this cloud type compared to SL WC, especially when assuming a constant LWC profile. In general, uncertainties in CRF of ML WC due to uncertainties in the LWC profile shape are in the same order of magnitude as uncertainties due to LWP.

As for the CRE, the results of these sensitivity studies emphasize that both LWP and its vertical distribution have to be derived properly in order to accurately describe the radiative forcing of clouds.

6.4 Summary and conclusions

In terms of the clear-sky radiative closure at the surface, the derived thermodynamic and aerosol profiles perform well with average differences in the SW and LW fluxes of less than 2.1% and 3.6%, respectively. The slight overstimation (understimation) of observed SW (LW) surface downward fluxes may be related to a slight underestimation in aerosol concentration, humidity and temperature. The radiation comparison in cloudy conditions reveals a reasonable agreement between observed and calculated fluxes with differences which are in the same order of magnitude as in the study by *Mather* et al. (2007) for a tropical region. In the SW, a negative bias of $-38\,\mathrm{W\,m^{-2}}$ is present, while the calculated LW downwelling surface fluxes are on average too large by $7\,\mathrm{W\,m^{-2}}$. These biases have several reasons. First, broken cloudiness has a strong impact on the surface fluxes and complicates the comparison of calculated fluxes to hemispheric irradiance measurements. Due to the assumption of a plane-parallel atmosphere in the radiative transfer model, the calculated downwelling SW (LW) surface fluxes would have the tendency to be too small (large) compared to observed fluxes in broken cloud situations and thus yield a negative (positive) SW (LW) bias. Restricting the analysis to more horizontally homogeneous cloud fields with cloud cover values greater than 90% considerably reduces the standard deviation and the bias to $73\,\mathrm{W\,m^{-2}}$ and $-13\,\mathrm{W\,m^{-2}}$ in the SW, for example, but also the sample size. This reduction of the sample size becomes an important factor when the analysis focuses on specific cloud types.

Another reason for the negative SW and positive LW bias, which was also observed for single-layer water clouds alone, might be an overestimation of the cloud optical thickness implying an overestimation of LWP and/or an underestimation of particle size. In the LW, the vertical distribution of liquid water within the cloud is also important. The LW downwelling flux at the surface primarily depends on the temperature of the lowest cloud layers. If the LWC had a positive bias or the effective radius had a negative bias in these cloud layers, the opacity of these layers and therefore the emission temperature would be overestimated. However, if the microphysical properties would primarily cause the bias in the radiative fluxes, a reduction of this quantity for higher cloud cover thresholds would not be expected. Although there is still potential to refine the retrieval of the atmospheric profiles, the results of the radiative closure studies are encouraging, especially for overcast water clouds. However, uncertainties in the derived cloud properties exist and must be taken into account when evaluating the CRE and the CRF.

At the surface, the CRE can be derived from the surface fluxes observed by the AMF instrumentation and the clear-sky estimates according to *Long and Ackerman* (2000) and *Long and Turner* (2008). In this manner, the largest net SFC CRE in terms of absolute values has been found for multi-layer clouds containing liquid water, namely $-110\,\mathrm{W\,m^{-2}}$ for ML WC and $-116\,\mathrm{W\,m^{-2}}$ for ML MC. The smallest effect is the net cooling SFC CRE of ice clouds which does not exceed an absolute value of $4\,\mathrm{W\,m^{-2}}$. Generally speaking, clouds have a cooling effect at the surface from April to October 2007 and a slight warming effect in November and December. It has to be noted that the CRE at the ARM site derived in this study is valid for the analyzed time periods, where $|\cos(\mathrm{SZA})| > 0.3$. The analysis of the excluded time periods is difficult due to the shadowing effects of the surrounding hills, which are not accounted for in the clear-sky fluxes and in the radiative transfer calculations neither. When interpreting the results, one should keep in mind that the results for other ARM sites may be different depending on cloud frequency, cloud types present, surface characteristics and solar insolation. At the ARM Southern Great Plains facility, for example, clouds have a net cooling effect during the whole year (*Dong* et al., 2006), while at the ARM NSA site,

positive net CREs occur in spring and autumn (*Dong and Mace*, 2003).

In order to assess the ATM and TOA CRE and the CRF, modelled fluxes have been used in this study. The analysis of CRE and CRF mainly focussed on water clouds, which are well represented in the data sample. In comparison to the calculated SFC SW CREs using the AMF observed and estimated clear-sky fluxes, the CRE for SL and ML WC is well reproduced by the radiative transfer calculations. SL and ML water clouds have a net cooling effect on the climate system, where for the latter the net TOA and SFC effect is more pronounced. Since ML WC rarely occur (only 48 cases are considered in the analysis) more cases are needed to provide a more robust estimate of the radiative effect of this cloud type. The estimated uncertainties in the modelled net SFC and TOA CRE are up to 39% and 26%, respectively. Changes in LWP result in noticeable variations of the SW and net CRE at the TOA and the surface. These variations are on average twice as large as variations due to uncertainties in effective radius. As the LW and SW atmospheric CRE, the net atmospheric CRE is nearly insensitive to changes in $r_{\mathrm{eff,liq}}$ and is more sensitive to changes in LWP, in particular to a reduction of this quantity. For low LWP values, uncertainties in SW SFC and TOA CRE are dominated by the uncertainty in LWP. For LWP values larger than $100\,\mathrm{g\,m^{-2}}$, the uncertainty in the CRE due to uncertainties in $r_{\mathrm{eff,liq}}$ is in the same order of magnitude as the one related to the LWP. Uncertainties in CRE due to uncertainties in the LWC profile shape are typically smaller by a factor of two compared to LWP uncertainties, but are not negligible nevertheless.

For the CRF of SL and ML WC, the LWP and its distribution within the cloud boundaries are the most important factors. The uncertainties in CRF due to uncertainties in effective radius are typically an order of magnitude smaller. The net CRF is dominated by the LW CRF. The derived uncertainties in net CRF are up to $1\,\mathrm{K\,day^{-1}}$ for SL and $1.7\,\mathrm{K\,day^{-1}}$ for ML WC, corresponding to relative uncertainties of about 25 and 40%, respectively. Uncertainties in net CRF which are related to uncertainties in the LWC profile shape are typically smaller than $0.2\,\mathrm{K\,day^{-1}}$ for SL WC and therefore smaller than uncertainties due to LWP. For ML WC, uncertainties in the LWC profile shape induce uncertainties in the net CRF which are roughly in the same oder of magnitude as those due to LWP.

The results underline the importance of accurate LWC profiles for the assessment of the radiative effects of clouds. This motivates the development and application of advanced LWC retrieval algorithms, such as the integrated profiling technique. In the next chapter, this technique is presented and its application to the measurements at the AMF site is discussed.

Chapter 7

Application of the integrated profiling technique (IPT)

In the previous chapters, the LWC of water clouds has been derived by applying a Z-LWC relationship and scaling the derived LWC profile with the MWR LWP. Additionally, a more sophisticated approach has been applied to the AMF measurements for the retrieval of LWC profiles, the so-called Integrated Profiling Technique (e.g., *Löhnert* et al., 2004; *Löhnert* et al., 2008). In this chapter, the IPT is presented, which combines MWR, cloud radar and a priori information via an optimal estimation approach in order to derive physically consistent profiles of LWC, temperature and humidity. Physically consistent means that given the derived profiles and the forward model, the measurements can be reproduced within their assumed errors. In the present study, focus is put on the LWC profiles derived by this technique. In particular, it is discussed how accurate LWC profiles can be derived and how this accuracy depends on the a priori and measurement information and their uncertainties.

In the first section of this chapter, the theoretical framework and the specific setup of the IPT are presented (Section 7.1). In Section 7.2, the interplay of the errors of the a priori profile, the measurements and the forward model in the LWC retrieval and the associated effect on the retrieved LWC error and on the information content of the measurements are analyzed. To this end, several sensitivity studies are performed employing the basic equations implemented in the IPT. The content of this section is the same as in the recent publication by *Ebell* et al. (2010) and also based on the studies by *Crewell* et al. (2009). In Section 7.3, the results of the IPT in its basic configuration are discussed with respect to its application to the measurements during the AMF deployment. In particular, the derived LWC profiles are compared to those from the basic LWC retrieval (cf. Section 4.1.2), and uncertainties in CRE and CRF of SL WC due to different LWC retrieval algorithms are assessed.

7.1 Retrieval technique

A general description of the optimal estimation theory which forms the basis of the IPT can be found in *Rodgers* (2000). The development of the IPT was part of the PhD work by Ulrich Löhnert and is described in detail in *Löhnert* (2002) and in subsequent publications (*Löhnert* et al., 2004; *Löhnert* et al., 2008). In the next section, a short summary of the retrieval technique is given, while the specific setup of the IPT used in this study is presented in Section 7.1.2.

7.1.1 Inversion theory

In general, deriving atmospheric profiles directly from ground-based measurements is an ill-conditioned problem, because many solutions fit the data and small errors in the measurements may have a large effect on the derived atmospheric profiles. While the forward model $\mathbf{F}$, which maps the atmospheric state $\mathbf{x}$ to the measurement space $\mathbf{y}$, is typically well known, deriving the state $\mathbf{x}$ from the measurements $\mathbf{y}$ is not straight forward. In order to constrain the solution space, a priori information $\mathbf{x}_a$ has to be included into the retrieval. The integration of a priori information and measurements can be done in the framework of the optimal estimation following *Rodgers* (2000). If the forward model is moderately nonlinear and the probability density functions of $\mathbf{x}$ and $\mathbf{y}$ are Gaussian distributed, the problem can be formulated by the so-called optimal estimation equation

$$\mathbf{x}_{i+1} = \mathbf{x}_i + \left(\mathbf{K}_i^T \mathbf{S}_e^{-1} \mathbf{K}_i + \mathbf{S}_a^{-1}\right)^{-1} \times \left[\mathbf{K}_i^T \mathbf{S}_e^{-1} \left(\mathbf{y} - \mathbf{y}_i\right) + \mathbf{S}_a^{-1} \left(\mathbf{x}_a - \mathbf{x}_i\right)\right]. \tag{7.1}$$

As Eq. (7.1) indicates, the atmospheric state $\mathbf{x}$ is derived via an interative procedure given the Jacobi matrix $\mathbf{K}_i = \partial \mathbf{F}\left(\mathbf{x}_i\right) / \partial \mathbf{x}_i = \partial \mathbf{y}_i / \partial \mathbf{x}_i$, the combined measurement and forward model error covariance matrix $\mathbf{S}_e$, and the a priori covariance matrix $\mathbf{S}_a$. For a given set of measurements and a given a priori information, the optimal estimation finds a physically consistent solution satisfying the measurements and the a priori profile within the assumed errors. The covariance matrices $\mathbf{S}_e$ and $\mathbf{S}_a$ determine the individual weights of the measurements and the a priori information in the solution. Measurements with large uncertainties, implying large variances in $\mathbf{S}_e$, have a smaller weight in the solution than measurements with small errors. It has to be noted that all errors are assumed to be random. Systematic errors cannot be included in $\mathbf{S}_e$, which might lead to bias errors in the retrieval solution.

An optimal solution $\mathbf{x}_{op}$ is found by minimizing a quadratic cost function between $\mathbf{F}\left(\mathbf{x}_{i+1}\right)$ and $\mathbf{F}\left(\mathbf{x}_i\right)$. The convergence criterium is formulated as:

$$\left[\mathbf{F}\left(\mathbf{x}_{i+1}\right) - \mathbf{F}\left(\mathbf{x}_i\right)\right]^T \mathbf{S}_{\mathbf{i}y}^{-1} \left[\mathbf{F}\left(\mathbf{x}_{i+1}\right) - \mathbf{F}\left(\mathbf{x}_i\right)\right] \ll d, \tag{7.2}$$

with d the dimension of $\mathbf{y}$ and $\mathbf{S}_{\mathbf{i}y}$ the covariance matrix between the measurement $\mathbf{y}$ and $\mathbf{F}\left(\mathbf{x}_{op}\right)$. The derived state $\mathbf{x}_{op}$ must not be interpreted as an explicit solution, but as the most probable solution of a Gaussian distributed probability density function. A decisive advantage of the inversion method is that, in addition to the retrieved profiles, corresponding error estimates are derived. To this end, the error covariance matrix of the optimal solution $\mathbf{S}_{op}$ is calculated by

$$\mathbf{S}_{op} = \left(\mathbf{K}^T \mathbf{S}_e^{-1} \mathbf{K} + \mathbf{S}_a^{-1}\right)^{-1}, \tag{7.3}$$

where the diagonal elements in $\mathbf{S}_{op}$ give an estimate of the mean quadratic error of $\mathbf{x}_{op}$.

In order to assess the information content of an observation in the retrieved atmospheric state, the number of degrees of freedom for signal (DGF) is calculated. The number of DGF provides the number of independent pieces of information that are determined from the measurement. It is given by the trace of the averaging kernel matrix $\mathbf{A}$. The averaging kernel matrix describes the sensitivity of the retrieved profile to the true state, i.e. $\mathbf{A} = \delta \mathbf{x}_{op} / \delta \mathbf{x}_{true}$. This matrix can be derived from the optimal estimation equations as

$$\mathbf{A} = \mathbf{S} \cdot \left(\mathbf{K}^T \mathbf{S}_e^{-1} \mathbf{K}\right). \tag{7.4}$$

In the following section, $\mathbf{x}$, $\mathbf{y}$, $\mathbf{x}_a$, $\mathbf{F}$, and the covariance matrices are specified.

7.1.2 IPT settings

Atmospheric state and measurement vector

In the IPT, the atmospheric state vector $\mathbf{x}$ consists of the profiles of temperature, humidity and, in cloudy cases, additionally of the LWC, so that $\mathbf{x} = (\mathbf{T}, \mathbf{q}, log_{10}(\mathbf{LWC}))$. Since the LWC is not Gaussian-distributed, the logarithm of LWC is derived instead, because it more closely resembles a Gaussian-distributed parameter. The vertical resolution of the retrieved temperature and humidity profiles is 50 m in the lowest 250 m and decreases gradually with increasing height to 500 m between 5 and 10 km and 5 km between 10 and 30 km above the surface. The spatial resolution of the LWC is determined by the resolution of the AMF cloud radar, which is about 43 m. As for the LWC retrieval described in Section 4.1.2, information on the presence of LWC in a certain height is included using the Cloudnet target classification. Since in melting layer situations, the radar signal can not be simply separated into the contributions from liquid water and from ice, the IPT can not be applied in these cases. Thus, profiles containing a melting layer are skipped in the retrieval.

The measurement vector $\mathbf{y}$ encompasses microwave radiometer brightness temperatures at different frequencies and cloud radar reflectivities of the corresponding detected cloud levels, so that $\mathbf{y} = (\mathbf{TB}, \mathbf{Z})$. In this study, $\mathbf{TB}$ consists of the HATPRO (K-band: 22-32 GHz, V-band: 51-59 GHz) and DPR (90, 150 GHz) brightness temperature measurements (see Section 3.2). If HATPRO elevation scans are available, the corresponding brightness temperatures (TBs) of the highest four channels of the V-Band are included in the retrieval in addition to the zenith measurements in order to provide a better accuracy of the temperature profile in the boundary layer (*Crewell and Löhnert*, 2007). As for the basic LWC retrieval (Section 4.1.2), radar reflectivity profiles of the AMF cloud radar are taken from the Cloudnet categorization product and are already corrected for gaseous and liquid attenuation.

A priori information

For temperature and humidity a priori profiles, radiosonde measurements of the AMF soundings are used. If the AMF radiosondes do not reach a height of 30 km, climatological data, that is monthly mean values of 10-year radiosonde ascents launched at Essen, which is about 330 km away from the AMF site, are used to fill in the upper levels. For LWC, the provision of an a priori profile is a more demanding task, since in situ measurements are strongly limited in space and time and can not provide a representative data set. Therefore, this information has to be obtained from the output of NWP models or from simple cloud models (e.g., *Karstens* et al., 1994; *Salonen and Uppala*, 1991; *Mattioli* et al., 2006; *Mattioli* et al., 2009), which diagnose the LWC from the humidity profiles measured during radiosonde ascents. In the IPT, the cloud model by *Karstens* et al. (1994) is implemented (cf. Eq. (4.12)), in order to provide an a priori LWC profile in non-drizzling cloud layers. Note that in drizzling cloud layers, no a priori information is available. In these layers, the LWC is set to a value of $10^{-4}\,\mathrm{g\,m^{-3}}$.

Forward model

The MWR measurements and the atmospheric profiles are related by a forward model, which is a microwave radiative transfer operator (RTO) for nonscattering cases (*Simmer*, 1994).

Absorption due to water vapor and oxygen is calculated by a fast absorption predictor (FAP) based on the Rosenkranz absorption model (*Rosenkranz*, 1998). Absorption due to liquid water is computed according to *Liebe* et al. (1991). In order to model the radar reflectivities, a Z-LWC relationship is used, so that the forward model can be written as

$$\mathbf{F}(\mathbf{x}) = \left\{ \begin{array}{c} \mathrm{RTO}(\mathbf{T}, \mathbf{q}, \mathbf{LWC}) \\ a \cdot \mathbf{LWC}^b \end{array} \right\} = \left\{ \begin{array}{c} \mathbf{TB} \\ \mathbf{Z} \end{array} \right\} = \mathbf{y}. \tag{7.5}$$

In non-drizzling cases, the parameters a and b are 0.012 and 1.6, respectively (*Fox and Illingworth*, 1997). In these cases, the Z-LWC relationship is the same used in the basic retrieval (Section 4.1.2). According to *Khain* et al. (2008), in light (heavy) drizzling situations, a and b are 323.59 (57.54) and 1.58 (5.17), respectively. In the IPT, radar reflectivity thresholds are used to distinguish heavy ($Z > -10\,\mathrm{dB}Z$), light (-10 dB$Z \geq Z > -30\,\mathrm{dB}Z$) and non-drizzling situations ($Z \leq -30\,\mathrm{dB}Z$). The parameters a and b given above are then adapted for each case.

Error covariance matrices

The accurate determination of the error covariance matrices is not trivial. In order to assess the sensitivity of the LWC retrieval to $\mathbf{S}_e$ and $\mathbf{S}_a$, sensitivity studies with varying entries in these matrices have been performed and are presented in the next section. For the application of the IPT to the nine-month AMF measurements as presented in Section 7.3, $\mathbf{S}_e$ and $\mathbf{S}_a$ have been defined as follows.

The $\mathbf{S}_e$ matrix comprises the meaurement and forward model errors of the brightness temperatures and the radar reflectivities. The measurement errors of the brightness temperatures are assumed to be uncorrelated. For the K-band channels, errors are 0.4 K, and for the V-band channels 0.5 K (51 and 52 GHz) and 0.2 K (53-58 GHz). Uncertainties in the 90 and 150 GHz observations are set to 3 and 1.5 K, respectively. The larger uncertainties in these channels are related to the tipping curve calibration which is automatically performed by the DPR. This calibration method is restricted to horizontally homogeneous clear-sky conditions. Comparisons between measurements of the DPR and the ARM 90/150 GHZ system suggest that in some cases the tipping curve calibration was performed by the DPR in less homogeneous atmospheric conditions leading to large differences between the measurements of both instruments.

For the random error in Z, time- and height-dependent Cloudnet error estimates are applied. These errors are assumed to be due to the finite signal-to-noise ratio and the finite number of radar pulses and due to uncertainties in the gaseous and liquid attenuation correction. Typical values are about 1-2 dB. As for the brightness temperatures, Z errors are assumed to be uncorrelated.

It is difficult to estimate the error of the forward model for the TBs, which may be associated to the FAP and to the Rosenkranz model itself. Differences in simulated and observed brightness temperatures may not only be attributed to deficiencies in the radiative transfer model but also to inaccurate input and measurement data. However, *Turner* et al. (2009) applied carefully checked, cloud-free radiosonde data to different microwave radiative transfer models and compared the computed brightness temperatures at 150 and 31.4 GHz to independent measurements of two collocated MWRs. Both MWRs showed an excellent agreement at 150 GHz with a bias of -0.12 K and a root mean square difference of 1.29 K. In case of the Rosenkranz model, the comparison between simulated and observed brightness temperatures

at 150 (31.4) GHz revealed a bias and a root mean square error of 0.74 (−0.08) K and 2.52 (0.28) K, respectively. Compared to other models, e.g. *Liebe* et al. (1993) and *Clough* et al. (2005), these differences are relatively small.

Since the accuracy of the forward model is not well known, in the IPT, uncertainties in the forward model for the brightness temperatures are assumed to be solely related to uncertainties due to the approximation of the absorption coefficient for water vapour and oxygen by the FAP. The corresponding errors and covariances are based on calculations using a 10-year data set of radiosonde ascents in Lindenberg. The errors are smallest for the 53-58 GHz channels (<0.04 K) and largest at 150 GHz (1.8 K).

Depending on the cloud type, i.e. a cloud without drizzle, with light or with heavy drizzle, the uncertainty in the forward model for the radar reflectivities, namely the Z-LWC relationship, can be considerable. Following *Khain* et al. (2008), the forward model error ranges between 1.5 and 3 dB in non-drizzling cases. In heavy drizzling cases, the error increases to about 5 dB, while in light drizzling situations, the Z-LWC relationship is very uncertain with estimated errors larger than 22 dB.

The $\mathbf{S}_a$ matrix includes information on the uncertainty of the assumed a priori T, q, and LWC profiles. As in *Löhnert* et al. (2008), temperature and humidity entries in $\mathbf{S}_a$ are based on an evaluation of a 10-year radiosonde climatology. Interpolated 6 and 18 UTC Lindenberg radiosonde ascents were compared to the actual 6 and 18 UTC ascents, and temperature and humidity variances and covariances derived. Temperature uncertainties are about 1 or 2 K. Humidity uncertainties are about $1\,\mathrm{g\,m^{-3}}$ up to a height of 3 km and decrease from then on with increasing height.

The uncertainty of the a priori LWC profile, which is derived from the cloud model by *Karstens* et al. (1994), is very difficult to characterize. Usually, these cloud models are tuned to fit observed MWR brightness temperatures (e.g. *Mattioli* et al., 2006). However, the accuracy of the LWC determined by the cloud models is not well known. The IPT provides an error estimate of the calculated a priori LWC profile by slightly perturbing the a priori LWC profile 200 times and calculating variances and covariances from these profiles. Note that, in drizzling situations, no a priori information is available and very large uncertainties are assumed in these cases implying large variances in $\mathbf{S}_a$.

The solution of the IPT and its corresponding errors are highly dependent on the error covariance matrices $\mathbf{S}_e$ and $\mathbf{S}_a$, which control how much weight is given to $\mathbf{x}_a$ and $\mathbf{y}$ in the retrieval process. Before discussing the results of the IPT application to the AMF data, the individual role of a priori, measurement and forward model errors in the LWC retrieval is investigated in detail in the next section.

7.2 Sensitivity studies on information content and error estimates

In this section, the interplay of the errors of the a priori profile, measurements and forward model in the LWC retrieval and the associated effect on the retrieved LWC error and on the information content of the measurements are analyzed by means of several sensitivity studies. Given realistic error estimates for the measurements and the forward model, the accuracy of the a priori profile required for a reasonable LWC error is assessed. Furthermore,

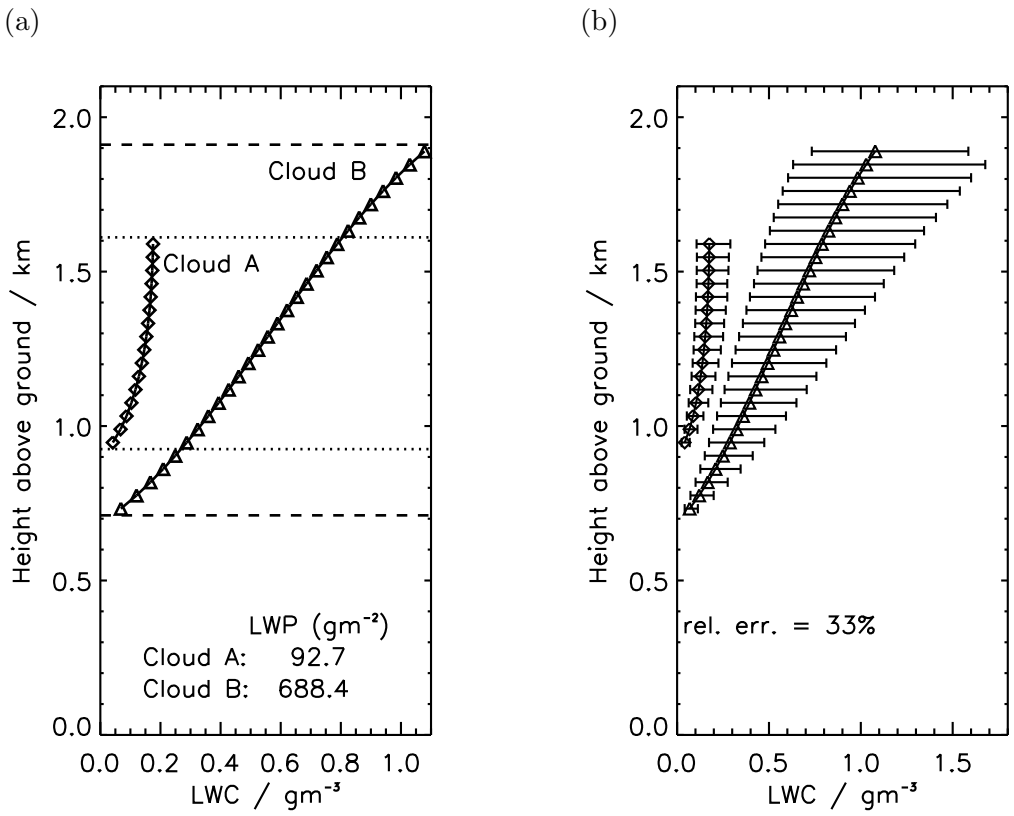

Figure 7.1: IPT-LWC profiles of two non-drizzling water clouds (a) and example for the derived LWC error in one experiment (b). Profiles are on 8 Sep 2007 at 14:19 UTC (cloud A) and on 12 Sep 2007 at 10:50 UTC (cloud B) at the AMF site. For the derived errors in (b), a TB error of 0.5 K and an a priori uncertainty of log(LWC / g m^{-3})=0.175 (corresponding to a relative a priori uncertainty of 34%) is assumed. In this example, the retrieval includes the MWR brightness temperatures of the K-band only.

the information content of different measurement combinations with respect to the derivation of cloud liquid water profiles is investigated. Depending on the chosen configuration of the experiment, the measurement vector **y** encompasses microwave radiometer brightness temperatures and/or cloud radar reflectivities.

7.2.1 Methodology

The experiments have been performed for two non-drizzling single-layer liquid cloud cases (Fig. 7.1) observed at the AMF site in the Black Forest. Both profiles are solutions of the IPT in its configuration as described in Section 7.1.2. The selected profiles represent a cloud with a LWP of about 90 g m^{-2} (case A) and a thickness of about 640 m, or 16 cloud radar levels, and a thick cloud (case B) having a LWP of about 690 g m^{-2} and a thickness of about 1160 m, or 28 cloud radar levels. The smoothness of both LWC profiles is related to the strong influence of the modified adiabatic a priori LWC profile in the IPT, which is discussed in detail in Section 7.3.

On the basis of these two profiles, the sensitivity analysis is performed employing Eqs. (7.3) and (7.4). For the sensitivity studies, the LWC error and the information content of a set of

observations are directly calculated from given $\mathbf{S}_e$, $\mathbf{S}_a$, and $\mathbf{K}$ matrices without the full IPT framework, i.e. the full iterative retrieval procedure.

If not explicitly mentioned, $\mathbf{S}_e$ and $\mathbf{S}_a$ are set to diagonal matrices in this analysis. This means that the measurement and forward model errors encapsulated by $\mathbf{S}_e$, as well as the errors of the a priori profile in $\mathbf{S}_a$, are assumed to be uncorrelated. The effect of correlated errors are discussed in Sections 7.2.4 and 7.2.5. For the brightness temperatures, a random error of 0.5 K is applied, which is in the order of magnitude of the measurement noise (*Rose* et al., 2005). For the radar reflectivities, a random error of 3 dB is assumed, which is slightly larger than the Cloudnet estimated error (Section 7.1.2). This error has been chosen because, intercomparison measurements of the AMF cloud radar and the collocated 35.5 GHz MIRA36-S cloud radar revealed differences in the radar reflectivities of 3 dB (*Handwerker and Miller*, 2008). As discussed in Section 7.1.2, uncertainties in the forward model may be larger than the measurement error itself and can not be generally neglected. However, for the first sensitivity studies an overall error of 0.5 K and 3 dB for the brightness temperatures and the radar reflectivities is assumed, respectively. The effect of larger errors in $\mathbf{S}_e$ on the retrieved error and the information content will be investigated in Section 7.2.3.

Given the diagonal matrices $\mathbf{S}_e$ and $\mathbf{S}_a$, corresponding error estimates according to Eq. (7.3) have been calculated for the profiles in Fig. 7.1a. An example for one experiment configuration is shown in Fig. 7.1b. Since log(LWC) is derived, errors in LWC are not symmetric. For the following analysis, a mean error of the profile is computed by calculating a mean relative error for each height and by averaging these errors over all height levels.

In order to characterize the influence of the a priori LWC profile on the retrieved LWC error and on the DGF, the uncertainty in the a priori profile is increased step-wise from $6{\cdot}10^{-4}\,\mathrm{g\,m^{-3}}$ (0.2% relative error) to $7\,\mathrm{g\,m^{-3}}$ (2733% relative error) for a fixed set of observations. A small uncertainty implies that the a priori profile has a large weight in the solution. If the uncertainty of the a priori LWC profile increases, the influence of the a priori profile in the LWC retrieval decreases and more weight is put on the measurements. This variation of the a priori uncertainty has an effect on the DGF as well as on the retrieved LWC error. As an example, Fig. 7.2 shows the impact of the a priori uncertainty on the DGF and on the retrieved LWC error for a retrieval including only the K-band measurements of the MWR. In Fig. 7.2a, the DGF and the retrieved LWC errors are shown as a function of the a priori uncertainty. For a better comparison to Fig. 7.2a, the chosen a priori errors are plotted against the retrieved LWC errors in Fig. 7.2b. Note however, that the retrieved error is a function of the a priori error, and not vice versa.

Increasing the magnitude of the diagonal elements in $\mathbf{S}_a$, i.e. increasing the a priori uncertainty, yields an increased LWC error and a larger number of DGF implying that the measurements have more weight in the solution. In other words, the better known the a priori profile is, the smaller is the error of the solution and the smaller is the influence of the measurements. If the a priori profile would be the true profile, the measurements would add no information at all. However, in virtually all cases the a priori profile is not the true profile (else there would be no need to perform a retrieval), and the DGF is much lower than the desired resolution of the LWC profile.

7.2.2 Dependence on measurement vector

The effect of different measurement combinations on the retrieved LWC error (diagonal elements of $\mathbf{S}_{op}$) and on the number of degrees of freedom (trace of $\mathbf{A}$) is investigated for the

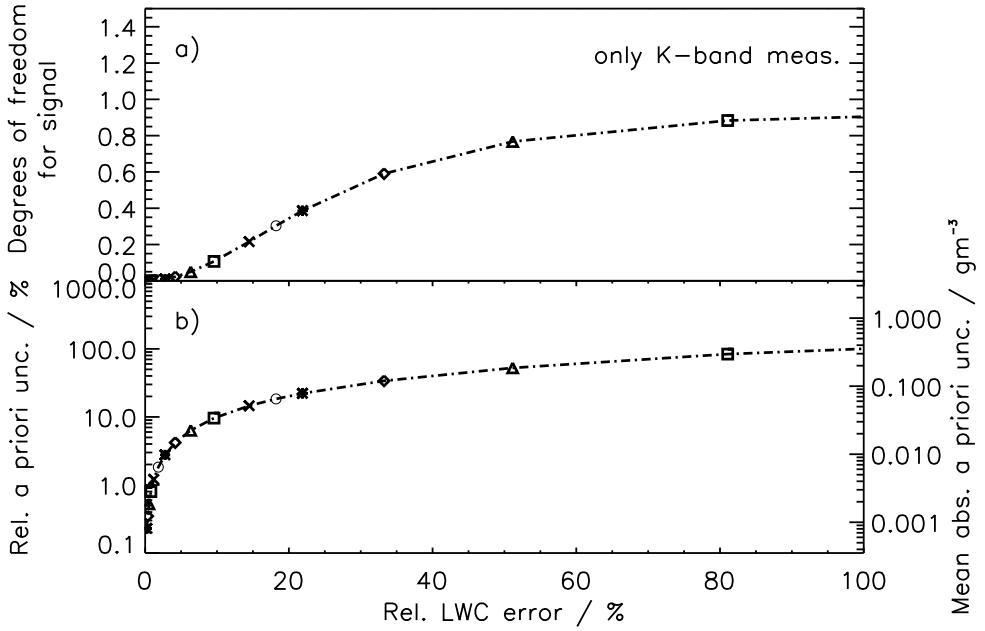

Figure 7.2: Degrees of freedom for signal and LWC errors for cloud A assuming different a priori errors (a). The corresponding a priori uncertainties (relative and absolute) are shown for reference (b). Different values of the a priori uncertainty are represented by different symbols. The retrieval only includes the MWR brightness temperatures of the K-band.

cloud A (Fig. 7.3a,e) and the thick cloud B (Fig. 7.3b,d). The different symbols in Fig. 7.3 represent different a priori uncertainties, which have been varied from $6 \cdot 10^{-4}$ to $7\,\mathrm{g\,m^{-3}}$ (cf. Fig. 7.2a). The maximum possible number of DGF corresponds to the number of cloud layers on which the LWC is retrieved, i.e. 16 for cloud A and 28 for cloud B. When using the K-band (22-32 GHz) channels only (for cloud A: same curve as in Fig. 7.2b), there is essentially only one piece of information in the measurements , which corresponds to the column integrated LWC, the LWP. Adding the V-band (51-59 GHz), 90, and 150 GHz channels leads to a slightly increased number of DGF for cloud A. Furthermore, this measurement combination reduces the error in the LWC. The maximum information content of the K-band retrieval, i.e. 0.9, is reached for an a priori uncertainty of about 100% corresponding to a LWC error in the same order of magnitude. When adding the other microwave radiometer channels, this value is reached already for a relative error of 10% in the a priori profile. This effect is due to the increased sensitivity of liquid water at 90 and 150 GHz relative to the channels in the K- and V-bands. The TB enhancement of the cloud A on the 90 and 150 GHz TBs is 17 and 19 K, respectively, and only 2-4 K for the K-band and maximum 4 K for the V-band channels (not shown). For the thick cloud (case B), the signal is strong in all channels, namely about 20 K for the K- and V-band and 100 K for the 90 and 150 GHz channels, so that the saturation value of 1 DGF for the K-Band retrieval is reached for a LWC error of 10%. If the V-Band channels and the 90 and 150 GHz frequencies are included, there is a small amount of information on the LWC profile (1.5 DGF). However, this increased information content is reached at a large error in LWC.

Extending this analysis for the inclusion of cloud radar reflectivity data, the analysis begins with the simple case that only cloud radar reflectivity data are used in the retrieval. Recall

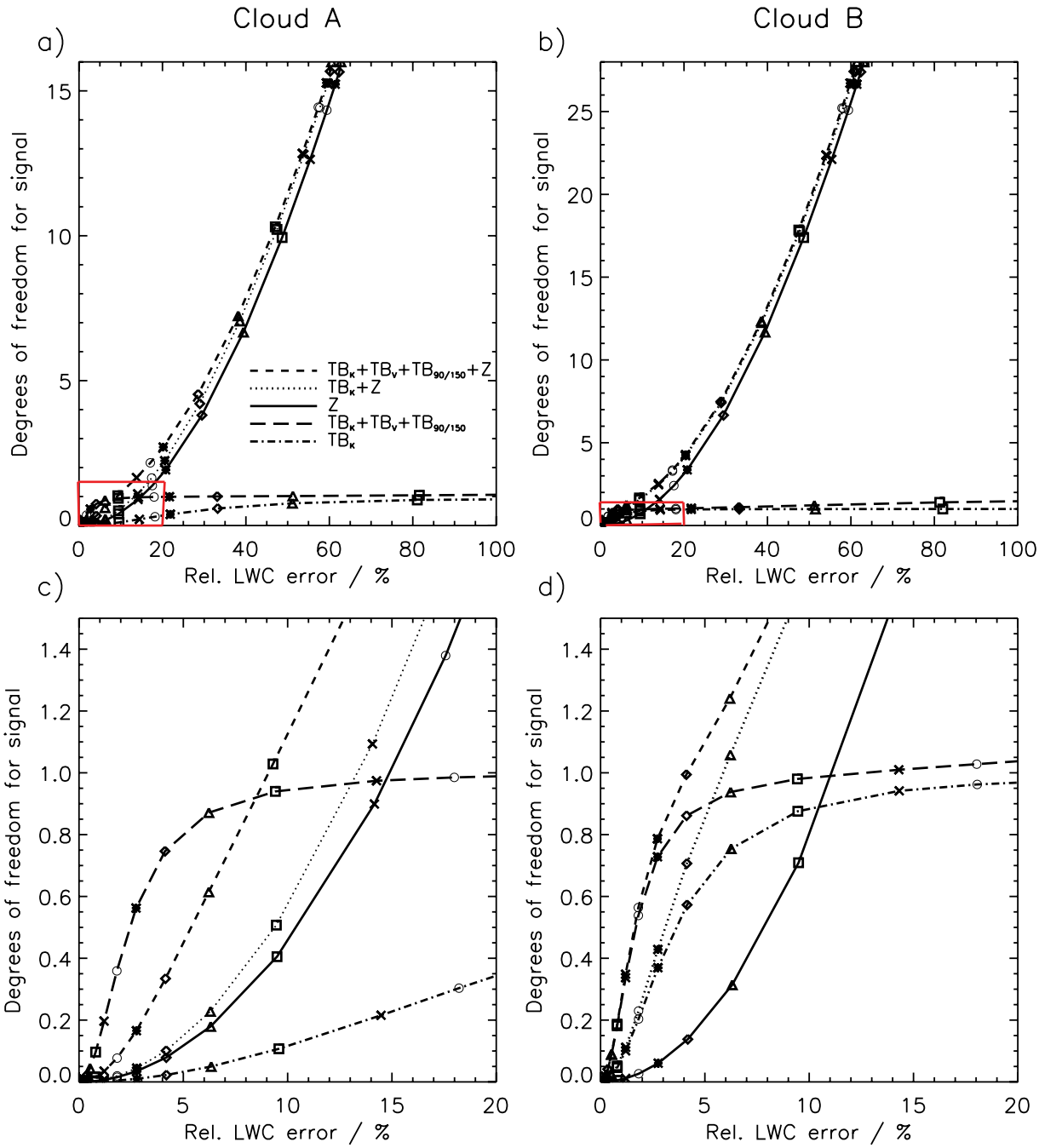

Figure 7.3: Degrees of freedom for signal and retrieved LWC errors for cloud A (left panels) and cloud B (right panels) assuming different a priori uncertainties and measurement combinations. The different curves in each panel correspond to different measurement combinations in the retrieval; the seven K-Band channels only (22-32 GHz)(dash-dotted), K- and V-Band channels (51-59 GHz) plus 90 and 150 GHz channels (long dashes), the cloud radar reflectivity measurements only (solid), K-band channels plus cloud radar reflectivities (dotted) and all microwave channels (K-, V-Band, 90, 150) plus cloud radar reflectivities (dashed). Same symbols aligned in the vertical indicate same a priori uncertainties. (c) and (d) show an image detail (red frame) of (a) and (b), respectively.

Table 7.1: Number of DGF for a retrieved LWC error of 30% assuming different measurement combinations. The maximum number of DGF is 16 for cloud A and 28 for cloud B.

	Cloud A (16 radar bins)	Cloud B (28 radar bins)
TB_K	0.5	1.0
TB_K + TB_V +TB_{90} + TB_{150}	0.9	1.1
Z	4.0	6.7
Z + TB_K	4.5	8.0
Z + TB_K + TB_V + TB_{90} + TB_{150}	5.0	8.0

that a Z error of 3 dB is assumed and, as for the microwave brightness temperatures, that the error is uncorrelated between different radar height bins. In this case, the DGF rapidly increases when the influence of the a priori information is reduced (i.e., when the uncertainty in the a priori profile is increased). The number of DGF is maximal (16 and 28 for cloud A and cloud B, respectively, corresponding to the number or radar bins) for a relative LWC error of 63% in both cases. In this situation, the a priori profile has virtually no effect on the retrieved LWC profile. If the MWR radiometer frequencies are additionally included in the retrieval, the amount of information increases roughly by the number of DGF that are in the MWR observations alone. In Table 7.1, the DGF associated to a retrieved LWC error of 30% are summarized for the different measurement combinations. A value of 30% is a realistic lower bound for a LWC error using the combination of a cloud radar and microwave radiometer (*Löhnert* et al., 2001). It is clearly visible that the retrieval including all measurements outperforms the other combinations. The amount of information coming from the measurements increases from about 3% (only K-Band TBs, i.e. 0.5 and 1 of the maximum 16 and 28 DGF, respectively) to 30% (all measurements, i.e. 5 and 8 of the maximum 16 and 28 DGF, respectively). For the thick cloud, the inclusion of the V-band and 90/150 GHz channels only marginally increases the information in the observations compared to the Z-TB_K retrieval.

In order to achieve a relative LWC error of 30%, the a priori uncertainty must be smaller than 34%. Thus for small LWC errors, the retrieved LWC error is in the same order of magnitude as the a priori error itself. However, the spread between a priori and retrieved error and therefore the benefit of the retrieval rapidly increases for a priori errors of about 30% or larger. If the a priori profile is not well known and its error is about 100%, for example, than the retrieval reduces the LWC error to 50%.

7.2.3 Dependence on measurement error

As mentioned in Section 7.2.1, the combined measurement and forward model error in $\mathbf{S}_e$ may be substantially larger. In the following, the effect on the DGF of increasing the measurement error, i.e. increasing the diagonal elements in $\mathbf{S}_e$, is analyzed. For this purpose, an experiment is performed in which the TB error is set to 1 K (Fig. 7.4a) and the Z error is not changed (3 dB) and another one in which the Z error is set to 4 dB and the TB error (0.5 K) is not modified (Fig. 7.4b).

Compared to Fig. 7.3a, increasing the error in the TB observations reduces the number of DGF for the same relative error in LWC. In other words, the microwave radiometer measurements contribute less to the retrieved LWC profiles as the uncertainty in the radiometers

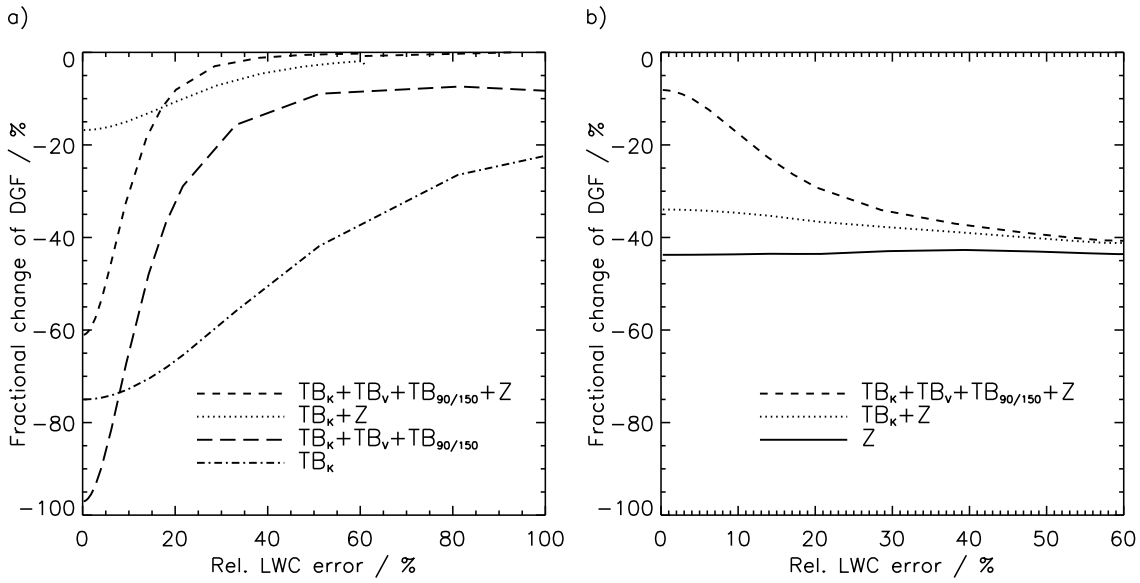

Figure 7.4: Percental changes in the DGF compared to results in Fig. 7.3 a) when assuming larger measurement errors in Se. (a) Results when setting the TB error to 1 K, leaving the Z error at 3 dB and (b) when setting the Z error to 4 dB, leaving the TB error at 0.5 K.

Table 7.2: Number of DGF for a retrieved LWC error of 30% assuming different measurement combinations and measurement errors for cloud A.

	TB_{err}=0.5 K, Z_{err}=3 dB	TB_{err}=1 K, Z_{err}=3 dB	TB_{err}=0.5 K, Z_{err}=4 dB
TB_K	0.5	0.2	0.5
TB_K + TB_V +TB_{90} + TB_{150}	0.9	0.8	0.9
Z	4.0	4.0	2.2
Z + TB_K	4.5	4.2	2.8
Z + TB_K + TB_V + TB_{90} + TB_{150}	5.0	4.8	3.1

TB measurements increase. This is especially true for the K-channels (Table 7.2), since the random error in this spectral band is in the same order of magnitude as the cloud signal in the TBs; the 90 and 150 GHz channels are less affected to small changes in the error in the TB observations because the signals in these channels are larger. In case of the modified Z errors, the maximum relative error in LWC increases to 88% (not shown) as opposed to the 63% shown in Fig. 7.3, if the measurements have full weight in the retrieval using reflectivity alone, i.e., if the uncertainty in the a priori profile is large. The increase in the maximum errors reduces the DGF compared to Fig. 7.3a (Fig. 7.4b). In terms of relative changes, the reduction of the DGF is strongest in the retrieval including Z only (about 44%). For small LWC errors, this reduction is significantly less pronounced in the retrievals which also encompass the MWR TBs, in particular the measurements at 90 and 150 GHz. For a 30% LWC error, the number of DGF is reduced by about 34% (radar plus all MWR TBs) to 44% (only radar) corresponding to about 1.8 DGF, so that the DGF range between 2.2 (only radar) and 3.1 (radar plus MWR). In other words, only 14 to 19% of the vertical information on the LWC profile comes from the measurement

7.2.4 Dependence on correlated measurement and forward model errors

In the previous sections, the measurement errors were assumed to be uncorrelated and random, and the errors in the forward model to also be uncorrelated and random. With regard to calibration and forward model errors, this assumption is generally not valid. For the MWR HATPRO, for example, an absolute calibration against an internal hot load target is performed every 5 to 10 minutes depending on the chosen scan strategy. If the temperature of this internal calibration load is not measured correctly, the MWR brightness temperatures will be systematically too high or too low and the errors of the different channels will be correlated among each other. While such a calibration error can be treated as a systematic error on shorter time scales, i.e. between two calibrations of the instrument, it may be described as a random error on longer timescales, i.e. over several calibration procedures, with significant off-diagonal entries in the covariance matrix $\mathbf{S}_e$.

The effect of such correlated errors on the retrieved error and on the DGF is investigated next. For this purpose, one experiment has been performed with brightness temperature covariances of $(0.2\,\mathrm{K})^2$ and another experiment assuming $(1\,\mathrm{dB})^2$ reflectivity covariances for all corresponding off-diagonal elements in $\mathbf{S}_e$. In general, assuming constant correlations is a rather strong simplification. Nevertheless, this is sufficient for a first qualitative assessment of the influence of correlations. The variances are set to $(0.5\,\mathrm{K})^2$ and $(3\,\mathrm{dB})^2$, respectively . If the measurement errors are correlated, we obtain more information about the measurement, than in the case when the off-diagonal elements are set to zero. Introducing correlated radar reflectivity errors leads to an increased number of DGF and a reduced LWC error calculated for the same a priori errors. For the chosen configuration, up to 0.4 DGF are added, while the relative LWC error is reduced by up to 3% (not shown)

Introducing TB covariances of $(0.2\,\mathrm{K})^2$ does not increase the information content of the microwave measurements with regard to the LWC retrieval. Only when very large TB error correlations of 0.95 and more are introduced, the DGF increases by about 0.6 for small a priori errors (not shown).

7.2.5 Dependence on cloud vertical correlation

In the previous sections, it has been assumed that the cloud layers in the a priori profile are uncorrelated, i.e. the off-diagonal components in $\mathbf{S}_a$ are zero. Since the LWC profiles of stratiform clouds are often close to quasi-adiabatic (*Korolev* et al., 2007), the cloud layers will generally not be independent from each other. In order to assess the effect of cloud vertical correlation on the DGFs and on the retrieved LWC, an experiment is performed in which it is assumed that the correlation of two cloud layers exponentially decreases with their distance to each other (Fig. 7.5a), such that the covariance of two layers m and n can be written as

$$S_{mn} = \sigma_{mm}^2 \exp\left(-0.5\,(m-n)^2\,/\beta^2\right), \tag{7.6}$$

where σ_{mm}^2 is the diagonal entry of $\mathbf{S}_a$. The parameter β is set to 1 and 3, respectively, where the larger value implies a stronger correlation of the cloud layers in the a priori profile. If the cloud layers are correlated and therefore also the errors, the a priori profile has more weight in the retrieval than in the uncorrelated case. The influence of the a priori profile on the solution increases with the correlation. The effect on the relative LWC error and on the pieces of information which come from the measurement is shown in Fig. 7.5b. Introducing correlation leads to a reduced LWC error, but also to a reduced number of DGF, since more confidence is put in the a priori profile.

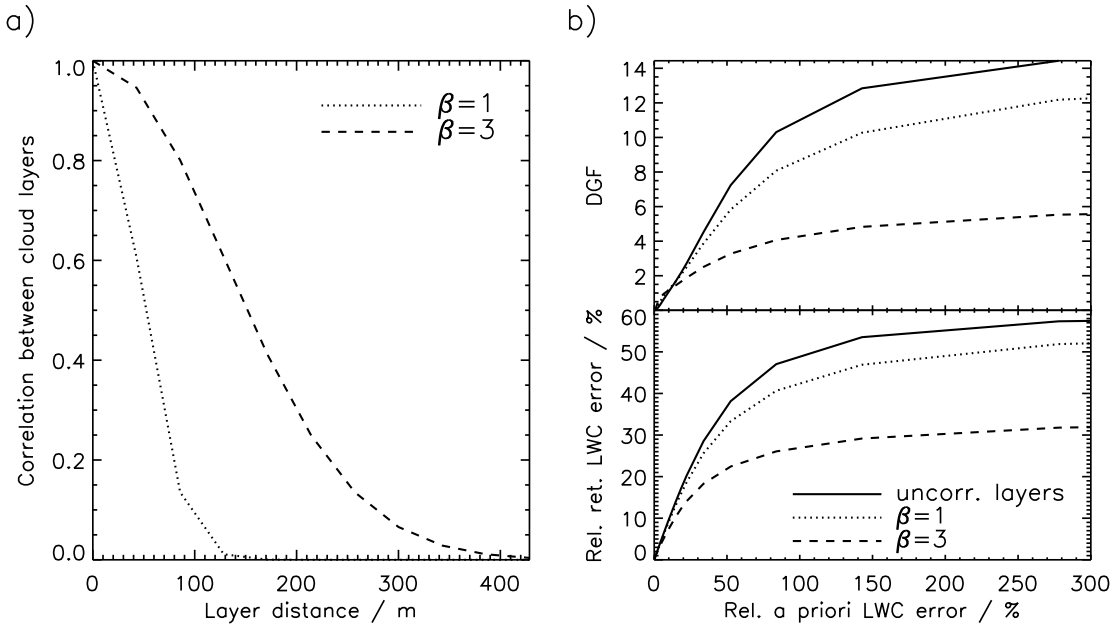

Figure 7.5: Sensitivity of the DGF to non-zero, off-diagonal elements in Sa. (a) Correlation between two layers within a cloud as a function of their distance to each other according to Eq. (7.6). (b) Relative LWC error (bottom) and degrees of freedom for signal (top) as a function of the a priori LWC error for cloud A using all microwave channels (K-, V-Band, 90, 150) and cloud radar reflectivities. The three curves in each panel of b) represent different values of β in $\mathbf{S}_a$. No correlation of cloud layers, i.e. zero off-diagonal elements (β=0, solid), correlation of cloud layers corresponding to curves in a) (β=1, dotted; β=3, dashed).

7.2.6 Drizzle case analysis

As mentioned in Section 7.2.1, Z-LWC relationships are less accurate for clouds including drizzle than for clouds without drizzle. In heavy drizzling situations, the forward model error increases to about 5 dB. Remember, that in non-drizzling situations this error has been estimated to be about 1.5 to 3 dB.

The analysis is repeated for cloud A and B assuming that these are heavy drizzling clouds. Since a different forward model is applied, i.e. the formulation for heavy drizzling clouds by *Khain* et al. (2008), with different error characteristics, the Jacobian $\mathbf{K}$ and the elements in $\mathbf{S}_e$ have to be adapted. The diagonal elements of $\mathbf{S}_e$ are now the sum of the square of the measurement error (3 dB) and the square of the forward model error (5 dB) and are therefore 34 dB^2.

Compared to Fig. 7.3, the trade-off between the relative error in LWC and the DGF is qualitatively similar (not shown). However, the maximum LWC error, i.e. the error associated with the maximum number of DGF, is 96% for the retrieval employing the radar reflectivities only. This means that, without a priori information and fully relying on the Z-LWC relationship, the error of the retrieved LWC is almost 100%. For a 30% error in the retrieved LWC, a priori information has to be included, whose accuracy must be at least 32%. However, in this case, only 1.9 DGF (cloud A) and 3.3 DGF (cloud B) are in the measurements. In other words, 88% of the vertical information comes from the a priori profile. When adding the MWR measurements, this is at least reduced to 81%, since the MWR TBs add about 1 DGF.

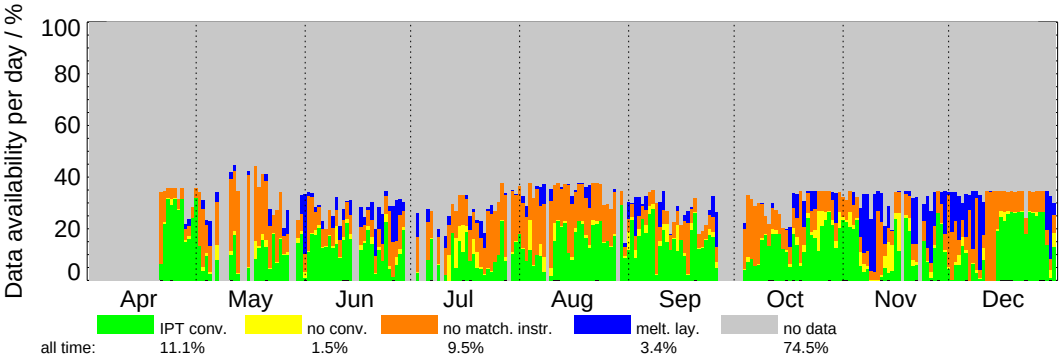

Figure 7.6: IPT data availability (defined on 30-s grid) during the nine-month measurement period. Note that in clear-sky cases, the IPT is performed for every third Cloudnet classification profile only (every 90 s).

7.3 Application of the IPT to AMF measurements

In the previous section, the retrieved LWC error and the information content of the measurements have been investigated without the full IPT framework. In the following, the derived error and information content of the IPT in its standard version as outlined in Section 7.1.2 are analyzed. Additionally, it is discussed how the IPT derived LWC profiles of SL WC differ from the LWC profiles of the basic retrieval (Section 4.1.2), and how these differences affect the corresponding CRE and CRF. These analyses focus on the estimation of uncertainties rather than deriving representative values for CRE and CRF themselves.

7.3.1 IPT data availability

On the basis of the 30-s Cloundet categorization profiles, the IPT has been applied to the nine-month measurements in the Black Forest. The data availability of the derived IPT profiles is depicted in Fig. 7.6. In total, 92,287 profiles converged corresponding to 11.1% of the time during the nine-month measurement period. LWC has been derived in 36,621 cases. In most of the time (74.5%), no retrieval was performed which is mainly due to missing HATPRO measurements (cf. Fig. 3.2). Furthermore, in clear sky or ice cloud cases, where no LWC is derived, the retrieval has been performed for every third profile only in order to reduce the computational costs. For the remaining Cloudnet profiles, the occurrence of melting layers and mismatching instrument times prevented the application of the retrieval in 3.4% and 9.5% of the time, respectively. For a small fraction of all Cloudnet profiles, the IPT did not find a solution. Possible reasons for the non-convergence are spurious measurements and/or inadequate a priori information which have a too large weight in the retrieval procedure.

These findings suggest that the analysis of water clouds at the AMF site based on the IPT derived LWC profiles alone is difficult. In particular, if the IPT LWC information is merged with the thermodynamic and IWC profiles as described in Section 4.1, only 5% of all detected cloudy profiles and only 14% of all SL WC are taken into account in this combined data set, preventing a meaningful analysis of the CRE and CRF at this site. However, the first concern of this section is the evaluation of the IPT performance in the configuration described in Section 7.1.2.

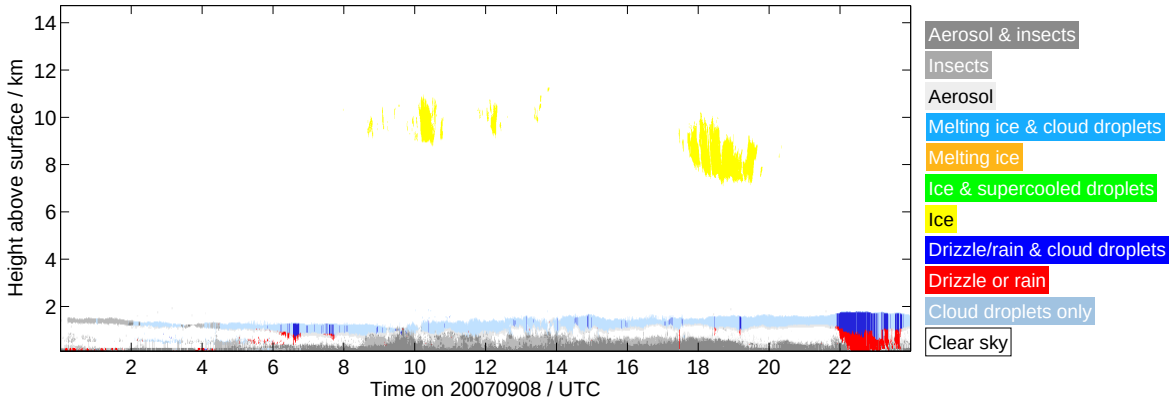

Figure 7.7: Cloudnet target classification on 8 September 2007.

7.3.2 Information content and error estimates

In the following, the interplay of the a priori and the measurement information in the retrieved LWC profile and the corresponding error are exemplarily analyzed for one day. On 8 September 2007, an almost continuous stratocumulus cloud layer has been detected between a height of 1 and 2 km (Fig. 7.7). The retrieved LWC profiles from the IPT and the corresponding error estimates are shown in Fig. 7.8. In non-drizzling situations, the mean relative errors do not exceed 30%. In these cases, the normalized DGF, i.e. the number of DGF divided by the total number of liquid layers, is about 10% corresponding to a number of DGF of up to 1.3. This result implies that only 10% of the LWC information comes from the measurements, that is from the MWR brightness temperatures and the cloud radar reflectivities, and 90% from the a priori profile. In drizzling cases, a priori information is only available for the non-drizzling parts of the cloud. Thus, in the drizzling cloud radar pixels, all LWC information is basically derived from the measurements alone. The number of DGF of these profiles is therefore almost linearly related to the number of radar pixels which contain drizzle (not shown). As discussed in Sections 7.1.2 and 7.2.6, Z-LWC relationships for drizzle are highly uncertain, especially for light-drizzling clouds. The large uncertainties of these relationships are reflected by the derived LWC errors of profiles containing drizzle, which are generally larger than 20% (Fig. 7.8c) and may be more than 200%.

In some non-drizzling situations, the derived LWC errors are very small with values down to 2%. Such an accuracy in the derived LWC profile is highly questionable. When relating these errors to the corresponding cloud thickness, a tendency to smaller errors with increasing cloud thickness can be observed (Fig. 7.9). In Section 7.2.5, it has been shown that correlated a priori errors yield LWC errors that are smaller than in the uncorrelated case. Since the a priori profile in this study, namely the modified adiabatic LWC profile, directly depends on the height above cloud base, cloud layers are strongly correlated among each other. If the number of the cloud layers increases, the error of the LWC in a specific layer is more and more constrained by the LWC of all other layers. Thus, the error space of the a priori profile is confined yielding a reduced error of the solution. These results suggest to reconsider the formulation of the a priori covariance matrix in the IPT. Clouds with large vertical extensions are presumably less adiabatic than clouds with smaller vertical extensions. However, in the IPT, for geometrically thick clouds, the weight of the modified adiabatic profile in the retrieval solution is even larger than for thin clouds. In order to improve the formulation of the LWC a priori covariance matrix, more in situ data are needed from which realistic layer to layer

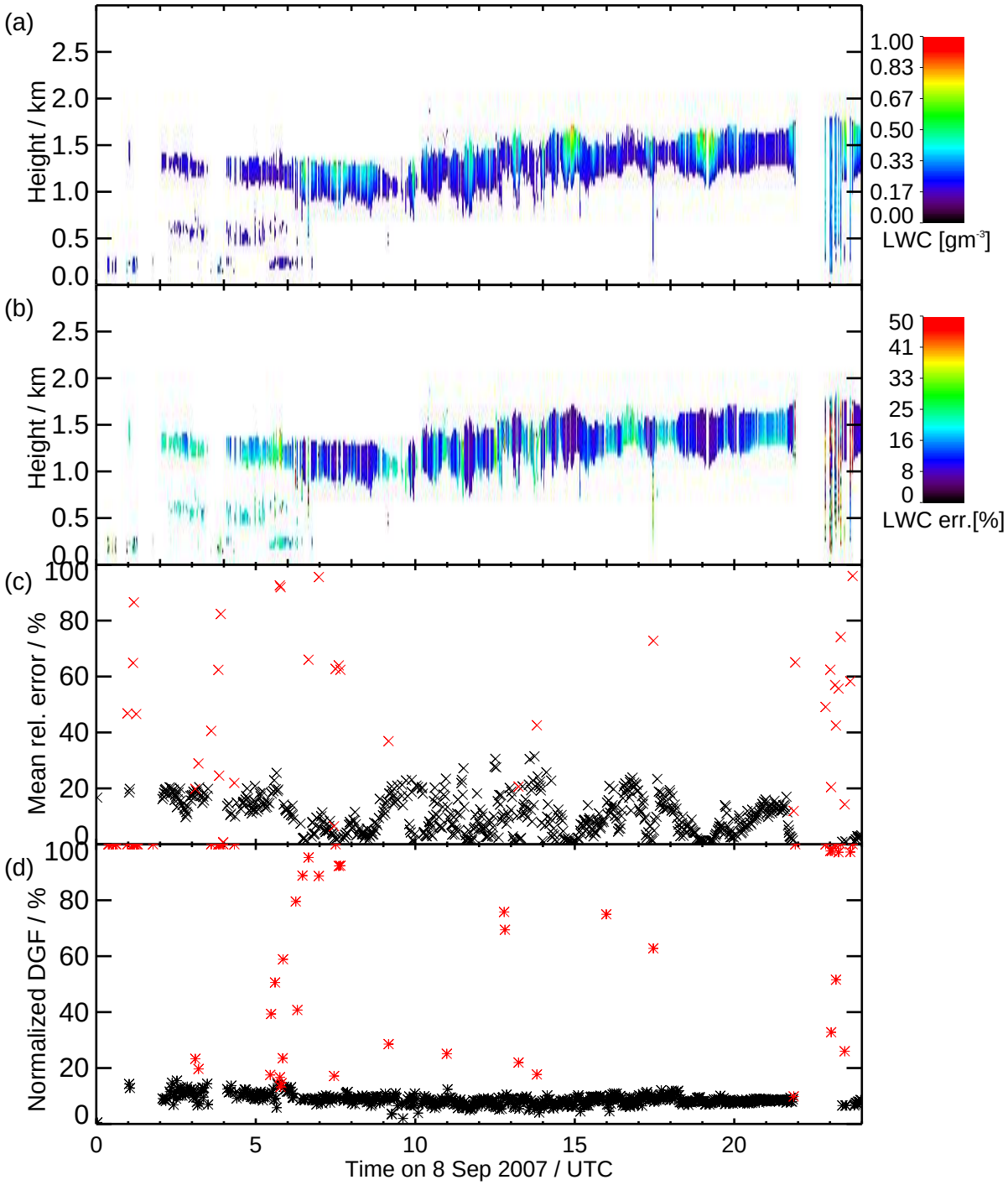

Figure 7.8: IPT results for 8 September 2007. (a) LWC, (b) relative LWC error, (c) mean rel. error of LWC profile, and (d) normalized DGF. The normalized DGF are the DGF divided by the number of cloud layers. The red symbols in (c) and (d) indicate profiles containing drizzle. Note that the mean relative error in 23 drizzling cases (38%) is larger than 100%.

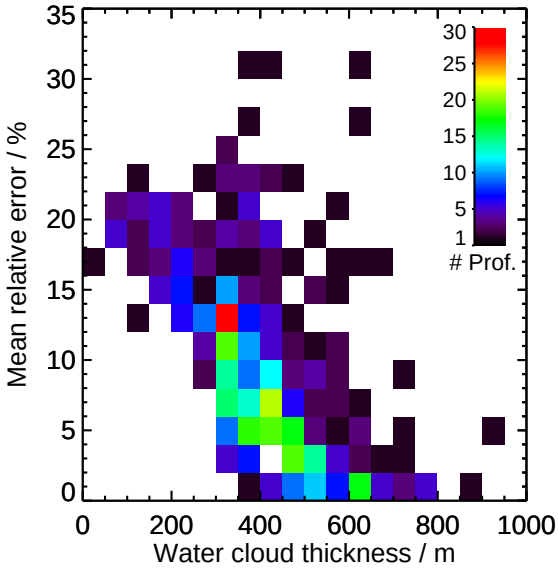

Figure 7.9: Frequency distributions of the mean LWC error with respect to the water cloud thickness. The analysis is based on all non-drizzling IPT LWC profiles (552) on 8 September 2007.

covariances could be derived.

7.3.3 Comparison of two LWC retrieval algorithms

For SL WC, the LWC profiles derived by the IPT are compared to those of the basic retrieval algorithm. As before, only those clouds are considered which are at least 15 minute persistent. This sampling results in 358 15-min intervals with a total of 2,579 single LWC profiles. The retrieved mean LWC profiles for different cloud thicknesses are shown in Fig. 7.10. The cloud boundaries are the same in both retrievals. For SL WC with a cloud thickness Δz_{cloud} of 1000 m or less, the IPT yields a smaller the maximum LWC compared to the basic retrieval, while for thicker clouds, the IPT reveals larger LWCs in most heights. In the latter case, however, the profile of the scaled Z-LWC approach is still within the estimated uncertainties of the IPT LWC.

The differences in the LWC profiles translate to differences in the LWP (Table 7.3). The IPT LWP of thin SL WC ($\Delta z_{\text{cloud}} < 500\,\text{m}$) is on average $10.7\,\text{g}\,\text{m}^{-2}$ smaller compared to the LWP of the statistical retrieval LWP_{STAT}, which is used to scale the LWC of the Z-LWC relationship. The difference reduces to -2.4 $\text{g}\,\text{m}^{-2}$ for the medium thick clouds ($500\,\text{m} < \Delta z_{\text{cloud}} < 1000\,\text{m}$), while a large positive difference of $37.2\,\text{g}\,\text{m}^{-2}$ occurs for thick clouds with $\Delta z_{\text{cloud}} > 1500\,\text{m}$. In all three cases, the derived LWP values reveal a considerable scatter with standard deviations between 27% ($\Delta z_{\text{cloud}} > 1500\,\text{m}$) and 56% ($\Delta z_{\text{cloud}} < 500\,\text{m}$) of the mean LWP of the statistical retrieval.

Since the solution of the IPT is controlled by the a priori information and the measurements together with the corresponding forward model, it is reasonable to take a closer look at the individual LWPs, namely the LWP of the modified adiabatic profile and the LWP derived from the Z-LWC relationships included in the IPT. These LWPs have been compared to the LWP

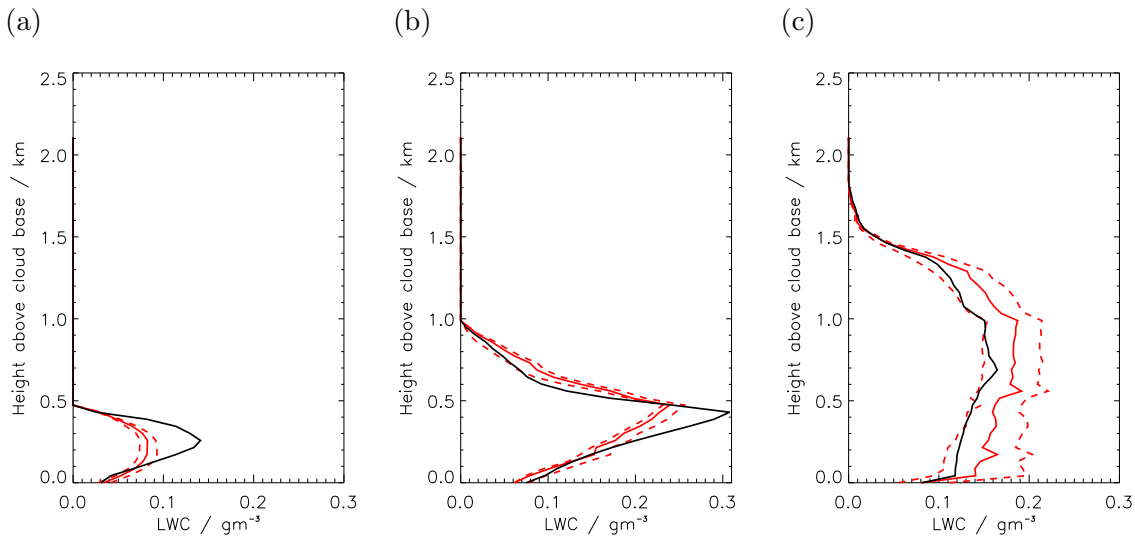

Figure 7.10: Mean LWC profiles of the basic retrieval algorithm (black) and the IPT (red) for clouds with a geometrical cloud thickness between 0-500 m (a, 1,532 profiles), 500-1000 m (b, 846 profiles) and greater than 1500 m (c, 201 profiles). The analysis is based on all 15-minute persistent SL WC situations.

Table 7.3: Comparison statistics of the LWP of the basic LWC retrieval (LWP_{STAT}) and of the IPT (LWP_{IPT}). Differences are expressed as LWP_{IPT} minus LWP_{STAT}. The analysis is based on all 15-minute persistent SL WC situations.

Δz_{cloud}	<500 m	500-1000 m	>1500 m	all
Number of profiles	1,532	846	201	2,579
BIAS / gm^{-2}	−10.7	−2.4	37.2	−4.2
RMS difference / gm^{-2}	25.8	44.9	64.2	37.1
STDDEV / gm^{-2}	23.5	44.8	52.3	36.8
LWP_{IPT} MEAN / gm^{-2}	30.0	123.5	231.5	76.4
LWP_{STAT} MEAN / gm^{-2}	40.6	125.9	194.3	80.6

of the statistical retrieval for all non-drizzling profiles on 8 September 2007 (Fig. 7.11). The differences between $LWP_{Z\text{-}LWC}$ and LWP_{STAT} and between LWP_{AP} and LWP_{STAT} exhibit a linear dependency on cloud thickness, which is more pronounced in the latter case. Differences between the a priori LWP and the LWP_{STAT} are negative for cloud thicknesses less than 300 m and shifted to positive values with increasing vertical extension of the cloud. A similar tendency can be observed for the $LWP_{Z\text{-}LWC}$. In most cases, however, $LWP_{Z\text{-}LWC}$ is smaller than LWP_{STAT}. Since both LWP_{AP} and $LWP_{Z\text{-}LWC}$ are smaller than LWP_{STAT} for thin clouds, it is reasonable that also the LWP derived by the IPT is smaller than LWP_{STAT}. The brightness temperatures of the MWR additionally constrain the solution, but they might not compensate for the deficiencies in the a priori profile and in the forward model in every case, especially if the a priori profile dominates the solution (Section 7.3.2). Figure 7.11 suggests that the overestimation of the LWP for thick clouds (Table 7.3) is related to the overestimation of LWP_{AP} combined with a large weight of the a priori profile in the IPT.

In addition to potential deficiencies in the formulation of the a priori information and in the Z-LWC relationship, other reasons may cause or at least enhance the differences between

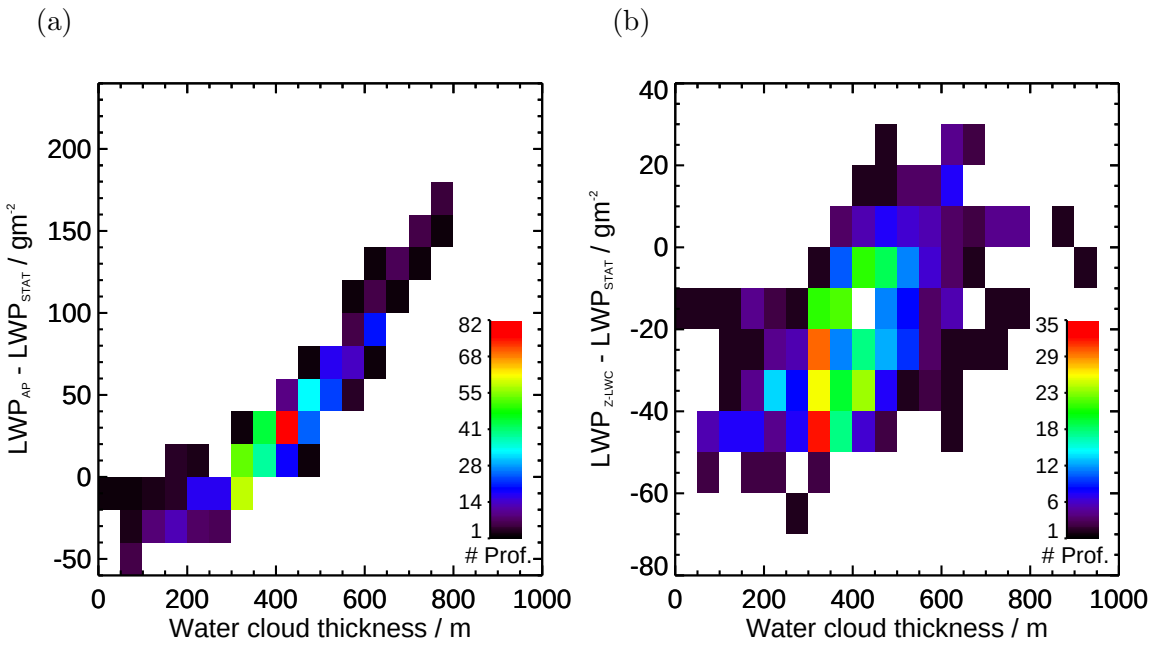

Figure 7.11: Frequency distributions of the LWP difference with respect to the water cloud thickness. The analysis is based on all non-drizzling IPT LWC profiles (552) on 8 September 2007. (a) a priori LWP (LWP_{AP}) minus LWP of statistical HATPRO retrieval (LWP_{STAT}), (b) LWP from Z-LWC relationshipt ($LWP_{Z\text{-}LWC}$) minus LWP of statistical HATPRO retrieval (LWP_{STAT}).

LWP_{IPT} and LWP_{STAT}. The negative bias of thin SL WC might as well be related to an underestimation of the cloud top height and therefore an underestimation of the cloud vertical thickness. Since small cloud droplets at the cloud boundaries are often below the detection threshold of the cloud radar, lidar measurements being sensitive to these particles are typically included. Due to the strong attenuation of the lidar signal in upper cloud layers, the lidar information is only available for the detection of cloud base heights. In the target categorization, the detection of the cloud top height primarily relies on the radar reflectivity. If the vertical extent of the cloud is underestimated, the a priori LWC profile is derived for a too thin cloud having a smaller LWP than a cloud with the actual vertical extent. Thus, the solution of the IPT would be constrained by a too small a priori LWC resulting in an erroneous LWP.

Another reason for the underestimation of the LWP in thin clouds might be related to the cloud radar reflectivity. It has been observed that the radar reflectivity factor of non-drizzling stratocumulus clouds can be significantly smaller than what would be expected from incoherent Rayleigh scattering (*Russchenberg* et al., 2009). Such a behavior was observed during the BBC campaign 2001 (*Crewell* et al., 2004), when comparing the cloud radar reflectivities with reflectivities derived from the dropsize distribution of in situ measurements and assuming incoherent Rayleigh scattering by the cloud droplets (*Russchenberg* et al., 2009). In this case, the radar reflectivities were on average smaller by about 12 dB compared to the expected values. Preliminary results of the analysis of a persistent stratocumulus cloud layer from 23 to 28 October 2007 at the AMF site suggest that the AMF cloud radar reflectivities might be also affected by the issue described above during some periods. Further investigations are required in order to better understand the processes resulting in these small radar reflectivity

Table 7.4: Mean cloud radiative effect (CRE, $W\,m^{-2}$) of 15-minute persistent single-layer water clouds. The mean CRE is calculated for times with |cos(SZA)| >0.3 and when both LWC retrievals are available (358 values).

	basic retrieval	IPT	+ IPT LWC err.	- IPT LWC err.
SW				
TOA	−98	−104	−107	−98
ATM	14	14	14	13
SFC	−112	−117	−121	−110
LW				
TOA	10	10	10	10
ATM	−60	−59	−60	−57
SFC	70	69	70	67
NET				
TOA	−88	−94	−97	−88
ATM	−46	−46	−46	−45
SFC	−42	−48	−51	−43

values.

As a last point, it has to be mentioned that the statistical LWP algorithm is derived from a training data set that should encompass a range of the LWP values representative for the specific site. However, the LWP of such a retrieval will always drift towards the mean value, such that the extremes (i.e., very small and very large LWP values) might be less well represented and, thus, differences compared to a physical retrieval are large.

7.3.4 Sensitivity of CRE and CRF to LWC retrieval

Although large differences in LWC between the IPT and the basic retrieval exist, the derived CRE for both retrievals is quite similar (Table 7.4). While the LW CRE and the atmopheric CRE is rather insensitive towards the applied retrieval, variations in SW and NET CRE at the SFC and TOA are up to 14%. The IPT based radiative transfer calculations yield a stronger CRE. This is related to the pronounced overestimation of LWP in thick cloud cases ($\Delta z_{\mathrm{cloud}}$ >1500 m). Note that the CRE values of the basic retrieval in Table 7.4 slightly deviate from the values given in Table 6.10 since only a subsample of SL WC situations are included in the comparison of the retrievals. Uncertainties in the IPT derived CRE due to the IPT estimated uncertainties in LWC are typically in the same order of magnitude as the uncertainties due to the chosen retrieval. Except for the NET SFC CRE, the IPT derived CREs reproduce the values of the basic retrieval within the derived uncertainties. Compared to Table 6.10, where uncertainties in CRE due to LWP are estimated to be about 30% or more, the derived IPT uncertainties are maximal 10%. As described in Section 7.3.2, these small uncertainties may be due to an overestimation of the accuracy of the a priori profile.

The CRF profiles of this subsample of SL WC are similar to those shown in Fig. 6.12b-d, except for an intensified mininum in LW and a net cooling by about -1 $K\,day^{-1}$ (not shown). Uncertainties in SW CRF due to the IPT derived LWC errors and due to the different retrievals are in the same order of magnitude and generally lower than 0.1 $K\,day^{-1}$. In the LW and net CRF, differences between both retrievals are smaller than 0.4 $K\,day^{-1}$, while IPT

related uncertainties are less than $0.2\,\mathrm{K\,day^{-1}}$. Thus, the IPT related uncertainties in CRF are in the same order of magnitude as uncertainties due to the profile shape (Fig. 6.13).

7.4 Summary and conclusions

In this chapter, the influence of a priori, measurement and forward model errors on the information content in the measurements with respect to the LWC retrieval and on the retrieved LWC errors has been assessed. If the a priori uncertainties are small compared to the measurement and forward model errors, the a priori profile dominates the solution; if they are large, the LWC profile information comes primarily from the measurements. The DGF and the retrieved LWC errors are also sensitive to the type of measurements included in the retrieval, namely MWR TBs, radar reflectivities or a combination of both.

By means of two case studies, it has been demonstrated that sensor synergy, i.e. the combination of cloud radar reflectivity and MWR brightness temperature observations, outperforms other retrievals which use data from one instrument alone. More precisely, MWR measurements can increase the information content compared to a retrieval using radar reflectivities alone and add about 1 degree of freedom for signal corresponding to the information of the LWP. However, in contrast to radar reflectivity measurements, MWR measurements alone do not contain enough information about the vertical profile of LWC. Although radar reflectivity measurements alone do include information on the vertical distribution of liquid water content, the error in the LWC derived for the two non-drizzling cloud cases is 63% assuming that the a priori profile is unknown and the measurement error is 3 dB. This error is reduced by a few percent if the individual measurement errors are correlated.

In drizzle situations, Z-LWC-relationships are less reliable and retrieved LWC errors are 100% or larger. LWC profiles with such large errors are not desirable, as the uncertainties in the CREs and CRFs that arise from the uncertainties in LWC can be considerable. In order to diminish the LWC errors, appropriate a priori information has to be included. By means of the two cloud cases, it has been shown that, for realistic measurement errors of 0.5 K and 3 dB for MWR brightness temperatures and radar reflectivities, respectively, the uncertainty of the a priori profile must be smaller than 100% in order to achieve a relative LWC error of 50% in non-drizzling cases. While, for small a priori uncertainties, the retrieved LWC error is in the same order of magnitude as the a priori error itself, the spread between a priori and retrieved error and therefore the benefit of the retrieval rapidly increases for a priori errors of about 30% or larger. The importance of the a priori profile is emphasized in drizzle situations, when the Z-LWC relationship is less accurate. In order to achieve a 50% (30%) LWC error in the drizzling cloud case, the a priori uncertainty must be smaller than 65% (32%). The derivation of accurate LWCs in drizzling clouds are important for the evaluation and the improvement of the representation of the drizzle process in climate and NWP models. Since drizzle is often present in stratocumulus clouds (*Fox and Illingworth*, 1997; *Khain* et al., 2008), an accurate representation of the drizzle process in numerical models is of interest.

In addition to these sensitivity studies, the interplay of the a priori and of the measurement information in the retrieved LWC profile and in the corresponding error have been analyzed with respect to the standard configuration of the IPT as applied for the AMF measurements. In this standard configuration, the a priori profile is a modified adiabatic profile whose errors are strongly correlated among each other. As a consequence, the a priori profile has a strong weight in the retrieval solution. In particular, only about 10% of the information in the LWC

profile comes from the measurements. The derived mean relative LWC error is about 20% for thin, non-drizzling water clouds ($\Delta z_{\text{cloud}} \lesssim 200\,\text{m}$). The error is much smaller for clouds with a larger vertical extension. In particular, the error is reduced with increasing cloud thickness. The more cloud layers exist, the more constrained is the a priori LWC value of a specific layer due to its dependence on the LWCs of all other layers. Thus, the error space of the a priori profile and the error space of the solution are confined.

When comparing LWCs derived by the IPT to the LWCs of the basic retrieval, a negative (positive) difference in cloud water content is visible for thin (thick) clouds. These differences may be related to a corresponding under- and overstimation of LWP in the a priori profile coupled with a too large weight of the a priori information in the retrieval. In addition, the underestimation of LWP in thin clouds can be the result of an underestimation of cloud vertical thickness or related to the measures radar reflectivity.

Although the LWC and LWP of SL WC may strongly vary between both retrievals, the mean CRE and CRF of SL WC are similar for both approaches. Variations in CRE do not exceed 14%. Due to the small LWC error estimates derived by the IPT corresponding uncertainties in CRE and in CRF are generally smaller than those for the assumed LWP errors as presented in the previous chapter.

The results of this chapter strongly suggest that the a priori information on the LWC profile including the representation of the a priori error has to be improved. It is likely that the a priori profile, and especially the correlation between different levels in the a priori profile, is very dependent on the synoptic and mesoscale conditions that are driving the cloud formation/evolution. Therefore, more in situ data are needed which span the wide range of atmospheric conditions and corresponding LWC profiles. This information could be gained, for example, from unmanned aerial vehicles, which are equipped with a LWC sensor. From such measurements, more accurate a priori LWC profiles and realistic layer to layer covariances could be derived and the IPT improved in this respect.

The IPT formalism allows for the inclusion of additional measurements or instruments to further constrain the solution. Since cloud radars are insensitive to the smallest droplets located near the bottom of the cloud, lidar measurements, which are sensitive to higher concentration of smaller particles, can provide valuable information for these layers. In this context, Raman lidar measurements can be used to derive vertical profiles of LWC (*Whiteman and Melfi*, 1999). Note that due to the strong extinction of the lidar signal by the cloud droplets, lidar measurements can only provide additional information on the LWC in the lowest cloud levels. The drizzling clouds (Section 7.2.6) can be identified and mitigated by using information of a dual-wavelength radar. *Hogan* et al. (2005) showed that, in boundary layer clouds, accurate LWC profiles can be retrieved from 35 GHz and 94 GHz cloud radar measurements, if the droplets scatter in the Rayleigh regime at both frequencies. The advantage of this technique is that no assumptions on the droplet size distribution have to be made. Spectral infrared measurements could also improve the solution in cases where LWP is low ($<50\,\text{g}\,\text{m}^{-2}$) since they are very sensitive to changes in liquid water in this regime (*Turner*, 2007).

Retrievals as the IPT have a large potential since the strengths of individual measurement systems are combined yielding a comprehensive characterization of the atmospheric state. In this way, also calculated cloud radiative effects and the corresponding uncertainties could be estimated more accurately.

Chapter 8

Summary and outlook

In this work, the cloud statistics during the nine-month deployment of the ARM Mobile Facility in the Murg Valley, Black Forest have been analyzed. To this end, high quality thermodynamic and cloud property profiles have been derived in a high vertical and temporal resolution using ground-based measurements of various active and passive remote sensing instruments and state-of-the-art retrieval techniques. Furthermore, the potential of the derived cloud properties to estimate the radiative effects of clouds has been assessed. By means of broadband radiative transfer calculations using a state-of-the art radiative transfer model, the cloud radiative effect and forcing of these clouds have been estimated. In particular, a detailed analysis of the uncertainties in the CRE and CRF due to uncertainties in the microphysical properties was performed for low-level water clouds. These clouds, which occur quite frequently and strongly affect the Earth-atmosphere's radiation budget (*Chen* et al., 2000), are still a challenge in terms of the accurate description of their microphysical properties (*Turner* et al., 2007).

The radiative effects of clouds have been studied since decades, but most of these earlier studies have focused on the effect of clouds on the radiation balance at the top of atmosphere employing satellite data. Although the satellite measurements give an insight into the net effect of clouds on the Earth-atmosphere system, they contain less information on the effect of clouds on the atmospheric and the surface radiation balance. In order to assess the effect of clouds on the atmospheric and surface radiation budget, the cloud climatology of the International Satellite Cloud Climatology Program ISCCP has been widely used (e.g., *Rossow and Zhang*, 1995; *Chen* et al., 2000). On the one hand, satellite observations have a large spatial coverage and thus provide a broad view on clouds in terms of their spatial distribution and to some extent on their macrophysial and microphysical properties. On the other hand, they include only limited information about the cloud vertical structure since they rely mostly on passive remote sensing techniques. More detailed measurements of cloud properties can be obtained from surface-based remote sensing techniques. The most accurate estimates of vertically resolved cloud properties can be gained from the synergy of ground-based instruments including at least a cloud radar, lidar, microwave radiometer and radiation sensors. Such detailed observations are very valuable in order to better understand the complex cloud processes and the effect of clouds on the radiation budget and on the vertical distribution of energy within the atmospere.

At present, such instrumentation is operated only at a few anchor sites world wide including the sites organized in the Cloudnet program (*Illingworth* et al., 2007) and the three permanent

sites and two mobile facilities of the ARM program (*Ackerman and Stokes*, 2003). Furthermore, only few studies exist which analyze the characteristics of clouds and their radiative effects on a long-term basis using synergetic ground based methods. These studies were performed for different locations and climatic regions with focus on the Tropics (*Mather* et al., 2007; *Mather and McFarlane*, 2009), on the high-latitudes (*Shupe and Intrieri*, 2004), and on a continental site in the Southern Great Plains (*Dong* et al., 2006; *Mace* et al., 2006b). The deployment of the ARM mobile facility from 1 April to 31 December 2007 in the Murg Valley, Black Forest, thus provided the unique oppurtunity to study clouds and their interaction with radiation at a low-mountain, mid-latitude site. On the basis of the AMF measurements and additional instrumentation, the present study thus improved the data basis of observed cloud characteristics in a high vertical and temporal resolution and gained new insights into the clouds and their radiative effects at a low-mountain, mid-latitude site. In contrast to previous studies, uncertainties in the cloud radiative effect and cloud radiative forcing for water clouds due to uncertainties in the microphysical properties have been analyzed in detail and the individual importance of LWC and $r_{\mathrm{eff,liq}}$ has been assessed.

Compilation of cloud macro- and microphysical properties

In the present work, macrophysical cloud properties, i.e. cloud boundaries and cloud phase, were analyzed using the Cloudnet target categorization product. In previous studies (e.g., *Mather* et al., 2007; *Mather and McFarlane*, 2009), temperature thresholds were simply used to detect the phase of the cloud particles in a cloud layer. The application of the categorization product in the present study allowed for a more detailed and accurate discrimination of the particle type due to the combination of various active and passive remote sensing instruments. Furthermore, state-of-the-art microphysical retrieval techniques and products were applied on the basis of the Cloudnet categorization product in order to characterize the microphysical properties of clouds, i.e. LWC, IWC, $r_{\mathrm{eff,liq}}$, and $r_{\mathrm{eff,ice}}$. This cloud property data set was complemented by a data set of derived thermodynamic profiles. Quality filters in the retrieval procedures, which deal with the consistency and reliability of the measurements, assured that the resulting microphysical and thermodynamic profiles give the optimal estimate for the atmospheric state at this time. Thus, the derived profiles are not only a valuable tool for the study of cloud-radiation interactions but also for the evaluation of the representation of clouds in NWP models. Since orographic terrain is particularly challenging for the simulation of cloud processes in NWP models, the operational output of the the high resolution NWP model COSMO-DE will be compared to the retrieved cloud properties in future studies to test the accuracy of the model. First comparisons between both data sets (Fig. 8.1) show that about 30% of low-level clouds are not resolved by the model grid. Thus, the representation of sub-grid scale clouds in the model is an important issue. Figure 8.1 shows that the diagnosis of subgrid-scale clouds increases the frequency of occurrence of low clouds by more than the triple fold. The comparison of observed and modeled clouds (Fig. 8.1) also suggest a possible tendency of the model to overestimate the frequency of occurrence of high clouds. These topics will be analyzed in detail in future.

Analysis of cloud properties

On the basis of the 768,838 30-s Cloudnet target categorization profiles, the occurrence of clouds and different cloud types, including single- (SL) and multi-layer (ML) water clouds

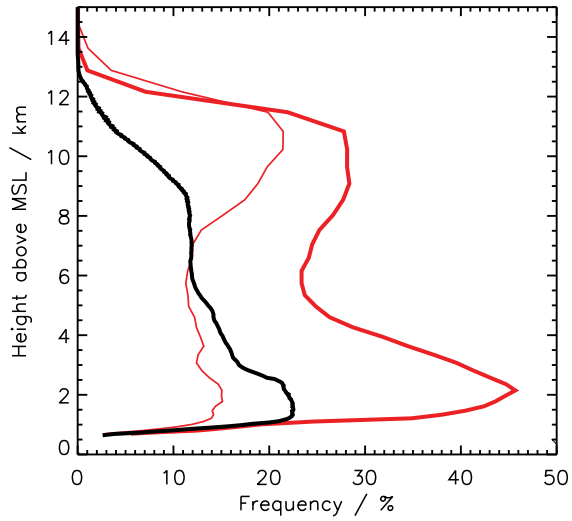

Figure 8.1: Frequency distribution of clouds in the atmospheric column during the AMF deployment on the basis of the Cloudnet target categorization (black line) and on COSMO-DE forecasts (red lines). The thin red line indicates the modelled grid-scale and the thick red line the modelled grid- and subgrid-scale clouds.

(WC), ice clouds (IC) and mixed clouds (MC) has been analyzed for the nine-month measurement period. Except for April, cloud frequency is greater than 60% in each month resulting in an overall cloud occurrence of 72%. The most common clouds are multi-layer mixed and single-layer water clouds occurring 28.4% and 11.3% of the time, respectively. Single-layer water clouds occur primarily in the lowest 2.5 km above the surface with a median thickness of 343 m.

The quality filters in the cloud microphysical retrieval techniques mostly affected the representativity of ice and mixed clouds in the data sample of the derived 364,850 atmospheric profiles. The excluded cases are mostly related to the limited observation capabilities of the MWR and the cloud radar. On the one hand, MWR radiometer measurements and therefore LWP measurements are not available if the radome is wet, i.e. during rain events or if dew has formed. On the other hand, IWC can not be derived from the cloud radar measurements if the radar signal can not be corrected for liquid attenuation or if the scattered signal is below the cloud radar's sensitivity. For future measurement campaigns, better heater and/or blower systems on MWRs are desirable which prevent the formation of dew on the radome and allow for a fast drying of the radome after rain events. Information on LWC during rain events may gained by using the measured Doppler spectra of a micro rain radar (*Peters* et al. (2002), 2002). The Doppler spectra can be transformed into number concentration versus drop size using the known relation between drop size and terminal fall velocity (*Atlas* et al., 1973) and the LWC can be estimated subsequently. In order to mitigate the low observing capability of high ice clouds or ice clouds above rain, satellite measurements could provide additional information. Since satellites can observe most of the high clouds with or without lower clouds underneath, and ground-based instruments see most of the low clouds, the combination of both observation systems is a reasonable consequence and has been proposed in the past (*van Lammeren* et al., 2000; *Feijt and van Lammeren*, 1996). In this way, ice and mixed clouds might be better represented in future studies.

It has been shown that water clouds can be characterized very well using ground-based remote sensing techniques. The observed SL WC have a median effective radius and LWP of

about 5.4 μm and 35.4 g m^{-2}, respectively. The LWP value found for the AMF site is lower than those found for the flat-terrain Cloudnet sites Chilbolton (49.6 g m^{-2}) and Lindenberg (40.0 g m^{-2}) for the same time period. In this respect, the representativity of column measurements for a site in orographic terrain and the horizontal variability of the LWP has to be mentioned. In particular, scanning observations during a two-month period in summer revealed higher (10-20 g m^{-2}) LWP in the direction to the hill crests on both sides of the Murg valley (*Kneifel*, personal communication). Furthermore, by comparing satellite and surface radiance measurements, *Deneke* et al. (2009) found a higher spatial inhomogeneity in clouds at the AMF site compared to those at Cabauw. In order to analyze the spatial variability of the LWP at the AMF site and associated orographic effects, the elevation and azimuth scans of the HATPRO instrument (*Kneifel* et al., 2008), which are partly available during the AMF deployment, could be analyzed in more detail in future studies. The HATPRO measurements, which have a high temporal resolution of about 1 s, could also be used to analyze the variability of water clouds within the 30-s integration interval used for the Cloudnet classification profiles. In this way, the temporal variabililty of clouds not described by the temporal resolution of the derived profiles could be assessed. At the moment, such analyses are performed for a persistent stratocumulus cloud layer, which was observed in October during several days with a mean LWP of 157 g m^{-2}. First results show that, in this rather homogeneous cloud field, the mean variabililty of LWP within 30-s intervals is about 6 g m^{-2} corresponding to 4% of the mean LWP value.

Evaluation of cloud properties

The retrieved thermodynamic and cloud property profiles have been evaluated in terms of radiative closure studies using the broadband radiative transfer model RRTMG. For clear-sky situations as indicated by a cloud flag from radiation measurements (*Long and Ackerman*, 2000), the calculated surface fluxes agree very well with observed ones. Average differences are less than 2.1% and 3.6% for the SW and LW fluxes, respectively, and are in the same order of magnitude as in other clear-sky comparisons in other studies (*Mather* et al., 2007; *Dupont and Haeffelin*, 2008). Compared to observations, SW (LW) surface downward fluxes are slightly overestimated (underestimated). These biases may be related to a slight underestimation in aerosol concentration, humidity and temperature. Since the humidity profile has been scaled with the IWV derived either from the HATPRO or the AMF two-channel MWR, a thorough analysis of both IWV along with the IWV derived from GPS will be performed in future.

The results of the cloudy flux comparison indicate that the derived cloud property profiles are consistent with the surface radiation budget, especially in the longwave part, and that the largest differences in the SW are related to broken cloud situations. As in similar studies that focused on the long-term radiative effect of clouds, a plane-parallel homogeneous atmosphere is assumed in the radiative transfer model. Due to this assumption, the calculated downwelling SW (LW) surface fluxes would have the tendency to be too small (large) compared to observed fluxes in broken cloud situations and thus yield a negative (positive) SW (LW) bias as observed in the present study. At the TOA, the calculated fluxes are in reasonable agreement with the observed fluxes by the GERB instrument given the large differences in temporal and spatial sampling. Restricting the analysis to more horizontally homogeneous cloud fields with cloud cover values greater than 90% considerably reduces the RMS difference and the bias. In particular, if only water clouds with cloud cover greater than 90% are considered, the SW (LW) bias is only about -10 W m^{-2} (1 W m^{-2}) and the standard deviation only about 50 W m^{-2} (4 W m^{-2}). The remaining small SW bias of -10 W m^{-2} might be

related to an overestimation of the cloud optical thickness. Since the cloud optical thickness is proportional to $\mathrm{LWP}/r_{\mathrm{eff,liq}}$ an overestimation of cloud optical thickness in turn may be a result of an overestimation of LWP and/or of an underestimation of particle size.

In order to better account for the spatial variabililty of clouds in the radiative transfer model, the Monte Carlo Independent Column Approximation, which is optionally implemented in the RRTMG, could be used if some vertical information on the cloud fraction is included. However, full 3-dimensional (3D) effects of clouds can only be assessed if 3D radiative transport calculations are performed using a different radiative transfer model. To this end, the 3D distribution of the clouds needs to be quantified. One way to account for horizontal cloud variability or, more precisely, for horizontal variability in the LWP is to make use of the previously mentioned HATPRO measurements in the azimuth or 3D scanning modus. It is planned to test the potential of these measurements to further increase the skill in describing the radiative feedback of clouds. In the framework of the new Atmospheric System Research program of the Department of Energy, the ARM measurement facilities will be provided with scanning cloud radars (*U.S. Department of Energy, Office of Science*, 2010). Since these scanning systems can capture the spatial variability of the cloud field, they will provide valuable information for future cloud-radiation interaction studies. In the near future, such a scanning system will also be installed at the Jülich Observatory for Cloud Evolution (JOYCE) maintained by the University of Cologne toghether with the Research Center Jülich. In addition, JOYCE hosts a HATPRO MWR, a total sky imager, and a ceilometer. In a future perspective, the JOYCE measurements will therefore increase the data base of long-term cloud observations and complement the long-term measurements of the ARM and Cloudnet sites.

Assessment of CRE and CRF

The good performance of the radiative transfer model in overcast water cloud situations and the good representation of water clouds in the data sample motivates the application of the derived cloud profiles in cloud-radiation interaction studies. At the surface, the CRE can be also derived from the surface fluxes observed by the AMF instrumentation and the clear-sky estimates according to *Long and Ackerman* (2000) and *Long and Turner* (2008). In this manner, the largest net SFC CRE in terms of absolute values has been found for multi-layer clouds containing liquid water, namely $-110\,\mathrm{W\,m^{-2}}$ for ML WC and $-116\,\mathrm{W\,m^{-2}}$ for ML MC. In terms of monthly mean values, it has been shown that clouds have a net cooling effect at the surface from April to October 2007 and a slight warming effect in November and December. In comparison to the SW SFC CREs calculated using the AMF observed and estimated clear-sky fluxes, the CRE for SL and ML WC is well reproduced by the radiative transfer calculations. The radiative transfer results reveal that SL and ML water clouds have a net cooling effect on the climate system, where the net TOA and SFC effect is more pronounced for the latter. Sensitivity studies revealed that variations due to uncertainties in LWP have an effect on the SW and net CRE at the TOA and surface, which is twice as large as the effect due to variations in effective radius. The higher sensitivity to LWP is related to clouds with low LWP values. For LWPs larger than $100\,\mathrm{g\,m^{-2}}$, the uncertainty in the CRE due to uncertainties in $r_{\mathrm{eff,liq}}$ is in the same order of magnitude as the one related to the LWP. Uncertainties in CRE due to uncertainties in the LWC profile shape are typically smaller by a factor of two compared to LWP uncertainties, but are not negligible.

For the CRF of SL and ML WC, the LWP and its distribution within the cloud boundaries are the most important factors. The uncertainties in CRF due to uncertainties in effective radius are typically an order of magnitude smaller. The derived uncertainties in net CRF,

which is dominated by the LW CRF, are up to $1\,\mathrm{K\,day^{-1}}$ for SL and $1.7\,\mathrm{K\,day^{-1}}$ for ML WC, corresponding to relative uncertainties of about 25 and 40%, respectively. Uncertainties in net CRF of SL WC which are related to uncertainties in the LWC profile shape are typically smaller than $0.2\,\mathrm{K\,day^{-1}}$ and therefore smaller than uncertainties due to LWP. For ML WC, uncertainties in the LWC profile shape induce uncertainties in the net CRF which are roughly in the same oder of magnitude as those due to LWP.

Integrated Profiling Technique

These results underline the importance of accurate LWC profiles for the assessment of the radiative effects of clouds and motivate the development and application of advanced LWC retrieval algorithms. In this respect, the performance of the Integrated Profiling Technique (IPT) has been discussed in the present study. This technique combines a priori information with MWR and cloud radar measurements in the framework of the optimal estimation (*Rodgers*, 2000). In the present study, it has been discussed in detail how a priori, measurement and forward model errors affect the retrieved LWC errors and the information content in the measurements with respect to the LWC retrieval. By means of two case studies, it has been demonstrated that sensor synergy, i.e. the combination of cloud radar reflectivity and MWR brightness temperature observations, outperforms other retrievals using data from one instrument alone. More precisely, MWR measurements can increase the information content compared to a retrieval using radar reflectivities alone and add about 1 degree of freedom for signal corresponding to the information of the LWP. In contrast to MWR measurements, radar reflectivity measurements alone do include information on the vertical distribution of liquid water content. However, in non-drizzling cloud cases, the error in the derived LWC is 63% assuming that the a priori profile is unknown and the measurement error is 3 dB. In drizzling cloud cases, where the forward model is less reliable, LWC errors are even larger. The necessity to include appropriate a priori information in order to diminish the LWC errors has been demonstrated. The results of the present work strongly suggest to improve the LWC a priori profile as well as the representation of the a priori error. In order to include improved a priori information, more in situ data are needed spanning the wide range of atmospheric conditions and corresponding LWC profiles. In this context, the experiment RACORO[1] of the ARM Aerial Vehicle Program is promising, which took place from January to June 2009 in the vicinity of the ARM Southern Great Plains measurement site (*ARM*, 2009). For the first time, a long-term aircraft campaign was undertaken for the systematic in situ sampling of boundary-layer water cloud properties.

The IPT is continuously improved. In particular, this retrieval technique allows for the inclusion of additional measurements of different kind of instruments to further constrain the solution. As a first step, *Löhnert* et al. (2009) successfully combined MWR measurements with information from an infrared spectrometer in the framework of the IPT to derive profiles of temperature and humidity for clear-sky cases. As a next step, it is planned to extend this retrieval to a combined scheme for thermodynamic and cloud properties, and to incorporate cloud radar measurements to aid in the retrieval of cloud microphysical properties. In the framework of the project ICOS[2], the IPT as used in this study will be extended by incorporating IR brightness temperatures and reflectances from the Spinning Enhanced Visible and Infra-red Imager (SEVIRI) on MSG. As discussed before, ground-based and satellite

[1]Routine ARM Aerial Facility (AAF) Clouds with Low Optical Water Depths (CLOWD) Optical Radiative Observations

[2]Integrating Cloud Observations from Ground and Space

measurements complement each other and are expected to improve the retrieval of the atmospheric state. On the one hand, the inclusion of the IR brightness temperatures will enhance the retrieval accuracy in LWP for low LWP clouds with LWPs smaller than $60\,\mathrm{g\,m^{-2}}$. On the other hand, the incorporation of the SEVIRI reflectances of the visible channels allows for the derivation of cloud optical thickness and cloud effective radius (*Roebeling* et al., 2006). As a precursor for the satellite extension, the IPT will be first amended by ground based observed IR brightness temperatures with a focus on the optimization of the forward model performance. In this respect, the various AMF measurements will provide the necessary input data.

Improved retrieval techniques of microphysical cloud properties will consequently increase the accuracy of calculated atmospheric fluxes and heating rates. In combination with the long-term ground-based measurements from the ARM, Cloudnet, and, in the near future, the JOYCE site as well as with satellite data, such techniques provide a powerful tool for the study of cloud-radiation processses and of the long-term radiative effect of clouds.

List of acronyms

AER	Atmospheric and Environmental Research, Incorporated
AMF	ARM Mobile Facility
AOD	Aerosol Optical Depth
AR4	4th IPCC Assessment Report
ARM	Atmospheric Radiation Measurement program
ATM	Atmospheric
CERES	Clouds' and Earth's Radiant Energy System
COPS	Convective and Orographically-induced Precipitation Study
COSMO-DE	NWP model of the Deutscher Wetterdienst
CRE	Cloud Radiative Effect
CRF	Cloud Radiative Forcing
DGF	Degrees of freedom for signal
DPR	Dual Polarization Radiometer
DWD	Deutscher Wetterdienst
ECHAM5	Global climate model based on the ECMWF GCM
ECMWF	European Centre for Medium-Range Weather Forecasts
ERBE	Earth Radiation Budget Experiment
FAP	Fast Absorption Predictor
GERB	Geostationary Earth Radiation Budget experiment
GCM	General Circulation Model
GME	Global model of the Deutscher Wetterdienst
GNDRAD	ARM radiometer system measuring upwelling sky irradiances
GPS	Global Positioning System
HATPRO	Humidity And Temperature Profiler
HR	Heating Rate
IC	Ice Clouds
ICOS	Integrating Cloud Observations from Ground and Space
IPCC	Intergovernmental Panel on Climate Change
IPT	Integrated Profiling Technique
IR	Infrared
ISCCP	International Satellite Cloud Climatology Program
IWC	Ice Water Content
IWP	Ice Water Path
IWV	Integrated Water Vapor
JOYCE	Jülich Observatory for Cloud Evolution
LBLRTM	Line-By-Line Radiative Transfer Model by AER
LDR	Linear Depolarization Ratio
LW	Longwave

LWC	Liquid Water Content
LWP	Liquid Water Path
MC	Mixed Clouds
MCICA	Monte Carlo Independent Column Approximation
MFRSR	Multi-Filter Rotating Shadowband Radiometer
ML	Multi-Layer
MODIS	Moderate Resolution Imaging Spectrometer
MonoRTM	Monochromatic Radiative Transfer Model by AER
MPL	Micropulse Lidar
MSG	Meteosat Second Generation
MT-CKD	Continuum Radiative Transfer Model by AER
MWR	Microwave Radiometer
MWRRET	MWR retrieval algorithm (*Turner* et al., 2007)
NASA	National Aeronautics and Space Administration
NCEP	National Centers for Environmental Prediction
NIR	Near Infrared
NWP	Numerical Weather Prediction
OPAC	Optical Properties of Aerosols and Clouds database
PPH	Plane-Parallel Homogeneous
RACORO	Routine ARM Aerial Facility (AAF) Clouds with Low Optical Water Depths (CLOWD) Optical Radiative Observations
RH	Relative Humidity
RMSD	Root Mean Square Difference
RRTM	Rapid Radiative Transfer Model by AER
RRTMG	Rapid Radiative Transfer Model for GCM applications by AER
RTE	Radiative Transfer Equation
RTO	Radiative Transfer Operator
ScaRaB	Scanner for Radiation Budget mission
SEVIRI	Spinning Enhanced Visible and Infrared Imager on MSG
SFC	Surface
SGP	Southern Great Plains
SIRTA	Site Instrumental de Recherche par Télédétection Atmosphérique
SKYRAD	ARM radiometer system measuring downwelling sky irradiances
SL	Single-Layer
SONDE	ARM radiosonde data product
STDDEV	Standard Deviation
SW	Shortwave
SZA	Solar Zenith Angle
TB	Brightness Temperature
TOA	Top Of Atmosphere
TRMM	Tropical Rainfall Measurement Mission
TSI	Total Sky Imager
UTC	Universal Time Coordinated
UV	Ultraviolet
VIS	Visible
VRTE	Vector Radiative Transfer Equation
WACR	W-Band ARM Cloud Radar
WC	Water Clouds

List of symbols

a	regression coefficient Z-LWC or Z-IWC relation
a_n	Mie coefficient
A	area
$\mathbf{A}$	averaging kernel matrix
b	regression coefficient Z-LWC or Z-IWC relation
b_n	Mie coefficient
B	black body intensity (Planck)
$\mathbf{BT}$	MWR brightness temperature vector
c	velocity of light
c_1, c_2	regression coefficient α_{dir}-α_{dif}-θ relation
C_p	specific heat capicity of air at constant pressure
CH_4	methane
CO_2	carbon dioxide
CRE	cloud radiative effect
CRF	cloud radiative forcing
d	dimension of $\mathbf{y}$
D	cloud particle diameter
DGF	degrees of freedom for signal
E	energy
F	irradiance or flux density (short: flux)
F_{BB}	black body flux density (Planck)
$F^{\downarrow}$, $F^{\uparrow}$, F^{net}	downward / upward / net flux density
$F^{\downarrow}_{SWdir}$, $F^{\downarrow}_{SWdif}$, $F^{\downarrow}_{SWtot}$	direct / diffuse / total SW downward flux density
$F^{\downarrow}_{SWtot}$, $F^{\downarrow}_{SWdir}$	total / reflected direct SW upward flux density
$\mathbf{F}$	forward model vector
g	asymmetry factor
$g(k_a)$	cumulative probability function in k_a space
h	height above cloud base
h_P	Planck constant
H_2O	water
HR	heating rate
i	iteration index
I	radiance or intensity
I_0	incident intensity
I_{emit}	emitted intensity
I_s	scattered intensity
IWC	ice water content

IWP	ice water path
IWV	integrated water vapor
$\mathrm{IWV_{MWR}}$	integrated water vapor of MWR
$\mathrm{IWV_{PROF}}$	integrated water vapor of radiosonde profile
J	source function
k_a, k_s, k_e	mass absorption / scattering / extinction coefficient
k_B	Boltzmann constant
k_W	Wien's constant
$\mathbf{K}$	Jacobi matrix
LWC	liquid water content
LWC_{ad}	adiabatic liquid water content
$\mathbf{LWC}$	LWC vector
LWP	liquid water path
$\mathrm{LWP_{AP}}$	liquid water path of the a prori profile
$\mathrm{LWP_{IPT}}$	liquid water path of the IPT
$\mathrm{LWP_{STAT}}$	liquid water path of the statistical MWR retrieval
m	array index
$\mathcal{M}_k$	kth moment of the cloud particle size distribution
n	array index
n_a	Angstrom exponent
N	cloud particle concentration
$\mathrm{N_2O}$	nitrous oxide
$\mathrm{O_2}$	molecular oxygen
$\mathrm{O_3}$	ozone
p	phase function
$\mathbf{q}$	humidity vector
Q_s	scattering efficiency
r	particle radius
r_{eff}	cloud droplet effective radius
r_m	modal droplet radius
$r_{\mathrm{eff,liq}}$	effective radius of liquid droplets
$r_{\mathrm{eff,ice}}$	effective radius of ice particles
R	arbitrary distance
RH	relative humidity
RTO	radiative transfer operator for MWR brightness temperatures
$\mathbf{s}$	position vector
$\mathbf{S}_a$	a priori covariance matrix
$\mathbf{S}_e$	forward model and measurement covariance matrix
$\mathbf{S}_{op}$	covariance matrix of optimal solution
t	time
T	temperature
T_s	surface temperature
$\mathbf{T}$	temperature vector
TB	brightness temperature
TB_K, TB_V, TB_{90}, TB_{150}	brightness temperature of K- / V-band / at 90 / 150 GHz
x	size parameter
$\mathbf{x}$	atmospheric state vector
$\mathbf{x}_a$	a priori atmospheric state vector
$\mathbf{x}_{op}$	atmospheric state vector of optimal solution

$\mathbf{x}_{true}$	true atmospheric state vector
$\mathbf{y}$	measurement vector
z	height
z_{bot}, z_{top}	height of cloud bottom / top
Z	radar reflectivity factor
$\mathbf{Z}$	radar reflectivity vector
α_{LW}	longwave albedo
α_{dif}, α_{dir}	albedo for diffuse / direct SW radiation
α_{dif}^{month}	monthly mean albedo for diffuse SW radiation
β	parameter for cloud layer correlation
β_a, β_s, β_e	volume absorption / scattering / extinction coefficient
ε	emissivity
θ	zenith angle
Θ	scattering angle
λ	wavelength; as index: monochromatic
λ_0	reference wavelength
λ_{max}	wavelength of maximum Planck intensity
μ	cosine of zenith angle
ρ	air density
ρ_l	density of liquid water
ρ_i	density of ice
σ	Stefan-Boltzmann constant
σ_a, σ_s, σ_e	absorption / scattering / extinction cross section
σ_{mm}	square root of diagonal entry in $\mathbf{S}_a$
σ_x	logarithmic spread of lognormal distribution
τ	optical thickness or depth of all atmospheric contributors
τ_c	cloud optical thickness or depth
ϕ	azimuth angle
$\tilde{\omega}$	single-scatter albedo
Ω	solid angle

Bibliography

Ackerman, T. and G. Stokes, The Atmospheric Radiation Measurement Program, *Physics Today*, 56, 38–45, 2003.

Angstrom, A., On the atmospheric transmission of sun radiation and on dust in the air, *Geografiska Annaler*, 11, 156–166, 1929.

ARM, Routine AAF Clouds with Low Optical Water Depths (CLOWD) Optical Radiative Observations (RACORO), 2009, http://acrf-campaign.arm.gov/racoro, Online; accessed 8 Septemer 2010.

Atlas, D., The estimation of cloud parameters by radar, 11, 309–317, 1954.

Atlas, D., S. Matrosov, A. Heymsfield, M.-D. Chou, and D. Wolff, Radar and radiation properties of ice clouds, *Journal of Applied Meteorology*, 34, 2,329–2,345, 1995.

Atlas, D., R. Srivastava, and R. Sekhon, Doppler radar characteristics of precipitation at vertical incidence, *Reviews of Geophysics and Space Physics*, 11, 1–35, 1973.

Baldauf, M., J. Förstner, S. Klink, T. Reinhardt, C. Schraff, A. Seifert, and K. Stephan, *Kurze Beschreibung des Lokal-Modells Kürzestfrist LMK und seiner Datenbanken auf dem Datenserver des DWD*, German Weather Service (DWD), Geschäftsbereich Forschung und Entwicklung, P.O. Box 100465, 63004 Offenbach, Germany, 2007.

Barker, H., A parameterization for computing grid-averaged solar fluxes for inhomogeneous marine boundary layer clouds. Part I: Methodology and homogeneous biases, *Journal of the Atmospheric Sciences*, 53, 2,289–2,303, 1996.

Barker, H., G. Stephens, P. Partain, J. Bergman, B. Bonnel, K. Campana, E. Clothiaux, S. Clough, S. Cusack, J. Delamere, J. Edwards, K. Evans, Y. Fouquart, S. Freidenreich, V. Galin, Y. Hou, S. Kato, J. Li, E. Mlawer, J. Morcrette, W. O'Hirok, P. Räisänen, V. Ramaswamy, B. Ritter, E. Rozanov, M. Schlesinger, K. Shibata, P. Sporyshev, Z. Sun, M. Wendisch, N. Wood, and F. Yang, Assessing 1D atmospheric solar radiative transfer models: Interpretation and handling of unresolved clouds, *Journal of Climate*, 16, 2676–2698, 2003.

Barkstrom, B., The Earth Radiation Budget Experiment (ERBE), *Bulletin of the American Meteorological Society*, 65, 1,170–1,185, 1984.

Bergman, J. and H. Hendon, Calculating monthly radiative fluxes and heating rates from monthly cloud observations, *Journal of the Atmospheric Sciences*, 55, 3,471–3,491, 1998.

Buchholtz, A., D. Hlavka, M. McGill, K. Schmidt, P. Pilewskie, S. Davis, E. Reid, and A. Walker, Directly measured heating rates of a tropical subvisible cirrus cloud, *Journal of Geophysical Research*, 115, D00J09, doi:10.1029/2009JD013128, 2010.

Cady-Pareira, K., M. Shephard, D. Turner, E. Mlawer, S. Clough, and T. Wagner, Improved daytime column-integrated precipitable water vapor from Vaisala radiosonde humidity sensors, *Journal of Atmospheric and Oceanic Technology*, 25, 873–883, 2008.

Cahalan, R., W. Ridgway, W. Wiscombe, T. Bell, and J. Snider, The albedo of fractal stratocumulus clouds, *Journal of the Atmospheric Sciences*, 51, 2434–2455, 1994.

Campbell, J., D. Hlavka, E. Welton, C. Flynn, D. Turner, J. Spinhirne, and V. Scott, Full-time eye safe cloud and aerosol lidar observation at the atmospheric radiation measurement program sites: Instruments and data processing, *Journal of Atmospheric and Oceanic Technology*, 19, 431–442, 2002.

Chandrasekhar, S., *Radiative Transfer*, Dover Publications, New York, 1960, 303 pp.

Chen, T., W. Rossow, and Y. Zhang, Radiative effects of cloud-type variations, *Journal of Climate*, 13, 264–286, 2000a.

Chen, T., Y. Zhang, and W. Rossow, Sensitivity of atmospheric radiative heating rate profiles to variations of cloud layer overlap, *Journal of Climate*, 13, 2941–2959, 2000b.

Clothiaux, E., M. Miller, B. Albrecht, T. Ackerman, J. Verlinde, D. Babb, R. Peters, and W. Syrett, An evaluation of a 94-GHz radar for remote sensing of cloud properties, *Journal of Atmospheric and Oceanic Technology*, 12, 201–229, 1995.

Clough, S., M. Shephard, E. Mlawer, J. Delamere, M. Iacono, K. Cady-Pereira, S. Boukabara, and P. Brown, Atmospheric radiative transfer modeling: a summary of the AER codes, *Journal of Quantitative Spectroscopy and Radiative Transfer*, 91, 233–244, 2005.

Crewell, S., K. Ebell, U. Löhnert, and D. Turner, Can liquid water profiles be retrieved from passive microwave zenith observations?, *Geophysical Research Letters*, 36, doi:10.1029/2008GL036934, 2009.

Crewell, S. and U. Löhnert, Accuracy of cloud liquid water path from ground-based microwave radiometry 2. Sensor accuracy and strategy, *Radio Science*, 38 (3), 8042, doi:10.1029/2002RS002634, 2003.

Crewell, S. and U. Löhnert, Accuracy of boundary layer temperature profiles retrieved with multifrequency multiangle microwave radiometry, *IEEE Transactions on Geoscience and Remote Sensing*, 45 (7), 2195–2201, 2007.

Crewell, S., C. Simmer, H. Bloemink, A. Feijt, S. García, D. Jolivet, O. Krasnov, A. van Lammeren, U. Löhnert, E. van Meijgaard, J. Meywerk, K. Pfeilsticker, M. Quante, S. Schmidt, M. Schrder, T. Scholl, T. Trautmann, V. V. an M. Wendisch, and U. Willén, The BALTEX Bridge Campaign: An integrated approach for a better understanding of clouds, *Bulletin of the American Meteorological Society*, 85(10), 1565–1584, 2004.

Delanoë, J. and R. Hogan, A variational scheme for retrieving ice cloud properties from combined radar, lidar and infrared data, *Journal of Geophysical Research*, 113, doi:10.1029/2007JD009000, 2008.

Deneke, H., W. Knap, and C. Simmer, Multiresolution analysis of the temporal variance and correlation of transmittance and reflectance of an atmospheric column, *Journal of Geophysical Research*, 114, D17206, doi:10.1029/2008JD011680, 2009.

Dick, G., G. Gendt, and C. Reigber, First experience with near real-time water vapor estimation in a German GPS network, *Journal of Atmospheric and Solar-Terrestrial Physics*, 63(12), 1295–1304, 2001.

Doms, G., J. Förstner, E. Heise, H.-J. Herzog, M. Raschendorfer, R. Schrodin, T. Reinhardt, and G. Vogel, *A Description of the Nonhydrostatic Regional Model LM. Part II: Physical Parameterization*, German Weather Service (DWD), P.O. Box 100465, 63004 Offenbach, Germany, 2005.

Dong, X. and G. Mace, Arctic stratus cloud properties and radiative forcing derived from ground-based data collected at Barrow, Alaska, *Journal of Climate*, 16, 445–461, 2003.

Dong, X., P. Minnis, and B. Xi, A climatology of midlatitude continental clouds from the ARM SGP Central Facility: Part 1: Low-level cloud macrophysical, microphysical, and radiative properties, *Journal of Climate*, 18, 1391–1410, 2005.

Dong, X., P. Minnis, and B. Xi, A climatology of midlatitude continental clouds from the ARM SGP Central Facility: Part 2: Cloud fraction and surface radiative forcing, *Journal of Climate*, 19, 1765–1783, 2006.

Donovan, D., Ice-cloud effective particle size parameterization based on combined lidar, radar reflectivity, and mean Doppler velocity measurements, *Journal of Geophysical Research*, 108 (D18), doi:10.1029/2003JD003469, 2003.

Donovan, D. and A. van Lammeren, Cloud effective particle size and water content profile retrievals using combined lidar and radar observations 1. Theory and examples, *Journal of Geophysical Research*, 106 (D21), 27425–27448, 2001.

Draine, B. and P. Flatau, Discrete-dipole approximations for scattering calculations, *Journal of the Optical Society of America A*, 11, 1,491–1,499, 1994.

Drusch, M. and S. Crewell, *Hydrological application of remote sensing: Basic principles and sensors: Radiative transfer*, John Wiley & Sons, Ltd., 2005, Edited by M.G. Anderson, ISBN:0-471-49103-9, 3,456 pp.

Dupont, J. and M. Haeffelin, Observed instantaneous cirrus radiative effect on surface-level shortwave and longwave irradiances, *Journal of Geophysical Research*, 113, D21202. DOI:10.1029/2008JD009838, 2008.

Ebell, K., U. Löhnert, S. Crewell, and D. Turner, On characterizing the error in a remotely sensed liquid water content profile, *Atmospheric Research*, 98, 57–68, 2010.

Ebert, E. and J. Curry, A parameterization of ice cloud optical properties for climate models, *Journal of Geophysical Research*, 97 (D4), 3,831–3,836, 1992.

Feijt, A. and A. van Lammeren, Ground-based and satellite observations of cloud fields in the Netherlands, *Monthly Weather Review*, 124 (9), 1914–1923, 1996.

Fox, N. and A. Illingworth, The retrieval of stratocumulus cloud properties by ground-based cloud radar, *Journal of Applied Meteorology*, 36, 485–492, 1997.

Frisch, A., C. Fairall, and J. Snider, Measurement of stratus cloud and drizzle parameters in ASTEX with a K_α-Band doppler radar and a microwave radiometer, *Journal of the Atmospheric Sciences*, 52, 2788–2799, 1995.

Frisch, A., G. Feingold, C. Fairall, T. Uttal, and J. Snider, On cloud radar and microwave radiometer measurements of stratus cloud liquid water profiles, *Journal of Geophysical Research*, 103, 23195–23197, 1998.

Frisch, A., M. Shupe, I. Djalalova, G. Feingold, and M. Poellot, The retrieval of stratus cloud droplet effective radius with cloud radars, *Journal of Atmospheric and Oceanic Technology*, 19, 835–842, 2002.

Fu, Q., An accurate parameterization of the solar radiative properties of cirrus clouds for climate models, *Journal of Climate*, 9, 2058–2082, 1996.

Fu, Q., P. Yang, and W. Sun, An accurate parameterization of the infrared radiative properties of cirrus clouds for climate models, *Journal of Climate*, 11, 2223–2237, 1998.

Gaussiat, N., R. Hogan, and A. Illingworth, Accurate liquid water path retrieval from low-cost microwave radiometers using additional information from a lidar ceilometer and operational forecast models, *Journal of Atmospheric and Oceanic Technology*, 24, 1562–1575, 2007.

Handwerker, J. and M. Miller, Intercomparison of measurements obtained by vertically pointing collocated 95 GHz and 35.5 GHz cloud radars, in *Proc. Fifth European Conference on Radar in Meteorology and Hydrology,*, 2008, Helsinki, Finland, Finish Meteorological Institute, P5.3. [Available online at http://erad2008.fmi.fi/proceedings/extended/erad2008-0124-extended.pdf.].

Harries, J., J. Russel, J. Hanafin, H. Brindley, J. Futyan, J. Rufus, S. Kellock, G. Matthews, R. Wrigley, A. Last, J. Mueller, R. Mossavati, J. Ashmall, E. Sawyer, D. Parker, M. Caldwell, P. Allan, A. Smith, M. Bates, B. Coan, B. Stewart, D. Lepine, L. Cornwall, D. Corney, M. Ricketts, D. Drummond, D. Smart, R. Cutler, S. Dewitte, N. Clerbaux, L. Gonzalez, A. Ipe, C. Bertrand, A. Joukoff, D. Crommelynck, N. Nelms, D. Llewellyn-Jones, G. Butcher, G. Smith, Z. Szewczyk, P. Mlynczak, A. Slingo, R. Allan, and M. Ringer, The Geostationary Earth Radiation Budget project, *Bulletin of the American Meteorological Society*, 86 (7), 945–960, 2005.

Harrison, L., J. Michalsky, and J. Berndt, Automated multifilter rotating shadow-band radiometer: an instrument for optical depth and radiation measurements , *Applied Optics*, 33, 5,118–5,125, 1994.

Hartmann, D., M. Ockert-Bell, and M. Michelsen, The effect of cloud type on Earth's energy balance: Global analysis, *Journal of Climate*, 5, 1,281–1,304, 1992.

Hess, M., P. Koepke, and I. Schult, Optical properties of aerosols and clouds: The software package OPAC, *Bulletin of the American Meteorological Society*, 79, 831–844, 1998.

Hogan, R., M. Mittermaier, and A. Illingworth, The retrieval of ice water content from radar reflectivity factor and temperature and its use in evaluating a mesoscale model, *Journal of Geophysical Research*, 45, 301–317, 2006.

Hogan, R. J., N. Gaussiat, and A. Illingworth, Stratocumulus liquid water content from dual-wavelength radar, *Journal of Atmospheric and Oceanic Technology*, 22, 1207–1218, 2005.

Hogan, R. J. and E. J. O'Connor, Facilitating cloud radar and lidar algorithms: the Cloudnet Instrument Synergy/Target Categorization product, page 14 pp, 2004, Cloudnet documentation: http://www.cloud-net.org/data/products/categorize.html.

Hu, Y. and K. Stamnes, An accurate parameterization of the radiative properties of water clouds suitable for use in climate models, *Journal of Climate*, 6, 728–742, 1993.

Illingworth, A. J., R. J. Hogan, E. J. O'Connor, D. Bounoil, M. E. Brooks, J. Delanoë, P. Donovan, J. D. Eastment, N. Gaussiat, J. W. F. Goddard, M. Haeffelin, H. Klein, H. K. Baltink, O. A. Krasnov, J. Pelon, J.-M. Piriou, A. Protat, H. W. J. Russchenberg, A. Seifert, A. M. Tompkins, G.-J. van Zadelhoff, F. Vinit, U. Willén, D. R. Wilson, and C. L. Wrench, CLOUDNET Continous evaluation of cloud profiles in seven operational models using ground-based observations, *Bulletin of the American Meteorological Society*, 88 (6), 883–898, 2007.

IPCC, Climate change 2001: The scientific basis., Contribution of working group I to the Third Assessment Report of the Intergovernmental Panel on Climate Change, Cambridge University Press, Cambridge, United Kingdom and New York, NY, USA, 2001.

IPCC, Climate change 2007: The physical science basis., Contribution of working group I to the Fourth Assessment Report of the Intergovernmental Panel on Climate Change, Cambridge University Press, Cambridge, United Kingdom and New York, NY, USA, 2007.

Ivanova, D., D. Mitchell, W. Arnott, and M. Poellot, A GCM parameterization for bimodal size spectra and ice mass removal states in mid-latitude cirrus clouds, *Atmospheric Research*, 59-60, 89–113, 2001.

Kandel, R. e. a., The ScaRaB Earth radiation budget dataset, *Bulletin of the American Meteorological Society*, 79, 765–783, 1998.

Karstens, U., C. Simmer, and E. Ruprecht, Remote sensing of cloud liquid water, *Meteorology and Atmospheric Physics*, 54, 157–171, 1994.

Khain, A., M. Pinsky, L. Magaritz, O. Krasnov, and H. Russchenberg, Combined observational and model investigations of the Z-LWC relationship in stratocumulus clouds, *Journal of Applied Meteorology and Climatology*, 47, 591–606, 2008.

Kneifel, S., S. Crewell, U. Löhnert, and J. Schween, Investigating water vapor variability by groundbased microwave radiometry: evaluation using airborne observations, *IEEE Geoscience and Remote Sensing Letters*, 6 (1), 157–161, 2008.

Korolev, A., G. Isaac, J. Strapp, S. Cober, and H. W. Barker, In situ measurements of liquid water content profiles in midlatitude stratiform clouds, *Quarterly Journal of the Royal Meteorological Society*, 133, 1693–1699, 2007.

L'Ecuyer, T., N. Wood, T. Haladay, G. Stephens, and P. S. Jr., Impact of clouds on atmospheric heating based on the R04 CloudSat fluxes and heating rates data set, *Journal of Geophysical Research*, 113, D00A15, doi:10.1029/2008JD009951, 2008.

Lenoble, J., *Radiative Transfer in Scattering and Absorbing Atmospheres: Standard Computational Procedures*, A. Deepak Publishing, Hampton, Virginia, 1985, 300 pp.

Lhermitte, R., A 94-GHz Doppler radar for cloud observations, *Journal of Atmospheric and Oceanic Technology*, 4, 36–48, 1987.

Liebe, H., G. Hufford, and M. Cotton, Propagation modeling of moist air and suspended water/ice particles at frequencies below 1000 GHz, in *Atmospheric propagation effects through natural and man-made obscurants for visible through mm-wave radiation*, 1993, AGARD-CP-542, 3.1.-3.10.

Liebe, H., G. Hufford, and T. Manabe, A model for the complex permittivity of water at frequencies below 1 THz, *International Journal of Infrared and Millimeter Waves*, 12 (7), 659–675, 1991.

Liou, K., *An Introduction to Atmospheric Radiation,International Geographical Series, Second Edition*, Academic Press, 2002, 583 pp.

Liu, C.-L. and A. Illingworth, Toward more accurate retrievals of ice water content from radar measurements of clouds, *Journal of Applied Meteorology*, 39, 1130–1146, 2000.

Löhnert, U., Derivation of cloud liquid water from ground-based active and passive microwave remote sensors, Doctoral Thesis, Meteorological Institute, Rheinische Friedrich-Wilhems-Universität Bonn, 2002.

Löhnert, U. and S. Crewell, Accuracy of cloud liquid water path from ground-based microwave radiometry 1. Dependency on cloud model statistics, *Radio Science*, 38 (3), doi:10.1029/2002RS002654, 2003.

Löhnert, U., S. Crewell, O. Krasnov, E. O'Connor, and H. Russchenberg, Advances in continuously profiling the thermodynamic state of the boundary layer: integration of measurements and methods, *Journal of Atmospheric and Oceanic Technology*, 25, 1251–1266, 2008.

Löhnert, U., S. Crewell, and C. Simmer, An integrated approach towards retrieving physically consistent profiles of temperature, humidity and cloud liquid water, *Journal of Applied Meteorology*, 43 (9), 1295–1307, 2004.

Löhnert, U., S. Crewell, C. Simmer, and A. Macke, Profiling cloud liquid water by combining active and passive microwave measurements with cloud model statistics, *Journal of Atmospheric and Oceanic Technology*, 18, 1354–1366, 2001.

Löhnert, U., D. Turner, and S. Crewell, Ground-based temperature and humidity profiling using spectral infrared and microwave observations: Part 1. Retrieval performance in clear sky conditions, *Journal of Applied Meteorology and Climatology*, 48 (5), 1,017–1,032, 2009.

Löhnert, U., E. van Meijgaard, H. Baltink, S. Groß, and R. Boers, Accuracy assessment of an integrated profiling technique for operationally deriving profiles of temperature, humidity, and cloud liquid water, *Journal of Geophysical Research*, 112, D04205, doi:10.1029/2006JD007379, 2007.

Long, C. and T. Ackerman, Identification of clear skies from broadband pyranometer measurements and calculation of downwelling shortwave cloud effects, *Journal of Geophysical Research*, 105 (D12), 15,609–15,626, 2000.

Long, C. and D. Turner, A method for continuous estimation of clear-sky downwelling longwave radiative flux developed using ARM surface measurements, *Journal of Geophysical Research*, 113, D18206, doi:10.1029/2008JD009936, 2008.

Lorenz, L., Lysbevaegelsen i og uder en plane lysbolger belyst kulge, *Det Kongelige Danske Videnskabernes Selskabs Skrifter*, 6, 1–62, 1890.

Mace, G., T. Ackerman, P. Minnis, and D. Young, Cirrus layer microphysical properties derived from surface-based millimeter radar and infrared interferometer data, *Journal of Geophysical Research*, 103 (D18), 23,207–23,216, 1998.

Mace, G., S. Benson, and S. Kato, Cloud radiative forcing at the Atmospheric Radiation Measurement Program Climate Research Facility: 2. Vertical redistribution of radiant energy by clouds, *Journal of Geophysical Research*, 111 (D11), D11S91, doi:10.1029/2005JD005922, 2006b.

Mace, G., S. Benson, K. Sonntag, S. Kato, Q. Min, P. Minnis, C. Twohy, M. Poellot, X. Dong, C. Long, Q. Zhang, and D. Doelling, Cloud Radiative Forcing at the Atmospheric Radiation Measurement Program Climate Research Facility: 1. Technique, Validation, and Comparison to Satellite-Derived Diagnostic Quantities, *Journal of Geophysical Research*, 111 (D11), D11S90, doi:10.1029/2005JD005921, 2006a.

Masuda, K., T. Kobayashi, E. Raschke, F. Albers, W. Koch, and U. Maixner, Short-wave radiation flux divergence in arctic cirrus: A case study, *Atmospheric Research*, 53, 251–267, 2000.

Mather, J. and S. McFarlane, Cloud classes and radiative heating profiles at the Manus and Nauru Atmospheric Radiation Measurement (ARM) sites, *Journal of Geophysical Research*, 114, D19204, doi:10.1029/2009JD011703, 2009.

Mather, J., S. McFarlane, M. Miller, and K. Johnson, Cloud properties and associated radiative heating rates in the tropical western Pacific, *Journal of Geophysical Research*, 112, D05201, doi:10.1029/2006JD007555, 2007.

Matrosov, S., Retrievals of vertical profiles of ice cloud microphysics from radar and IR measurements using tuned regressions between reflectivity and cloud parameters, *Journal of Geophysical Research*, 104 (D14), 16,741–16,753, 1999.

Mattioli, V., P. Basili, S. Bonafoni, P. Ciotti, L. Pulvirenti, N. Pierdicca, F. Marzano, F. Consalvi, E. Fionda, and E. Westwater, Cloud liquid models for propagation studies: Evaluation and refinements, in *Proc. of EuCAP 2006*, 2006, Nice, France, 6-10 November 2006 (ESA SP-626, October 2006).

Mattioli, V., P. Basili, S. Bonafoni, P. Ciotti, and E. Westwater, Analysis and improvements of cloud models for propagation studies, *Radio Science*, 44, doi:10.1029/2008RS003876, 2009.

McFarlane, S., J. Mather, T. Ackerman, and Z. Liuand, Effect of clouds on the calculated vertical distribution of shortwave absorption in the tropics, *Journal of Geophysical Research*, 113, D18203, doi:10.1029/2008JD009791, 2008.

Météo France, Quality Control on GTS data at Météo France, Technical report, Météo France, Service Central d'Exploitation, SCEM/TTI/DEV, 42, Avenue G. Coriolis, 31057 Toulouse Cedex 1, 1997, ftp://cnrm-ftp.meteo.fr/pub-fastex/doc/GTS_QC_handbook.ps.gz. Online; accessed 25 May 2010.

Mie, G., Beiträge zur Optik trüber Medien, speziell kolloidaler Metalllösungen, *Annalen der Physik*, 25, 377–445, 1908.

Miles, N., J. Verlinde, and E. Clothiaux, Cloud droplet size distributions in low-level stratiform clouds, *Journal of the Atmospheric Sciences*, 57, 295–311, 2000.

Mishchenko, M., L. Travis, and D. Mackowski, T-Matrix computations of light scattering by non-spherical particles: A review, *Journal of Quantitative Spectroscopy and Radiative Transfer*, 55, 535–575, 1996.

Mlawer, E., S. Traubman, P. Brown, M. Iacono, and S. Clough, Radiative transfer for inhomogeneous atmospheres: RRTM, a validated correlated-k model for the longwave, *Journal of Geophysical Research*, 102 (D14), 16663–16682, 1997.

Morcrette, J.-J., H. Barker, J. Cole, M. Iacono, and R. Pincus, Impact of a new radiation package, McRad, in the ECMWF integrated forecasting system, *Monthly Weather Review*, 136, 2008, 4773-4798.

Nörenberg, D., Development of ground equipment for atmospheric propagation conditions assessment from 10 up to 90 GHz frequency bands (ATPROP), Software documentation, Institute for Geophysics and Meteorolgy, University of Cologne, and Radiometer Physics GmbH, Meckenheim, 2008, ESA CONTRACT 19839/06/NL/GLC.

Oreopoulos, L., R. Cahalan, and S. Platnick, The plane-parallel albedo bias of liquid clouds from MODIS observations, *Journal of Climate*, 20, 5,114–5,125, 2007.

Oreopoulus, L. and H. Barker, Accounting for subgrid-scale cloud variability in a multilayer 1-D solar radiative transfer algorithm, *Quarterly Journal of the Royal Meteorological Society*, 125, 1999, 301-330.

Peters, G., B. Fischer, and T. Andersson, Rain observations with a vertically looking Micro Rain Radar (MRR), *Boreal Environment Research*, 7, 353–362, 2002.

Petty, G., *A first course in atmospheric radiation, Second Edition*, Sundog Publishing, Madison, Wisconsin, 2006, 458 pp.

Pincus, R., H. Barker, and J.-J. Morcrette, A fast, flexible, approximate technique for computing radiative transfer in inhomogeneous cloud fields, *Journal of Geophysical Research*, 108 (D13, 2003, doi:10.1029/2002JD003322.

Protat, A., J. Delanoë, A. Plana-Frattori, P. May, and E. O'Connor, The statistical properties of tropical ice clouds generated by the West African and Australians monsoons from ground-based radar-lidar observations, *Quarterly Journal of the Royal Meteorological Society*, 136, 345–363, 2010.

Ramsey, P. and D. Vincent, Computation of vertical profiles of longwave radiative cooling over the equatorial Pacific, *Journal of the Atmospheric Sciences*, 52, 1,555–1,572, 1995.

Rayleigh, L., On the light from the sky, its polarization and colour, *Philosophical Magazine*, 41, 107–120, 1871.

Rodgers, C., *Inverse methods for atmospheric sounding: theory and practice*, World Scientific, 2000, 238 pp.

Roebeling, R., A. Feijt, and P. Stammes, Cloud property retrievals for climate monitoring: implications of differences between SEVIRI on METEOSAT-8 and AVHRR on NOAA-17, *Journal of Geophysical Research*, 111, D20210, doi:10.1029/2005JD006990, 2006.

Rogers, R. and M. Yau, *A short course in cloud physics*, Butterworth-Heinemann, 1989, 290 pp.

Rose, T., S. Crewell, U. Löhnert, and C. Simmer, A network suitable microwave radiometer for operational monitoring of the cloudy atmosphere, *Atmospheric Research*, 75, 183–200, 2005.

Rosenkranz, P., Water vapor microwave continuum absorption: A comparison of measurements and models, *Radio Science*, 33, 919–928, 1998.

Rossow, W. and R. Schiffer, Advances in understanding clouds from ISCCP, *Bulletin of the American Meteorological Society*, 80 (11), 2,261–2,287, 1999.

Rossow, W. and Y.-C. Zhang, Calculation of surface and top of atmosphere radiative fluxes from physical quantities based on ISCCP data sets: 2. Validation and first results, *Journal of Geophysical Research*, 100 (D1), 1,167–1,197, 1995.

Russchenberg, H., U. Löhnert, C. Brandau, and K. Ebell, Radar scattering by stratocumulus: often much lower than expected. Why?, in *Proceedings of the 8th International Symposium on Tropospheric Profiling, Delft, The Netherlands*, edited by A. Apituley, H. Russchenberg, and W. Monna, 2009, ISBN: 978-90-6960-233-2.

Salonen, E. and S. Uppala, New prediction method of cloud attenuation, *Electronic Newsletter*, 27 (12), 1106–1110, 1991.

Sassen, K., Z. Wang, V. Khvorostyanov, G. Stephens, and A. Bennedetti, Cirrus cloud ice water content radar algorithm evaluation using an explicit cloud mirophysical model, *Journal of Applied Meteorology*, 41, 620–628, 2002.

Sauvegeot, H. and J. Omar, Radar reflectivity of cumulus clouds, *Journal of Atmospheric and Oceanic Technology*, 4, 264–272, 1987.

Schiffer, R. and W. Rossow, The International Satellite Cloud Climatology Project (ISCCP): The first project of the World Climate Research Programme, *Bulletin of the American Meteorological Society*, 64, 779–784, 1983.

Schmetz, J., P. Pili, S. Tjemkes, D. Just, J. Kerkmann, S. Rota, and A. Ratier, An introduction to Meteosat Second Generation (MSG), *Bulletin of the American Meteorological Society*, 83, 977–994, 2002.

Sengupta, M., E. Clothiaux, T. Ackerman, S. Kato, and Q. Min, Importance of accurate liquid water path for estimation of solar radiation in warm boundary layer clouds: an observational study, *Journal of Climate*, 16, 2997–3009, 2003.

Shupe, M. and J. Intrieri, Cloud radiative forcing of the Arctic surface: The influence of cloud properties, surface albedo, and solar zenith angle, *Journal of Climate*, 17, 616–628, 2004.

Shupe, M., P. Kollias, S. Matrosov, and T. Schneider, Deriving mixed-phase cloud properties from Doppler radar spectra, *Journal of Atmospheric and Oceanic Technology*, 21, 660–670, 2004.

Simmer, C., *Satellitenfernerkundung hydrologischer Parameter der Atmosphäre mit Mikrowellen*, Verlag Dr. Kovac, 1994, 313 pp.

Slingo, A GCM parameterization for the SW radiative properties of water clouds, *Journal of the Atmospheric Sciences*, 46, 1419–1427, 1989.

Spinhirne, J., Micro pulse lidar, *IEEE Transactions on Geoscience and Remote Sensing*, 31, 48–55, 1993.

Stephens, G., Cloud feedbacks in the climate system: A critical review, *Journal of Climate*, 18, 237–273, 2005.

Stephens, G., D. Vane, R. Boain, G. Mace, K. Sassen, Z. Wang, A. Illingworth, E. OConnor, W. Rossow, S. Durden, S. Miller, R. Austin, A. Benedetti, C. Mitrescu, and the CloudSat Science Team, The CloudSat mission and the A-Train: A new dimension of spacebased observations of clouds and precipitation, *Bulletin of the American Meteorological Society*, 83, 1,771–1,790, 2002.

Tiedtke, M., A comprehensive mass flux scheme for cumulus parameterization in large-scale models, *Monthly Weather Review*, 117, 1779–1799, 1989.

Turner, D., Arctic mixed-phase cloud properties from AERI lidar observations: Algorithm and results from SHEBA, *Journal of Applied Meteorology*, 44, 427–444, 2005.

Turner, D., Improved ground-based liquid water path retrievals using a combined infrared and microwave approach, *Journal of Geophysical Research*, 112, D15204, doi:10.1029/2007JD008530, 2007.

Turner, D., S. Ackerman, B. Baum, H. Revercomb, and P. Yang, Cloud phase determination using ground-based AERI observations at SHEBA, *Journal of Applied Meteorology*, 42, 701–715, 2003.

Turner, D., S. Clough, J. Liljegren, E. Clothiaux, K. Cady-Pareira, and K. Gaustad, Retrieving liquid water path and precipitable water vapor from the Atmospheric Radiation Measurement (ARM) microwave radiometers, *IEEE Transactions on Geoscience and Remote Sensing*, 45 (11), 3680–3690, 2007a.

Turner, D., U. Löhnert, M. Cadeddu, S. Crewell, and A. Vogelmann, Modifications to the water vapor continuum in the microwave suggested by ground-based 150 GHz observations, *IEEE Transactions on Geoscience and Remote Sensing*, 47, 3326–3337, doi:10.1109/TGRS.2009.202262, 2009.

Turner, D., A. Vogelmann, R. Austin, J. Barnard, K. Cady-Pereira, J. Chiu, S. Clough, C. Flynn, M. Khaiyer, J. Liljegren, K. Johnson, B. Lin, C. Long, A. Marshak, S. Matrosov, S. McFarlane, M. Miller, Q. Min, P. Minnis, W. O'Hirok, Z. Wang, and W. Wiscombe, Thin Liquid Water Clouds: Their Importance and Our Challenge, *Bulletin of the American Meteorological Society*, 88, 177–190, 2007b.

U.S. Department of Energy, Office of Science, Atmospheric System Research (ASR) Science and Program Plan, 2010, http://www.sc.doe.gov/ober/Atmospheric System Research Science Plan.pdf. Online; accessed 8 Septemer 2010. 77 pp.

Van de Hulst, H., *Light scattering by small particles*, Dover Publications, New York, 1981, 470 pp.

van Lammeren, A., A. Feijt, J. Konings, E. van Meijgaard, and A. van Ulden, Combination of ground-based and satellite cloud observations on a routine basis, *Meteorologische Zeitschrift*, 9 (2), 125–134, 2000.

van Meijgaard, E. and S. Crewell, Comparison of model predicted liquid water path with ground-based measurements during CLIWA-NET, *Atmospheric Research*, 75, 201–226, 2005.

van Zadelhoff, G.-J., D. Donovan, H. K. Baltink, and R. Boers, Comparing ice cloud microphysical properties using CloudNET and Atmospheric Radiation Measurement Program data, *Journal of Geophysical Research*, 109, D24214, doi:10.1029/2004JD004967, 2004.

van Zadelhoff, G.-J., A. Heymsfield, D. Donovan, and M. McGill, Evaluating lidar-radar microphysics retrieval using in situ measurements, *Journal of Geophysical Research*, 112, D09213, doi:10.1029/2006JD007202, 2007.

Vömel, H., H. Selkirk, L. Miloshevich, J. Valverde, J. Valdés, E. Kyrö, R. Kivi, W. Stolz, G. Peng, and J. Diaz, Radiation dry bias of the Vaisala RS92 humidity sensor, *Journal of Atmospheric and Oceanic Technology*, 24, 953–963, 2007.

Wang, Z. and K. Sassen, Cloud type and macrophysical property retrieval using multiple remote sensors, *Journal of Applied Meteorology*, 40, 1665–1682, 2001.

Warner, J., The water content of cumuliform clouds, *Tellus*, 7, 449–457, 1955.

Westwater, E., The accuracy of water vapor and cloud liquid determination by dual-frequency ground-based microwave radiometry, *Radio Science*, 13 (4), 677–685, 1978.

Whiteman, D. and S. Melfi, Cloud liquid water, mean droplet radius, and number density measurements using a Raman lidar, *Journal of Geophysical Research*, 104 (D24), 31,411–31,419, 1999.

Wielicki, B., B. Barkstrom, E. Harrison, R. L. III, G. Smith, and J. Cooper, Clouds and the Earth's Radiant Energy System (CERES): An Earth observing system experiment, *Bulletin of the American Meteorological Society*, 77, 853–868, 1996.

Wielicki, B., R. Cess, M. King, D.A.Randall, and E. Harrison, Mission to planet Earth: Role of clouds and radiation in climate, *Bulletin of the American Meteorological Society*, 76, 2,125–2,153, 1995.

Wulfmeyer, V., A. Behrendt, H.-S. Bauer, C. Kottmeier, U. Corsmeier, A. Blyth, G. Craig, U. Schumann, M. Hagen, S. Crewell, P. D. Girolamo, C. Flamant, M. Miller, A. Montani, S. Mobbs, E. Richard, M. Rotach, M. Arpagaus, H. Russchenberg, P. Schlüssel, M. König, V. Gärtner, R. Steinacker, M. Dorninger, D. Turner, T. Weckwerth, A. Hense, and C. Simmer, The Convective and Orographically-induced Precipitation Study: A Research and Development Project of the World Weather Research Program for improving quantitative precipitation forecasting in low-mountain regions, *Bulletin of the American Meteorological Society*, 89 (10), 1477–1486, 2008.

Yang, F., K. Mitchell, Y.-T. Hou, Y. Dai, X. Zeng, Z. Wang, and X.-Z. Liang, Dependence of land surface albedo on solar zenith angle: Observations and model parameterization, *Journal of Applied Meteorology and Climatology*, 47, 2963–2982, 2008.

Zhang, Y., W. Rossow, A. Lacis, V. Oinas, and M. Mishchenko, Calculation of radiative fluxes from the surface to top of atmosphere based on ISCCP and other global data sets: Refinements of the radiative transfer model and the input data, *Journal of Geophysical Research*, 109, D19105, doi:10.1029/2003JD004457, 2004.

Zickfeld, K., M. Morgan, D. Frame, and D. Keith, Expert judgments about transient climate response to alternative future trajectories of radiative forcing, *Proceedings of the National Academy of Sciences of the United States of America*, 107 (28), 12,451–12,456, 2010.

Danksagung

Part of the work has been funded by the German Research Foundation within the priority program SPP 1167 Quantitative Precipitation Forecast under grants CR 111/5-2 and WU356/4-2. Part of the data was obtained from the Atmospheric Radiation Measurement Program sponsored by the U.S. Department of Energy, Office of Science, Office of Biological and Environmental Research, Environmental Sciences Division.

An dieser Stelle möchte ich zudem all jenen danken, die durch ihre fachliche und persönliche Unterstützung zum Gelingen dieser Arbeit beigetragen haben.

Vielen Dank, Susanne, dass Du mir diese Arbeit ermöglicht hast und mir während der letzten Jahre mit Rat und Tat zur Seite standest. Ich habe mich stets gut betreut gefühlt.

Ich danke Prof. Dr. Kerschgens dafür, dass er sich bereit erklärt hat, diese Arbeit zu begutachten.

Vielen Dank, Uli, dass Du mir Deine IPT anvertraut hast und für Fragen immer ein offenes Ohr hattest. Danke, für die vielen hilfreichen Diskussionen. Es tut mir sehr Leid, dass ich Dich wegen Deiner Zucchiniabneigung aufgezogen habe. Es ist völlig in Ordnung, wenn man keine Zucchinis mag.

Ein großer Dank gilt zudem Wen, ohne den die Durchführung der RRTMG-Läufe nicht so schnell möglich gewesen wäre. Danke für Deine Unterstützung!

I also thank Ewan O'Connor who provided the Cloudnet target categorization product and promptly answered my various e-mails. The discussions with Dave Turner always helped to improve this work. Thank you both for your support and advice. A special thank you also goes to Nicolas Clerbaux who provided the GERB data.

Liebe Infernos, danke für die schöne Zeit in den letzten Jahren. Ich habe mich sehr wohl gefühlt. Insbesondere danke ich meinen alten und neuen Zimmerkollegen für die vielen fachlichen und sehr vielen nicht-fachlichen Gespräche in Raum 307: Mario, Thorsten, Jan, Christoph, Sonja und Gerrit. Sonja gebührt ein Extra-Dank für das Korrekturlesen der Arbeit. Dorle und Bernhard, auch wenn Ihr nicht mehr hier seid, seid Ihr nicht vergessen! Bernhard, ich würde immer wieder die EGU mit Dir schwänzen. Dorle, danke dass Du mir immer Mut gemacht hast. Mir fehlen Deine Flüche, die weit über den Flur zu hören waren.

Ich danke meinen Freunden, dass sie mich von Zeit zu Zeit von der Arbeit abgehalten haben. Insbesondere danke ich Elli und den Beckumer Mädels. Ihr habt mich immer wieder aufgebaut.

Ohne die Unterstützung meiner Familie, vor allem meiner Eltern, wäre diese Arbeit nicht möglich gewesen. Danke, dass Ihr immer für mich da seid.

Ich danke Dir, Simon, dass Du mir gezeigt hast, dass Probleme nie so groß sind, dass man sie nicht bewältigen kann – et hätt noch immer jot jejange. Danke für Deine großartige Unterstützung, insbesondere während der Endphase Deiner eigenen Promotion.

Erklärung

Ich versichere, dass ich die von mir vorgelegte Dissertation selbständig angefertigt, die benutzten Quellen und Hilfsmittel vollständig angegeben und die Stellen der Arbeit - einschließlich Tabellen, Karten und Abbildungen -, die anderen Werken im Wortlaut oder dem Sinn nach entnommen sind, in jedem Einzelfall als Entlehnung kenntlich gemacht habe; dass diese Dissertation noch keiner anderen Fakultät oder Universität zur Prüfung vorgelegen hat; dass sie - abgesehen von unten angegebenen Teilpublikationen - noch nicht veröffentlicht worden ist sowie, dass ich eine solche Veröffentlichung vor Abschluss des Promotionsverfahrens nicht vornehmen werde. Die Bestimmungen dieser Promotionsordnung sind mir bekannt. Die von mir vorgelegte Dissertation ist von Prof. Dr. S. Crewell betreut worden.

Köln, den 29. 09. 2010

Kerstin Ebell

Teilveröffentlichungen

- Crewell, S., K. Ebell, U. Löhnert, D.D. Turner, Can liquid water profiles be retrieved from passive microwave zenith observations?, *Geophysical Research Letters*, 36, doi:10.1029/2008GL036934, 2009.
- Ebell, K., U. Löhnert, S. Crewell und D.D. Turner, On characterizing the error in a remotely sensed liquid water content profile, *Atmospheric Research*, 98, 57–68, 2010.
- Ebell, K., S. Crewell, U. Löhnert, D.D. Turner und E.J. O'Connor, Cloud statistics and cloud radiative effect for a low-mountain site, *Quarterly Journal of the Royal Meteorological Society*, accepted.